Lentivirus-meditated frataxin gene delivery reverses genome instability in Friedreich ataxia patient and mouse model fibroblasts

Thesis submitted for the degree of Doctor of Philosophy by

Hassan Khonsari

November 2015

College of Health and Life Sciences

ABSTRACT

Friedreich ataxia (FRDA) is a progressive neurodegenerative disease with primary sites of pathology in the large sensory neurons of the dorsal root ganglia (DRG) and dentate nucleus of the cerebellum. FRDA is also often accompanied by severe cardiomyopathy and diabetes mellitus. FRDA is caused by loss of frataxin (*FXN*) expression, which is due to GAA repeat expansion in intron 1 of the *FXN* gene. Frataxin is a mitochondrial protein important in iron-sulphur cluster (ISC) biogenesis and in the electron transport chain (ETC). As a consequence of impaired mitochondrial energy metabolism, FRDA cells show increased levels of and sensitivity to oxidative stress, which is known to be associated with genome instability. In this study, we investigated DNA damage/repair in relation to *FXN* expression via immunostaining of γ-H2AX, a nuclear protein that is recruited to DNA double strand breaks (DSBs). We found FRDA patient and YG8sR FRDA mouse model fibroblasts to have inherently elevated DNA DSBs (1.8 and 0.9 foci/nucleus) compared to normal fibroblasts (0.6 and 0.2 foci/nucleus, in each case P <0.001). By delivering the *FXN* gene to these cells with a lentivirus vector (LV) at a copy number of ~1/cell, *FXN* mRNA levels reached 48 fold (patient cells) and 42 fold (YG8sR cells) and protein levels reached 20 fold (patient cells) and 3.5 fold (YG8sR cells) that of untreated fibroblasts, without observable cytotoxicity. This resulted in a reduction in DNA DSB foci to 0.7 and 0.43 (in each case P <0.001) in human and YG8sR fibroblasts, respectively and an increase in cell survival to that found for normal fibroblasts. We next irradiated the FRDA fibroblasts (2Gy) and measured their DSB repair profiles. Both human and mouse FRDA fibroblasts were unable to repair damaged DNA. However, repair returned to near normal levels following LV *FXN* gene transfer. Our data suggest frataxin may be important for genome stability and cell survival by ensuring ISC for DNA damage repair enzymes or may be required directly for DNA DSB repair.

ACKNOWLEDGEMENTS

First I would like to express the deepest gratitude to my first and second supervisors Dr. Michael Themis and Dr. Mark Pook for their guidance, support and encouragement throughout my PhD. I am highly grateful for this opportunity and I thank them for accepting me as their student.

I would like to thank Dr. Sahar Al-Mahdawi and Dr. Matthew Themis for the training, advice and assistances they have always provided in every step of the way.

I am grateful to Dr. Christopher Parris for his input in the DNA damage study and also his suggestions with the immunofluorescence assays.

I would like to express my sincere thanks to Dr. Yaghoub Gozaly and Dr. Hemad Yasaei for being helpful whenever needed.

I would like to thank Dr. Steve Howe (UCL, UK) for providing the vectors used in this project.

It is my pleasant honour to thank Ataxia UK, FARA Australia and FARA USA for providing financial support.

Finally I would like to thank my parents for been patient and supportive during these years and also I would like to thank my wife for being with me in every step of the way.

DECLARATION

I hereby declare that the research presented in this thesis is my own work, except where otherwise specified, and has not been submitted for any other degree.

Hassan Khonsari

TABLE OF CONTENTS

LIST OF TABLES

LIST OF FIGURES

ABBREVIATIONS

5-aza-CdR	5-aza-2'-deoxycytidine
AAV	Adeno-associated virus
ACK	Ammonium chloride potassium (K)
ADA	Adenosine deaminase
AMV RT	Avian myeloblastosis virus reverse transcriptase
APC	Antigen presenting cell
APOBEC3G	Apolipoprotein B mRNA editing enzyme catalytic polypeptide-like 3G
A-T	Ataxia-telangiectasia
ATM	Ataxia telangiectasia mutated
ATP	Adenosine triphosphate
ATP	Adenosine triphosphate
BAC	Bacterial artificial chromosome
BCA	Bicinchoninic acid
BER	Base excision repair
BME	Beta-mercaptoethanol
bp	Base pair
BPB	Bromophenol blue
BSA	Bovine serum albumin
CA	Capsid
CAI	Codon adaptation index
cAMP	Cyclic adenosine monophosphate
CCCD	Cooled charged-coupled device camera
cDNA	Complementary DNA
ChIP	Chromatin immunoprecipitation
Ci	Curie
CMV	Cytomegalovirus
CNS	Central nervous system
CO_2	Carbon dioxide
CoQ	Coenzyme Q
CpG	Cytosine and guanine separated by a phosphate
cpm	Counts per minute
cPPT	Central polypurine tract
DAPI	4', 6-diamidino-2-phenylindole
DDR	DNA damage response
DEPC	Diethyl pyrocarbonate
dH_2O	Distilled water
DMEM	Dulbecco's Modified Eagle Medium
DMSO	Dimethyl sulfoxide
DNA	Deoxyribonucleic acid
dNTP	Deoxynucleotide triphosphate
DRG	Dorsal root ganglia
DSB	Double strand break
EDTA	Ethylene diamine-tetra acetic acid
GFP	Enhanced green fluorescent protein
EIAV	Equine Infectious Anaemia Virus

ELISA	Enzyme-linked immunosorbent assay
Env	Envelope
ETC	Electron transport chain
EtOH	Ethanol
FACS	Fluorescence-activated cell sorter
FBS	Fetal bovine serum
FCS	Foetal calf serum
Fe	Iron
Fe-S	Iron-sulphur
FISH	Fluorescent *in situ* hybridization
FIV	Feline Immunodeficiency Virus
FIX	Coagulation Factor IX
FRDA	Friedreich Ataxia
FVIII	Coagulation Factor VIII
Gag	Group specific antigens
GAPDH	Glyceraldehyde-3-phosphate dehydrogenase
GP	Glutathione peroxidase
GSH	Glutathione
H2AX Histone	H2AX phosphorylated on serine-139
H_2O_2	Hydrogen peroxide
HAT	Histone acetyltransferase
HD	Huntington disease
HEPES	4-(2-hydroxyethyl)-1-piperazineethanesulfonic acid
HIV-1	Human Immunodeficiency Virus-1
HMTases	Histone methyltransferases
HR	Homologous recombination
HSC	Haematopoietic stem cell
HSV	Herpes simplex virus
i.p.	Intraperitoneally
ICL	Interstrand crosslink
IDLV	Integration deficient lentiviral vector
IFU	Infectious units
Ig	Immunoglobulin
ILV	Integrating lentiviral vector
IMS	Industrial methylated spirit
IN	Integrase
iPS	Induced pluripotent stem cells
ISC	Iron Sulfur Cluster
kb	Kilobases
kDa	Kilo Dalton
LB	Luria-Bertani
LCL	Lymphoblastoid cell line
LMO2	LIM domain only 2
LMW	Low molecular weight
LTR	Long terminal repeat
LV	Lentiviral vector
ml	Millilitre
M	Molar

MA	Matrix
MAP-2	Microtubule associated protein 2
mg	Milligram
MHC	Major histocompatibility complex
MIU	Molecular Immunology Unit
MLV	Murine leukaemia virus
MMR	Mismatch repair
MOI	Multiplicity of infection
MRC	Mitochondrial respiratory chain
mRNA	Messenger RNA
n	Nano
NaCl	Sodium chloride
NADP	Nicotinamide adenine dinucleotide phosphate
NC	Nucleocapsid
NER	Nucleotide excision repair
NF-κB	Nuclear factor κB
NHEJ	Non-homologous end-joining
NMR	Nucleic magnetic resonance
NSC	Neural stem cells
OD	Optical density
p24Gag	HIV-1 p24 gag capsid protein
PAGE	Polyacrylamide gel electrophoresis
PBMC	Peripheral blood mononuclear cell
PBS	Phosphate buffered saline
PCR	Polymerase chain reaction
PD	Parkinson disease
PEI	Polyethyleneimine
pen-strep	Penicillin and streptomycin
PFA	Paraformaldehyde
PIC	Pre-integration complex
PNS	Peripheral nervous system
PR	Protease
Prx	Peroxiredoxin
qRT-PCR	Quantitative real-time PCR
RBC	Red blood cells
RCLs	Replication competent lentiviruses
RCR	Replication competent retrovirus
RNA	Ribonucleic acid
ROS	Reactive oxygen species
rpm	Revolutions per minute
RRE	Rev-response element
RSV	Rous sarcoma virus
RT	Reverse Transcriptase
RT-PCR	Reverse transcriptase PCR
SCID	Severe combined immunodeficiency
SCID-X1	X-linked severe combined immunodeficiency
SDS	Sodium dodecyl sulphate
SEM	Standard error of the mean

SFFV	Spleen focus forming virus
SIN	Self-inactivating
SOD	Superoxide dismutase
Sp1	Specificity protein 1
SP-PCR	Small-pool PCR
SSB	Single strand break
T cell	Thymus derived lymphocyte
TAE	Tris-acetate-EDTA
TBE	Tris-borate-EDTA
TCR	T cell receptor
TE	Tris-EDTA
TEMED	Tetramethylethylenediamine
TM	Transmembrane glycoprotein
TNR	Trinucleotide repeat
Tris	Tris (hydroxymethyl) aminomethane
TRS	Trinucleotide/triplet repeats sequence
TrxS2	Thioredoxin
TSA	Trichostatin A
TSS	Transcription start sites
U	Units
UTR	Untranslated region
UV	Ultra violet
v/v	Volume per volume
VSV-G	Vesicular stomatitis virus glycoprotein
w/v	Weight per volume
w/w	Weight per weight
WPRE	Woodchuck hepatitis virus posttranscriptional regulatory element
WR	Working reagent
WT	Wild-type
X-SCID	X-linked severe combined immunodeficiency
YAC	Yeast artificial chromosome
γc	Common cytokine receptor gamma chain
μ	Micro
Ψ	Packaging signal

CHAPTER 1 - FRIEDREICH ATAXIA: LITERATURE REVIEW

1.1 Ataxia

The ataxias are a group of progressive neurodegenerative disorders with ataxia as the leading symptom (Klockgether, 2007, Harding, 1984). Ataxia comes from a Greek word α- taxia, meaning lack of order. Ataxia involves dysfunction of the parts of the nervous system that coordinate movement, such as the cerebellum (Nardin and Johns, 2001). Ataxias are classified into two groups of hereditary and non-hereditary (sporadic). The hereditary ataxias are further divided into two subgroups of autosomal recessive ataxias that include Friedreich ataxia and autosomal dominant spinocerebellar ataxias. In addition, the non-hereditary ataxias are categorized into acquired ataxias and sporadic degenerative ataxias (Table 1.1) (Klockgether, 2007).

1. **Hereditary ataxias**

- ***Autosomal recessive ataxias***

  Friedreich ataxia (FRDA) [Most common type of this group]
  Ataxia telangiectasia (AT)
  Autosomal recessive ataxia with oculomotor apraxia type 1 (AOA1)
  Autosomal recessive ataxia with oculomotor apraxia type 2 (AOA2)
  Spinocerebellar ataxia with axonal neuropathy (SCAN1)
  Abetalipoproteinemia
  Ataxia with isolated vitamin E deficiency (AVED)
  Refsum's disease
  Cerebrotendinous xanthomatosis
  Other autosomal recessive ataxias

- ***Autosomal dominant ataxias***

  Spinocerebellar ataxias (SCA)

2. **Non-hereditary degenerative ataxias**

- **Sporadic degenerative ataxias**

  Multiple system atrophy, cerebellar type (MSA-C)
  Sporadic adult-onset ataxia of unknown origin (SAOA)

- **Acquired ataxias**

  Alcoholic cerebellar degeneration
  Ataxia due to other toxins

Table 1.1: Classification of progressive ataxias**.**

1.2 Friedreich ataxia

Friedreich ataxia (FRDA) (OMIM 2290300), was first reported in 1863 by Nikolaus Friedreich (1825-1882) in Heidelberg Germany (Alper and Narayanan, 2003). This German pathologist wrote five long articles on a seemingly new spinal disease (Friedreich, 1863, Friedreich, 1876), but the relatively short postscript on the fourth paper (Friedreich, 1877) pointed out his first insights into what is now known as 'Friedreich's ataxia' and articulated the hereditary nature of the disorder (Koeppen, 2013). 120 years after these reports Campuzano *et al.* in 1996 discovered the genetic defect underlying FRDA (Campuzano *et al.*, 1996). Identification of this mutation within the gene encoding frataxin (*FXN*) led to considerable interest in FRDA as a model disorder. Being the most common autosomally recessive neurodegenerative disorder, FRDA represents a fascinating example of so-called 'triplet-repeat' diseases. The vast majority of FRDA cases are linked to an expansion mutation of (GAA)n repeats within the intron 1 of *FXN* gene, leading to a largely reduced expression of the mitochondrial protein frataxin.

1.2.1 Clinical Features

Symptoms of FRDA normally becomes an evident feature around puberty (Harding, 1981), but age at onset may vary significantly. The earliest onset may be around the age of 2 years, while late-onset FRDA is defined as having onset after the age of 25 years. (De Michele *et al.*, 1994, Moschner *et al.*, 1994). The first symptom is usually gait instability and in rare cases, hypertrophic cardiomyopathy is diagnosed before the onset of ataxia. Ataxia of mixed cerebellar and sensory type is the cardinal symptom. Other clinical features include degenerative atrophy of the posterior columns of the

spinal cord contributing to progressive ataxia, sensory loss and muscle weakness, scoliosis, foot deformity and cardiac symptoms. (Table 1.2)

- Progressive ataxia (legs, arms, and speech)
- Dysarthria
- Atrophy of the spinal cord (MRI)
- Heart disease (abnormalities on ECG)
- Eye movements
- Areflexia (fixation instability)
- Extensor plantar responses
- Foot deformity
- Diabetes
- Vision loss

Table 1.2: Clinical features of Friedreich ataxia.

With progression, gait becomes broad-based, with frequent losses of balance, fine motor skills deteriorate and evident feature of advanced FRDA is limb weakness. On average, 10 to 15 years after onset, patients lose the ability to walk, stand, and sit without support (Harding, 1981) In any case, because of substantial physical disability, FRDA often has a substantial effect on academic, professional, and personal development (Pandolfo, 2008).

1.2.2 Pathophysiology

FRDA neuropathology involves peripheral nerves, the spinal cord and the cerebellum (Pandolfo, 2009). The first site of neurodegeneration is at the dorsal root ganglia (DRG) (Figure 1.1), with loss of large sensory neurons and cells in the posterior columns, followed by degeneration of the corticospinal and spinocerebellar tracts of the spinal cord. Frataxin deficiency also leads to axonal neuropathy with a progressive reduction of large myelinated fibers (Morral *et al.*, 2010).

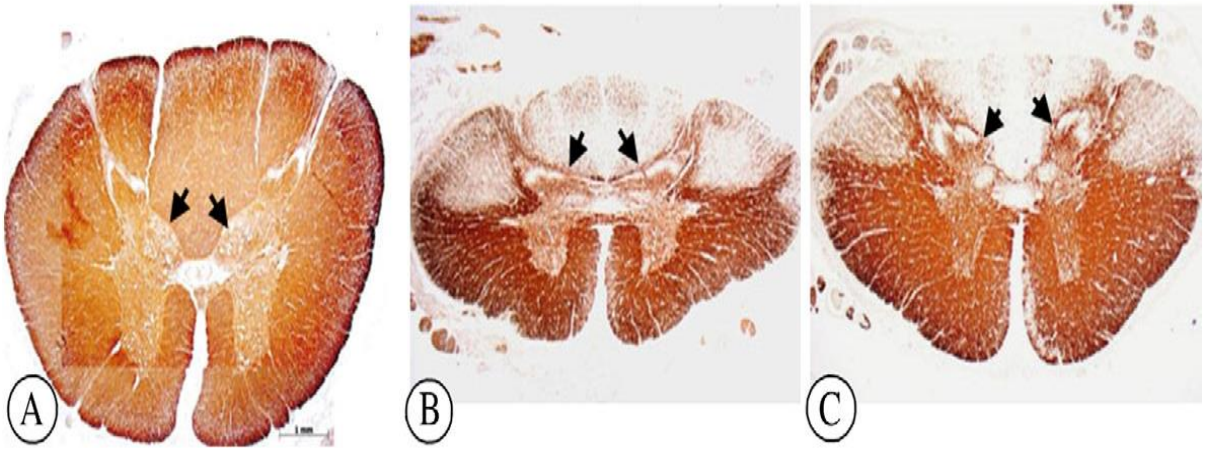

Figure 1.1: Thoracic spinal cord size comparison in a normal control and FRDA patients. (A) Normal control. (B&C) FRDA. Great reduction of the spinal cord areas in FRDA, irrespective of age of FRDA onset. Bars, 1mm picture modified from (Koeppen *et al.*, 2011).

Hypertrophic cardiomyopathy with thickening of the left ventricular wall and the septum can be detected by heart ultrasonography in most patients, and the electrocardiogram is almost always abnormal in the repolarization phase, indicating that subclinical heart disease is almost universal in FRDA. Iron deposits in the myocardium have also been reported (Figure 1.2).

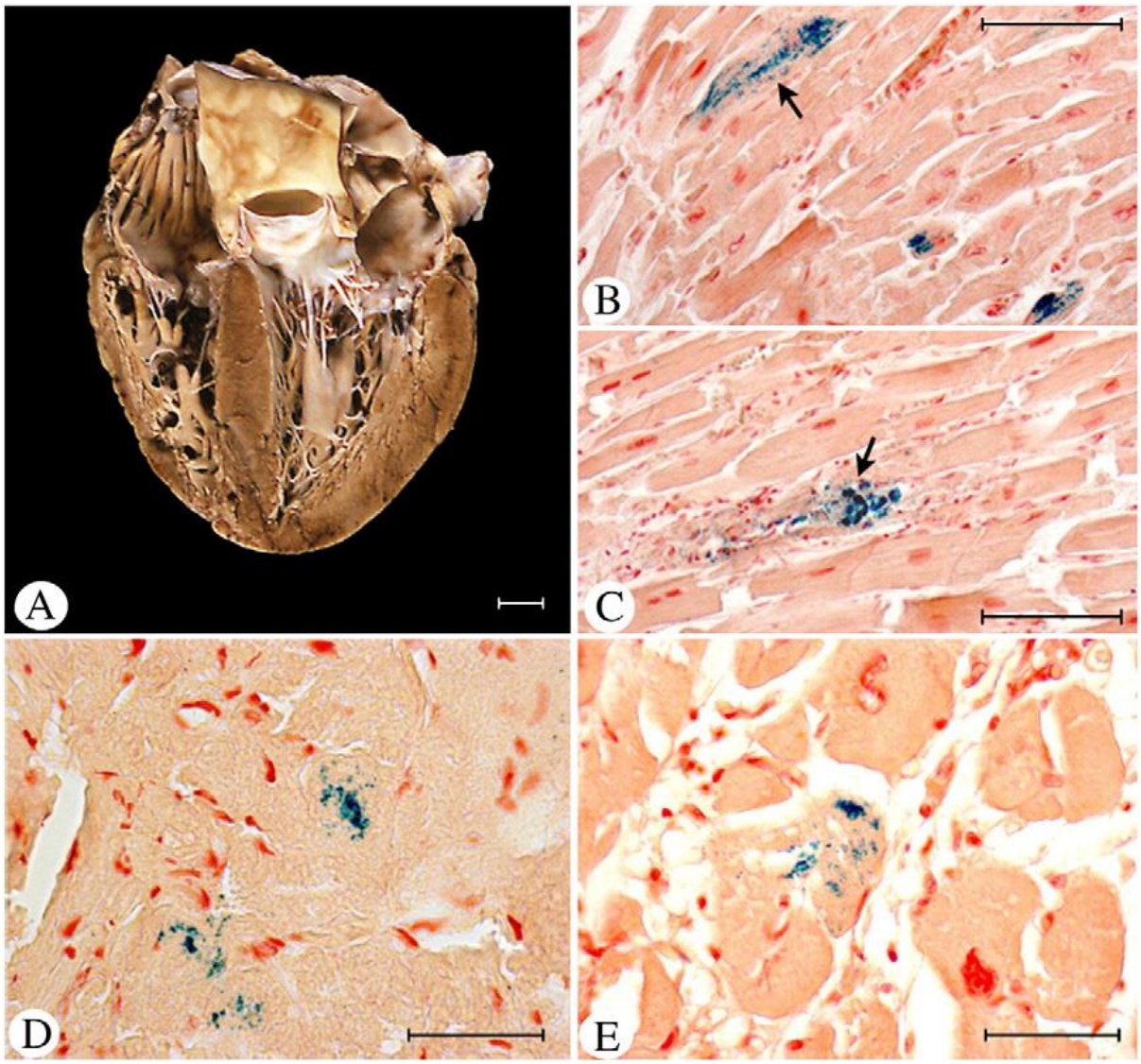

Figure 1.2: Gross pathology of an FRDA heart and light microscopy of iron-reactive granules in sarcoplasm and endomysium. (A) Gross specimen. Left and right ventricular walls are greatly thickened. (B–E) Iron histochemistry. The stain shows finely granular reaction product that lie parallel to the long axis of cardiomyocytes (arrow in B). A cluster of much larger iron-positive granules lies adjacent to or within a necrotic muscle fibre (arrow in C). (D–E) Iron histochemistry of an endocardial biopsy of an FRDA patient at the age of 9 years (D) and a section of the autopsy specimens at the age of 26 years (E). Both sections display iron-positive granules in cardiac muscle fibers, and the frequency of iron-reactive fibers among all cardiomyocytes is similar. Markers: A, 1 cm; B–C, 100 µm; D–E, 50 µm. Picture modified from (Michael *et al.*, 2006).

Diabetes mellitus is much more frequent in patients with FRDA than in the general population. A combination of insulin resistance and inadequate insulin response contributes to diabetes in FRDA; both forms are likely to be a direct consequence of the mitochondrial dysfunction that occurs in this disease (Schoenle *et al.*, 1989).

1.2.3 Prevalence

This disease is rare in sub-Saharan African and Far East populations (Hirayama *et al.*, 1994) and mainly occurs in Caucasians (Labuda *et al.*, 2000, Vankan, 2013) The age of the FRDA founding mutation in Western Europe was estimated at least 682 ± 203 generations ago, suggesting a Palaeolithic origin. The prevalence of FRDA in Caucasians is usually quoted as being 1 in 20 000 to 1 in 50 000 (Vankan, 2013). One study assessing the prevalence of FRDA in the United Kingdom proposed a prevalence 1 in 54 000 with approximately 1100 patients in the UK today (Figure 1.3) (Winter *et al.*, 1981, Vankan, 2013).

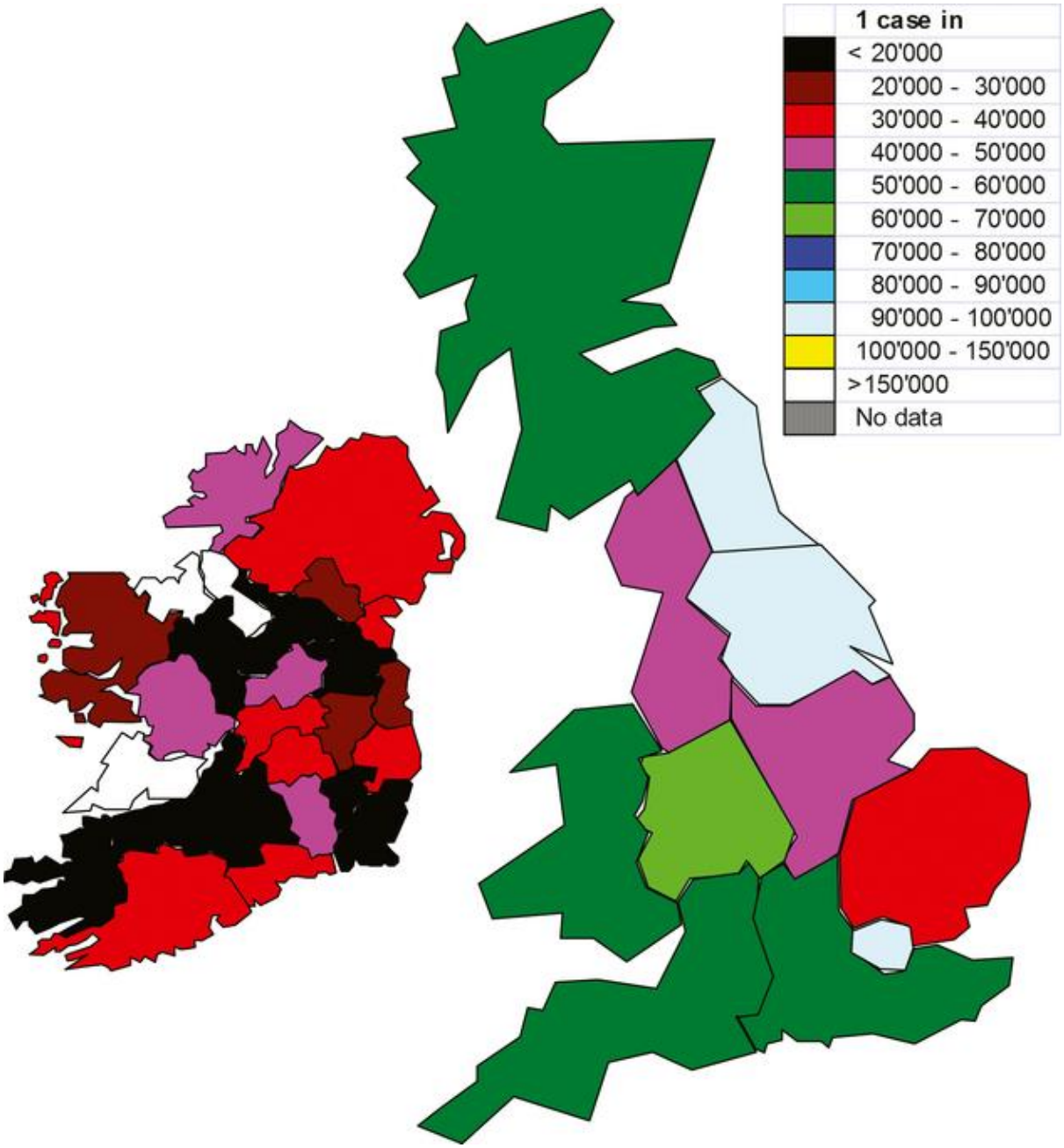

Figure 1.3: Prevalence of FRDA in the UK and Ireland. Numbers of FRDA patients per region of the UK were provided by Ataxia UK. Prevalence ranges from low levels along the North Sea coast to higher prevalence in the remaining regions. Picture modified from (Vankan, 2013).

1.2.4 Friedreich ataxia gene structure

The FRDA gene (*FXN*) was mapped to the long arm of chromosome 9 in 1988 by linkage analysis in families suffering from FRDA (Chamberlain *et al.*, 1988), and later it was localized at position 9q13-21.1(Ensembl 2010) (Figure 1.4A). Initially, the expressed region of *FXN* gene was identified as X25 using complementary DNA (cDNA) selection and sequence analysis, and intensive studies for a mutation in X25 led to detection of an expanded trinucleotide repeat GAA within the first intron (Campuzano *et al.*, 1996). The *FXN* gene is composed of seven exons (1-5a, 5b, 6) (Figure 1.4B), in which the 6th exon is non-coding and spans 95 kb of genomic DNA. The main functional messenger RNA has the size of 1.3 kb, arising from the first five exons (1-5a), which encodes a 210 amino acid protein named frataxin. In addition by alternative splicing a 171 amino acid protein can be transcribed from exon 5b The *FXN* gene is transcribed in the centromere to telomere direction; (Campuzano *et al.*, 1996, Hanauer *et al.*, 1990) (Figure 1.4B).

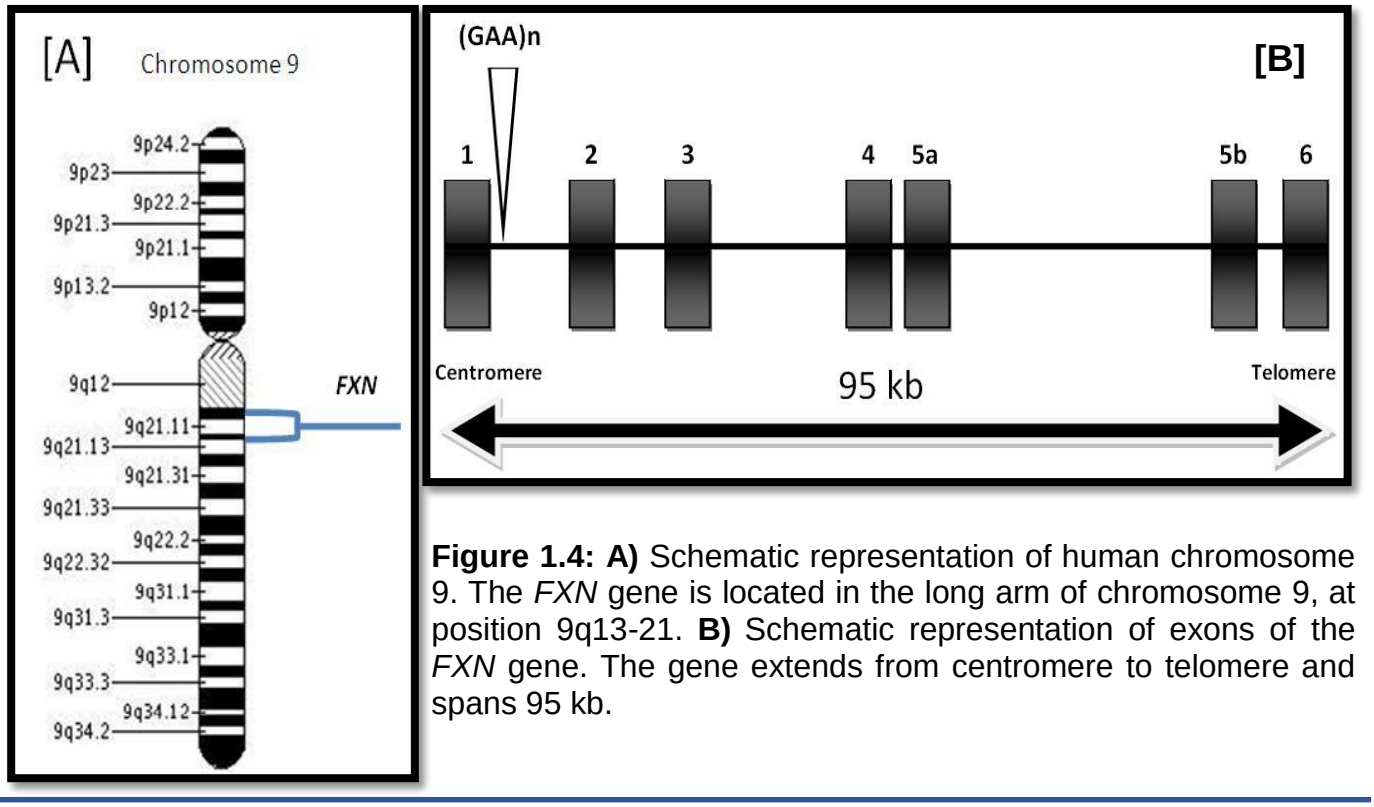

Figure 1.4: A) Schematic representation of human chromosome 9. The *FXN* gene is located in the long arm of chromosome 9, at position 9q13-21. **B)** Schematic representation of exons of the *FXN* gene. The gene extends from centromere to telomere and spans 95 kb.

Two major transcription start sites (TSS) were identified in the frataxin gene. Using 5′ rapid amplification of cDNA ends experiments Campuzano *et al.,* located a TSS (TSS1) 221bp upstream of the ATG translation start site (Campuzano *et al.*, 1996) and Kumari *et. al.,* located another TSS (TSS2) 62bp upstream of the ATG by primer extension (Kumari *et al.*, 2011). It is not clear which TSS is more dominant, however, Kumari et al. suggested that TSS2 could be the primary transcription start site in Epstein-Barr virus-transformed lymphoblastoid cell lines (Kumari *et al.*, 2011). The region between TSS1 and the first exon is thought to be a TATA-less downstream promoter, which contains Inr/downstream promoter element-like elements.

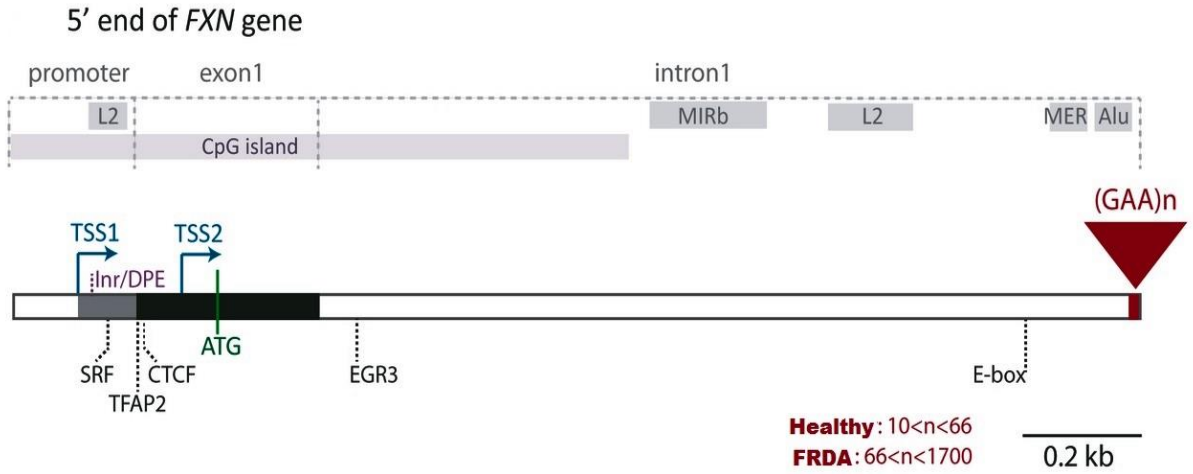

Figure 1.5: Regulatory elements at the 5′ end of *FXN*.

Moreover, binding sequences were identified for transcription factors serum response factor, TFAP2 and EGR3 (Tourtellotte and Milbrandt, 1998) as well as for the insulator protein CCCTC-binding factor (CTCF) (De Biase *et al.*, 2009). An E-box is present in the vicinity of (GAA)n repeats and this element was shown to be crucial for *FXN* expression via reporter assays (Greene *et al.*, 2007). Interestingly, apart from (GAA)n repeats, a number of repetitive DNA elements have been identified at the *FXN* locus. These include L2 (LINE) (Greene *et al.*, 2005) and Alu (SINE) elements as well

as MIRb and mariner DNA transposon (Campuzano *et al.*, 1996, Cossée *et al.*, 1997). Although the deletion of these elements significantly impaired a reporter *FXN* construct, their exact function on *FXN* regulation is not known (Greene *et al.*, 2005) (Figure 1.5).

1.2.5 Friedreich ataxia gene expression

The *FXN* gene is expressed in all cells but at variable levels in different tissues and during development (Koutnikova *et al.*, 1997). In adult human, *FXN* gene expression is slightly higher in dorsal root ganglia and the granular layer of the cerebellum as well as in tissues with high metabolic rate such as heart, and relatively lower levels in liver, skeletal muscle and pancreas (Rotig *et al.*, 1997, Koutnikova *et al.*, 1997, Al-Mahdawi *et al.*, 2006). In mouse embryos the developing brain is rich in frataxin mRNA, and the highest levels are found in spinal cord and in the dorsal root ganglia (DRG). The level of frataxin mRNA is reduced in the adult mouse brain, but remains high in spinal cord and DRG (Jiralerspong *et al.*, 1997, Koutnikova *et al.*, 1997). Cells such as neurons and cardiac muscle that are heavily dependent on oxidative respiration contain high numbers of mitochondria and generally have higher frataxin expression. Protein levels remain high in the adult human, and mouse brain and cerebellum (Koutnikova *et al.*, 1997). It is reported that over-expression of frataxin was shown to be toxic for cells, perhaps implying that a fine balance is needed for the regulation of its expression (Fleming *et al.*, 2005, Navarro *et al.*, 2011).

1.2.6 Frataxin protein structure

Frataxin is a mitochondrial protein and highly conserved in most organisms from bacteria to mammals (Gibson *et al.*, 1996, Adinolfi *et al.*, 2002). The precursor form of frataxin is a 210 amino acid protein containing an N-terminal mitochondrial import sequence that conducts its transport into the mitochondria, where two cleavages occur. These two proteolytic steps convert the precursor protein to a 19 kDa intermediate and a 17 kDa mature form of frataxin, respectively. The final protein in mitochondria is recognised as the mature form of frataxin which is a compact, globular protein containing an N-terminal α helix, a middle β sheet region composed of seven β strands, a second α helix, and a C-terminal coil (Figure 1.6). The α helices are folded upon the β sheet, with the C-terminal coil filling a groove between the two α helices. The size and nature of the conserved surface regions suggest that they interact with a large ligand, probably a protein (Condò *et al.*, 2007).

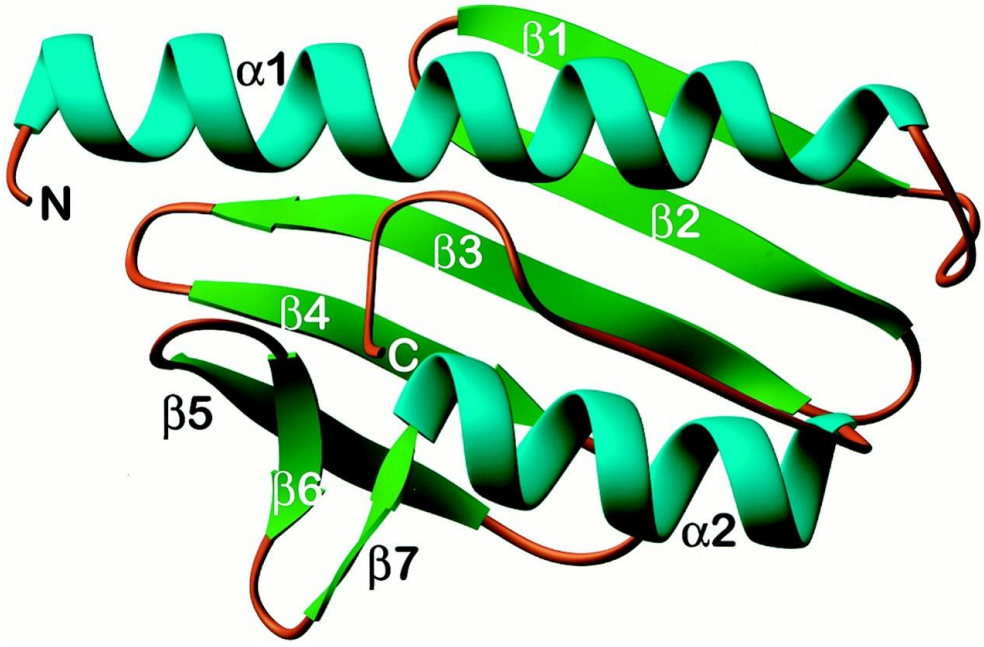

Figure 1.6: Structure of frataxin. Crystal structure of human frataxin shows the fold of human frataxin, a compact αβ sandwich, with α helices and β sheets. Strands β1 – β5 formed a flat antiparallel construct that interact with the two helices, α1 and α2.

1.2.7 Cellular function of frataxin

The function of frataxin is not completely understood and clues to the function of frataxin protein comes from identification of its interacting partners. A bioinformatics study have demonstrated a link between frataxin and the proteins from the iron sulphur cluster machinery. (Huynen *et al.*, 2001) In S. cerevisiae (Δyfh1) cells, yeast frataxin (Yfh1) deficiency will lead to reduction of the activity of Fe-S-containing enzymes such as aconitase, succinate dehydrogenase and cluster incorporation into apo-ferredoxin (Duby *et al.*, 2002, Mühlenhoff *et al.*, 2002). In addition it was found that yeast and human frataxin bind to the central Fe-S cluster assembly complex, which is composed of the Nfs1 enzyme and the scaffold protein Isu, (Gerber *et al.*, 2003, Ramazzotti *et al.*, 2004).

Studies involving FRDA patients, conditional knockout mouse models, and yeast mutants containing a disruption of the frataxin gene have shown intramitochondrial iron accumulation, oxidative stress, and reduced activity of iron-sulphur (FeS) cluster-containing subunits of the mitochondrial ETC (complexes I–III) and of aconitase (Koutnikova *et al.*, 1997, Cavadini *et al.*, 2000, Puccio *et al.*, 2001). Although the physiological function of frataxin is still unknown but it may be involved in mitochondrial iron homeostasis and/or the assembly of FeS proteins (Bradley et al. 2000) (Figure 1.7).

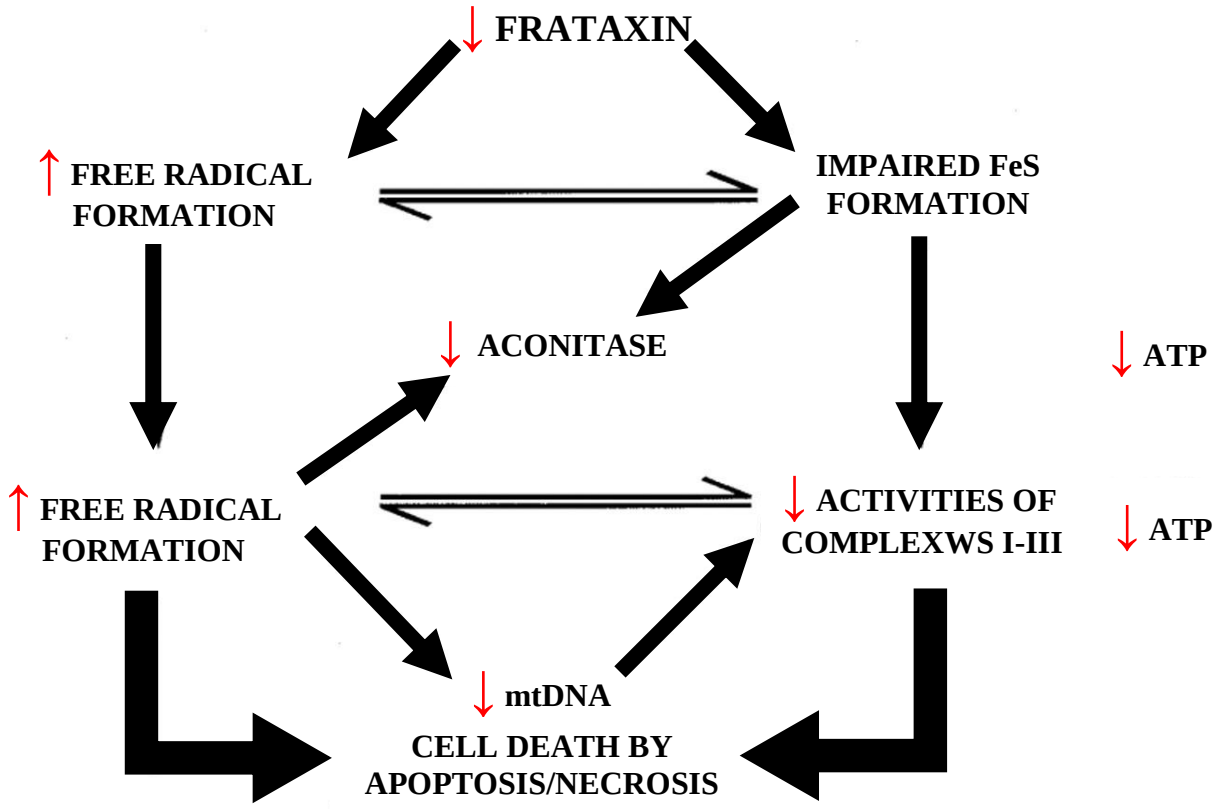

Figure 1.7: Schematic representation of events leading to cell death in FRDA. Although the exact sequence of events in FRDA pathogenesis is uncertain. It is proposed that impaired intramitochondrial iron metabolism results in defective Fe-S formation resulting in decreased complex I–III and mitochondrial aconitase activities and iron overload. Increased free iron levels and a defective mitochondrial respiratory chain will result in increased free radical generation, which will cause oxidative damage including further inhibition of aconitase activity. Impaired respiratory chain activity and decreased aconitase activity will impair ATP synthesis, which, together with oxidative damage to cellular components, will compromise cell viability. Figure modified from (Bradley *et al.* 2000).

1.3 GAA repeat mutation

Molecular studies of FRDA have led to identification of several mutations in the *FXN* gene. Almost 95% of FRDA cases are caused by hyperexpansion of the GAA triplet repeat sequence, in the first intron of the *FXN* gene. This mutation is known to reduce the frataxin expression (Campuzano *et al.*, 1996) (Figure 1.8). Affected individuals generally have GAA expansion on both alleles of *FXN* gene due to the recessive nature of this disease; whereas heterozygous carriers show no sign of disease and are clinically normal. Normally alleles contain less than 30 triplets, whereas in FRDA patients alleles contain more than 60 triplets and in some cases up to 1700 triplets (Cossée *et al.*, 1997). There is a direct correlation between the size of the GAA expansion and the severity of the disease (Filla *et al.*, 1996). Evidence shows that about 5% of FRDA individuals are heterozygous for the GAA expansion and in some cases a missense or a nonsense point mutation may lead to disrupting the frataxin coding sequence. In addition, there has been no report of FRDA patients carrying a point mutation in both copies of *FXN* gene so far. FRDA is the only known disease to be result of an expansion of GAA triplets (Cossée *et al.*, 1997) (Grabczyk and Usdin, 2000b) (Montermini *et al.*, 1997a). The most common point mutations known to date include I154F, M1I and G130V. The I154F mutation exhibits a typical FRDA

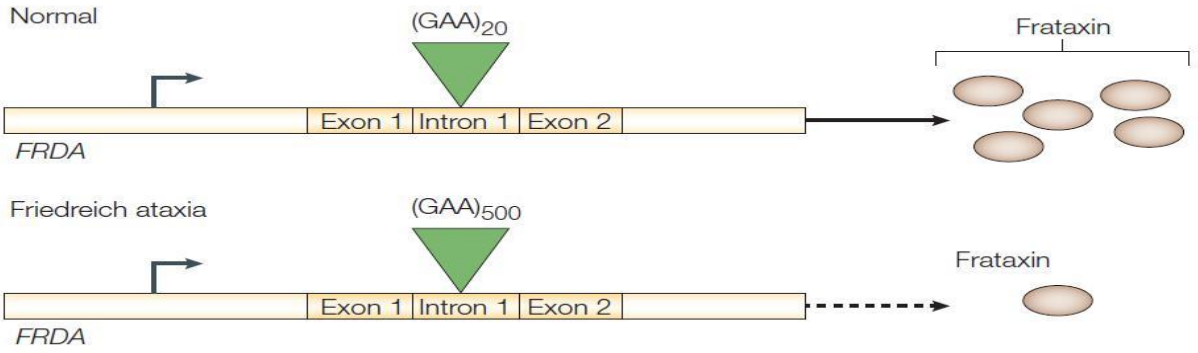

Figure 1.8: GAA repeat mutation results in decrease frataxin production.

phenotype, whereas the other mutations demonstrate early-onset FRDA features (Alper and Narayanan, 2003).

1.3.1 Instability of the GAA repeat:

Trinucleotide repeat expansion is one of the mutational mechanisms that contributes to several inherited disorders, including myotonic dystrophy, Huntington disease and Friedreich ataxia (Cossée *et al.*, 1997). Trinucleotide repeat instability contributes to more than 40 neurodegenerative disorders, and repeat mutation is a process that may increase within tissues and across generations (Kovtun and McMurray, 2008). Normally positions of trinucleotide repeats are divided into coding and non-coding regions. Non-coding trinucleotide repeat expansion disorders typically result in loss of gene function or toxic effects at the mRNA level; while coding trinucleotide repeat expansions usually cause either a polyglutamine or polyalanine tract in the protein products resulting in protein malfunction (Pizzi *et al.*, 2007). Approximately 30% of the human genome consists of repetitive nucleotide sequences which may undergo insertion, deletion, contraction and expansion (Potaman *et al.*, 2004). The FRDA GAA expansion instability can be categorised into two main groups: somatic and meiotic instability.

1.3.2 Somatic instability is tissue and age dependent

Somatic instability, identified in many repeat disorders carries variable lengths of trinucleotide repeats in different tissues from the same patient (Pearson *et al.*, 2005). Heterogeneity occurs at a variable degree among cells in different tissues, for example cultured fibroblasts show very little heterogeneity in expansion sizes among cells, whereas lymphocytes are more heterogeneous, and the majority of brain regions show a complex pattern of allele sizes, indicating extensive cellular heterogeneity (Montermini *et al.*, 1997b). Recent investigation of six autopsies of FRDA patients showed that DRGs had a significantly greater frequency of large expansions and relative paucity of large contractions compared with other tissues (De Biase *et al.*, 2007a) (Figure 1.9).

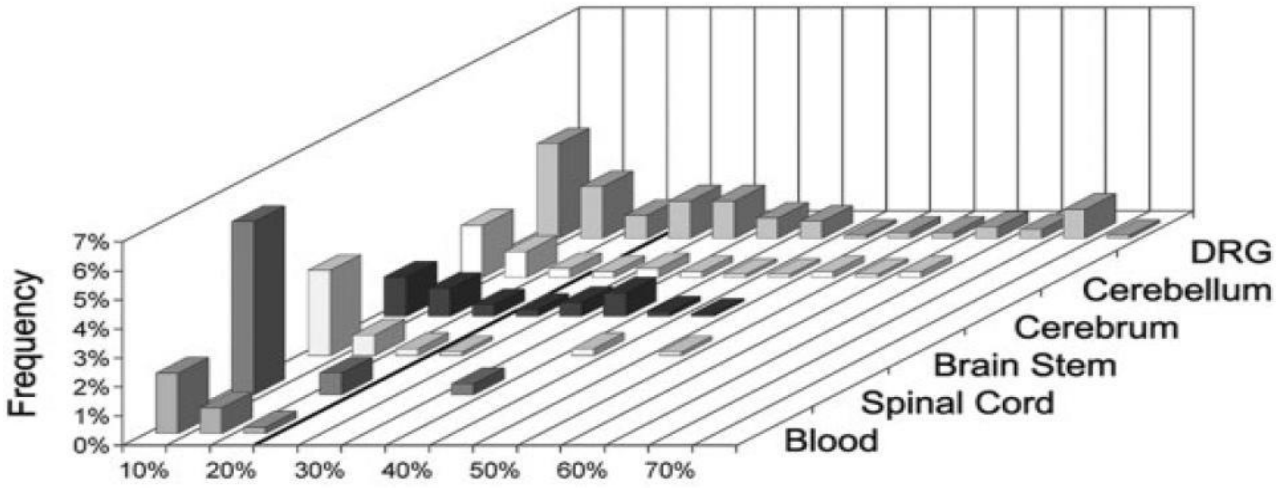

Figure 1.9: Small pool–PCR analysis demonstrating greater occurrence of large expansions in DRG. Frequency distribution (plotted on the Y-axis) of expansions (magnitude plotted on the X-axis as increase in size (%) over the constitutional allele) seen in various tissues derived from the patient. All data points to the right of the bold line, plotted at 20%, represent large expansions (De Biase *et al.*, 2007a).

Using small-pool PCR analysis from tissue of an 18 week fetus homozygous for expanded GAA alleles revealed very low levels of instability compared with adult derived tissues (De Biase *et al.*, 2007b). Furthermore, mutation load in blood samples from FRDA patients increased significantly with age ranging from 7.5% at 18 weeks gestation to 78.7% at 49 years of age (R=0.91; *P* <0.0001). Hence somatic instability in FRDA occurs mainly after early embryonic development and progresses throughout life supporting the role of postnatal somatic instability in disease pathogenesis (De Biase *et al.*, 2007b) (Figure 1.10). Studies of transgenic mouse models shows the GAA triplet repeat is unstable in the context of the human *FXN* locus and displays age-dependent expansions in the cerebellum and the DRG (Clark *et al.*, 2007).

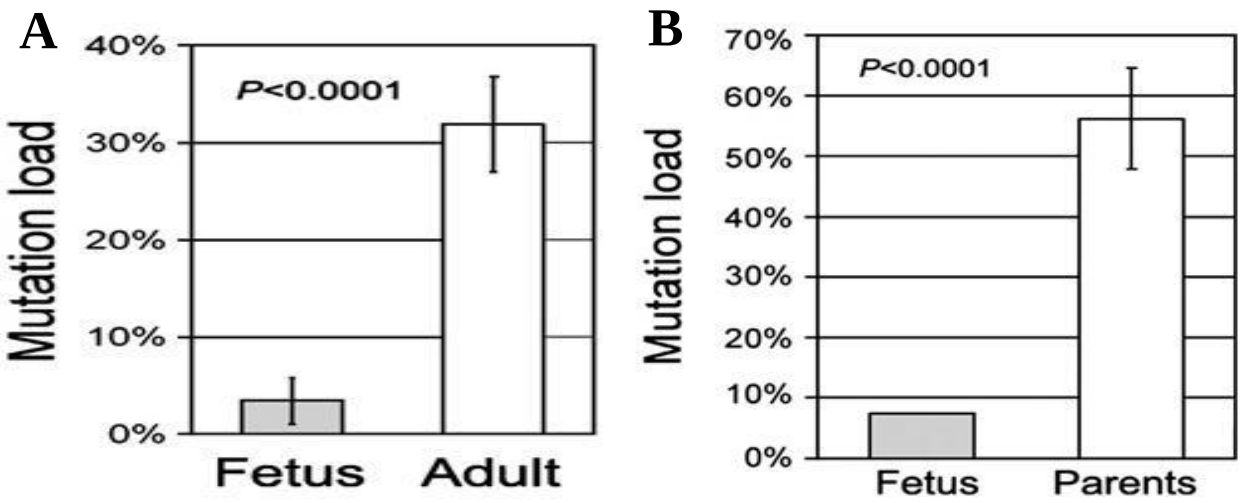

Figure 1.10: Small-pool PCR analysis showing different GAA mutation load in fetus versus adults. **A)** Mutation load of fetal versus adult tissues analyzed by SP-PCR showing highly significant, 7.3 fold lower level of somatic instability in fetal tissues compared with adult tissues. Error bars -/+ 2 SEM. **B)** Bar graph of mutation load in the blood of fetus versus both parents combined showing a highly significant, seven fold lower levels of somatic instability in fetal tissues compared with adult tissue. Error bar -/+ 2 SEM (De Biase *et al.*, 2007a).

1.3.3 Meiotic (intergenerational) instability of GAA repeats

Both contraction and expansion could be observed when transmitted from parent to child (Campuzano *et al.*, 1996). It is suggested that expanded alleles are likely to further expand or contract during maternal transmission, but in most cases contract during paternal transmission. Parental age and the intergenerational change in expansion are directly correlated in maternal transmission and inversely correlated in paternal transmission (Kaytor *et al.*, 1997).

1.4 Mechanisms reducing *FXN* transcription

Frataxin deficiency is the main cause of FRDA. Reduction in *FXN* mRNA is caused at the transcriptional level, and not at post-transcriptional RNA processing (Delatycki *et al.*, 2000). It is suggested that expansion of long GAA repeats in intron 1 results in transcriptional silencing by the formation of non-B DNA structures such as triplexes or sticky DNA (Wells, 2008). In addition, other studies have linked silencing mechanisms with FRDA including histone modification and DNA methylation (Herman *et al.*, 2006, Al-Mahdawi *et al.*, 2008).

1.4.1 Triplex formation

The GAA expansion in the *FXN* primary transcript is not part of the spliced message, so reduction in frataxin expression must result from an effect on transcription initiation. This deficiency may be induced by a block to transcription elongation or/and interference with proper splicing (Grabczyk and Usdin, 2000b) (Figure 1.11).

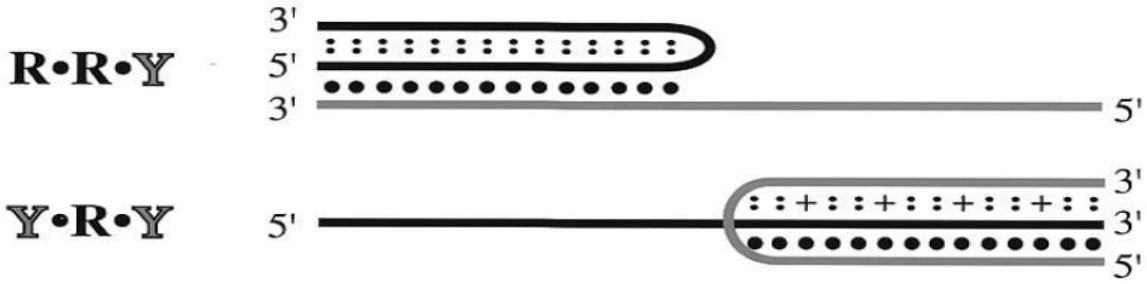

Figure 1.11: Schematic representation of intramolecular R.R.Y and Y.R.Y triplexes. The purine (R) strand is black, the pyrimidine (Y) strand is grey. The single black dots indicate normal Watson-Crick base pairs and the smaller double dots indicate alternative hydrogen bonding interactions that are pH independent (Grabczyk and Usdin, 2000b).

The GAA.TTC tract is a purine.pyrimidine (or R.Y) polymer and may adopt a number of unusual nucleic acid structures including triple helices (Wells *et al.*, 1988). Generally, the triplex formation is seen in two forms R.R.Y or Y.R.Y, and depending on whether the third strand is purine rich or pyrimidine rich it can be formed as either intermolecular structures or as folded intramolecular structures (Wells *et al.*, 1988). Some models have previously been proposed for triplex formation (Grabczyk and Fishman, 1995, Reaban and Griffin, 1990), but recent investigations led to the construction of a new model, which proposes that a transient intramolecular R.R.Y triple helix is formed behind the RNA polymerase during transcription pausing the polymerase within the GAA.TTC tract (Grabczyk and Usdin, 2000b). The conditions favouring the triplex formation comes from the movement of RNA polymerase along

the template, locally unpairing the DNA duplex and generating a wave of negative supercoil in its wake (Figure 1.12A).

At the transcription bubble the polymerase covers the Y (TTC) template strand but the single-stranded portion of the GAA non-template strand is available to initiate triplex formation promoting the formation of the R.R.Y structure (Figure 1.12B). The initial folding may be analogous to the formation of the folded R.R.Y structure by an oligodeoxyribonucleotide (Figure 1.12) The spread of triplex formation (Figure 1.12C) is driven by the release of the standing wave of negative super helical energy that had formed behind the polymerase. This model illustrates that the polymerase has trouble negotiating the junction between the triplex and the duplex in the distal end of the repeat tract (indicated by the black arrow in Figure 1.12C). This can result in truncation of a transcript at the 3′ end of the structure; an outcome not predicted by previously proposed models for GAA.TTC mediated transcription inhibition (Grabczyk and Usdin, 2000b). Further investigations by Grabczyk *et al.,* demonstrated the formation of a persistent RNA-DNA hybrid by transcription of the *FXN* GAA_TTC repeat sequence in *E. coli* and by T7 RNA polymerase *in vitro*. During transcription of the longer repeats, T7 RNA polymerase arrested at the promoter distal end of the GAA_TTC tracts and an extensive RNA_DNA hybrid was tightly linked to this arrest (Figure 1.12D). This indicates that the RNA_DNA hybrid formation appears to be an intrinsic property of transcription through long GAA_TTC repeats. Initially, the repeating DNA d(TTC)*n* strand serves as the template for synthesis of r(GAA)*n* to form a moderate length of DNA_RNA hybrid. Due to the stability of this hybrid, the DNA triplex is dislodged behind the growing transcription complex to give an even longer RNA-DNA hybrid. The waves of negative supercoiling behind the translocating RNA polymerase facilitates these processes from a topological standpoint (Grabczyk *et al.*, 2007).

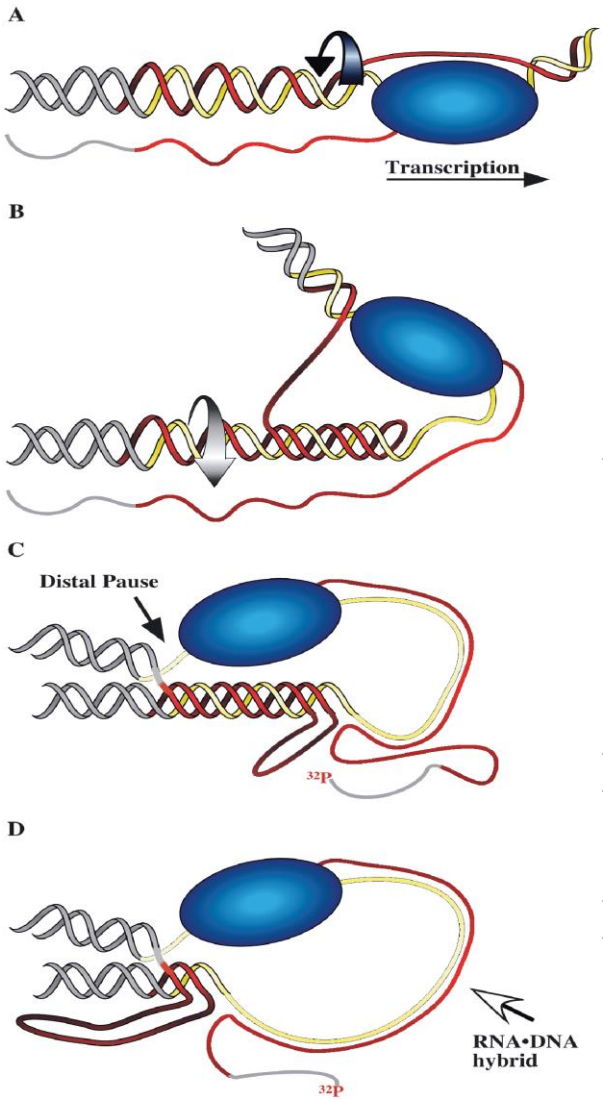

Figure 1.12: Transcription-coupled RNA·DNA hybrid formation in a GAA·TTC repeat. A model for transient transcription-dependent triplex formation leading to an RNA polymerase pause and RNA·DNA hybrid formation. The purine (GAA or R) strand of the repeat is red, the pyrimidine (TTC or Y) strand is yellow and the flanking DNA is grey.

(A) A standing wave of negative supercoiling follows RNA polymerase. At the transcription bubble, the non-template (GAA) strand is available to fold back in an R·R·Y interaction; the template strand is covered by RNA polymerase.

(**B**) Rotation of the helix (curved arrow) as it winds in the third strand relaxes the negative supercoils caused by transcription and leaves a length of the template single-stranded.

(**C**) RNAP is impeded at the distal template–triplex junction and the nascent transcript can anneal to the single-stranded stretch of template.

(**D**) The RNA·DNA hybrid displaces the much less stable triplex structure (Grabczyk *et al.*, 2007).

1.4.2 Sticky DNA

Recent investigations have focused on the types of triplexes that are adopted by the long GAA_TTC repeats, both *in vitro* and *in vivo*, to determine the effects of triplexes on other DNA metabolic events, and their involvement in replication, repair, and recombination-mediated genetic instabilities. A new type of DNA structure, is described for lengths of (GAA.TTC)n found in intron 1 of the *FXN* gene of FRDA patients called sticky DNA (Sakamoto *et al.*, 1999). Sticky DNA is a long GAA_GAA_TTC triplex that is formed intramolecularly *in vivo* and *in vitro* (Son *et al.*, 2006). Sticky DNA is formed by the association of two long GAA•TTC repeat

sequences that are distal to each other (two R.R.Y triplexes). Studies demonstrated that the two long repeat sequences must be within the same topologically closed plasmid and in a direct repeat orientation with each other in order for the two tracts to associate (Vetcher *et al.*, 2002). A correlation was also established between the length of repeat and sticky DNA formation. Repeat lengths of greater than 60 are required for sticky DNA formation and repeat lengths shorter than 60 repeats failed to demonstrate the formation of this non- B structure (Figure 1.13) (Sakamoto *et al.*, 1999).

It has been suggested that the disruption of GAA.TTC sequence may destabilize sticky DNA structure and promote transcription. Analysis of the effects of introducing interruptions into a $(GAA.TTC)_{150}$ repeat by substituting an increased number of As with Gs has confirmed that sticky DNA structure is progressively destabilized and is unable to form when the sequence becomes $(GAAGAA.TCCTTC)_{75}$ (Ohshima *et al.*, 1999). Furthermore, inhibition of transcription is reduced as the tendency to form a sticky DNA structure is decreased *in vivo* and *in vitro* (Ohshima *et al.*, 1999).

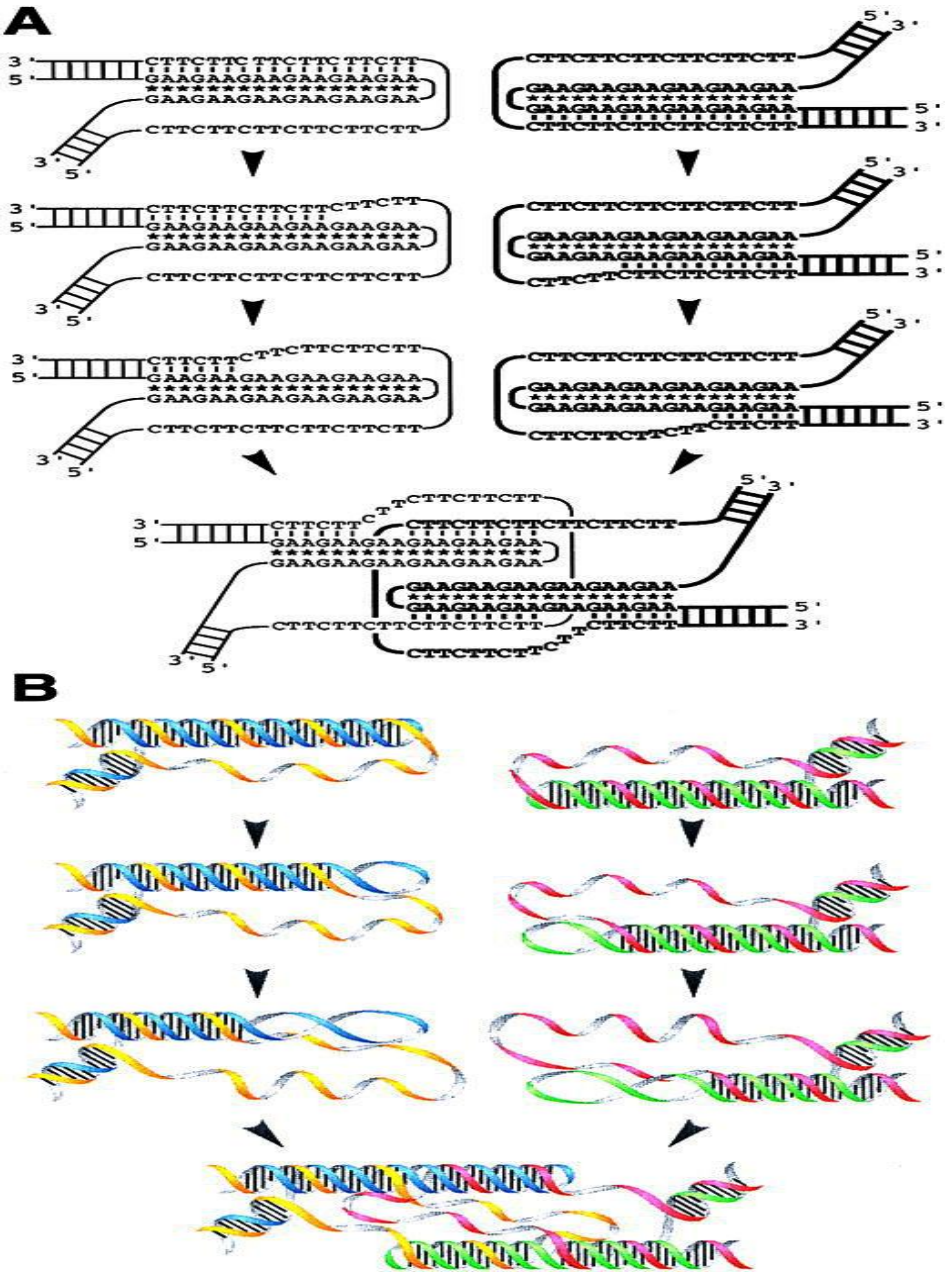

Figure 1.13: A model of the association of two triplexes formed by long GAA.TTC tracts. **A)** Schematic representation of the strand exchange model. The two triplexes are represented as thin and thick lines. The short vertical lines between the bases represent Watson-Crick pairs, and the stars represent the reversed Hoogsteen base pairs. **B)** Two dimensional picture of the strand exchange model. Different colours represent different strands. In the left molecule, blue shows the purine strand, while yellow shows the pyrimidine strand. In the right molecule, green shows the purine strand and red shows the pyrimidine strand (Sakamoto *et al.*, 1999).

1.4.3 Histone modifications

Recent findings have recognized a link between chromatin modifications and FRDA. Initial investigation of the acetylation state of the *FXN* gene in a FRDA lymphoblastoid cell line demonstrated significantly low levels of histone acetylation in H3K9, H3K14, H4K5, H4K8, H4K12 and H4K16 surrounding the GAA repeat compared to a normal cell line (Herman *et al.*, 2006) (Figure 1.14a). Moreover, the levels of H3K9 mono-, di- and trimethylation, upstream of the GAA repeat was shown to be higher in the FRDA cell line in particular those of H3K9 trimethylation (Herman *et al.*, 2006) (Figure 1.14b).

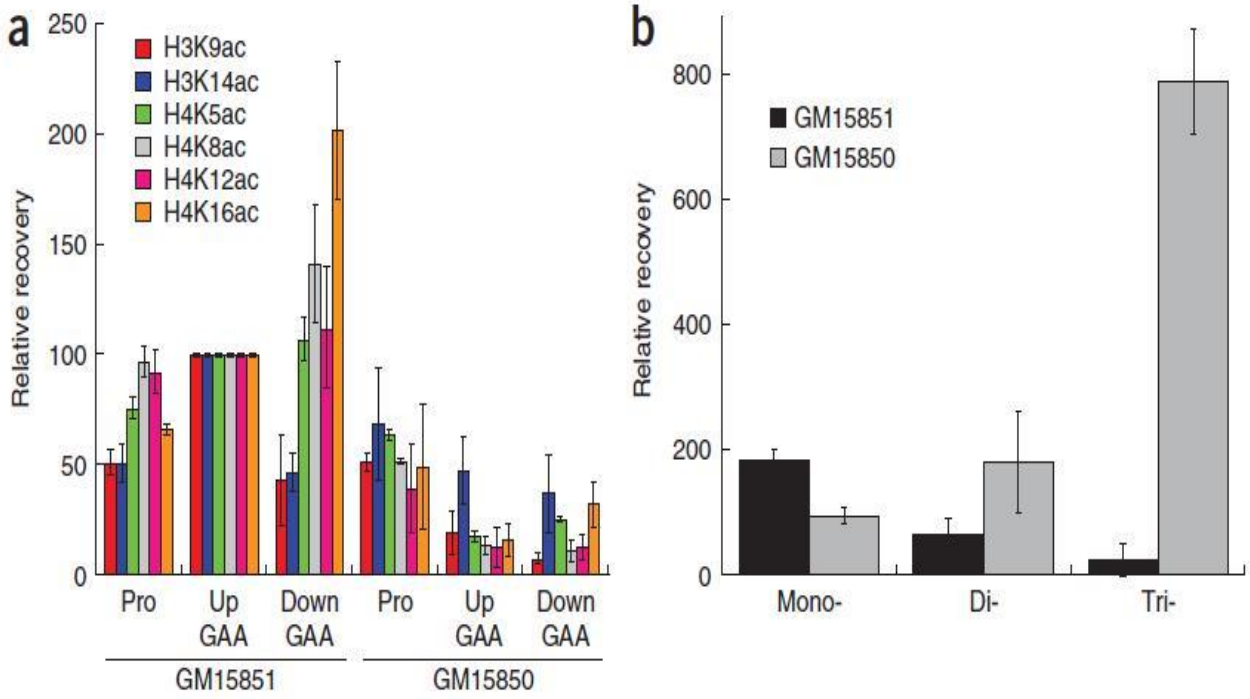

Figure 1.14: Investigation of histone modification in the *FXN* gene by ChIP analysis on a FRDA (GM15850) versus a normal lympholastoid cell line (GM15851). In FRDA, **a)** histone acetylation levels at specified lysine residues are generally lower immediately upstream and downstream of the GAA repeat. **b)** while levels of H3K9 methylation are significantly higher upstream of the GAA, when compared to the normal cell line (Herman *et al.*, 2006).

Using ChIP analysis Al-Mahdawi *et al.,* further investigated the H3 an H4 acetylation and H3K9 methylation in autopsy brain tissues from two FRDA patients and two normal individuals (Figure 1.15). All acetylated histone residues studied showed a GAA-induced gradient of comparative acetylation that is highest in the *FXN* 5'UTR and lowest in the downstream GAA region, with a single most altered residue being H3K9. Additionally H3K9 showed increased levels of di- and trimethylation in all three of the *FXN* regions (Al-Mahdawi *et al.*, 2008).

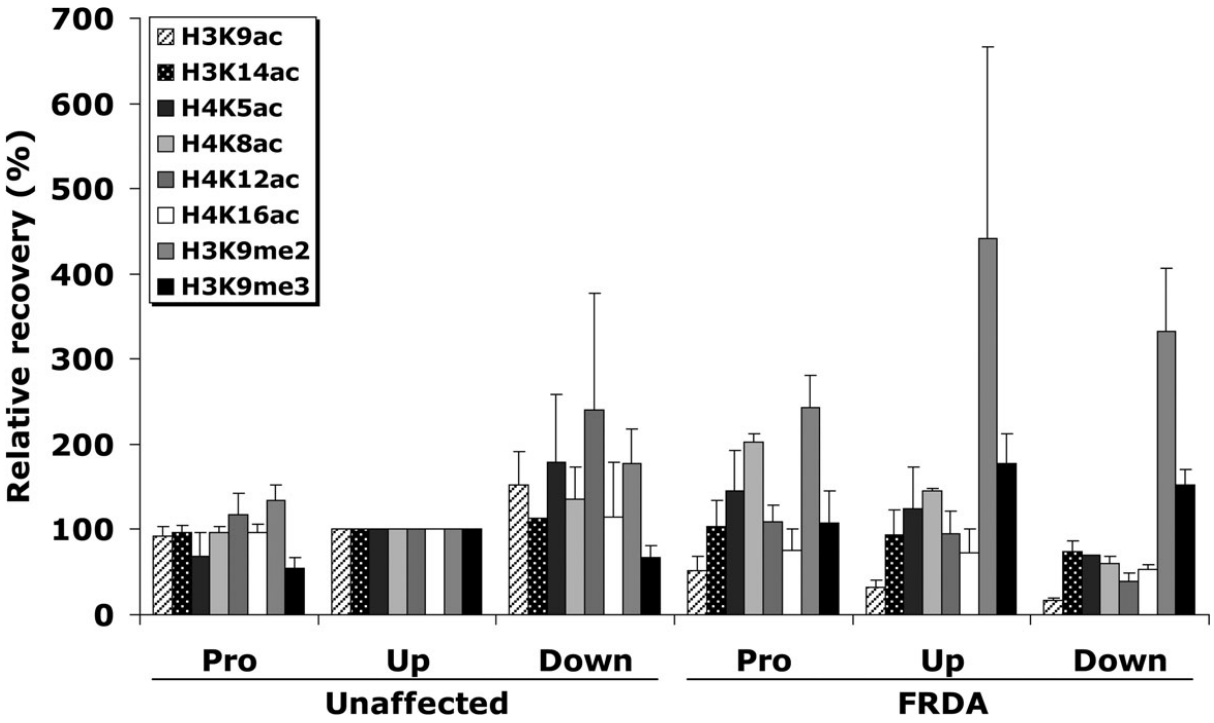

Figure 1.15: Analysis of histone modifications in human brain tissue. ChIP quantitative PCR results for the *FXN* promoter/exon1 (Pro), upstream GAA (Up) and downstream GAA (Down) amplified regions are represented as the relative amount of immunoprecipitated DNA compared with input DNA, having taken negligible 2Ab control values into account. *FXN* values were normalized with human GAPDH and all values have been adjusted so that all of the upstream GAA mean values from the unaffected individuals are 100%. In each case, two individual ChIP samples from two FRDA patients and two unaffected controls were analysed in triplicate (Al-Mahdawi *et al.*, 2008).

1.4.4 DNA methylation changes

Bisulfate sequence analysis of the *FXN* flanking GAA regions in FRDA patient brain, heart and cerebellum tissues, revealed a shift in the FRDA DNA methylation profile, with upstream CpG sites becoming consistently hypermethylated and downstream CpG sites becoming hypomethylated. Variable levels of DNA methylation at three specific CpG sites within the *FXN* promoter and one CpG site within exon 1 was identified (Al-Mahdawi *et al.*, 2008) (Figure1.16).

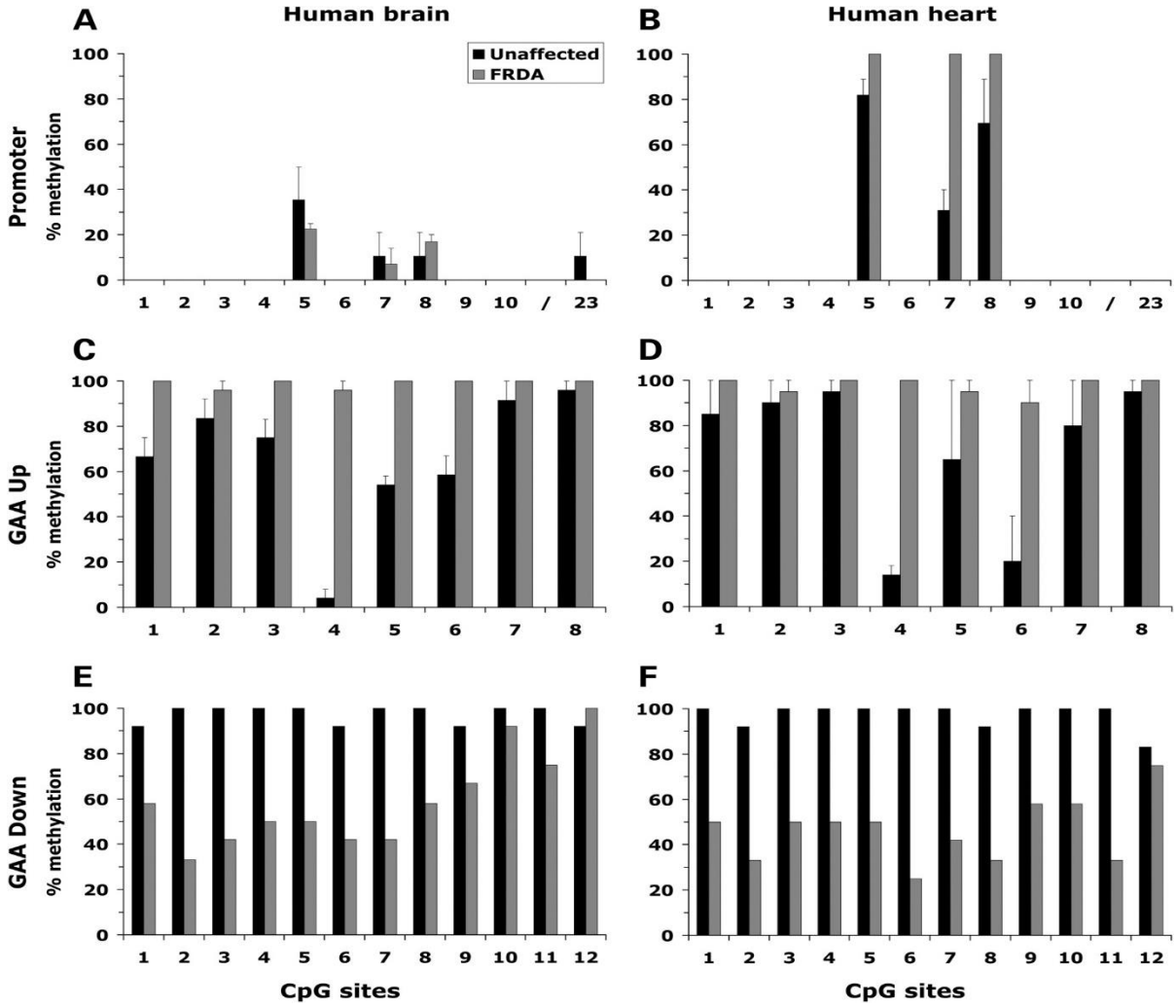

Figure 1.16: DNA methylation analysis of the *FXN* promoter (A and B), upstream GAA (C and D) and downstream GAA (E and F) regions of human brain and heart tissue. In each case the mean percentage of methylated CpG sites is shown, as determined by bisulfate sequencing (Al-Mahdawi *et al.*, 2008).

1.5 Friedreich ataxia mouse models

In order to broaden the understanding of FRDA pathogenesis, the physiological function of frataxin and developing an effective system for testing potential therapies, mouse models of FRDA have been developed and considered essential.

1.5.1 Knockout mouse models

Knockout mouse models are ideal to replicate most features of FRDA, since in most recessive diseases a reduced or destroyed biological function of proteins is observed (Watase and Zoghbi, 2003). To study the mechanism of the FRDA, Cossée and colleagues carried out an attempt using targeted deletion of *FXN* exon 4, to generate a mouse model. However, their effort was unsuccessful as mice that are homozygous die as result of embryonic lethality a few days after implantation. Although a mouse model was not accomplished, this result indicated that frataxin has a vital role during early development (Cossée *et al.*, 2000). Through a conditional gene-targeting approach, conditional knockout mice were generated using a loxP-flanked allele and Cre-lines that are driven by the neuron-specific enolase (NSE) and muscle creatine-kinase promoters (Puccio *et al.*, 2001). This mouse model showed that reduction in frataxin causes sensory-neuron dysfunction, cardiomyopathy, iron-sulphur enzyme deficiencies and finally premature death. However, the most important sites of FRDA pathology such as the dorsal column of the spinal cord remained unaffected in these mice (Puccio *et al.*, 2001).

1.5.2 Knockin mouse models

Since GAA expansion is the main cause of FRDA, insertion of GAA repeats into *FXN* intron 1 of mice was investigated and 230-repeat GAA tract was introduced into the mouse frataxin gene by homologous recombination (Miranda *et al.*, 2002). GAA repeat

knockin mice were crossed with the frataxin knockout mice. The heterozygous mice expressed a 25% reduction in the frataxin level in all tissues compared to wild type. However, these mice did not develop anomalies of motor coordination, iron metabolism or response to iron loading (Miranda *et al.*, 2002). These levels of frataxin expression are associated with mild FRDA in humans, and these mutants are viable and do not show apparent phenotype (Miranda *et al.*, 2002). This result indicated that longer repeats are necessary in order to generate an accurate FRDA mouse model.

1.5.3 *FXN* YAC transgenic mouse model

In an effort to overcome the issues in knockout mice such as embryonic lethality, and to study human frataxin in a mouse cellular environment, Pook *et al.,* suggested that the human *FXN* transgene that contained a large GAA repeat expansion at the correct intronic position, would enable the study of both GAA repeat instability and reduced frataxin expression in FRDA within the single model (Pook *et al.*, 2001).

1.5.4 Human frataxin is functional and rescues *FXN* knockout mouse

In order to investigate whether human frataxin is functional in a mouse background and whether it can substitute for a loss of endogenous murine frataxin, a human wild type *FXN* yeast artificial chromosome (YAC) transgenic mouse line was established and crossbred twice with heterozygous *FXN* exon 4 deletion knockout mouse (Cossée *et al.*, 2000, Pook *et al.*, 2001) (Figure. 1.17). The outcome was a phenotypically normal homozygous *Fxn* knockout offspring that had no endogenous murine frataxin, rescued by expression of YAC-derived human frataxin (Pook *et al.*, 2001). These findings have established that the 370kb human *FXN* YAC transgenic construct is fully functional, can express frataxin and can overcome the embryonic lethality. Transgenic

human frataxin was able to interact with other proteins and achieve its normal function (Pook *et al.*, 2001).

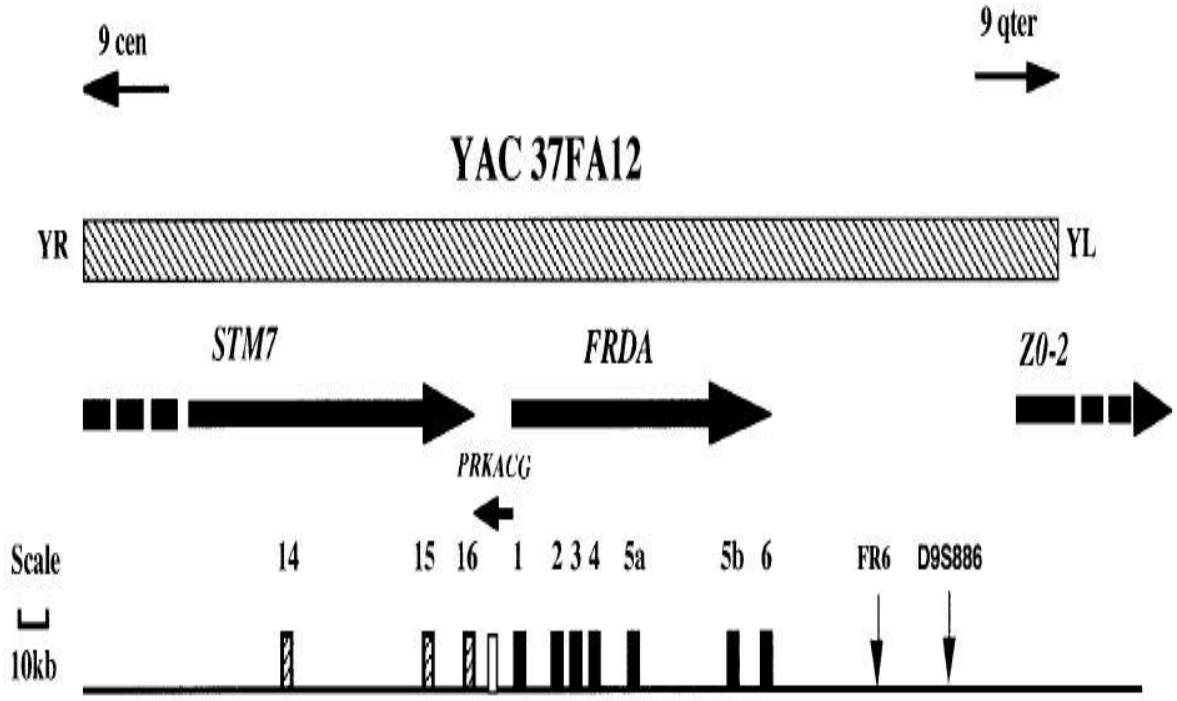

Figure 1.17: The position of YAC 37FA12 with respect to the *FXN* locus at 9q13. Genes are represented as solid arrows, which indicate the direction of transcription, and the broken lines represent incomplete gene sequence. Individual exons are numbered and are shown below the relevant gene (Pook *et al.*, 2001).

1.5.5 Human *FXN* YAC transgenic mouse containing a GAA repeat

Once the generation of a 370kb human *FXN* YAC transgenic mouse model was created, Al-Mahdawi *et al.,* made further advances by the addition of a GAA expansion mutation into this transgenic model (Al-Mahdawi *et al.*, 2004).

A PCR product containing 700 GAA repeats and 1.8kb of flanking intron 1 sequence was amplified from FRDA patient genomic DNA followed by cloning into pCR2.1 and then Yep24 vectors, where GAA repeat contraction to a maximum size of 230 repeats was observed (Al-Mahdawi *et al.*, 2004). This contraction has previously been observed by cloning of GAA repeats expansion sequence into plasmid (Ohshima *et al.*, 1999). Yeast pop in/pop out homologous recombination between the 230 GAA plasmid sequence and retrofitted YAC 37FA12 resulted in a final modified YAC designated 1(38), which contained 190 GAA repeats, and was used to generate transgenic mice (Al-Mahdawi *et al.*, 2004) (Figure 1.18).

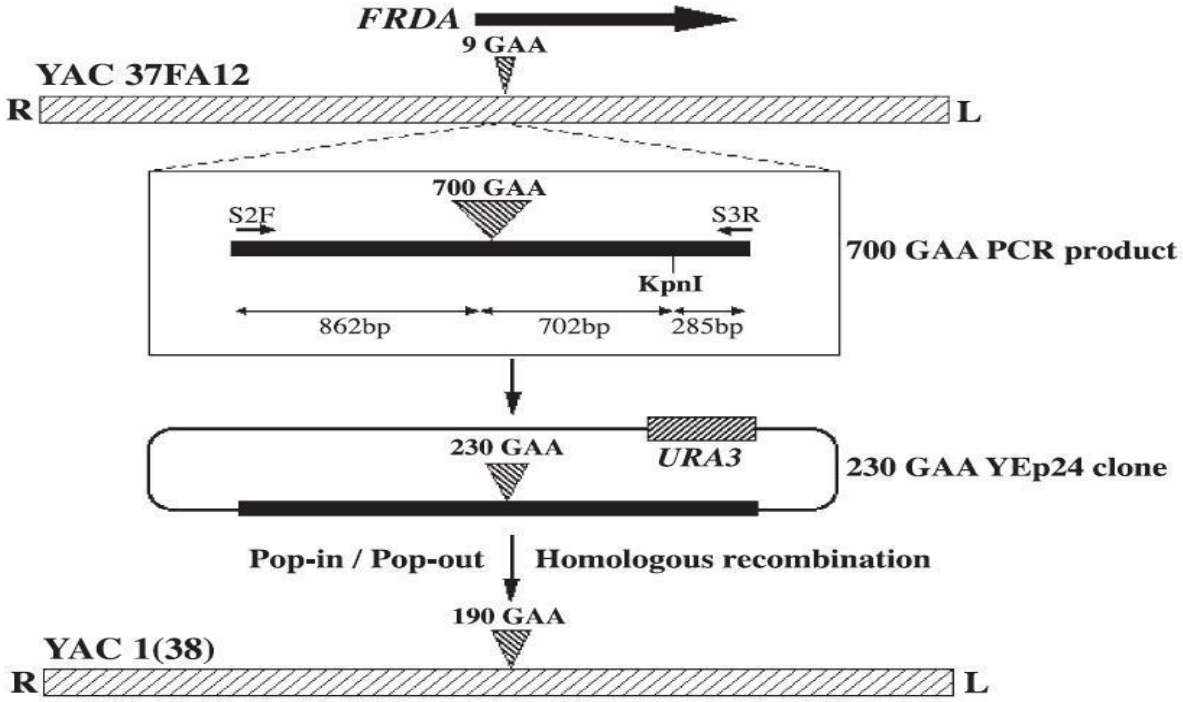

Figure 1.18: GAA repeat modification of YAC 37FA12. The position and orientation of the normal FRDA gene (9 GAA repeats) within the human YAC clone 37FA12 are indicated by the arrow. L and R indicate left and right arms of the YAC. A 700-GAA PCR product was amplified from FRDA patient DNA using primers S2F and S3R. The PCR product was first cloned into pCR2.1 and then into YEp24, with resultant contraction to 230 GAA repeats. Pop-in/pop-out homologous recombination between Yep24 and YAC 37FA12 FRDA sequences produced the 190-GAArepeat YAC clone 1(38), which was subsequently used to generate transgenic mice (Al-Mahdawi *et al.*, 2004).

Two lines of transgenic mouse models have been generated: YG8 and YG22. (Table 1.3) Both YG8 and YG22 contain transgene sequence spanning the whole 370 kb human YAC clone, including the left and right arms of the YAC and the entire FRDA gene together with GAA expansion. The main distinction between these two lines is that YG8 contained two GAA sequences of 90 and 190 repeats, while YG22 contained a single 190 GAA repeat sequence (Al-Mahdawi *et al.*, 2004).

Transgenic line	YAC transgene integrity	*FXN* copy number	Founder GAA repeat length	Range of GAA repeats
YG8	Complete	2	190+90	<9 to 223
YG22	Complete	1	190	<9 to 235

Table 1.3: Overall characterization of *FXN* YAC transgenic mouse line (Anjomani Virmouni *et al.*, 2015).

Recently due to intergenerational expansion, a colony of YG8sR mice that contain ~200 GAA repeats is established. Insertion of a single copy of FXN transgene at a single site was confirmed by fluorescence in situ hybridisation (FISH) analysis of metaphase and interphase chromosomes. Behavioural deficits, together with a degree of glucose intolerance and insulin hypersensitivity was observed in YG8sR FRDA mice compared with control Y47R and wild-type (WT) mice. Also increased somatic GAA repeat instability in the brain and cerebellum of YG8sR mice, together with significantly reduced expression of FXN and reduced aconitase activity was detected compared with Y47R mice. Furthermore, the presence of pathological vacuoles within neurons of the dorsal root ganglia (DRG) of YG8sR mice was confirmed (Anjomani Virmouni *et al.*, 2015).

1.6 Therapeutics

So far there is no efficient treatment for FRDA. However, based on new understandings of the role of frataxin and disease pathogenesis, many new therapeutic strategies have been approached.

1.6.1 Antioxidants and oxidative stress

Recent studies have suggested that low levels of frataxin may cause a delay in antioxidant defences response (Cooper and Schapira, 2007). Therefore, the use of an antioxidant agent to protect from increased oxidative stress has been suggested as a therapy. Coenzyme Q10 (CoQ10) a CoQ10 analogue, idebenone, are potent free radical scavengers that have shown some signs of promise (Lodi *et al.*, 2001, Rustin *et al.*, 1999). In addition, a combined therapy of CoQ10 and vitamin E resulted in improvement in cardiac and skeletal muscle bioenergetics (Cooper and Schapira, 2007, Hart *et al.*, 2005). Overall, therapeutic studies with antioxidants did not produce very promising effects on disease progression and the pathology of FRDA, due to the fact that these agents are probably unable to reach the primary sites of FRDA or because of the lack of ability to remove the iron accumulation.

1.6.2 Removal of mitochondrial iron

Frataxin promotes the mitochondrial synthesis of iron-sulfur cluster (ISC)-containing proteins and heme, hence disruption of frataxin levels may cause dysfunction of ISC metabolism and consequently will result in mitochondrial iron accumulation(Yoon and Cowan, 2003). As a therapeutic approach the removal of excess iron accumulation in the mitochondria should resolve this concern. However, the use of desferrioxamine (DFO), the most commonly used iron chelator in the clinic, proved to be challenging

as it lacks the ability to target mitochondrial iron pools, indicating that DFO may cause general iron deficiency rather than specifically removing mitochondrial iron (Richardson, 2003). Furthermore, an investigation has reported that when cytosolic iron is chelated by DFO, the frataxin mRNA and protein expression decrease further. (Li *et al.*, 2008). Interestingly, a recent study proposes that in FRDA patients lymphoblasts and fibroblasts the concentration of chelatable iron in the mitochondria is not increased, hence frataxin deficiency does not affect the labile mitochondrial iron pool and challenges the current treatment using mitochondrion-specific iron chelators (Sturm *et al.*, 2005).

1.6.3 Increasing frataxin levels

Since the main cause of FRDA is frataxin deficiency, the obvious solution would be to increase frataxin expression. This can be done using different strategies such as inhibition of triplex formation, inhibition of heterochromatin-mediated silencing and gene therapy.

1.6.3.1 Inhibition of triplex formation

The length of GAA repeats may play a role in the levels of frataxin gene transcription. Consequently, inhibition of triplex formation during transcription can be considered as a potential therapy (Grabczyk and Usdin, 2000a). Oligodeoxyribonucleotides are able to block particular types of triplex formation *in vitro* to provide specific increase in the complete transcript (Grabczyk and Usdin, 2000a). Other molecules such as polyamides have been shown to bind to GAA.TTC tracts with high affinity and disrupt the intramolecular DNA. DNA associated region of the sticky DNA conformation (Burnett *et al.*, 2006). Frataxin expression has been increased by these synthetic

ligands in cell culture, but DNA microarray analysis revealed a limited number of genes that are significantly affected in FRDA cells (Burnett *et al.*, 2006).

1.6.3.2 Inhibition of heterochromatin mediated silencing

Acetylation and deacetylation of histone proteins have critical roles in regulating gene expression (Herman *et al.*, 2006), and these processes are regulated by two main enzymes called histone acetyltransferases (HATs) and histone deacetylase (HDACs), respectively (Kondo *et al.*, 2003). Histone acetylation is catalysed by transcriptional coactivators such as CREB-binding protein, which possess HAT activity (Lee and Workman, 2007). HATs interact with a large number of transcription factors and serve as crucial hubs, integrating the activity of multiple signalling cascades (Abel and Zukin, 2008). The effect of HATs can be reversed by HDACs, which remove the acetyl groups from lysine/arginine residues in the amino-terminal tails of core histones and other proteins (Lee and Workman, 2007). Deacetylation of histone proteins will result in chromatin condensation and subsequent silencing of gene expression. HDAC enzymes are known to reduce transcription activity and thereby play an important role in cell growth, differentiation, and apoptosis progressions (Abel and Zukin, 2008, Wilson *et al.*, 2006) HDACs are divided into four main classes: I-IV. Class I and class II HDACs are more predominant in nervous system (Carey and La Thangue, 2006). Class I HDACs (1, 2, 3 and 8) are nuclear proteins that are widely expressed. Moreover they are homologs of HDAC RPD3, in yeast. Class II HDACs (4, 5, 6, 7, 9 and 10) are partly regulated by shuttling between the nucleus and cytoplasm and are expressed in a tissue and cell-specific manner (Abel and Zukin, 2008). Class III HDACs, otherwise known as sirtuins, in mammals comprise 7 enzymes (SIRT1-7) that have been implicated in control of cell proliferation (Carey and La Thangue, 2006).

Finally, Class IV HDACs consist of one member, HDAC 11 that contains conserved residues in the catalytic core regions shared by both class I and II mammalian HDAC enzymes (Gao *et al.*, 2002). HDACs can be further classified into Zn dependent (Class I, II and IV)) and Zn independent, NAD-dependent (Class III) (Carey and La Thangue, 2006). Sequence specificity of HDAC action is acquired by recruitment of HDACs to specific genetic loci by repressor, corepressors and methyl-DNA binding proteins (Abel and Zukin, 2008).

1.6.3.3 HDAC inhibitors as a therapy for FRDA

Indeed, a modest increase in FXN expression after treatment with benzamide histone deacetylase (HDAC) inhibitors, which inhibit class 1 HDACs, resulted in improved locomotor activity and coordination in an FRDA mouse model (Sandi *et al.*, 2011). Evidence in humans also supporting this was shown in two recent studies where disease severity, as measured by the Friedreich Ataxia Rating Scale, inversely correlated with FXN transcript and frataxin protein levels (Evans-Galea *et al.*, 2012, Plasterer *et al.*, 2013). Several pharmacological compounds have been trialed and others are in development to treat FRDA (Perlman, 2012). These include the antioxidant coenzyme Q and its synthetic analog idebenone (Parkinson *et al.*, 2013), the iron chelator deferiprone (Goncalves *et al.*, 2008), the drug pioglitazone that can stimulate mitochondria by activating PGC-1a (Marmolino *et al.*, 2010) and agents aimed at increasing frataxin like the antioxidant resveratrol (Li *et al.*, 2013) and benzamide HDAC inhibitors. Success has varied to date with several agents showing promise in animal and cellular models not always effective in clinical trial. There are new data, however, that the ‘‘drug pipeline’’ is starting to yield potential treatment options for FRDA. HDAC inhibitors like RG2833 (Repligen Corporation) increase

frataxin levels (Herman *et al.*, 2006, Rai *et al.*, 2010), and it has recently completed early-phase clinical trials. New derivatives to increase safety and efficacy are currently in development (BioMarin Pharmaceuticals).

1.7 Developing gene therapies for FRDA

Gene and cell therapies are being developed as promising treatments for several genetic diseases. Pioneering proof of-principle clinical trials for cell and gene therapy have successfully treated patients with the demyelinating disease X-linked adrenoleukodystrophy (Cartier *et al.*, 2009), adenosine-deaminase-deficient severe combined immunodeficiency (SCID) (Aiuti *et al.*, 2002, Aiuti *et al.*, 2009), chronic granulomatous disease (CGD) (Ott *et al.*, 2006), X-linked SCID (Cavazzana-Calvo *et al.*, 2010), Leber congenital amaurosis (Cideciyan *et al.*, 2009), haemophilia (Nathwani *et al.*, 2011), and, more recently, Wiskott–Aldrich syndrome (Aiuti *et al.*, 2013) and metachromatic leukodystrophy (Biffi *et al.*, 2013).

Following these successes, cell and gene therapy for FRDA is being pursued with many approaches currently being tested for potential efficacy (Table 1.4). A significant advantage in developing cell and gene therapy for FRDA is that affected individuals already produce frataxin, although at very low levels, so therapeutic introduction of frataxin will not illicit an immune response. Restoring function to even a small percentage of cells could have a positive effect on the surrounding microenvironment and improve overall clinical outcome.

Increasing *FXN*	Reported outcomes	References
Yeast artificial chromosome expressing human *FXN*	Rescues embryonic lethality of *FXN*-deficient mice	(Pook *et al.*, 2001)
Bacterial artificial chromosome expressing human *FXN*	Human BAC-mediated rescue of the Friedreich ataxia knockout mutation in transgenic mice	(Sarsero *et al.*, 2004)
Lentiviral or adeno-associated vector expression of human *FXN*	Reduced sensitivity to oxidative stress in fibroblasts from individuals with FRDA	(Fleming *et al.*, 2005)
HSV-1 amplicon vectors with 135 kb genomic *FXN* locus	Reduced sensitivity to oxidative stress in fibroblasts from individuals with FRDA Prolonged *FXN* expression in the brain of wild-type mice	(Gomez-Sebastian *et al.*, 2007) (Gimenez-Cassina *et al.*, 2011)
HSV-1 amplicon vectors expressing human *FXN* cDNA	Improved motor coordination in a conditional *FXN* knock-out mouse	(Lim *et al.*, 2007)
induced pluripotent stem cells derived from fibroblasts of individuals with FRDA	Successful development of iPSCs and differentiation to neural and cardiac cells	(Ku *et al.*, 2010) (Liu *et al.*, 2011) (Hick *et al.*, 2013) (Lim *et al.*, 2013)
Bone marrow-derived mesenchymal stem cells	Increased frataxin expression and resistance to oxidative stress; neuroprotection	(Kemp *et al.*, 2011) (Jones *et al.*, 2013)
TAT-frataxin fusion protein	Increased lifespan and cardiac function in a conditional *FXN* knock-out mouse	(Vyas *et al.*, 2012)
TALE proteins fused to an activation domain targeting the *FXN* promoter	Increased *FXN* transcript and frataxin protein in human FRDA fibroblasts	(Chapdelaine *et al.*, 2013)
Adeno-assocciated virus expressing human *FXN*	Increased lifespan and cardiac function in a conditional *FXN* knock-out mouse	(Perdomini *et al.*, 2014)

Table 1.4: Studies that have contributed to the development of gene and cell therapies for FRDA.

1.7.1 Retroviral and lentiviral vectors.

Oncoretroviral vectors and lentiviral vectors integrate into the host genome. For retroviral vectors, particularly those derived from the murine leukaemia virus (MLV), one of the greatest challenges is the risk of insertional mutagenesis upon integration near oncogenes and growth control genes (Baum *et al.*, 2006a) (Nienhuis *et al.*, 2006). This can lead to vector dependent side effects, such as clonal dominance, as seen during clinical trials for CGD (Ott *et al.*, 2006) and X-SCID (Hacein-Bey-Abina *et al.*, 2003, Howe *et al.*, 2008). Derived from the human immunodeficiency virus (HIV), lentiviral vectors are 80–120 nm replication-defective particles that can spread a relatively short distance in dense tissue (Segura *et al.*, 2013). They are an appealing vector for gene therapy given their flexible packaging capacity (12 kb) and ease of use. The vesicular stomatitis virus glycoprotein (VSV-G) pseudotype is the most commonly used envelope protein since it facilitates efficient transduction of multiple cell types and allows concentration of particles if required (Segura *et al.*, 2013). Use of multiple packaging helper vectors, characterizing the integration pattern, and introducing novel regulatory elements have significantly increased the safety profile of lentiviral vectors (Schambach *et al.*, 2013). Different pseudotypes have also increased cell targeting specificity.

Injection of lentiviral particles into the substantia nigra of rats showed that particles with Mokola virus pseudotypes transduced neurons, while those with lymphocytic choriomeningitis or the Moloney MLV pseudotypes transduced astrocytes (Cannon *et al.*, 2011). Fusion envelopes of VSV-G and other virus glycoproteins, such as the rabies virus, are also proving effective in transducing neuronal cells (Hirano *et al.*, 2013, Kato *et al.*, 2014). A key safety feature of lentiviral vectors is their selfinactivating

(SIN) design (Zufferey *et al.*, 1998). SIN vectors lack nonessential enhancer and transcriptional control sequences in the long terminal repeats of conventional retroviral vectors (Yu *et al.*, 1986). An encouraging trial demonstrated that symptoms in two boys with neurodegenerative X-linked adrenoleukodystrophy were reduced after autologous transplant of lentiviral-corrected BM (Cartier *et al.*, 2009). Common integration sites identified postcorrection were because of a benign integration bias and not oncogenic selection (Cartier *et al.*, 2009, Biffi *et al.*, 2011), indicating SIN lentiviral vectors have a superior safety profile over conventional oncoretroviral vectors (such as those used in the X-SCID trials). Latest-generation lentiviral vectors represent an appropriate system to potentially treat FRDA, and one study demonstrated that lentiviral vector-dependent expression of human FXN in fibroblasts isolated from FRDA patients increases their resistance to oxidative stress (Fleming *et al.*, 2005). Several groups are currently developing lentiviral vectors for gene therapy of FRDA.

1.7.2 Adeno-associated virus

Adeno-associated virus (AAV) is a small, nonenveloped single-strand DNA parvovirus its small size (approximately 26nm in diameter) allows AAV-derived gene therapy vectors to spread further in some tissues compared with other viral vectors. With 11 naturally occurring serotypes (AAV1-11), a variety of hybrid serotypes (including mixed and/or modified capsids) have also been developed in the last decade (Choi *et al.*, 2005). This has broadened tropism and increased cell targeting specificity; however, serotypes 2 and 5 remain the most commonly used (Choi *et al.*, 2005, Wang *et al.*, 2011). The primary limitation of AAV vectors is their small packaging capacity within the vector genome (4.8 kb). AAV can also integrate at chromosome breakage sites (Miller *et al.*, 2004) and a specific site in chromosome 19 (Kotin *et al.*, 1990). AAV

(serotype 2) has also been demonstrated to preferentially integrate with low efficiency in active genes in mice (Nakai *et al.*, 2003). An important advance has been the development of selfcomplementary AAV (scAAV) vectors that generate a single stranded genome with both the coding and complementary sequences packaged (McCarty, 2008). The scAAV vector removes the lag time for second-strand synthesis (a required step with AAV), facilitates more rapid expression once in the nucleus, and increases transduction efficiency. A major disadvantage, however, is that scAAV vectors have only half (2.3 kb) of the already small packaging capacity of AAV (McCarty, 2008). An early study evaluated AAV correction in human FRDA fibroblasts and demonstrated that cells experienced reduced sensitivity to oxidative stress upon AAV-dependent expression of human FXN (Fleming *et al.*, 2005). A very recent study demonstrated not only correction, but also reversal, of a severe cardiomyopathy phenotype in a conditional FRDA mouse model [where frataxin is deleted in cardiac and skeletal muscle; the muscle creatine kinase-Cre or MCK mouse (Puccio *et al.*, 2001), following a single intravenous injection of AAV constitutively expressing human FXN (Perdomini *et al.*, 2014). This study reports for the first time that MCK mouse cardiomyocytes that have already undergone severe energy failure, iron–sulfur cluster deficiency, and mitochondria and sarcomere ultrastructural changes can be fully rescued with vector-dependent FXN expression. Importantly, FXN expression also restored compromised ventricular function to wild-type levels (Perdomini *et al.*, 2014).

1.7.3 Herpes simplex virus type 1

Herpes simplex virus type 1 (HSV-1) is a well-characterized human DNA virus with a large packaging capacity in comparison to other viral vectors: 160 kb (Lim *et al.*, 2013). This means that HSV-1 has superior versatility with respect to the size and number of transgenes/regulatory regions that can be introduced, which is a distinct advantage when aiming to recapitulate endogenous expression in the therapeutic context. While HSV-1 is not as user friendly as retro/lentiviral vectors or AAV, bacterial artificial chromosome ‘‘recombineering’’ has overcome some of the technical issues, and packaging helper plasmids have increased its safety (Lim *et al.*, 2013, Laimbacher and Fraefel, 2014).

As a neurotropic virus, HSV-1 gene therapy vectors are primarily developed for neurological diseases such as FRDA. Introduction of the FXN genomic locus to FRDA fibroblasts via HSV1-based amplicon vectors also reduced sensitivity to oxidative stress (Gomez-Sebastian *et al.*, 2007), and this construct resulted in long-term persistent FXN expression in the brain of wild-type mice after injection into the adult mouse cerebellum (Gimenez-Cassina *et al.*, 2011). In 2007, Lim and colleagues developed a localized Fxn knock-out mouse lacking Fxn in the olivary neurons of the brain stem (Lim *et al.*, 2007). Using a rota rod assay, the authors demonstrated this FRDA model developed motor incoordination, a hallmark feature of disease, within 4 weeks of Fxn deletion. Importantly, this neurological phenotype was reversed upon stereotaxic injection of an HSV1 amplicon expressing human FXN into the brain stem (Lim *et al.*, 2007). This proof-of-principle study demonstrates that vector-dependent FXN expression can rescue neurological deficits to restore motor coordination in FRDA mice.

1.7.4 Nonviral-based delivery

Introduction of frataxin to cells does not need to be via viral-based vector delivery. Bacterial and yeast artificial chromosomes expressing human FXN can rescue the embryonic lethality of Fxn-deficient mice (Pook *et al.*, 2001, Sarsero *et al.*, 2004). In a recent study, human frataxin was directed to the mitochondria via an N-terminal fusion of the transduction domain of the cationic peptide transactivator of the HIV transcription protein TAT (Vyas *et al.*, 2012). TAT frataxin was introduced to fibroblasts isolated from individuals with FRDA and also the severe conditional frataxin knock-out mouse (neuron-specific enolase-Cre; NSE) with deletion of Fxn in cardiac and neural crest-derived tissues (Puccio *et al.*, 2001). This exogenous replacement of frataxin to mitochondria improved cardiac function and increased lifespan in the NSE mouse model (Vyas *et al.*, 2012). A very recent study demonstrated increased FXN expression after nucleoinfection of human FRDA fibroblasts with a transcription activator-like effector protein (TALE), engineered to bind to the FXN promoter, fused to a transcription activation domain (VP64). A 1.6-fold increase in mature FXN transcript and a 1.6–1.8-fold increase in frataxin protein were observed (Chapdelaine *et al.*, 2013).

In combination, these studies indicate that increasing frataxin levels can improve phenotype and ultimately clinical outcome, validating further studies testing the corrective potential of gene therapy for FRDA. Several international collaborations that focus on developing gene therapy for FRDA have recently formed—including GENEFA, AAV Life, and Voyager Therapeutics.

1.7.4 The challenges faced in gene therapies for FRDA

FRDA is a multifaceted disease that can vary in its age of onset, severity, and progression. FRDA also affects multiple organs and this presents several challenges for the development of effective cell and gene therapies. For gene therapy to be of lifelong clinical benefit, it requires long-term, stable, and effective expression of the therapeutic transgene. Gene therapy vectors ideally need to transduce long-term repopulating cells for stable correction. Progenitor and/or terminally differentiated cells have limited survival requiring multiple sources and treatments. Effective targeting of therapies Localized delivery of cells and/or gene therapy vectors by direct injection into specific sites could effectively correct enough cells to improve function of the targeted organ and ameliorate phenotype. However, targeting each tissue with significant pathology presents logistical and financial challenges and is especially difficult in a single individual.

While systemic delivery of viral vectors can result in high transduction rates, there is limited control of vector copy number and the specific cell types targeted, which can raise additional safety concerns. The delivery of vectors and/or corrected cells presents significant challenges in clinical translation. Specific targeting and distribution of vectors and/or sufficient engraftment of corrected cells in the main sites of pathology (the heart, DRG, and cerebellum) will be essential for therapeutic benefit. While increased tropism of gene therapy vectors will improve overall targeting capacity, correct homing and engraftment of corrected cells could pose the greater challenge. This is especially difficult if there is no inherent selective advantage for frataxin-expressing cells.

1.8 Gene therapy strategies for monogenic diseases

Research for treatment of monogenic disease remains foremost. When considering gene therapy for monogenic disorders, parameters for treatment include whether the gene mutation leads to a loss or gain of function, whether the gene product's function affects survival of the cell or development, and if the disease gene has cellular specificity (Fischer and Cavazzana-Calvo, 2008). There are four different gene therapy strategies for monogenic diseases:

(1) Addition of a normal copy of the mutated gene; best suited to loss-of function mutations and the focus of most gene therapy strategies so far (O'Connor and Crystal, 2006).

(2) Modification of messenger RNA to avoid the consequences of mutation; a possible option when the mutated exon is not indispensable. mRNA modifications can be brought about by small nuclear RNAs (snRNAs) (Gorman *et al.*, 1998).

(3) Inhibition of expression of the mutated gene; used to prevent the expression of a protein in a gain-of-function mutation or to inhibit cryptic splice sites which lead to expression of an abnormally spliced protein. Small interfering RNAs (siRNAs) have been used in this approach (Thompson and Patel, 2009).

(4) Repair of the mutated gene in the host DNA sequence and reversal of the disease. This strategy utilises a DNA-sequence-specific binding domain and an

endonuclease capable of inducing site-specific double-strand breaks in DNA. Simultaneously, a template encompassing the wild-type sequence that corresponds to the mutated stretch of DNA is introduced into the cell and acts as a substrate for repair. Zinc finger nucleases are a promising tool for this strategy. However, many technical concerns and low efficiency keep them far from clinical application at present (Rémy *et al.*, 2010).

In order to achieve clinical benefit two approaches for delivering genetic material exist; *in vivo* and *ex vivo*.

The *in vivo* strategy involves the direct delivery of DNA (usually via a viral vector) to resident cells of the target tissue (Figure 1.19A). There are two requirements for such a strategy: firstly, that target cells be easily accessible for infusion or injection of virus, and secondly, that the transfer vector readily and specifically infects, integrates, and then expresses the therapeutic gene in target cells and not surrounding cells at effective levels for extended time periods. Adenoviral vectors are the mainstay of *in vivo* strategies owing to their high transfection efficiency. However, the virus is plagued by antigenicity (Byrnes *et al.*, 1995) and is limited to short term expression of transgenes because it does not permanently integrate into the host genome (Mitani and Kubo, 2002). Currently, the lentivirus-derived vectors appear to be the most promising for future *in vivo* clinical applications (Selkirk, 2004).

The *ex vivo* approach involves the transfer of a therapeutic gene to cells in vitro (in culture) followed by transplantation of these modified cells to the target tissue (Figure 1.19B). The modified, transplanted cells act as an engineered secretory tissue, synthesising and releasing desired proteins to the local environment (Selkirk, 2004).

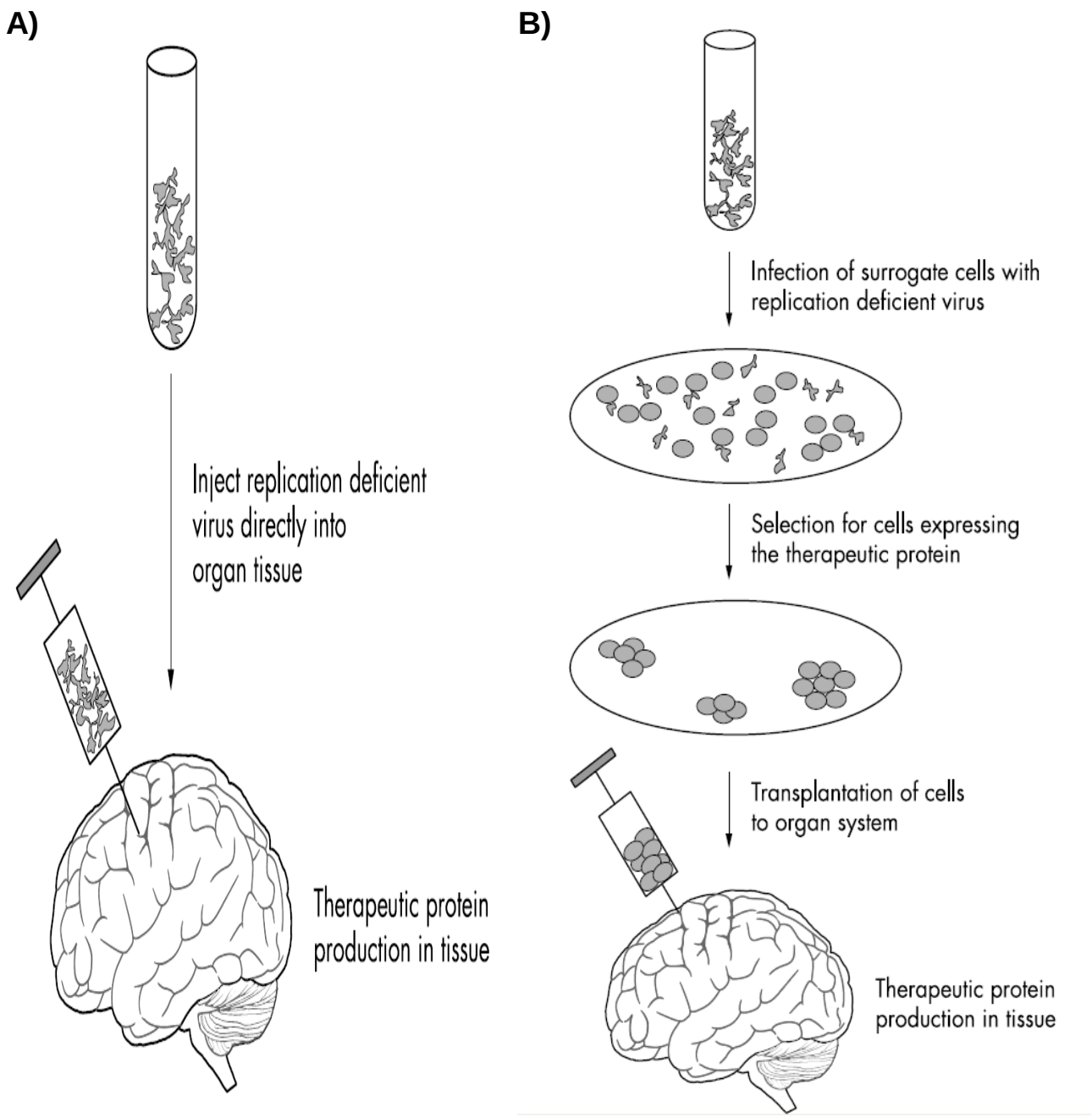

Figure 1.19: Schematic of *in vivo* and *ex vivo* gene therapy strategies. A) *In vivo* gene transfer. The *in vivo* strategy is based on directly injecting or infusing a gene transfer vector to cells of the target tissue. The therapeutic gene will then be expressed in target cells. B) *Ex vivo* gene transfer. The *ex vivo* strategy is based on transfer of the therapeutic gene to selected surrogate cells *in vitro* and subsequent transfer of the cells into the target tissue to express the gene (Selkirk 2004).

1.9 Viral vectors for gene therapy

Many different types of vector, both viral and non- viral, have been explored as a means of transporting corrective DNA into target cells (Kay *et al.*, 2001, Glover *et al.*, 2005). However, it is viral vectors which currently represent the most effective means of gene delivery and have been used in the majority of gene therapy clinical trials (over 70%), with adenoviral and retroviral vectors used in 22% and 18.8% of all clinical trials to date, respectively. The choice of which viral vector to use for a particular application depends mainly on the cell type to be targeted and duration of expression required (Gillet *et al.*, 2009). However, desirable properties of all viral vectors are the ability to be reproducibly propagated, to be purified to high titres, and to mediate transgene delivery and expression to the target cell without substantial toxicity (Wanisch and Yanez-Munoz, 2009). Many viruses with different properties have been exploited to produce gene therapy vectors; some of the most commonly used are derived from gamma retroviruses, lentiviruses, adenoviruses, adeno- associated viruses (AAVs) and herpes simplex viruses (HSVs) (Table 1.5).

	Packaging capacity	Vector Yield (TU/mL)	Tropism re-targeting	Duration of transgene expression	Vector genome forms	Genotoxicity	Inflammatory potential	Transduction of quiescent cells
Gamma retrovirus	7 kb	$1x10^{10}$	Broad	Long-term (years)	Integrated	Integration may cause oncogenesis	Low	No
Lentivirus	8kb	$1x10^{10}$	Broad	Long-term (years)	Integrated	Integration may cause oncogenesis	Low	Yes
Integration Deficient Lentivirus	8kb	$1x10^{10}$	Broad	Transient	Episomal	Low	Low	Yes
Herpes Simplex Virus	>30kb	$1x10^{12}$	Broad (strong for neuron)	Transient	Episomal	Low	High	Yes
Adenovirus	30kb	$1x10^{13}$	Broad	Transient (Weeks)	Episomal	Low	High	Yes
Adeno Associate Virus	5kb	$1x10^{13}$	Broad	Medium to long- term.	Episomal	Low	Low	Yes

Table 1.5: The properties of commonly used viral gene transfer vectors table modified from (Bouard *et al.*, 2009). TU; Transducing Units

1.10 Retroviruses

Retroviruses are a large group of enveloped RNA viruses belonging to the Retroviridae family which are characterised by their diploid, single stranded RNA genomes, reverse transcription of the RNA genome into a double stranded DNA intermediate (the provirus), and integration of the provirus into the host cell chromatin. Virions are on average approximately 100nm in size and contain an RNA genome of 7-12 kb in size. The hallmark of retroviruses is their replicative strategy which involves reverse transcription of the viral RNA into linear DNA and the subsequent integration of this DNA into the host cell genome. Within the family *Retroviridae* there are seven genera; *Alpharetrovirus*, *Betaretrovirus*, *Gammaretrovirus*, *Deltaretrovirus*, and *Epsilonretrovirus* (containing simple retroviruses with oncogenic potential), and *Lentivirus* and *Spumavirus* (containing complex retroviruses). Each genus is characterised by differences in genetic structure, genome complexity, site of particle assembly, and virion morphology. For the development of vectors for gene therapy the focus has mainly been on utilising *Gammaretroviruses*, Lentiviruses, and Spumaviruses (Baum *et al.*, 2006b). The retroviral vector used in this study was a HIV- 1- based lentiviral vector, so the following summary is focused principally on this virus. However, where important differences exist between lentiviruses and other retroviruses are described.

The family Retroviridae shares three common features that are of major interest for gene delivery:

(1) receptor-mediated uptake of a membrane-coated viral particle into target cells,

(2) reverse transcription of a plus-stranded RNA genome into a double-stranded DNA that is integrated into cellular chromosomes to establish active or latent infection.

(3) cytoplasmic assembly of particles with incorporation of the full-length retroviral mRNA as the mobile form of genetic information.

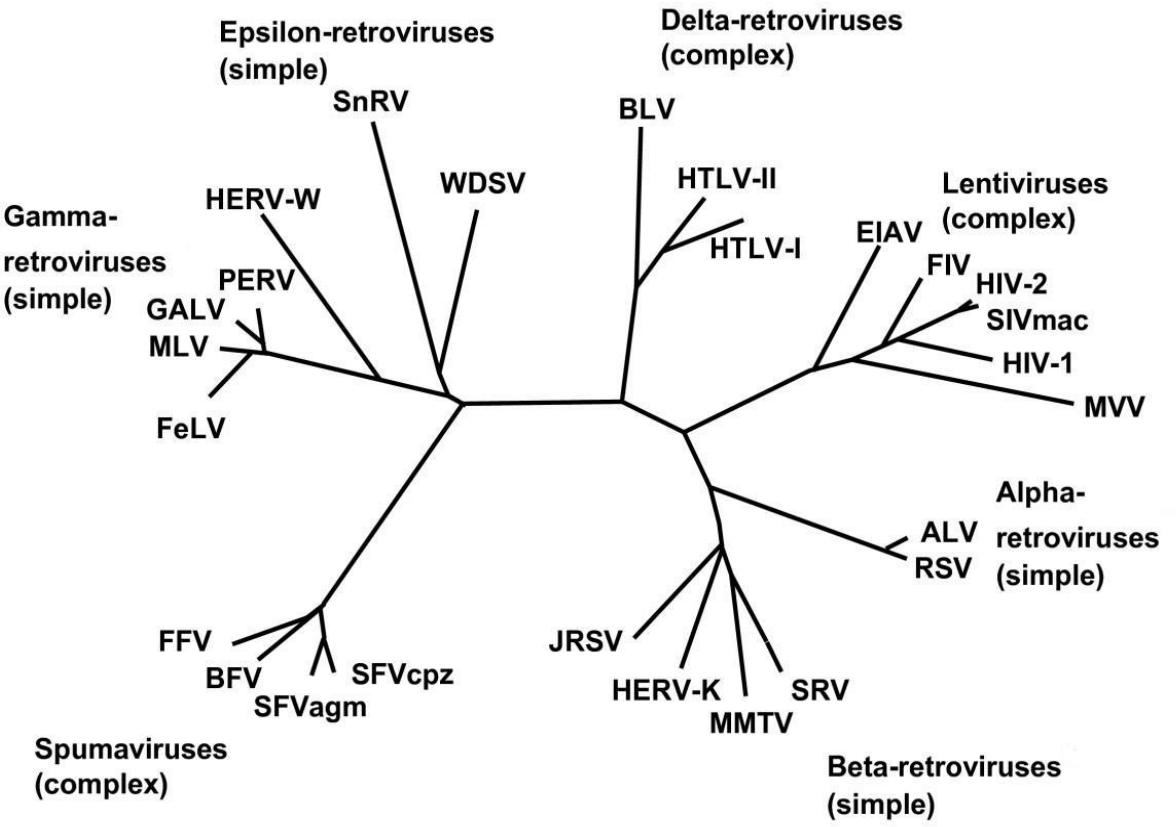

Figure 1.20: Phylogeny of Retroviruses. Alpharetrovirus; Avian leukosis virus (ALV); Rous sarcoma virus (RSV). Genus Betaretrovirus; Mouse mammary tumour virus (MMTV). Genus Gammaretrovirus Murine leukemia virus (MLV); Feline leukemia virus (FeLV). Genus Deltaretrovirus; Bovine leukemia virus (BLV); cancer-causing Human T-lymphotropic virus (HTLV-I-II). Genus Epsilonretrovirus; Walleye dermal sarcoma virus (WDSV). Genus Lentivirus; Human immunodeficiency virus 1(HIV-1) Simian, Feline immunodeficiency viruses (SIV mac, FIV) Genus Spumavirus; Simian foamy virus SFV cpz (Weiss, 2006).

1.10.1 Retrovirus biology

In most viruses, DNA is transcribed into RNA, and then RNA is translated into protein. However, retroviruses function differently, their RNA is reverse-transcribed into DNA, which is integrated into the host cell's genome (provirus), and then undergoes the usual transcription and translational processes to express the genes carried by the virus. During the course of their life cycle, retroviruses alternate between two principal forms: the provirus and the virion. Virions consist of enveloped particles about 100 nm in diameter. The virions also contain two identical single-stranded RNA molecules 7-10 kilobases (kb) in length. Although virions of different retroviruses do not have the same morphology or biology, all the virion components are very similar (Weiss, 2006). The provirus consists of double-stranded DNA integrated into a host cell chromosome. Viral RNA and proteins are then expressed from the provirus using the host transcription and translation apparatus, and are subsequently packaged at the host plasma membrane into a virion. After reverse transcription the integrated proviral genome comprises both coding genes and non-coding *cis*-acting gene regulatory sequences (Weiss, 2006).

1.10.1.1 Coding sequences

Retroviruses are broadly divided into two categories; simple and complex. The basic retroviral genome contains four genes: *gag, pro, pol,* and *env* which encode proteins found in all retroviruses (Eisenman and Vogt, 1978). Simple retroviruses contain only these four basic genes, while complex retroviruses possess additional regulatory and accessory genes (Figure 1.21). The *gag, pro, pol* and *env* genes are expressed as polyproteins which are processed into mature forms during assembly of the virion and maturation. The major structural protein of the virion is encoded by *gag* and is cleaved during maturation to form the matrix (MA), capsid (CA), and nucleocapsid (NC) proteins. The *pol* gene codes for the viral enzymes reverse transcriptase (RT) and integrase (IN), essential for reverse transcription of the viral RNA genome to double stranded DNA and integration of the DNA genome into a host cell chromosome, respectively. *Env* codes for the surface (SU) and transmembrane (TM) components of the viral envelope protein which are targeted to the virion lipid bilayer. Finally, *pro* encodes the viral protease (PR) which acts to process the viral polypeptides formed by *gag, pro, pol,* and in some strains *env (Kay et al., 2001)*. HIV- 1 also contains genes coding for the regulatory proteins Tat (trans- activator of transcription) and Rev (regulator of virion) and the accessory proteins Vif, Vpr, Vpu, and Nef which can act to protect the virus from host restriction factors (Malim and Emerman, 2008).

1.10.1.2 Non-coding sequences

The provirus is flanked by long terminal repeats (LTRs), subdivided into U3, R, and U5 regions (Tipper *et al.*, 2012). U3 (unique in 3') is approximately 450 nucleotides long in both murine leukaemia virus (MLV) and HIV- 1 and acts as a promoter of viral transcripts. The R (repeat) region is approximately 100 nucleotides long in HIV- 1 and contains a polyadenylation signal, typically AAUAAA, which allows efficient processing of viral RNA. Homology between the two R regions is also essential for reverse transcription of the genome. U5 (unique in 5') consists of a GU- rich stretch of roughly 80 nucleotides which enhances the recognition and processing of the polyadenylation signal contained within R (Huthoff *et al.*, 2003). Other *cis* acting regulatory sequences sites include the primer binding site (PBS). This site is complementary to an 18bp region of a host- derived tRNA which unwinds and binds to this region to act as a primer for minus strand DNA synthesis during reverse transcription (Verma *et al.*, 1971, Dahlberg *et al.*, 1974). The region downstream of the primer binding site forms the encapsidation signal (Ψ) which allows efficient, preferential encapsidation of viral genomic RNA into virions. It is removed during splicing, so only full length (unspliced) transcripts can be packaged into virions (Mann and Baltimore, 1985). The polypurine tract (PPT), just 16 nucleotides long in HIV- 1, is located immediately upstream of the 3' U3 and acts as a primer for plus strand DNA synthesis during reverse transcription (Smith *et al.*, 1984, Finston and Champoux, 1984). Lentiviruses such as HIV- 1 also possess a second origin for plus strand DNA synthesis called the central polypurine tract (cPPT) located within the integrase component of the *pol (Charneau et al., 1994)*.

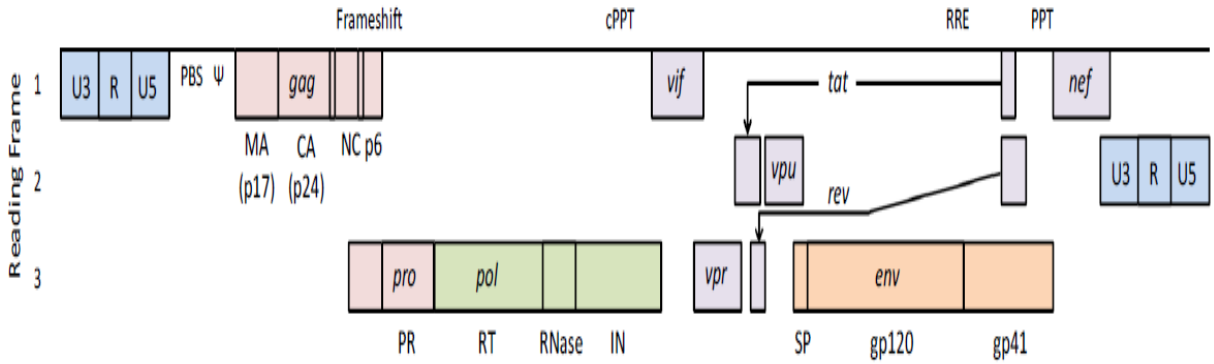

Figure 1.21: Proviral genome organisation of a complex wildtype human immunodeficiency virus type I genome. This genome contain the basic structural genes: *gag* which encodes matrix (MA), capsid (CA) and nucleocapsid (NC) proteins, *env* which encodes surface (SU) and transmembrane (TM) glycoproteins, *pol* and *pro* which encode the enzymes protease (PR), reverse transcriptase (RT), integrase (IN) and RNase. HIV-1 also contains the regulatory genes *tat* and *rev*, and the accessory genes *vif, vpr, vpu* and *nef*; Primer binding site (PBS); encapsidation signal (Ψ); Polypurine tract (PPT); Central Polypurine tract (cPPT); Rev response element (RRE), spacer peptide (p6). Figure modified from (Coffin *et al.,* 2007), (Watts *et al.,* 2009) and (Sinn *et al.,*2005).

1.10.2 Retrovirus Structure

In mature virions of retroviruses the matrix (MA) protein is bound to the envelope obtained from the host plasma membrane during the budding process. The envelope contains the viral glycoprotein where the surface (SU) receptor protrudes from the virion and is anchored by the transmembrane (TM) region which spans the lipid bilayer (Perez *et al.*, 1987). A dense virion core is contained inside the matrix and can be cone shaped (as for HIV- 1) or round (as for MLV). Around 2000- 4000 copies of capsid (CA) protein form the outer shell of the core inside which is a nucleocapsid (NC)- RNA complex. Viral proteins including reverse transcriptase (RT) and integrase (IN), and some host- derived proteins including the host tRNA used during minus strand DNA synthesis are packaged inside the virion (Halwani *et al.*, 2004) (Figure 1.22).

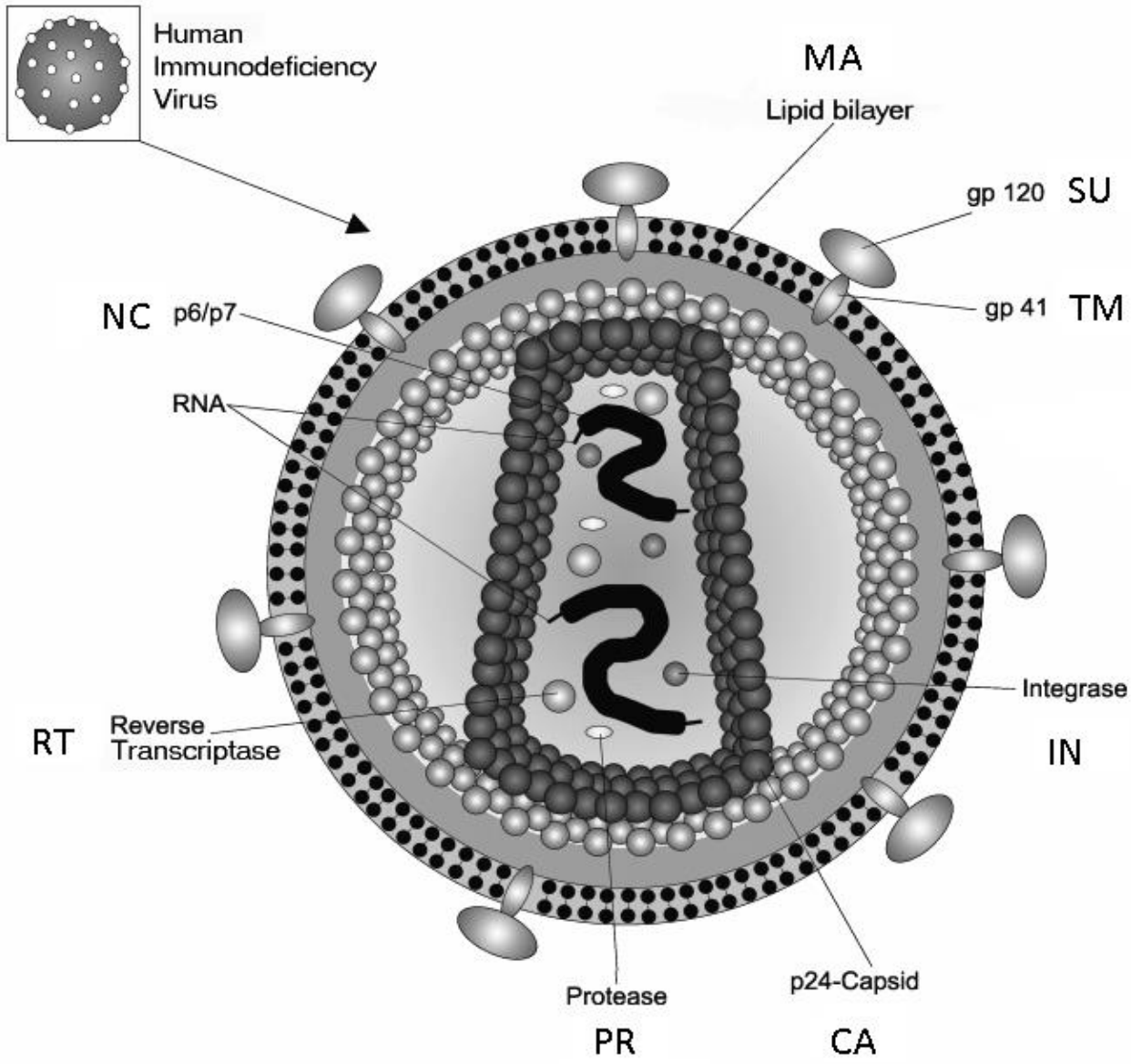

Figure 1.22: A schematic representation of a mature HIV-1 virion. Viral proteins depicted in this picture: transmembrane glycoprotein (TM); surface glycoprotein (SU); matrix (MA); protease (PR); capsid (CA); nucleocapsid (NC); single stranded RNA genome (RNA); integrase (IN); reverse transcriptase (RT) (Baum *et al.*, 2006b, Watts *et al.*, 2009).

1.11 Lentiviral life cycle

Unlike retroviruses, they rely on active transport of the preintegration complex through the nucleopore by the nuclear import machinery of the target cell. The lentiviral strategy for nuclear targeting enables infection of non-dividing cells, an attractive attribute for a gene therapy vector (Vigna and Naldini, 2000). The HIV- 1 viral life cycle can be divided into two temporarily distinct phases: infection and replication. Infection results in the introduction of the viral genome into the cell. Lentiviruses differ from other retroviruses due to their long latent period during infection. This leads to an early phase of gene expression characterised by the appearance of viral regulatory products involved in replication, followed by a late phase when structural genes are expressed and assembly of new viral particles occurs (Kay *et al.*, 2001). A schematic view of the lentiviral life cycle is shown in Figure 1.23.

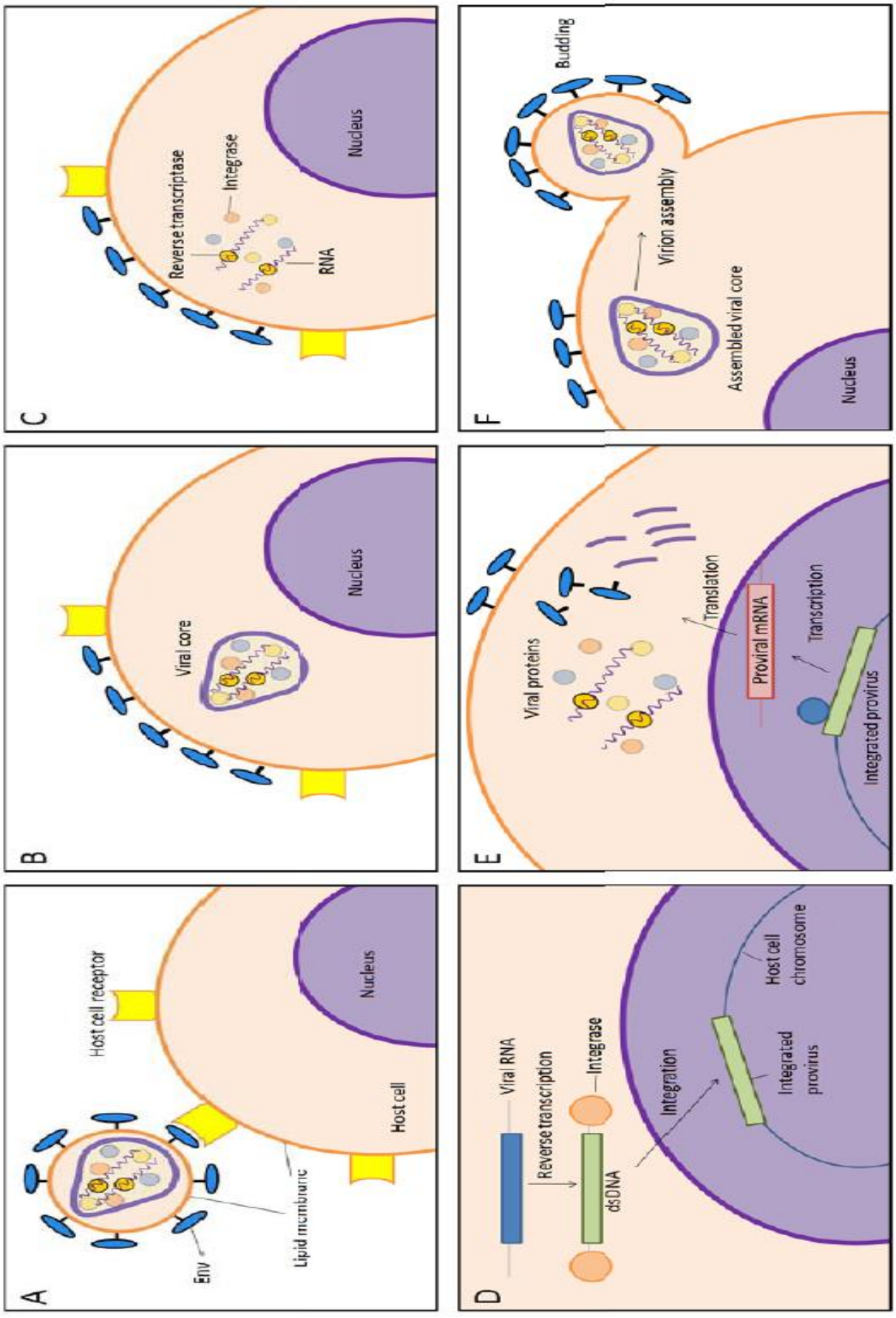

Figure 1.23: A schematic representation of the lentiviral life cycle showing (A) attachment, (B) entry, (C) uncoating, (D) reverse transcription and integration, (E) transcription and translation (F) assembly and budding. Figure modified from http://www.sumanasinc.com/webcontent/animations/content/hiv.html.

1.11.1 Entry and uncoating

The first stage of the viral life cycle is entry of the virion into a target cell. This is mediated by recognition of a host cell surface receptor by Env; the major determinant of viral tropism. The primary receptor for HIV- 1 is CD4 51, along with coreceptors CCR5 (Dragic *et al.*, 1996, Choe *et al.*, 1996), and CXCR4 57. SU and CD4 binding induces a conformational change in surface glycoprotein (SU) revealing a conserved, high affinity, coreceptor binding domain. Coreceptor binding leads to exposure of the transmembrane glycoprotein (TM) fusion peptide, a hydrophobic region which interacts with the cell membrane, allowing fusion of the cell and viral membranes and internalization of capsid (Bosch *et al.*, 1989). Once inside the cell, the protein composition of the HIV- 1 core changes in a process known as uncoating. Firstly, a complex called the reverse transcription complex (RTC) in which DNA synthesis occurs is produced, and then a pre-integration complex (PIC) which is transported to the nucleus for integration into the host genome.

1.11.2 Reverse transcription

During uncoating, the capsid protein dissociates and the core forms the RTC which contain the proteins RT, IN, NC, phosphorylated MA, and Vpr (Bukrinsky *et al.*, 1993, Miller *et al.*, 1997). Reverse transcription of the viral RNA takes place prior to nuclear entry mediated by RT and is one of the defining features of retroviruses. It occurs in a series of steps:

1. A specific cellular tRNA (tRNAlys3) acts as a primer and hybridizes to the complementary primer binding site (PBS) on the viral RNA initiating DNA synthesis.

2. Synthesis proceeds to the 5' end of the genome so the U5 and R regions are encoded on this short (-)ssDNA.

3. The synthesis results in a RNA:DNA duplex and the RNA template strand is degraded by the RNase H activity of RT. The (-)ssDNA is then transferred to the RNA 3' end, a process made possible by the homology between the 5' and 3' R elements, this is known as minus strand transfer.

4. The first strand of complementary DNA is extended and the majority of viral RNA is degraded by RNase H. Once the strand is completed, second strand synthesis is initiated at the PPT.

5. Additionally, other RNA sequences such as the central polypurine tract (cPPT) are not degraded and act as primers for positive strand synthesis. This proceeds from the PPT to the end of the tRNA primer.

6. This creates an area of homology at the PBS (18 nucleotides) between the plus and minus DNA strands which enables plus strand transfer.

7. Synthesis continues from the transferred section of the plus strand but stops at the cPPT, where plus strand DNA initiated at the PPT displaces plus strand DNA initiated at the cPPT. This creates a discontinuous 'DNA flap' of 99 nucleotides between the cPPT and a central termination sequence (CTS) thought to aid nuclear entry (Charneau *et al.*, 1994).

8. Following plus strand transfer, DNA synthesis continues in both directions to the ends of the LTRs and can be incorporated into the host genome. While

reverse transcription takes place, the complex migrates to the nucleus. RT then dissociates forming the PIC and translocation occurs through the nuclear pore. Gammaretroviruses are unable to cross the nuclear envelope, therefore they are only able to integrate their genetic material when the envelope breaks down during mitosis. As lentiviruses, and the vectors based upon them, can cross the nuclear envelope they have the ability to integrate into non- dividing cells this makes them very useful tools in gene therapy.

1.11.3 Integration

The second defining feature of retroviruses is integration of proviral DNA into the host chromosome. This is mediated by the integrase (IN) encoded by *pol.* IN binds to attachment (att) sites in the U3 and U5 LTRs and integration occurs in two catalytic steps. The first step, known as 3'- processing, occurs in the cytoplasm within the PIC and involves cleavage of the 3' terminal dinucleotide (pGpT) at both ends of the viral DNA. The resulting recessed 3'- OH groups provide the sites of viral genome attachment to the host DNA (Miller *et al.*, 1997). The second step, strand transfer, occurs in the nucleus. Here, IN mediates a nucleophilic attack via the viral 3'- OH groups against phosphodiester bonds on opposite strands of the host target DNA. During this step, the energy of the broken phosphodiester bonds in the chromosome is used for the formation of new bonds joining the viral 3' ends to the target DNA (Engelman *et al.*, 1991). In the final step of integration, the unpaired dinucleotides from the 5’ ends of the viral DNA are removed and the single- stranded gaps created between the 5’ end and the target DNA are filled causing the integrated DNA to be flanked by the same five base pairs (Craigie, 2001). DNA episomes are also generated as by- products of integration. Aside from the linear DNA precursor, two types of

circular episome with intact viral coding regions are produced. These molecules can have one LTR - formed by homologous recombination between the two LTRs, or two LTRs – formed by non- homologous end- joining of the double stranded blunt viral DNA (Cara and Reitz, 1997). Non- integrated viral DNA can support transcription (Wu and Marsh, 2003), and it is on this basis that integration defective lentiviral vectors mediate expression (Philippe *et al.*, 2006, Yanez-Munoz *et al.*, 2006).

1.11.4 Transcription

Once integrated into the host genome, the provirus relies on cellular machinery for transcription and translation. Transcription of the integrated proviral DNA involves the interaction of both *cis*- acting regulatory sequences in the LTR and trans- acting proteins made by the cell and the virus. The HIV-1 promoter does not assemble a particularly efficient RNA polymerase complex; the initiation rate is slow and the elongation rate is poor. The transcriptional activator protein, Tat, binds a stem loop structure (TAR) present at the immediate 5' end of all mRNA transcripts recruiting host cellular elements, such as cyclin T and Cdk9 to the transcriptional complex increasing transcription 100- fold (Romano *et al.*, 1999). Rev then binds to unspliced mRNA at a Rev responsive element (RRE) site and this complex is then exported from the nucleus into the cytoplasm, where Rev stabilizes viral transcripts (Pollard and Malim, 1998, Schneider *et al.*, 1997).

1.11.5 Translation

The Gag and Gag- Pro- Pol polyproteins are translated from unspliced mRNA in a ratio of 20:1. The reading frame of Pol is - 1 with respect to Gag therefore translation of Gag- Pol- Pro requires a translational frameshift by the ribosome. After translation the Gag and Gag- Pol- Pro polyproteins associate to the cellular membrane where

Gag multimerisation occurs and the viral genome is bound by NC through an encapsidation signal (Ψ) which is present only on unspliced mRNA, allowing it to be packaged. The *env* gene is transcribed as one full mRNA product and is then translated to produce a precursor protein to the viral glycoproteins gp120 and gp41. During translation Env is inserted into the rough endoplasmic reticulum membrane through the signal recognition particle (SRP) and subsequently recruited to the virion (Perez *et al.*, 1987).

1.11.6 Virion assembly and budding

Virions are packaged with a number of host proteins and are then released from the cell surface as immature, non- infectious particles. The Gag and Gag- Pol- Pro polyproteins are then cleaved by protease (PR) to produce the IN and RT as well as the structural proteins MA, CA, and NC. This proteolytic processing is required for condensation of immature spherical Gag to the mature cone- shaped core for the development of HIV- 1 infectivity and gives rise to a mature HIV- 1 virion (Briggs *et al.*, 2003).

1.12 Lentiviral vectors

The concept of viral-based tools for gene delivery emerged for the first time in the early 1980s with vectors based on the Moloney Murine Leukaemia Virus (Mo-MLV) (Mann *et al.*, 1983). Vectors rely on the physical separation into different plasmids of proteins required for viral particle formation and infectivity (the packaging and the envelope constructs) and of *cis*-acting sequences sufficient to mobilize the viral genome (the transfer vector).

Lentiviruses owe their *lenti* appellative (slow in *latin*) to the long period of time elapsing between the initial infection and the onset of the disease, that can protract over a period of months or even years. The ability to transduce non-dividing cells is a unique feature of lentiviruses which distinguishes them from simple retroviruses (Buchholz *et al.*, 2009). The viral life cycle can be divided into two main phases: firstly, in which the viral genome is transferred into the host cell and secondly, in which this genome is expressed and viral propagation is assured. The main interest of viral vectors for gene therapy purposes lies in the first phase, collectively referred to as the early steps of the viral life cycle. This process can be defined as gene transduction or single cycle infection (Durand and Cimarelli, 2011).

Lentiviral vectors have many other advantageous features making them an extremely attractive asset in gene therapy:

I. The proteins for reverse transcription and integration are carried within the virion allowing the viral genes that code for them to be deleted from vector constructs.

II. Large coding capacity of 8-10 kb of transgene cassette, in addition to all the required *cis*-acting sequences (Zufferey *et al.*, 1998).

III. Reduced *in vivo* immunogenicity in comparison to other gene therapy vectors (Chirmule *et al.*, 1999).

IV. Stable transmission of the transgene to the target cell and subsequent generations through integration of the provirus into the host cell genome.

1.12.1 Early HIV-1 vectors

Early lentiviral vectors comprised of viruses carrying transgenes that were capable of replication. These were used as a tool to track viral replication in vitro and in vivo and as platforms to screen for anti-HIV-1 drugs. In order to increase the safety of HIV vectors a series of modifications was introduced to separate viral sequences needed for packaging and production from those encoding viral proteins. The first prototypes separated virus elements into two plasmid (Helseth *et al.*, 1990, Page *et al.*, 1990):

- Plasmid encoding HIV-1 proviral DNA with a deletion in the env gene.
- Plasmid expressing Env.

Viruses undergo only a single round of infection since they did not carry the env gene, this was accomplished by Trans-complementation of Env protein from the separate plasmid. These early HIV vectors had transgenes inserted in nef or env with their expression driven by the 5'-LTR (Page *et al.*, 1990, Landau *et al.*, 1991, Helseth *et al.*, 1990).

Further enhanced HIV-1-based vectors were generated carrying essential cis-acting elements for genome packaging, reverse transcription, and integration (LTRs, Ψ and RRE), but no viral proteins (Richardson *et al.*, 1993). Mainly a heterologous internal promoter such as CMV (cytomegalovirus) drives the expression of the foreign genes in these vectors.

1.12.2 Expanded tropism through pseudotyping with vesicular stomatitis virus envelope-glycoprotein G (VSV-G).

Early HIV vectors could only infect human cells expressing CD4, since HIV-1 Env recognizes human CD4 as a primary receptor.

Burns *et al.* produced pseudotyped murine leukaemia virus based retroviral vectors (MLV) by replacing the retroviral Env glycoprotein with the viral attachment protein of VSV-G. These pseudotyped particles had two major advantage over unmodified vectors. First, VSV-G is substantially more stable than retroviral or lentiviral envelopes, allowing pseudotyped viruses to be concentrated by ultracentrifugation to higher titres than ever before (Burns *et al.*, 1993). Secondly, despite the controversy of the receptor for VSV-G (Coil and Miller, 2004), it was known that VSV-G binds to a ubiquitous membrane component, allowing this envelop to transduce a markedly wider set of cells, even including non-mammalian cells. In light of these developments Akkina *et al.,* used VSV-G to pseudotype HIV-1 vectors and demonstrated production of highly concentrated vectors that mediated high efficiency gene transfer into CD34+ haematopoietic stem cells (Akkina *et al.*, 1996). The majority of lentiviral vectors are now pseudotyped with VSV-G giving them robust transduction into many cell types.

1.12.3 First-generation HIV-1-based lentiviral vectors

By splitting the viral components into three separate plasmids first generation HIV-1 based lentiviral vectors with increased safety was accomplished. Since lentiviral vectors are derived from the pathogen HIV-1 virus there are bio-safety considerations in developing and using these as gene delivery vectors, mainly because of the possibility of generating replication competent lentiviruses (RCLs) with pathogenic potential.

Despite safety concerns the ability of the lentiviral vectors to mediate stable gene transfer into both dividing and non-dividing cells makes them potent vectors for basic and translational research (Naldini *et al.*, 1996b).

Many laboratories have developed a number of 'generations' of lentiviral vector to reduce the likelihood of the production of RCLs in vector preparations. However, the first generation vectors are referred to as those vectors that first split the system into three separate plasmids to increase safety. These three separate elements include:

- Packaging construct.
- Env plasmid encoding a viral glycoprotein;
- Transfer vector genome construct (Figure 1.24 A).

The packaging construct expresses HIV Gag, Pol and regulatory/accessory proteins from a strong mammalian promoter (CMV) to generate viral particles. The Env plasmid expresses a viral glycoprotein, such as VSV-G, to provide the vector particles with a receptor-binding protein. To prevent their transmission into vector particles and to reduce the production of RCL in vector preparations these two plasmids have been specifically engineered without either a packaging signal or LTRs. The transfer vector plasmid contains all of the essential *cis*-acting elements (LTRs, Ψ and RRE) for packaging/reverse transcription/integration and the transgene(s), but expresses no HIV proteins. Since the transactivator Tat is not encoded by the transfer genome, the promoter activity by the 5'-LTR is minimal. Instead, transfer genomes use an internal promoter to express transgenes in transduced cells. This three-plasmid system allows the delivery of a gene of interest without expressing viral proteins in target cells. Splitting the vector components into three plasmids means at least two recombination events are required to yield a replication-competent HIV-1-like virus during vector production (Durand and Cimarelli, 2011).

1.12.4 Second generation lentiviral vectors

Second generation vectors have been developed by modifying accessory genes in the system, to increase the safety of gene delivery (Figure 1.24B).

The accessory HIV-1 Vif, Vpu, Vpr and Nef proteins were removed, as they can be deleted without affecting viral replication in certain human lymphoid cell lines

However, these proteins are actually essential for efficient HIV-1 propagation/virulence in primary cells or *in vivo* (Fouchier *et al.*, 1996).

Nef promotes the degradation of host proteins, such as MHC class I and CD4, to augment virus production and facilitate immune evasion (Collins *et al.*, 1998) and Vif is necessary to inactivate a host antiviral factor, apolipoprotein B mRNA editing enzyme-catalytic polypeptide-like 3G (APOBEC3G), to ensure efficient virus production (Harris *et al.*, 2003). Similarly, Vpu neutralizes another cellular antiviral factor called Tetherin (Neil *et al.*, 2008, Sakuma *et al.*, 2009). Although these accessory genes are important for HIV pathogenicity, they can be deleted in second-generation lentivectors (Zufferey *et al.*, 1997) (Figure 1.24B). By replacing HIV-1 Env with VSV-G, these second-generation vectors include only four of the nine HIV genes: gag, pol, tat and rev (Zufferey *et al.*, 1997).

1.12.5 Self-inactivating (SIN) vectors with a deletion in the U3 region of the 3'-LTR

Conventional lentiviral vectors integrate transgene cassettes flanked by two LTRs into the host genome (Figure 1.25). However, if replication-competent recombinant lentiviruses are produced or if vector-transduced cells are subsequently infected by a wild-type lentivirus they may be able to replicate in a similar manner to that of wild-type viruses and spread transduction beyond the original target cell. Since LTRs have

an enhancer [binding sites for host transcription factors, including specificity protein 1 (Sp1) or nuclear factor κB (NF-κB)] and promoter regions this will raise another serious issue which is undesired activation of adjacent cellular genes by integrated vectors. If semi-random integration of the transgene occurs near a proto-oncogene, these enhancers/promoters can activate transcription of these genes, resulting in oncogenesis. This has led to development of SIN lentivectors. A standard vector genome is flanked by two LTRs that each contain three regions: U3, R and U5 (Figure 1.25). U3 acts as a viral enhancer/promoter and R in the 3'-LTR acts as the polyadenylation signal. The 5' U3 and the 3' U5 element are therefore not present in mRNA from the provirus and instead, the R region caps both ends (Figure 1.25). During reverse transcription prior to integration when U3 in the 3'-LTR is copied and transferred to the 5'-LTR, duplication of LTR elements occurs. In MLV vectors It was demonstrated that if part of U3 in the 3'-LTR is deleted, its duplication will transfer the same deletion into the 5'-LTR's promoter/enhancer region and therefore results in transcriptional inactivation of potentially packageable viral genomes in the transduced cell (Yu *et al.*, 1986). Subsequently this SIN approach was applied to HIV vectors by deletion of 3'-LTR elements, including its TATA-box-, Sp1-, NF-κB- and NFAT (nuclear factor of activated T-cells)-binding sites (Miyoshi *et al.*, 1998, Zufferey *et al.*, 1998, Iwakuma *et al.*, 1999). This SIN modification reduces the likelihood of:

- Propagation of spontaneously produced replication-competent recombinant HIV-like viruses.
- Insertional activation of cellular oncogenes by residual promoter activities of integrated LTRs.
- Mobilization of integrated vectors by a wild-type virus.
- Transcriptional interference and suppression by LTRs.

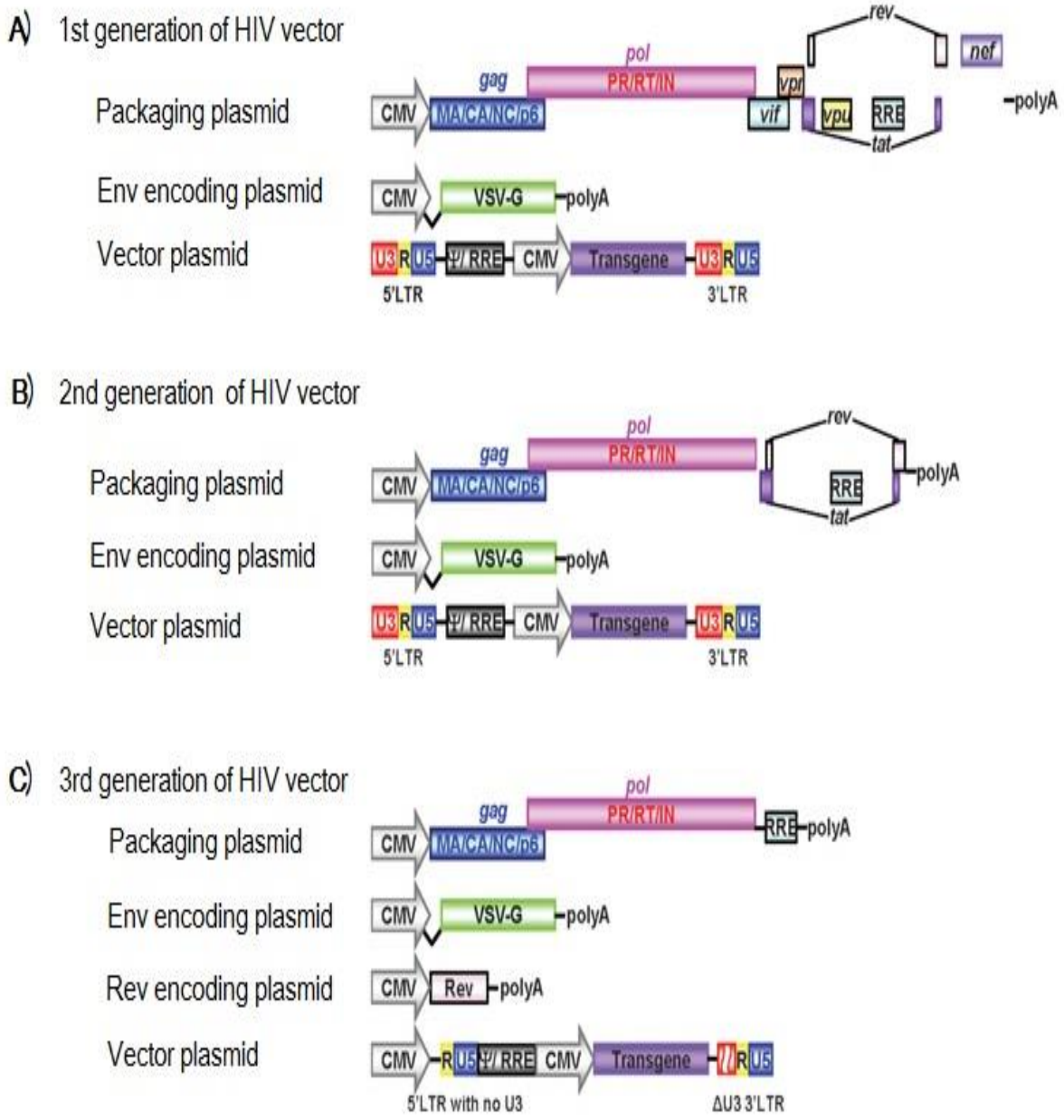

Figure 1.24: Schematic representation of HIV vectors. **A**) The first generation of HIV vectors includes all of the viral proteins, except Env protein, in a packaging plasmid. VSV-G is provided by a different plasmid. The HIV vector plasmid contains LTRs and the transgene is expressed under a strong viral promoter such as the CMV promoter. **B**) For the second generation of HIV vectors, all of the accessory proteins are excluded from the packaging plasmid. Similar to the first generation of HIV vectors, expression of glycoprotein and transgene are provided by different plasmids. **C**) The third generation of HIV vectors requires four different plasmids. In addition to the three plasmids (i.e. a packaging plasmid, an Env-encoding plasmid and a vector plasmid), Rev protein is provided by a different plasmid. The vector plasmid is also modified by deleting the U3 region from 5'-LTR and partially deleting 3'-LTR to reduce the possible production of replication-competent viruses, and a strong viral promoter such as RSV or CMV is inserted for expression of the vector (Sakuma *et al.*, 2012).

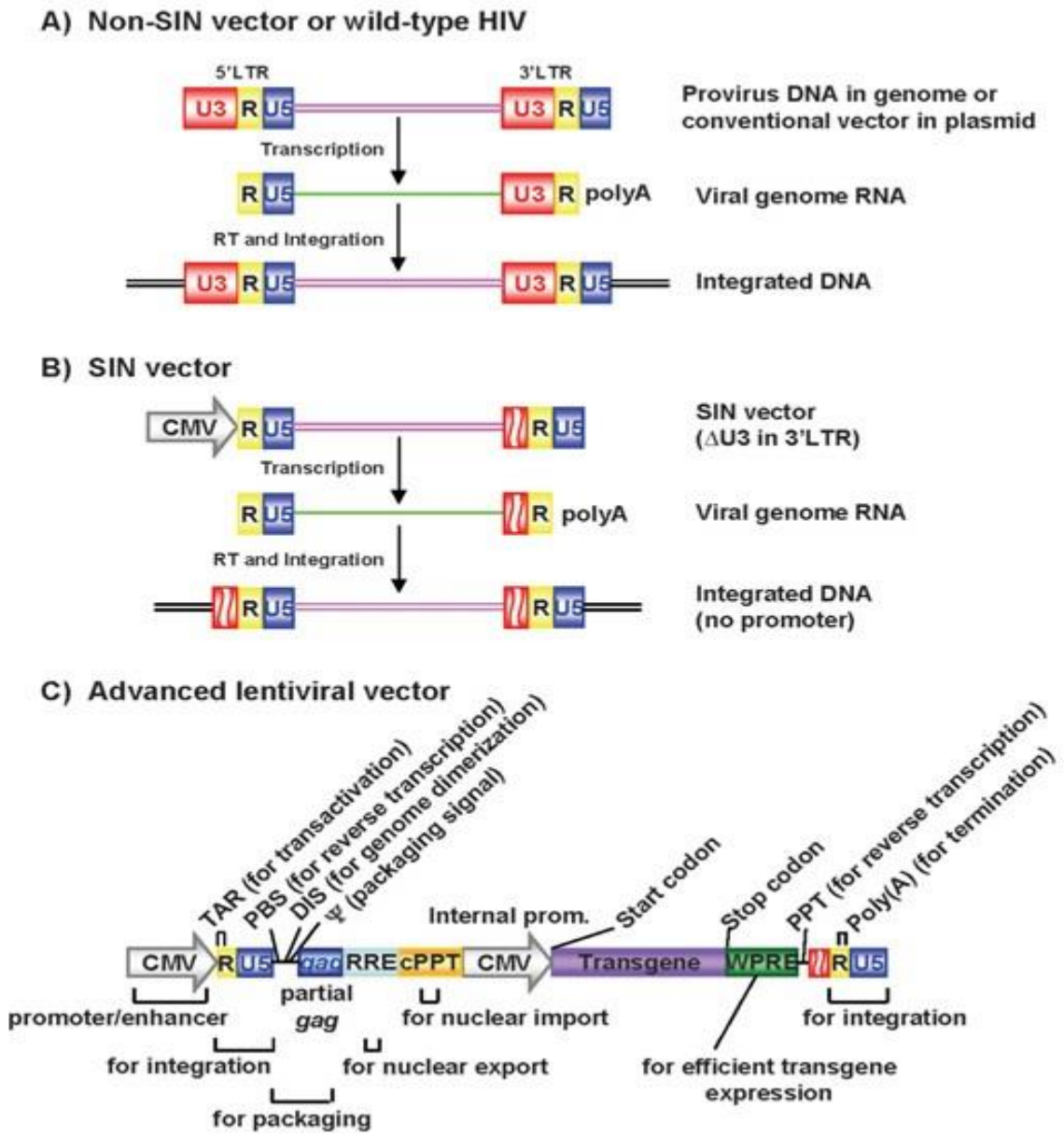

Figure 1.25: Schematic representation of HIV vector constructs and integrated proviruses**. A**) Non-SIN vectors or wild-type HIV contains LTRs at both the 3' and 5'-ends.Viral transcription starts at the U3/R region in the 5' LTR and terminates at the R/U5 region in the 3' LTR. Integrated viral DNA contains a cis-element (such as the TATA box and binding site for transcriptional factors Sp1 and NF-*κ*B) of the LTR, thus leading to the potential activation of proto-oncogenes by random integration of the vector/virus. **B**) With the SIN vector, the 5' LTR U3 region has been replaced with a CMV promoter, and the 3' LTR U3 region, which contains the cis-element, has also been partially deleted. As a result, the viral transcript contains no complete U3 sequence, and reduces the possible generation of replication-competent virus or activation of proto-oncogenes after the vector integration. **C**) The cis-acting elements of advanced lentivectors. The location and role of each cis-element are displayed. DIS, dimerization-initiation site. PBS, primer-binding site. Psi (packaging signal) (Sakuma *et al.*, 2012).

1.12.6 Third generation Tat-independent vectors from four plasmids

Unlike HIV-1 accessory proteins, Tat and Rev are essential for HIV-1 replication. These regulatory proteins are used for viral transcription and nuclear export of intron-containing transcripts (Laspia *et al.*, 1989, Terwilliger *et al.*, 1988).

To further increase the safety the new system has been designed to be Tat-independent with Rev provided from a separate plasmid (Figure 1.25C). Tat-independence is achieved by replacing the U3 promoter region of the 5'-LTR in the transfer vector with strong viral promoters from CMV or Rous Sarcoma Virus (RSV) (Dull *et al.*, 1998, Kim *et al.*, 1998). Therefore four plasmids were used to generate third-generation vectors which include:

- Packaging construct containing only gag and pol genes.
- Plasmid expressing Rev.
- Env (VSV-G) plasmid.
- Transgene plasmid driven by a heterologous strong promoter.

In addition the SIN property was added and this system consisted of only three of the nine genes of HIV thus increasing its predicted biosafety. At least three recombination events are required to generate a replication-competent HIV-1-like virus because the vector elements are split into four plasmids. Even if these occurred, the resulting viruses would have only HIV-1 Gag, Pol, Rev and VSV-G proteins, with no active LTRs, Tat or accessory proteins (Escarpe *et al.*, 2003).

1.12.7 Introduction of a cis-acting central polypurine tract (cPPT) for increased vector transduction efficiency

Plus strand DNA synthesis starts from the PPT and the cPPT during reverse transcription of HIV-1 which leads to a plus strand overlap called the central DNA flap (Charneau *et al.*, 1992). Although this is a subject of debate (Dvorin *et al.*, 2002), it has been suggested that the central DNA flap enhances nuclear import of HIV-1 proviral DNA (Zennou *et al.*, 2000). Nonetheless in practice, introduction of cPPT into HIV-based vectors significantly increases vector transduction efficiency *in vitro* and *in vivo* (Zennou *et al.*, 2001, Van Maele *et al.*, 2003, Demaison *et al.*, 2002).

1.12.8 Using WPRE [WHV (woodchuck hepatitis virus) post-transcriptional regulatory element] for increased transgene expression

WPRE is another *cis*-acting element that has been used to improve lentiviral vector expression. This sequence increases the amount of unspliced RNA in both nuclear and cytoplasmic compartments (Donello *et al.*, 1998, Zufferey *et al.*, 1999). Addition of WPRE into lentiviral vectors significantly increases transgene expression in target cells (Zufferey *et al.*, 1999, Brun *et al.*, 2003). Although increased expression is useful, the use of WPRE may raise safety concerns since it contains a truncated form of the WHV X gene, which has been implicated in animal liver cancer (Kingsman *et al.*, 2005). WPRE safety has subsequently been improved by a mutation of the open reading frame of the X gene (Zanta-Boussif *et al.*, 2009).

.

1.13 Promoters

Gene promoter regions are DNA sequences typically located upstream of genes and are the key *cis*-acting regulatory regions that control transcription. Promoters contain specific sequences which act as binding sites for RNA polymerase II, which transcribes DNA to mRNA, and *trans*- acting factors (transcription factors) which can help activate or suppress transcription by binding the DNA and help recruit or block binding of the polymerase enzyme. Promoters also work in conjunction with other regulatory elements, such as enhancers, silencers, and insulators, to direct the level and cell specificity of transcription of a given gene (Frecha *et al.*, 2008).

In vivo gene therapy strategies are largely dependent upon the therapeutic gene being expressed at an appropriate amount in the target cells, during the correct developmental stage, without developing toxicity, and without being eliminated by the immune system. Depending upon the disease, different profiles of expression are also required, for example, constant or regulated. Without this control, off target, over- and under- expression can cause unwanted effects (Frecha *et al.*, 2008).

Several strong, ubiquitous viral promoter elements, such as the immediate/early promoter/enhancer from Cytomegalovirus (CMV) and the 3' LTR from Spleen Focus Forming Virus (SFFV) and Murine Stem Cell Virus (MSCV) promoter have also been extensively studied. The aim with these constructs is to achieve high transgene expression in all cells transduced in order to produce therapeutic levels of transgene expression. SFFV elements have been explored during this project in the context of a SIN lentiviral vector.

1.13.1 Spleen focus forming virus LTR (SFFV) promoter

The polycythemic strain of spleen focus- forming virus is a replication- incompetent virus related to Friend mink cell focus- forming viruses (Ruscetti, 1995). The retroviral enhancer/promoter is contained in the U3 region of the long terminal repeat (LTR) and consists of an array of *cis*-acting elements condensed into two direct repeats. Flanking this region, at the 5' end is a high affinity binding site for the ubiquitous transcription factor Sp1, and at the 3' end, a binding site for Friend Virus factor c (FVc) (Baum *et al.*, 1997). The core motif in the direct repeat contains targets for transcription factors including:

1. CAAT/enhancer binding protein (C/EBP): This family of proteins contribute to tissue- specific gene expression in the liver, adipocytes, and myeloid cell.
2. Core binding factor (CBF) also known as polyomavirus enhancer binding protein (PEBP) involved in the regulation of both retroviral and endogenous genes in lymphoid and myeloid precursor cells (Baum *et al.*, 1998).

Within a retroviral vector, the SFFV LTR was shown to provide extremely high transgene expression in haematopoietic cells (TSUJI *et al.*, 2000), spermatogenic cells (Danno *et al.*, 1999), and hepatocytes *in vivo (Yamaguchi et al., 2003)*, and has been used a number of times within the context of SIN lentiviral vectors to confer high transgene expression in a number of cell types .

CHAPTER 2 - GENERAL MATERIALS AND METHODS

2.1 Materials

2.1.1 Equipment and instruments

7900HT Fast Real-Time PCR System	Applied Biosystems
Centrifuges: Heraeus Multifuge 1	Kendro Laboratory Products
Heraeus Megafuge 1.0	Kendro Laboratory Products
Cobalt radiation source	Puridec Technologies
Gel Doc™ XR+ Gel and blot imaging System	Bio-Rad
Heating block	Dri-block DB2A Techne
Image Stream^X	Amnis Corporation
Immunochromato Reader MS1000	MitoSciences, Abcam
Incubator Hera Cell 240 Kendro	Laboratory Products
JuLi smart fluorescent cell analyser	Digital Bio Tech
Axioscope 2 microscope	Zeiss
Microscope CK2	Olympus
Pipette gun, Accurpette	VWR
Pipettes, P10, P20, P200, P1000	Gilson
Rotator	Stuart
Spectrophotometer nanodrop 2000c	Thermo Scientific™
Sterile bench: Laminar Flow,	Hera safe Thermo Electron
Tabletop centrifuge (1-14)	Sigma
Tabletop centrifuge (5415R)	Eppendorf
Thermo cycler DNA engineTetrad 2	Bio-Rad Laboratories, Inc
Vortexer	Fisher Scientific
Water bath GD 100	Grant Instruments

2.1.2 Software

Dipstick Reader Software	MitoSciences, Abcam
IDEAS®	Amnis Corporation
Image J	NIH (USA)

ImageLab™	Bio-Rad Laboratories, Inc
Isis Fluorescence Imaging Software	MetaSystems
LaserGene	DNASTAR, Inc.
Microsoft Office 2010	Microsoft Corporation
Primer BLAST	National Center for Biotechnology
RQ Manager	Applied Biosystems
SDS 2.1 software	Applied Biosystems
Sequence Detection Systems Version 2.4	Applied Biosystems

2.1.3 Consumables

1.5 ml reaction tube	Fisher Scientific
10 cm dish	Fisher Scientific
10 ml pipette, sterile	Fisher Scientific
15 ml centrifugation tube	Fisher Scientific
25 ml pipette, sterile	Fisher Scientific
45 µm syringe Filter	Fisher Scientific
500 ml glass bottles	Fisher Scientific
50 ml centrifugation tube	Fisher Scientific
6 well plate	Fisher Scientific
96 well plate	Fisher Scientific
Cryo tubes	Fisher Scientific
Eppendorf tube	Fisher Scientific
Pasteur pipettes	Fisher Scientific
Pipette tip with filter, 1000 µl, sterile	Fisher Scientific
Pipette tip with filter, 10 µl, sterile	Fisher Scientific
Pipette tip with filter, 200 µl, sterile	Fisher Scientific

2.1.4 Antibodies and dyes

Alexa Fluor 488 rabbit anti-mouse secondary antibody	Invitrogen
Anti-phospho-Histone H2A.X (Ser139), clone JBW301	Millipore
DAPI (4′, 6-diamidino-2-phenylindole)	Fisher Scientific
DRAQ5™ Fluorescent Probe Solution	Biostatus

2.1.5 Table of primers

Primer Name	Sequence (5'-3')	Product length
	GAA PCR	
GAA Forward	GGGATTGGTTGCCAGTGCTTAAAAGTTAG	457bp + 3xGAAn
GAA Reverse	GATCTAAGGACCATCATGGCCACACTTGCC	
	***FXN* expression (Human Specific)**	
***FXN*RT-F**	CAGAGGAAACGCTGGACTCT	172bp
***FXN*RT-R**	AGCCAGATTTGCTTGTTTGGC	
	***FXN* expression (Human and Mouse)**	
FRT I-F	TTGAAGACCTTGCAGACAAG	121bp
RRT II-R	AGCCAGATTTGCTTGTTTGG	
	Gapdh expression (Mouse Specific)	
Gapdh-m-F	ACCCAGAAGACTGTGGATGG	81bp
Gapdh-m-R	GGATGCAGGGATGATGTTCT	
	Gapdh (Human Specific)	
Gapdh-h-F	GAAGGTGAAGGTCGGAGT	226bp
Gapdh-h-R	GAAGATGGTGATGGGATTTC	
	***FXN* cloning primers**	
HKH *FXN* F	CTAGGGATCCCCGGAGCAGCATGTGGACTC	626bp
HKH *FXN* R	AGTTCTCGAGGCATCAAGCATCTTTTCCGG	
	WPRE Copy number primer and probe set	
(WPRE) Forward	TGGATTCTGCGCGGGA	138bp
(WPRE) Reverse	GAAGGAAGGTCCGCTGGATT	
(WPRE) Probe	(FAM) CTTCTGCTACGTCCCTTCGGCCCT (TAMRA)	

	Lenti construct vector sequencing primers
LNT *FXN* SEQ 1	CTCTAAACCTGTGATTCCTCTG
LNT *FXN* SEQ 2	GGGTGCGAGAGCGTCAGTAT
LNT *FXN* SEQ 3	CTGGCTGTGGAAAGATACCTAAAG
LNT *FXN* SEQ 4	GGAATGAAAGACCCCACCTGTAG
LNT *FXN* SEQ 5	TATCAAGCTTATCGATGAATGTC
LNT *FXN* SEQ 6	AGACCAATGACTTACAAGGCAGC
LNT *FXN* SEQ 7	CTAGGGATCCCCGGAGCAGCATGTGGACTC
LNT *FXN* SEQ 8	TGGATTCTGCGCGGGA

2.1.6 Assay standards and kits

2x KAPA Taq Ready Mix Conventional PCR kit + dye	KAPA Biosystems
Cloned AMV First-Strand cDNA Synthesis Kit	Invitrogen
DNaseI treatment RNase free kit	Thermo Scientific™
Frataxin Protein Quantity Dipstick Assay Kit	Abcam plc.
Lenti-X qRT-PCR Titration Kit	Clontech
NucleoSpin® RNA Virus kit	Clontech
OxyBlot Protein Oxidation Detection Kit	Millipore
Pierce™ BCA Protein Assay Kit	Thermo Scientific™
Plasmid miniprep/ maxiprep/ megaprep kit	Qiagen
QIAquick gel extraction kit	Qiagen
QIAquick PCR purification kit	Qiagen
Quant-X™ One-Step qRT-PCR SYBR® kit	Clontech
SYBR Green PCR Master Mix qPCR kit	Applied Biosystems
TaqMan® Universal Master kit	Applied Biosystems
TOPO-TA® cloning vector pCR4® cloning kit	Invitrogen

2.1.7 Chemicals

1kb Plus DNA Ladder	Invitrogen
50 KDa Polyethyleneimine (PEI)	Sigma Aldrich
Acetone	Fisher Scientific
Acumax	Millipore
Agar	MERCK

Agarose	Fisher Scientific
Ampicillin	Stratagene
Boric acid	Fisher Scientific
Bovine Serum Albumin (BSA)	Invitrogen
Chemiluminescent	Bio-Rad
Chloroform	Sigma-Aldrich
Dimethyl sulfoxide (DMSO)	Sigma-Aldrich
Ethylenediaminetetraacetic acid (EDTA)	Fisher Scientific
dNTPs	Qiagen
Dulbecco's Modified Eagle Medium (DMEM)	Life Technologies
Ethanol	Hayman limited
Foetal bovine serum (FBS)	Life Technologies
Gel loading dye, orange	New England Biolabs
GlutaMAX	Life Technologies
Methanol	Fisher Scientific
Natrium Chloride (NaCl)	Fisher Scientific
One Shot® Stbl3TM chemically competent *E. coli*	Invitrogen
Paraformaldehyde	Sigma Aldrich
PenStrep	Life Technologies
Pfu DNA polymerase	Promega
Phosphate buffered saline (PBS) tablets	Fisher Scientific
Polyethyleneimine (PEI)	Sigma-Aldrich
Primers	Invitrogen
Propan-2-ol	Fisher Scientific
Proteinase K, PCR grade	Roche
Quick load 100bp DNA ladder	New England Biolabs
Rabbit Serum	Millipore
Restriction Enzymes	New England Biolabs
Sodium Dodecyl Sulfate(SDS)	Sigma Aldrich
T4 DNA Ligase	Invitrogen
Taq DNA polymerase	Qiagen

Tryptone	Fisher Scientific
Tris base	Fisher Scientific
Triton X-100	Fisher Scientific
TRIzol	Invitrogen
Trypan-Blue	Fisher Scientific
Trypsin	Life Technologies
Yeast Extract	Fisher Scientific

2.1.8 Buffers and Solutions

Multispectral imaging flow cytometry

Block buffer:

PBS 0.1% Triton-X 100 10% Rabbit serum.

Permeabilisation buffer (PB):

PBS, 0.5% Triton-X 100.

Wash buffer:

PBS, 0.1% Triton-X 100.

Fixing solution:

50% Acetone, 50% Methanol.

Western blot analysis

Running buffer:

25 mM Tris, 190mM glycine, 3.5mM SDS.

Sample buffer:

80 mM Tris-HCl (pH 6.8), 12.5% glycerol, 10% SDS, 0.5% BPB, 1% BME.

Transfer buffer:

25 mM Tris, 190 mM glycine, 10% methanol.

PBS/T:

0.2% Tween-20 in PBS.

5% milk PBS/T:

5% w/v milk, 0.2% Tween-20 in PBS.

OxyBlot analysis

Dilution buffer:

60 mM Tris-HCl (pH 6.8), 2% SDS, 10% glycerol.

Loading buffer:

62.5 mM Tris-HCl (pH 6.8), 180 mM BME, 0.002% BPB.

Transfer buffer:

12 mM Tris-HCl (pH 8.3), 96 mM glycine, 20% methanol.

General buffers and solutions

1x TBE:

90 mM Tris, 90 mM Boric acid, 2 mM EDTA.

DMEM-Complete medium:

DMEM + 2 mM L-Glutamine, 10% FBS, 1% PenStrep.

Luria-Bertani (LB) medium

For 1 L: 10 g NaCl, 5 g Yeast extract, 10 g tryptone peptone. Autoclave.

LB (Luria-Bertani) Agar

For 1 L: 10 g NaCl, 5 g Yeast extract, 10 g tryptone peptone,15 g bacto agar. Autoclave.

Orange G loading dye (6x):

0.35% Orange G dye, 30% sucrose

1x Phosphate buffer saline PBS:

For 1L: 8.0 g NaCl, 1.15 g Na2HPO4, 0.2 g KH2PO4, 0.2 g KCl.

TBE buffer:

(5x concentrated, 1L dH2O), 54 g Tris base, 27.5 g Boric acid, 20 ml of 0.5 M EDTA.

Digestion buffer:

100 mM Tris-HCl (pH 8), 5 mM EDTA, 200 mM NaCl, 0.2% SDS.

RIPA buffer:

10 mM Tris-Cl (pH 8.0), 1 mM EDTA, 0.5 mM EGTA, 1% Triton X-100, 0.1% SDS, 140 mM NaCl.

TE buffer:

10 mM Tris-HCl (pH 7.5), 1mM EDTA.

2.1.9 Cell lines

ID	Gender	Age (Yrs)	Ethnicity	Number of GAA repeats
GM04503	Female	31	Caucasian	Normal
GM07492	Male	17	Caucasian	Normal
GM03665	Female	13	Caucasian	445/740

Table 2.1: Details of the human primary fibroblasts.

ID	Gender	Average Age (month)	Genotype	Number of GAA repeats
Y47	Male	4.5	Transgenic Control	9
YG8sR	Male	13.5	FRDA YG8 Small Rescue	120

Table 2.2: Details of the mouse primary fibroblasts.

ID	Gender	Age	Ethnicity	Organism	Tissue	Cell Type
HEK 293T	----------	Fetus	----------	Homo sapiens	embryonic kidney	----------

Table 2.3: Details of general cell lines.

2.2 Methods

2.2.1 General cell culture maintenance

Cells were routinely cultured in Dulbecco's Modified Eagle Medium (DMEM) (Invitrogen) which was supplemented with 10% FBS, 2 mM L-glutamine and 100 units/ml penicillin and streptomycin (Invitrogen). Cells were grown in 100 mm Petri dishes (Fisher Scientific) as monolayers at 37^{o}C in a humidified atmosphere of 5% CO_2 in air. All cell culture was carried out in a temperature-controlled laboratory.

2.2.2 Trypsinisation of cells

Cells were left to reach about 95% confluency before sub-culturing them. When sub-culturing cells, medium was first aspirated off using a glass Pasteur pipette and cells were rinsed with 10 ml of versene (Phosphate Buffered Saline (PBS) + 0.2% EDTA) to remove any traces of medium. Approximately 1 ml of 0.25% trypsin-EDTA (Fisher Scientific) was added to the plate and the cells were kept at 37^{o}C for 10 minutes to allow cells to detach from the dish. Cells were then recovered from the plate in 10 ml of medium and seeded into plates at an approximate density of $1x10^5$ cells per plate.

2.2.3 Cell counting

Cell counting was performed using either a glass haemocytometer or the Countess (Invitrogen). Cell counts were primarily performed using the Countess. However the Countess is limited by its measurement range ($1x10^4$ - $1x10^7$ cells/ml). Therefore if cell concentrations were below this, then accurate cell counts could not be obtained. In these circumstances, a traditional Neubauer glass haemocytometer was used instead.

When counting cells using the haemocytometer, cells were detached from petri dishes using 1 ml of Trypsin (Fischer Scientific). Once cells had detached, they were recovered in 10 ml of complete medium. 10 µl of the cell suspension was added to 10 µl of Trypan blue to allow for exclusion of dead cells from the cell count. 10 µl of the cell suspension mixed with the Trypan blue was loaded onto a glass haemocytometer and cell counts were performed at 20x magnification using an Olympus CK2 microscope.

2.2.4 Cell freezing

Cell freezing was deemed necessary to conserve stocks of the cell lines being used. They were frozen in freezing medium which was comprised of 20% FCS, 10% dimethyl sulfoxide (Sigma-Aldrich) and 80% DMEM medium containing penicillin/streptomycin and L-glutamine.

Cells were grown in 10 cm^2 Petri dishes until they were 95% confluent. The medium was aspirated off the cells and the cells were then rinsed with 10 ml of PBS. Cells were then detached from the dish using 1 ml of 0.25% trypsin-EDTA. After recovering the cells in 10 ml of medium, they were transferred into a 15 ml tube (Sarstedt) and centrifuged for 5 minutes at 1500 rpm. The supernatant was then discarded and the cell pellet was resuspended in 1 ml of freezing medium.

The cell suspension was transferred to cryo-vials (Sarstedt) and placed in cell freezing containers (Sigma-Aldrich). These containers have a foam insert soaked in isopropanol which allows for a gradual freezing rate of 1^{o}C/minute. Cells were kept in these containers at -80^{o}C for twenty-four hrs to ensure they had reached the correct temperatures before being transferred to liquid nitrogen dewars for long term storage.

2.2.5 Cell viability

It is important to know the number of cells in the culture at given stages and whether these cells are viable. The use of haemocytometer and a dye, such as trypan blue, gives a quantitative standard for the viability of the cells. Cells that exclude trypan blue are considered viable, whereas cells that take up the dye are dead. To perform this, cells were first detached with 1 ml of 1X trypsin-EDTA and a cell suspension was made with 1 ml of DMEM medium. 100-200 µl of cell suspension was taken into a fresh Eppendorf and an equal volume of 0.4% (w/v) trypan blue (Sigma) was added, mixed well by pipetting up and down. Cells were counted by using a haemocytometer and their viability was determined by the following formula:

$$\text{Viability (\%)} = \left(\frac{\text{No of Viable Cells}}{\text{Total no. of cells}} \right) \text{X } 100$$

2.2.6 Clonogenic assay

Cell count and seeding

Following treatment of the cells with lentivirus and a specific substance (i.e. H_2O_2), single cell suspensions are obtained by trypsinisation, then the number of cells in each sample were counted carefully using a hemocytometer and diluted so that appropriate cell numbers are seeded into petri dishes (5 to 10 replicates of each in 15 mm dishes). A range of between 20-150 colonies was achieved for each sample and were incubated in a 5% CO_2 environment at 37°C for colony formation. The incubation time

for colony formation varies from 2-4 weeks for different cell lines; it is accepted that the time must be equivalent to at least six cell divisions.

Fixing and Staining Colonies

Media was gently removed from each plate by aspiration and washed with 5 ml of PBS. Colonies were fixed with 5 ml of 10% neutral buffered formalin solution for 15-30 minutes and stained with 5 ml of 0.01% (w/v) crystal violet in dH_2O for 30-60 minutes. Excess crystal violet was washed with dH_2O and dishes were air dried.

Colony Counting

Colonies containing more than 50 individual cells are counted using a stereomicroscope. Digital images of the colonies are obtained using a camera or scanning device and colonies are counted using imaging analysis software ImageJ.

2.2.7 Growth and maintenance of *E. coli*

Escherichia coli (*E. coli*) were grown in liquid LB media at 37°C with agitation at 250 rpm or streaked out on solid LB plates containing 1.5% bacto agar. *E.coli* transformed with plasmid was grown on the same media supplemented with ampicillin (50 µg/ml). For long- term storage, bacterial cultures were stored in 15% volume for volume (v/v) glycerol at -80°C.

2.2.8 Transformation of One Shot® TOP10 competent *E. coli*

One Shot® TOP10 chemically competent *E. coli* cells are transformed by heat shock; one 50 µl vial of cells is thawed on ice for each transformation. 10 pg to 100 ng of DNA is added to the vial, gently mixed and incubated on ice for 30 minutes. Cells are then heat- shocked for 45 seconds at 42°C without shaking. The vial is then placed on ice

for 2 minutes without shaking. 250 µl of pre-warmed S.O.C. media is added and cells shaken at 250 rpm at 37°C for 1 hour, after which they were diluted in LB media and spread on LB agar plates containing ampicillin (50 µg/ml). The plates were incubated overnight at 37°C, after which colonies were picked using sterile 20 µl pipette tips and grown overnight in 5 ml liquid LB cultures.

2.2.9 Plasmid DNA preparation

Plasmid DNA was prepared using Qiagen Mini-Prep kits (Qiagen) as per the manufacturer's instructions from 5 ml overnight cultures. For large-scale plasmid DNA preparation 250 ml LB media containing ampicillin (50 µg/ml) was inoculated with 500 µl of a fresh 5 ml culture and incubated over night at 37°C with agitation (250 rpm). Plasmid DNA was subsequently prepared using Qiagen Maxi-Prep endo-free plasmid kits (Qiagen) as per the manufacturer's instructions.

2.2.10 Restriction enzyme digest

1 µg of plasmid DNA was routinely digested in a final volume of 20µl containing 1x buffer (supplied by the manufacturer), and the restriction enzyme. The volume of enzyme used varied depending of the concentration of the enzyme stock but did not exceed 10% (v/v) of the total reaction volume. Reactions were carried out as per the manufacturer's instructions at the recommended temperature for 1 hour and DNA digestion was verified by agarose gel electrophoresis. Double or triple digestions were performed either in compatible buffers or sequentially, after clean-up of DNA by ethanol precipitation using the QiaQuick PCR purification kit as per the manufacturer's instructions (Qiagen).

2.2.11 DNA ligation

Ligation of DNA fragments were performed using a vector to insert ratio of 1:2, 1:3 and 1:5 (molar) depending on the vector, and carried out in a final volume of 20 µl containing: 1x T4 DNA Ligase buffer and 1 µl of T4 DNA Ligase. The vector DNA concentration used was always 100 ng of DNA. Ligation reactions were incubated for 3 hours at room temperature or overnight at 16°C, after which they were immediately transformed into One Shot® TOP10 *E.coli* cells.

2.2.12 Construction of frataxin encoding lentiviral vectors

Human frataxin cDNA containing specific restriction digest sites at the 5′-end and 3′-end was obtained by PCR from the plasmid pTLX1 (ATCC No: 99619). PCR products were extracted from the agarose gel using a QIAquick gel extraction kit (Qiagen) and then ligated into the TOPO TA cloning vectors pCR4-TOPO (Invitrogen). The correct orientation and integrity of the frataxin open reading frame in each construct were confirmed by restriction fragment analysis and sequencing. The frataxin cDNA was then excised (by restriction digestion) from TOPO TA cloning vectors pCR4-TOPO (Invitrogen) and then subcloned into the multiple cloning site of the lentivirus backbone vector.

2.2.13 Isolation of DNA fragments by gel electrophoresis

DNA fragments were resolved by electrophoresis through 1% agarose gels in 1X TBE buffer. To prepare the gels, agarose was dissolved in 1X TBE buffer by boiling in a microwave oven. After cooling, ethidium bromide was added to obtain a final concentration of 0.5g/ml for visualisation of DNA. DNA samples were mixed with DNA

loading buffer before loading onto agarose gels. A 1 kb plus DNA ladder was included in each gel to enable size determination of DNA fragments. Gels were electrophoresed using a voltage of 50-70 V (up to 150 mA) and the separated DNA fragments were subsequently visualised by exposure to ultra- violet light using a Gel Doc™ XR system. Following electrophoresis, DNA fragments were excised from agarose gels using a clean scalpel blade under ultra- violet light. The DNA was then extracted from the agarose using a QIAquick gel extraction kit as per the manufacturer's instructions.

2.2.14 Polyethylenimine (PEI) transfection of HEK 293T cells with a GFP-expressing plasmid

HEK 293T cells were split one day before transfection in 6-well plate in DMEM/10% FBS medium and incubated at 37°C, 5% CO_2 to become 60%-70% confluent. A DNA solution was made containing 5 µg vector backbone construct in 100 µl OptiMEM and sterilised by filtration (0.22 µm). This was then added to 100 µl of OptiMEM containing 10 µg of Polyethylenimine (PEI) which had been sterilised by filtration (0.22 µm), gently mixed, and incubated for twenty minutes at room temperature prior to addition onto the cells. Cells were washed with PBS and 3 ml of OptiMEM was added to the cells, then 200 µl of transfection solution was added to the cells for 3-4 hours at 37°C and 5% CO_2. The transfection media was then removed and 3 ml of fresh complete DMEM was added to the cells and incubated at 37°C, 5% CO_2 overnight. On the following day the cells were visualised under UV light microscope and transfection efficiency was measured using Image stream.

2.2.15 PEI toxicity test

PEI is a cationic polymer that encloses anionic DNA-molecules and binds it to anionic residues in the plasma membrane. Endocytosis of these complexes results in the delivery of DNA into the cell (Boussif *et al.*, 1995).

PEI is toxic to cells. Thus, its toxicity level to HEK 293T cells was determined by performing a titration experiment. In a 6-well plate 2x105 cells were seeded 24 hours before conducting the experiment to allow attachment of the cells to the plate. Five different concentrations of PEI were used ranging between 5µg to 25µg of PEI. The appropriate amount of PEI was added in 1 ml of DMEM to the corresponding well after the old medium was aspirated. One well served as a control, where no PEI was added. After 24 and 48 hours of incubation at 37°C and 5% CO2 the cells were examined under a microscope and pictures were taken.

2.2.16 Determination of the optimal plasmid DNA amount for transfection

In a 6-well plate $2x10^5$ cells were seeded 24 hours prior to performing the experiment and the LV GFP vector was used to carry out this experiment. Five different concentrations of DNA were used ranging between 2 µg to 6 µg of DNA and twice the amount of PEI ranging between 4 µg to 12 µg of PEI per well. This is equivalent with a ratio of DNA to PEI of 1 to 2. The respective amounts of DNA and PEI were pre-diluted in 500µl of OptiMEM each. The DNA mix was added into the PEI mix by mixing it thoroughly, vortexing it and spinning it down briefly. After incubation at room temperature for 30 minutes the medium on the cells was removed and the DNA/PEI mix was added to the cells. One well was kept as a control. After 4 hours incubation

at 37°C at 5% CO_2 the medium was replaced by 1 ml of fresh DMEM. The expression of GFP expressing cells was counted 24 hours after transfection by taking images using the JuLI™ Smart Fluorescent Cell Analyser microscope (Ruskinn Technology). Using image processing software, Image J (U. S. National Institutes of Health), the acquired images were merged and the number of GFP-positive cells were analysed.

2.2.17 Polymerase Chain Reaction (PCR)

PCR reactions were performed in a total volume of 50 µl containing 100 ng plasmid template DNA, 5 µM of both forward and reverse primers, 200 µM of each dNTP, 1x PCR buffer and 1U of *Taq* DNA polymerase. Cycling conditions depended upon the annealing temperatures of the primers used and whether a restriction enzyme recognition site was added into a primer. However, typical cycling conditions included: 30 cycles of 94°C for 1min, 60°C for 1min, 72°C for 1 min.

2.2.18 Production of VSV-G Pseudotyped Lentivectors

15 x 10^6 HEK 293T cells were seeded in complete DMEM medium in a T175 cm^2 flask and incubated at 37°C, 5% CO_2 overnight. A DNA solution was made containing 50 µg vector backbone construct, 32.5 µg gag-pol packaging plasmid, and 17.5 µg envelope plasmid for VSV-G pseudotypes in 6 ml of OptiMEM and sterilised by filtration (0.22 µm). This was then added to 6 ml of OptiMEM containing 2 nM of Polyethylenimine (PEI) which had been sterilised by filtration (0.22 µm), gently mixed, and incubated for 20 minutes at room temperature prior to addition onto cells. Cells were washed with PBS, the transfection media was added to the cells for 4-6 hours at 37°C and 5% CO_2. The transfection media was removed and 15 ml of fresh complete

DMEM was added to the cells. On the following day, the media was removed and 15ml of fresh complete DMEM was added to each flask. 48 and 72 hours after transfection, the media was collected and cell debris were removed by filtration through a 0.22 µm filter. For VSV-G pseudotypes media was then centrifuged at 100,000x g in a Beckman coulter ultracentrifuge (Optima™ XPN) for 2 hours at 4°C or media was centrifuged at 10,000 rpm in a Sigma 4K15 centrifuge overnight at 4°C. Supernatant was removed and 100 µl of cold OptiMEM was added to each tube on ice. The pellet was resuspended and aliquots were prepared and rapidly frozen at –80°C.

2.2.19 Viral titration using Image stream^{X}

This method can only be used to titer stocks of vectors that carry a transgene which is easily monitored by imaging flow cytometry. (such as GFP, or other living colours). About 1 to $5x10^5$ HEK 293T cells/well were seeded in a 12-well plate with 1 ml of complete DMEM and incubated at 37ºC and 5% CO_2. It is important that the cells are well separated and uniformly distributed in the well. 24 hours after incubation 1 well was used to count the cells. For non-concentrated vector the cells were transduced with: 500 µl, 100 µl, 50 µl, 20 µl and 10 µl of crude supernatant and the volume was mad up to 500 µl with complete DMEM. One well was kept as a non-transduced control (NI). For concentrated vector the cells were transduced with: 1µl, 10^{-1}, 10^{-2}, 10^{-3} and 10^{-4} µl of vector in 500 µl of fresh complete DMEM (Figure 2.1). 48 hours post viral infection the cells were washed with 1 ml PBS and were detached by adding 200 µl of trypsin-EDTA per well and incubated for 5 minutes at 37°C, 5% CO_2. Then 800 µl of complete DMEM was added and mixed well to resuspend the cells. Cells were

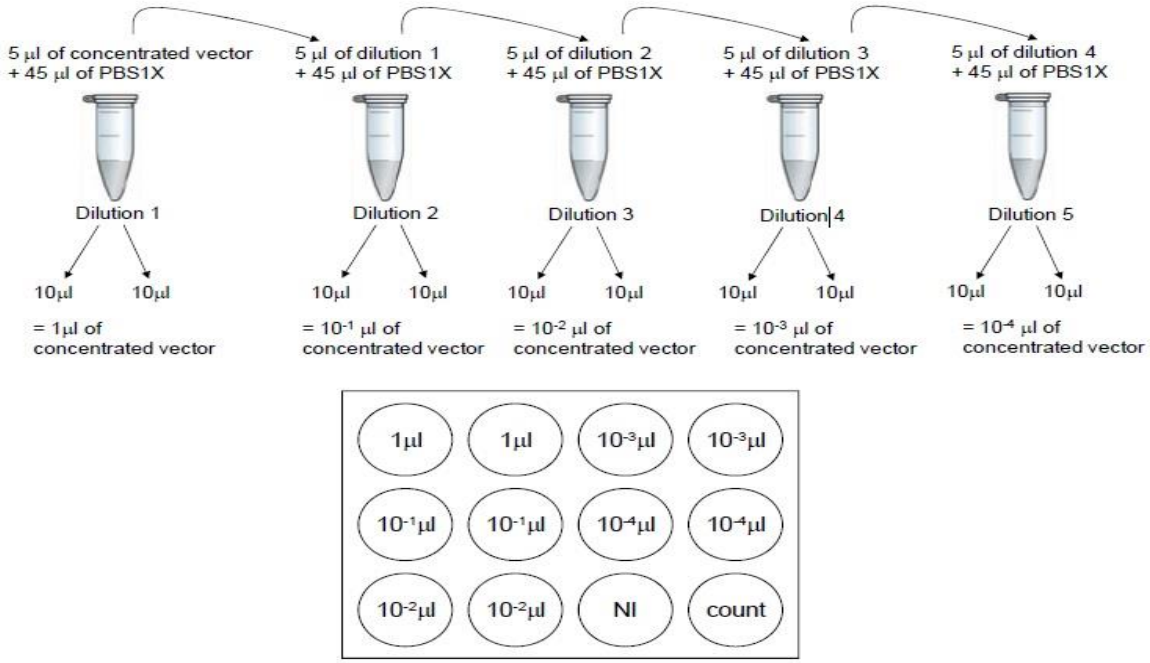

Figure 2.1: Schematic diagram of serial dilution of concentrated viral particles and the layout of the plate.

transferred into a 1.5 ml tube and centrifuged for 5 minutes at 500x g at 4°C. The supernatant was removed and the pellet was resuspended in 500 µl of 1% formaldehyde in PBS and incubated for 5 minutes at room temperature. Cells were washed with 1X PBS, centrifuged for 5 minutes at 500x g at 4°C and the pellet was resuspended in 1ml of 1X PBS. Cells were analysed for GFP expression using Imagestream^X, as previously described. Only dilutions yielding 1% to 20% of GFP-positive cells were considered for titer calculations. Viral titer was calculated using the following equation:

$$\text{Titer (units/ml)} = \frac{\text{Number of target cells (Count at day 1)} \times \left[\frac{\text{\% of GFP-positive cells}}{100}\right]}{\text{Volume of supernatant in (mL)}}$$

2.2.20 Viral titration using qRT-PCR

Batches of LV *FXN* and LV *GFP* lentiviruses were prepared in parallel and virus titers of both was calculated by quantifying the number of lentiviral genome copies using a commercial titration kit, Lenti-X qRT-PCR (Clontech, USA). The viral RNA was isolated using NucleoSpin® RNA Virus kit (Clontech, USA) and was treated with DNaseI (Thermo scientific) to remove any residual plasmid DNA prior to qRT-PCR. Serial dilutions of the stock of viral RNA and a control RNA of known copy number, provided in the kit, was subjected to Quant-X™ One-Step qRT-PCR SYBR® kit (Clontech, USA). The lentiviral copy number contained from the viral stock LV *FXN* and LV GFP lentivurses was determined by comparing its C_t value to the standard curve (Figure 2.2). The following program was used for qRT-PCR reaction cycles.

RT Reaction	
42°C	5 min
95°C	10 sec
qPCR x 40 Cycles	
95°C	5 sec
60°C	30 sec
Dissociation Curve	
95°C	15 sec
60°C	30 sec
All	(60°C–95°C)

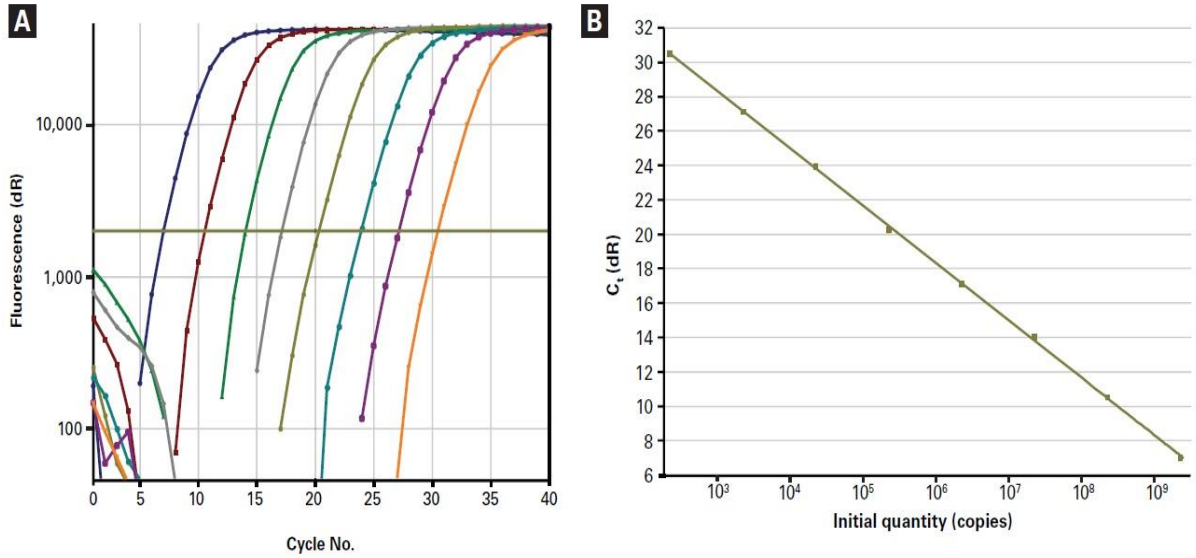

Figure 2.2: Using the Lenti-X RNA Control Template to generate a standard curve. **A)** Amplification plots of a qRT-PCR reactions using serial dilutions of the Lenti-X RNA Control Template (10^9–10^2 copies) and the Lenti-X qRT-PCR Titration Kit. **B)** A standard curve created from the plots shown in Panel A demonstrates a strong linear correlation between the Ct values and the RNA copy numbers (log scale).

Data Analysis

To generate a standard curve average C_t values from the control dilution duplicates was determined and was plotted against copy number (log scale) (Figure 2.2). Average C_t values for each duplicate sample dilution was calculated and the corresponding copy number value from the standard curve was established.

A starting copy number value for the original sample for each dilution was then back-calculated using the formula below:

$$\text{Copies/ml} = \frac{(1 \times 10^7 \text{ copies})(1000 \text{ µl/ml})(2\text{x DNase})(50 \text{ µl elution})}{(150 \text{ µl sample})(2 \text{ µl added to well})}$$

Note: 150 µl of a sample was purified and eluted in 50 µl. The undiluted sample corresponded to a raw copy number of $1\text{x}10^7$ copies on the qRT-PCR Standard Curve.

Calculating viral RNA copy numbers and infectivity coefficients:

The first time the qRT-PCR titration to determine RNA copy number was performed, IFU value was also determined by independent means (e.g. via Imagestream^X) in order to establish a relationship between the two values. Subsequently, for similarly prepared virus supernatants, the qRT-PCR titration value may be used as a reference to determine a relative IFU value for the supernatant and then, the MOI for the infection experiment (Carmo et al., 2004). Viral infectivity was determined via Imagestream^X as previously described and RT:Imagestream ratio (copies/IFU) or infectivity coefficient was calculated by dividing the qRT-PCR copies/ml by the IFU/ml value from the FACS titration. This coefficient was then be used to calculate the IFU/ml for subsequent qRT-PCR titration results.

2.2.21 Determination of MOI for the transduction of the FRDA fibroblasts

$5X10^4$ human and mouse FRDA fibroblasts that were growing exponentially were seeded into 6-well plates and incubated for 18-20 hours at 37°C and 5% CO_2. Three 6-well plates were prepared to have triplicate wells for each range of MOI and a control. The medium was removed and 500 µl of fresh medium was added to each well, then an appropriate volume of the LV *GFP* (0.5 µl-10 µl) was added to each well to achieve a MOI of 1, 5, 10, 15 and 20 (Table 2.4). Cells were incubated at 37 °C and 5% CO_2 with viral supernatant for 6 hours and then the supernatant was replaced with 1 ml fresh medium and incubated at 37 °C and 5% CO_2 for 72 hours to allow cells to recover and to allow time for the expression of the reporter gene. Following transduction of human and mouse FRDA fibroblasts live cells were counted using

trypan blue (Fisher Scientific) and analysed using Imaging flow cytometry Imagestream^X was used to measure the number of the GFP-positive cells. In this method live cells were trypsinized, washed with ice-cold PBS and fixed with 4% paraformaldehyde. Fixed cells were put through Imaging flow cytometry using the Imagestream^X system (Amnis Inc.). This permits image capture of each cell in flow using a maximum of six optical channels. Using the Inspire™ data acquisition software (Amnis Inc.), images of approximately 10,000 cells were captured on channel 1 for brightfield (BF); on channel 2 for GFP representing the green GFP expression; and on channel 5 for the blue DRAQ5™ staining of the nuclear region of each cell. Following excitation with a 488 nm laser at a power setting of 70 mW, all images were captured using a 40× objective.

MOI	1	5	10	15	20
Volume used from lentivirus titer of 1x10^8	0.5µl	2.5µl	5µl	7.5µl	10µl

Table 2.4: Volume of the LV GFP with the titer of 1X10^8 added to each to achieve a range of MOI. The volumes calculated are based on seeding 5x10^4 cells per well.

2.2.22 DNA extraction: ethanol method (Wang and Storm 2006)

This method was used to quickly extract genomic DNA from cell culture. Samples were collected in Eppendorf tubes and 400 µl of digestion buffer and 10 µl of 50 mg/ml Proteinase K was added, followed by brief vortexing and overnight incubation at 55°C in a water bath. After digestion, samples were vortexed and centrifuged at 14000 rpm for 5 minutes. Avoiding transferring any of the cell debris, the supernatant was

collected into a new Eppendorf tube. 1ml of absolute ethanol was added, immediately followed by brisk inversion several times. Samples were incubated for 10 minutes at -80°C followed by centrifugation at 14000 rpm for 30 minutes at 4°C. The ethanol was drained off and the pellet was washed with 1 ml of 70% ethanol. Samples were recentrifuged at 14000 rpm for an extra 20 minutes at 4°C and the ethanol carefully drained off. The tubes were left to dry inverted on paper towels for ~10 minutes. The DNA pellet was resuspended in 50-100 µl of TE buffer and stored at 4°C.

2.2.23 DNA extraction: phenol/chloroform method (Sambrook et al. 1989)

This method was used to extract genomic DNA from samples where greater DNA quality was necessary. Proteinase K digestion was performed as previously described. After digestion, samples were vortexed and 400 µl of phenol (equilibrated with Tris-HCl pH 8.0) was added. Samples were mixed by vortexing (2x 15s) and centrifuged at 14000 rpm for 5 minutes at 4°C. 380 µl of the upper aqueous phase was removed and replaced into a fresh Eppendorf tube and 380 µl of chloroform/isoamyl alcohol (24:1) was added, followed by a brief vortex and the centrifugation at 14000 rpm for 5 minutes at 4°C. 350 µl of the resulting upper aqueous phase was transferred to a fresh Eppendorf tube and 35 µl of 3 M Na-acetate (pH 5.2) was added. 700 µl of absolute ethanol was then added and ethanol precipitation performed, as previously described.

2.2.24 Determination of proviral copy number

48 to 72 hours post-infection with LV *FXN* and LV *GFP,* the genomic DNA was extracted from human and mouse fibroblasts using the phenol/chloroform method, as described previously (Section 2.2.23). Quantitative PCR was performed by an ABI

7700 Sequence Detection System (ABI, Applied Biosystems) using the following oligonucleotide primers and TaqMan probes: Total viral DNA was quantified using primers specific for the viral woodchuck hepatitis regulatory element (WPRE) sequence contained in the vector 5'- TGTGTGCCCGTCTGTTGTGT -3' and 5'-GAG TCCTGCGTCGAGAGAGC -3' and TaqMan probe (FAM) 5-CGCCCGAACAGGGA CTTGAA -3' (TAMRA) 109. The plasmid pHR'SIN-cPPT-SFFV-*FXN*-WPRE served as an external homologous DNA standard of known copy number to produce standard curves. To generate standard curves, the plasmids were serially (1:10) diluted in siliconized tubes over the appropriate concentration range. To achieve a reliable standard curve for each measured parameter, the plasmids were PCR-amplified in five replicates for each standard dilution point over the complete standard-curve range. A genomic DNA sample with a known copy number of 4 was also used to confirm the reliability of the standard curve.

2.2.25 Extraction of total RNA

About $1x10^6$ cells were used to extract the RNA. The cell pellet was first washed once with PBS and collected by centrifugation at 1500 rpm for 5 minutes. The cell pellet was loosened by flicking the tube gently and resuspended in 1 ml of Trizol®. Mouse tissues were similarly homogenized in 1 ml of Trizol® using an Eppendorf and a homogenizing rod. Samples were then incubated for 10 minutes at room temperature. 0.2 ml of chloroform per 1 ml of Trizol® was added followed by vigorous shaking of samples for 15 seconds and incubated for further 15 minutes at room temperature. Samples were phase separated by centrifugation at 14000 rpm for 15 minutes at 4°C. The upper aqueous phase (~0.5 ml) was then transferred to a fresh labelled Eppendorf tube and

RNA was precipitated by adding 0.5 ml of isopropyl alcohol. Samples were incubated for 10 minutes at room temperature and centrifuged at 14000rpm for 15 minutes at 4°C. The supernatant was carefully removed and the RNA pellet was washed once with 1 ml of 75% ethanol (made with DEPC-water) and centrifuged again at 7500 rpm for 5 minutes at 4°C. The supernatant was removed carefully and the RNA pellet was briefly dried for a period of 5-10 minutes and resuspended in 10-20 µl of DEPC-water. RNA samples were stored at -80°C.

2.2.26 DNase I treatment of RNA

Deoxyribonuclease I, Amplification Grade (DNase I, Amp Grade, ThermoScientific) digests single and double stranded DNA to oligodeoxy-ribonucleotides containing 5´-phosphate. It is suitable for eliminating DNA during critical RNA purification procedures such as those prior to RNA-PCR amplification. DNase I, Amp Grade is purified from bovine pancreas and has a specific activity of ≥10,000U/mg.

To remove any genomic DNA and inhibit RNase enzymes, following reagents were added to 1 µg of total RNA:

- 1µl 10× DNase I reaction buffer
- 1µl DNase I, Amp Grade, (1U/µl)
- Nuclease free water to 10µl

The samples were left for 15 minutes at room temperature. DNaseI reaction was inactivated by adding 1 µl of 25 mM EDTA solution to the reaction mixture and heating it for 10 minutes at 65˚C. The RNA samples were subsequently used for reverse transcription.

2.2.27 Complementary DNA (cDNA) synthesis

Complementary DNA (cDNA) was synthesized by using cloned AMV first-strand cDNA synthesis kit (Invitrogen). On ice, 2 µl of RNA was added to 10 µl of primer component mastermix (7 µl of DEPC-water, 2 µl of 10 mM dNTP mix and 1 µl of Oligo (dT)20 primer). The RNA and primer were denatured by keeping the samples at 65°C for 5 minutes and placing the samples on ice immediately after. The following reagents were then added in order: 4 µl of 5X cDNA synthesis buffer, 1 µl of DEPC-water, 1 µl of 0.1M DTT, 1 µl of RNase OUT™ (40 U/µl) and 1 µl of cloned AMV RT (15 units/µl). The 20 µl reaction mixture was gently mixed by flicking the tube and briefly centrifuged to bring all the contents to the bottom. The reaction mixture was incubated at 55°C for 60 minutes. The reverse transcriptase reaction was terminated by keeping the samples at 85°C for 5 minutes. The cDNA samples were used immediately or stored at -20°C.

2.2.28 Plasmid DNA preparation

Plasmid DNA was prepared using Qiagen Mini-Prep kits as per the manufacturer's instructions from 5 ml overnight cultures. For large-scale plasmid DNA preparation 1L LB media containing ampicillin (50 µg/ml) was inoculated with 500 µl of a fresh 5 ml culture and incubated over night at 37°C with agitation (250 rpm). Plasmid DNA was subsequently prepared using Qiagen Mega-Prep kits (Qiagen) as per the manufacturer's instructions.

2.2.29 Measurement of DNA and RNA concentration

DNA concentration was calculated by measuring the absorbance of light with a wavelength of 260 nm (A260) using a NanoDrop™ 2000c spectrophotometer with a 0.2 mm pathlength; at this wavelength 50 µg/ml of double-stranded DNA has an absorbance of 1. The absorption (A) of ultra violet light (UV-light) was measured at 260 nm and the quality was determined by using A260/280 ratio.

2.2.30 Real-time PCR/RT-PCR

The expression of genes of interest was quantitated on an ABI Prism 7900HT Sequence Detection System (Applied Biosystems) using 2x SYBR® Green PCR Master Mix (Applied Biosystems). SYBR® Green dye is attached to the cDNA and produces a fluorescent signal. The signal intensity is proportional to the quantity of the cDNA present in the reaction. Consequently, in each step of the PCR reaction, the intensity of the signal increases while the amount of product increases. Each PCR-reaction was performed in triplicate on a MicroAmp optical 96-well PCR plate (Applied Biosystems), and each reaction well contained 5 µl of 5× diluted cDNA products, 0.5 µl of each 50 µM optimised respective forward and reverse primers, 4.8 µl of nuclease free water and 10 µl of SYBR® Green Master Mix (2x concentration). Target and endogenous master mixes were prepared separately and added to the plate. Subsequently, the plate was sealed with a real time plate sealer (MicroAmp, Applied Biosystems) and then centrifuged for 1 minute at 100 rpm to bring all the contents to the bottom of the well. The real time PCR reactions were run using the following programs: (Figure 2.3)

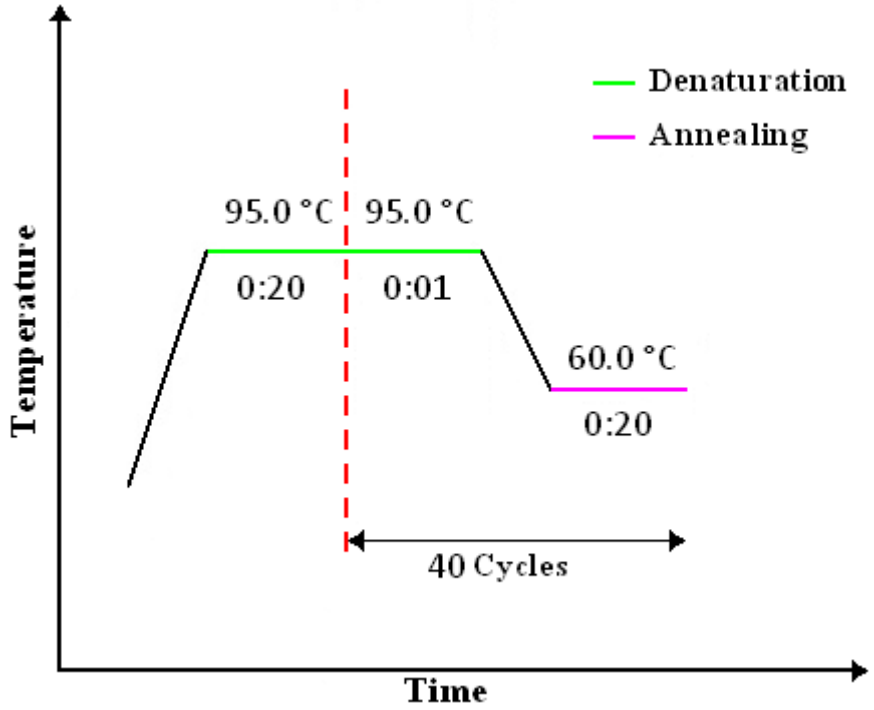

Figure 2.3: Schematic diagram of the real-time PCR program.

Product specificity and efficiency was determined by SDS 2.1 software (Applied Biosystems) using dissociation curve analysis after each PCR run. The dissociation curve allows the check for primer dimer and non-specific amplification that may affect the quality of the data. Nonspecific PCR products are characterised by curves with several peaks. The best set of primers would only amplify the product of interest with no or a minimal quantity of primer dimer formation and decrease the distortion of the final fluorescence reading. Figure 2.4 represents the dissociation curve from real time PCR without primer dimer formation.

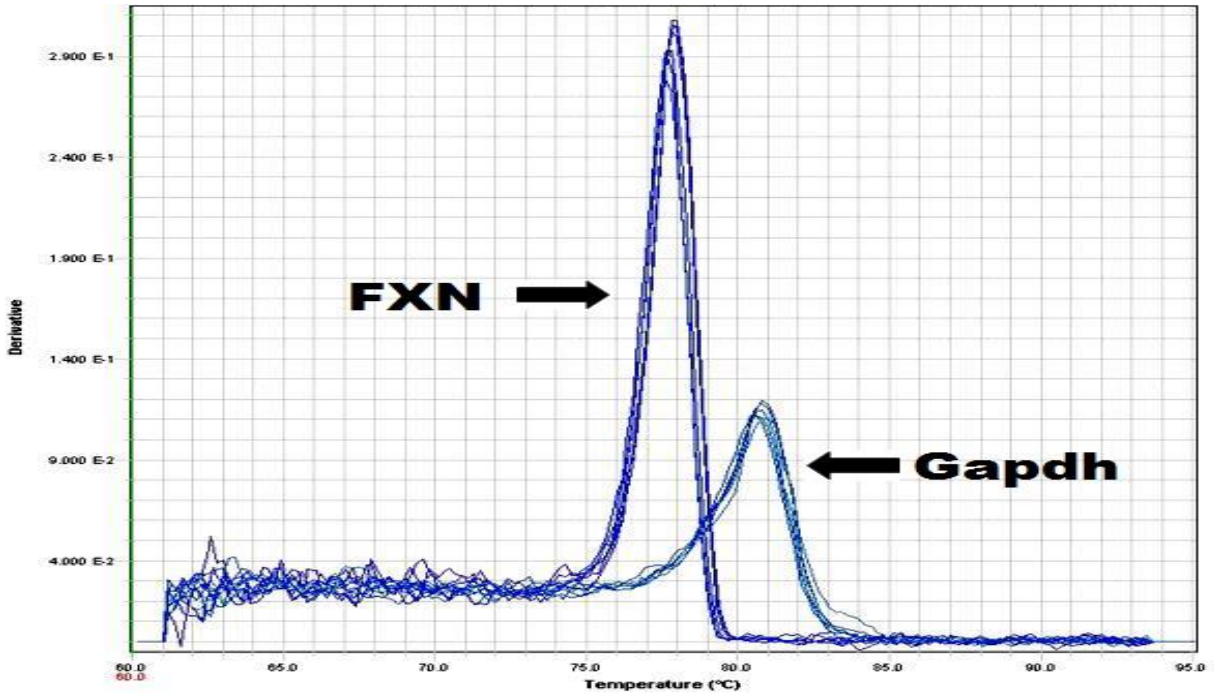

Figure 2.4: Dissociation curve for *Gapdh* and *FXN* primers showing a clean PCR product amplified under real time conditions without any signs of primer dimmer formation or secondary products.

2.2.31 Preparation of protein lysates

Following the method of Campuzano *et al.* 1997, 1x 10^7 cells were collected in a 1.5 ml Eppendorf tube and homogenised on ice in 312 µl of Tris/glycerol homogenisation buffer, in the presence of protease inhibitors, using an Eppendorf homogenising plastic rod. This was followed by the addition of 60 µl of 10% SDS. The homogenates were subsequently incubated at 100°C for 10 minutes and then put on ice. The samples were centrifuged at 14000 rpm for 10 minutes at 4°C and the clear supernatant was collected in a fresh Eppendorf tube. DTT was added at a final concentration of 1mM and the final protein lysates were stored at -80°C. Protein concentrations were determined by the BCA protein assay method, on samples without DTT.

2.2.32 Determination of protein concentration using the BCA protein assay

The protein concentration was estimated using the BCA Protein Assay Reagent Kit. This is a detergent-compatible formulation based on bicinchoninic acid (BCA) for the colorimetric detection and quantification of total protein. A set of protein standards (samples with known protein concentration) was produced by diluting the contents of one bovine serum albumin (BSA) ampoule [2 mg/ml] with Tris/glycerol homogenisation buffer into several Eppendorf tubes as shown on Table 2.5.

Tube	Volume of homogenisation buffer	Volume and source of BSA	Final BSA concentration
A	---	300 µl of stock	2,000 µg/ml
B	125 µl	375 µl of stock	1,500 µg/ml
C	325 µl	325 µl of stock	1,000 µg/ml
D	175 µl	175 µl of tube B dilution	750 µg/ml
E	325 µl	325 µl of tube C dilution	500 µg/ml
F	325 µl	325 µl of tube E dilution	250 µg/ml
G	325 µl	325 µl of tube F dilution	125 µg/ml
H	400 µl	100 µl of tube G dilution	25 µg/ml
I	400 µl	----	0 µg/ml

Table 2.5: Preparation of diluted BSA standards for BCA analysis**.**

200 µl of working buffer (WR) was prepared for each sample/standard and added to individual wells of a 96-well microplate. 25 µl of protein lysate, diluted 1:20 with homogenisation buffer, was added to the respective wells, followed by a gentle mix. 25 µl of the BSA standards was also added. The plate was incubated at 37°C for 30 minutes in an incubator and then allowed to cool at room temperature. The A562 of the standards and protein lysates was then measured using a microplate readers (Biohit HealthCare), a standard curve was prepared by plotting the blank-corrected

measurement for each BSA standard against its concentration. The standard curve was then used to determine the protein concentration of each study sample.

2.2.33 Dipstick assay

The level of frataxin protein was measured by lateral flow immunoassay with the Frataxin Protein Quantity Dipstick Assay Kit (MitoSciences) according to the manufacturer's instructions. 2 µg of protein in 25 µl of extraction buffer (buffer A) was mixed with 25 µl of 2x blocking buffer (buffer B) and was added to individual wells on a 96-well plate with gold-conjugated monoclonal antibody at the bottom of each well. The samples were incubated for 5 minutes, allowing the gold-conjugate to hydrate. The mixture was then resuspended gently using a pipette and dipsticks were inserted into the wells. Subsequently, frataxin within each sample was immunocaptured onto designated capture zones on the dipstick and the signal appeared 5-7 mm from the bottom of the dipstick in approximately 20 minutes. When the signal was developed, the dipsticks were washed for 20 minutes with 30 µl of washing buffer (buffer C) in an empty well of the microplate. The dipstick was air-dried for approximately 20 minutes and the signal intensity was measured with a MS-1000 Immunochromatographic Reader (MitoSciences).

2.2.34 Measurement of population doubling

The population doubling (PD) of the human and mouse fibroblast cell lines was measured to determine their growth rates. In this setup $5x10^5$ cells were seeded per 10 cm^2 dish. Cells were trypsinised with 0.05% Trypsin-EDTA when 80% confluence, pelleted and resuspended in 1 ml PBS. 10 µl of the cell suspension was stained by 10 µl of trypan blue (Sigma). Subsequently, 10 µl of the mixture was added to a cell

counting chamber slide (Invitrogen) and was counted by a CountessTM automated cell counter (Invitrogen). Live and dead cells were counted for a period of time and the PD was calculated using the following equation.

$$PD = \frac{\log(\text{final cell number})}{\text{Log2}} - \frac{\log(\text{initial cell number})}{\text{Log2}}$$

2.2.35 Aconitase assay

Aconitase is a Fe-S cluster protein that catalyzes the conversion of citrate to isocitrate. The assay used for this study was based on a combined protocol provided by Cayman Chemical Company (USA, Cat. No. 705502) and Dr. Mark Cooper (Royal Free Hospital). It involves coupled enzymatic reactions that convert citrate to isocitrate, which is then converted to α-ketoglutarate in a reaction catalysed by isocitric dehydrogenase (IDH). An increase in the absorbance at 340 nm is measured, which monitors the formation of NADPH. The production of NADPH is proportional to the aconitase activity.

To perform the assay, whole-cell extracts of human and mouse fibroblast cell lines were obtained by lysis in 50 mM Tris-HCl, pH 8.0, 10% (v/v) glycerol, 5 mM EDTA, 150 mM KCl, 1 mM phenylmethylsulphonyl. Lysates were centrifuged at 800x g for 10 minutes at 4^{o}C and used immediately.

A substrate reaction premix was made up as follows:

Component	Final Concentration
Tris/HCl (pH 7.4)	50 mM
NADP	0.4 mM
Na Citrate	5 mM
MgCl2	0.6 mM
Triton X-100	0.1%
Isocitrate dehydrogenase	1 U

Table 2.6: Aconitase assay substrate reaction premix.

200 µl of substrate premix was added to each well of a preheated 96-well plate, and reactions were initiated by adding 50 µl of a 1 in 10 dilution of homogenised tissue sample. Reactions were incubated at 37ºC for 15 minutes in the dark and then the absorbance was measured once every minute at 340 nm for 15 minutes at 37ºC using a spectrophotometer. The aconitase activity was determined from the slope of a graph by plotting the absorbance value over time.

2.2.36 Western blot analysis

Polyacrylamide gel electrophoresis (PAGE)

The gel plates were sealed and assembled in an upright position and held in place with bulldog clips. An appropriate well forming comb was slotted in place and the bottom of the wells was marked on the glass plate. A 12% resolving polyacrylamide gel (37.5:1 acrylamide, 0.5 mM Tris (pH 8.8), 0.1% SDS) was prepared in a glass flask. Polymerisation was initiated by adding 0.05% TEMED. The resolving gel was gently poured between the gel plates up to ~1 cm below the comb marking. Water-saturated butanol was immediately added over the gel mix to prevent air contact and the gel was left to polymerise for 30-40 minutes. The butanol was drained and the gel rinsed with

dH2O. A 4% stacking polyacrylamide gel (37.5:1 acrylamide, 0.125mM Tris (pH 6.8), 0.1% SDS) was then prepared in a glass flask and polymerisation was started by adding 0.1% TEMED. The stacking gel was gently poured on top of the resolving gel and the well comb was then fitted. The gel was allowed to polymerise for 45-60 minutes. The gel cast was then put inside the PAGE tank and approximately 1 L of 1x running buffer was poured into the two compartments of the tank in order to establish an electric current through the gel, from the upper to the lower end. The comb was then removed and the wells carefully flushed with running buffer, using a syringe and needle. The tank was connected to the power pack and the presence of current was checked. After loading of samples, gels were run at 120 V for 2-3 hours.

Transfer to membrane – Western blotting

Transfer of protein from gel to membrane was performed using a Hoefer TE22 Transport tank transfer unit (Amersham Biosciences). The transfer tank was filled with approximately 1 L 1x transfer buffer, attached to a water cooling system and placed on a magnetic stirrer. The stacking gel was removed and the resolving gel was divided into upper and lower sections by cutting the gel at approximately 30 kDa, so that the protein of interest and the internal control were in separate gel sections. For each gel section one piece of PVDF membrane (Amersham Biosciences) and two pieces of 3MM Whatman paper were cut to match the gels' sizes. The PVDF membranes were appropriately labelled with a pencil to distinguish the top from the bottom section of the gel. The blotting sponges and filter paper pieces were soaked in 1x transfer buffer for 5 minutes. Separately, the gel sections were also equilibrated in 1x transfer buffer for 5 minutes. The blotting system was assembled in 1x transfer buffer as shown in

Figure 2.5. At every step of layering a 10 ml pipette was used to smooth the surface and remove any air bubbles. The blotting cassette was placed in the transfer tank in a vertical position oriented so that negatively charged molecules would migrate towards

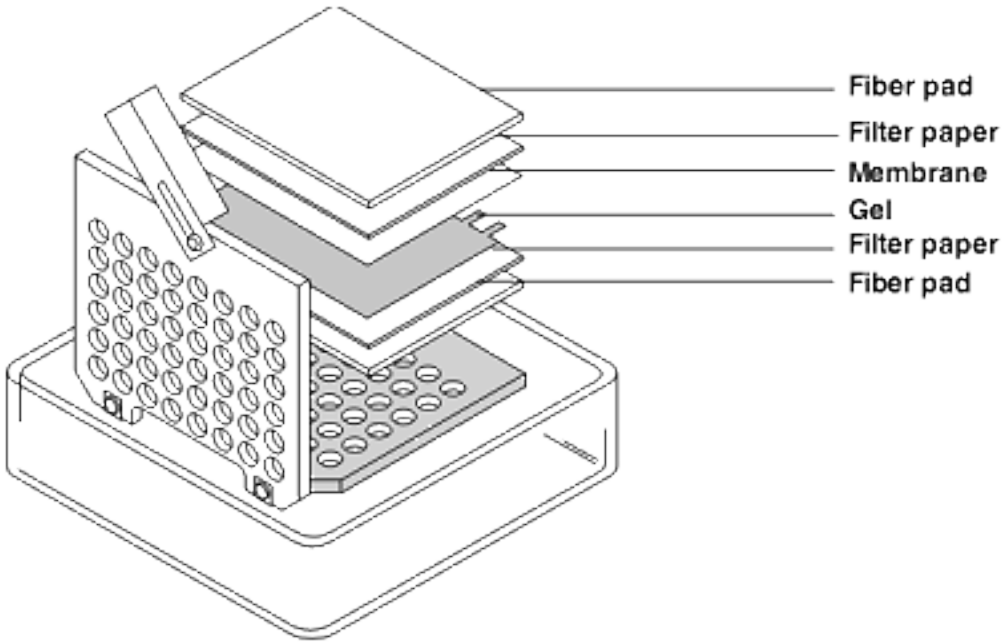

Figure 2.5: Schematic representation of Western blotting transfer cassette assembly. The cassette panels are colour coded: grey is the cathode side and white the anode side.

the grey anode, transferring from the gel into the nitrocellulose membranes. Transfer was carried out at constant 400 mA and 60-80 V for 15 minutes.

Hybridisation of membrane with antibodies

Separately, each PVDF membrane was briefly washed in PBS/T, transferred to a small plastic box and blocked at room temperature in 10 ml 5% milk in PBS/T for 30 minutes with gentle shaking. Primary antibody was applied and incubated at 4°C overnight, with shaking. Each membrane was extensively washed in PBS/T buffer for 2 hours, at room temperature, with several changes of wash, with shaking. Blocking with 10 ml 5% milk in PBS/T was carried out for 1 hour at room temperature, with shaking. 5 µl

of secondary antibody was added to each membrane. The membrane was then incubated at room temperature for 2 hours, with shaking. Extensive washing in PBS/T buffer for 2 hours with several changes of wash was repeated.

Chemiluminescent visualisation and densitometry

Clarity™ Western ECL Blotting Chemiluminescent Substrate (Bio-Rad) was used to detect HRP on the immunoblots. The membranes were placed on Saran wrap with the protein side upwards. The chemiluminescent reagent mix (1:1 ratio of substrate components) was prepared and 2 ml were pipetted onto the membrane covering its entire surface. Incubation was carried out for 5 minutes. The excess reagent was discarded and the membrane was covered with Saran wrap and exposed to Amersham Hyperfilm ECL films (GE Healthcare) for various lengths of time up to 1hour.

Imaging and X-ray film processing

Imaging was performed using Gel Doc XR+ System and ImagLab software that permits immediate analysis of data. Radiographic imaging was also performed in a dark room under red safety light. Amersham Hyperfilm ECL films (GE Healthcare) were exposed to radioactive gels/chemiluminescent blots in x-ray cassettes. The films were developed using an automatic film processing unit (Xograph).

Densitometry analysis

Densitometry was carried out using ImageLab software (Bio-Rad) initially the bands of interest were automatically selected then the area of interest was highlighted to measure the intensity of each band (Figure 2.6).

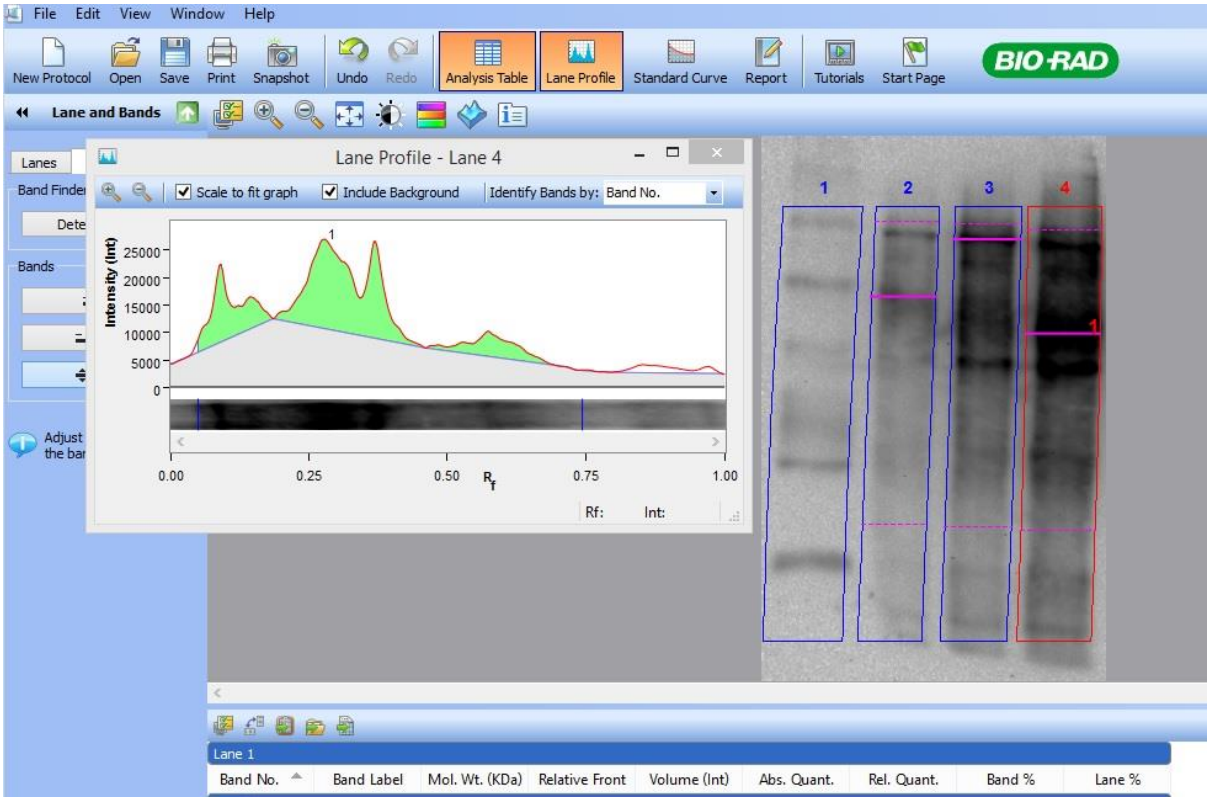

Figure 2.6: Screenshot capture of ImageLab software densitometry for Oxyblot analysis.

2.2.37 Oxyblot analysis: detection of protein oxidation

Overall, this method is as previously described by Al-Mahdawi *et al.,* (2006) and consists on the use of a protein oxidation detection kit (OxyBlot, Millipore). This kit detects protein oxidation by targeting the carbonyl groups introduced into protein side chains by oxygen free radicals and other reactive species.

Derivatisation of protein samples

Initially, protein lysates were prepared as previously described and the concentration was determined using BCA assay as previously described. Protein samples were diluted with dilution buffer so that 30 µg of protein was present in a final volume of 15 µl. The protein sample was denatured by adding 15 µl of 12% SDS and then split into two 10 µl aliquots, each containing 10 µg of protein. One aliquot was derivatised with

10 µl of DNPH while the other was used as a negative control sample and 10 µl of derivatisation-control solution was added instead. The derivatisation reaction was performed at room temperature for 15 minutes, and stopped by adding 7.5 µl of neutralization solution to both aliquots.

Hybridisation, transfer and analysis

Loading of the samples and hybridisation of membrane with antibodies was performed as previously described for the Western blot, using the primary (rabbit anti-DNP, 1:150 dilution) and secondary (goat anti-rabbit IgG, 1:300 dilution) antibodies included in the OxyBlot kit. Finally, the bands were visualised using the Molecular Imager® Gel Doc XR+ system (Bio-Rad), and. densitometry was carried out using Image Lab™ 4.1 analysis software (Bio-Rad).

2.2.38 Treatment of the cells with increasing concentrations of H_2O_2

1×10^5 cells were grown in DMEM supplemented with 10% FBS 24 h prior to use. Cells were given fresh media (MEM, 8 mM glutamine and 10% FBS) before the addition of H_2O_2 for 6 hours. Cells were trypsinized and the number of cells in each sample were counted carefully using a haemocytometer and diluted so that appropriate cell numbers are seeded into petri dishes. A range of between 20 - 150 colonies was achieved for each sample and were incubated in a 5% CO_2 environment at 37°C for colony formation. A clonogenic assay was then performed, as described previously (section 2.2.6)

2.2.39 Multispectral imaging flow cytometry for the γH2AX radiation assay

Cell irradiation

Cells were cultured and maintained as previously described in T75 flasks (Fisher Scientific) to reach 70% to 80% confluency. All cell lines were irradiated as proliferating monolayers with 2 Gy gamma irradiation from a Cobalt 60 source (Puridec Irradiation Technologies Ltd, Oxon, UK) at a distance of 25 cm from the gamma source. This provided a dose rate of 1.3 – 1.4 Gy/min. cells were fixed and total nuclear fluorescence was determined through immunoflurescent microscopy.

Cell fixation

Untreated control cells and cells subjected to Lentiviral treatment were fixed. Cells were detached using 1 ml of 0.25% trypsin-EDTA and washed twice in ice-cold PBS. They were then fixed in 50:50 (V:V) methanol:acetone at 4^{o}C.

Antibodies and immunocytochemistry

Fixed cells were rehydrated by three washes in PBS and then permeabilised in PBS containing 0.25% Triton X-100 (Fisher Scientific) for 5 minutes at room temperature (RT). After blocking the cells in blocking buffer comprised of PBS containing 0.1% Triton X-100 and 0.5% non-fat milk protein (Premier International Food Ltd. UK, Spalding, Lincolnshire, UK), cells were incubated at 4^{o}C overnight in mouse monoclonal anti-serine139 γ-H2AX antibody (Millipore) at 1:10000 dilution.

Following three washes in wash buffer made up of PBS containing 0.1% Triton X-100, cells were incubated for 2 hours at room temperature in Alexa Fluor®488 rabbit anti-mouse IgG antibody (Invitrogen) diluted in block buffer to 1:50. Cells were washed again in wash buffer three times and once in PBS. Samples were then resuspended

in 100 µl of Accumax flow cytometry buffer with 5 µM Draq5 (Biostatus Ltd.). Two samples for fluorescence compensation were prepared with either the secondary antibody (Alexa Fluor®488 conjugate) or Draq5 being omitted from the process.

Imaging flow cytometry

The Imagestream^X (Amnis Inc., Seattle, Washington) enables images of individual cells in flow to be captured using up to six different optical channels (Refer to Table 2.7). Using the Inspire ^{TM} data acquisition software, 20000 images were captured using Channel (Ch) 01 for brightfield (BF), Ch02 for AF488 representing the γH2AX foci and Ch05 for Draq5 to represent the nuclear staining of each cell. The lasers used were

- 800 nm to capture BF images
- 488 nm to capture PE and Draq5 fluorescence
- 765 nm to capture side scatter images

Cell classifiers were applied to BF in order to only capture objects between 50 and 300 units on an arbitrary scale. This range of values was previously established empirically from preliminary experiments to primarily show single cell images. Using a 488 nm laser set at 75 mW power, images were captured at 40X magnification at an approximate rate of 150 images per second, creating a raw image file (rif).

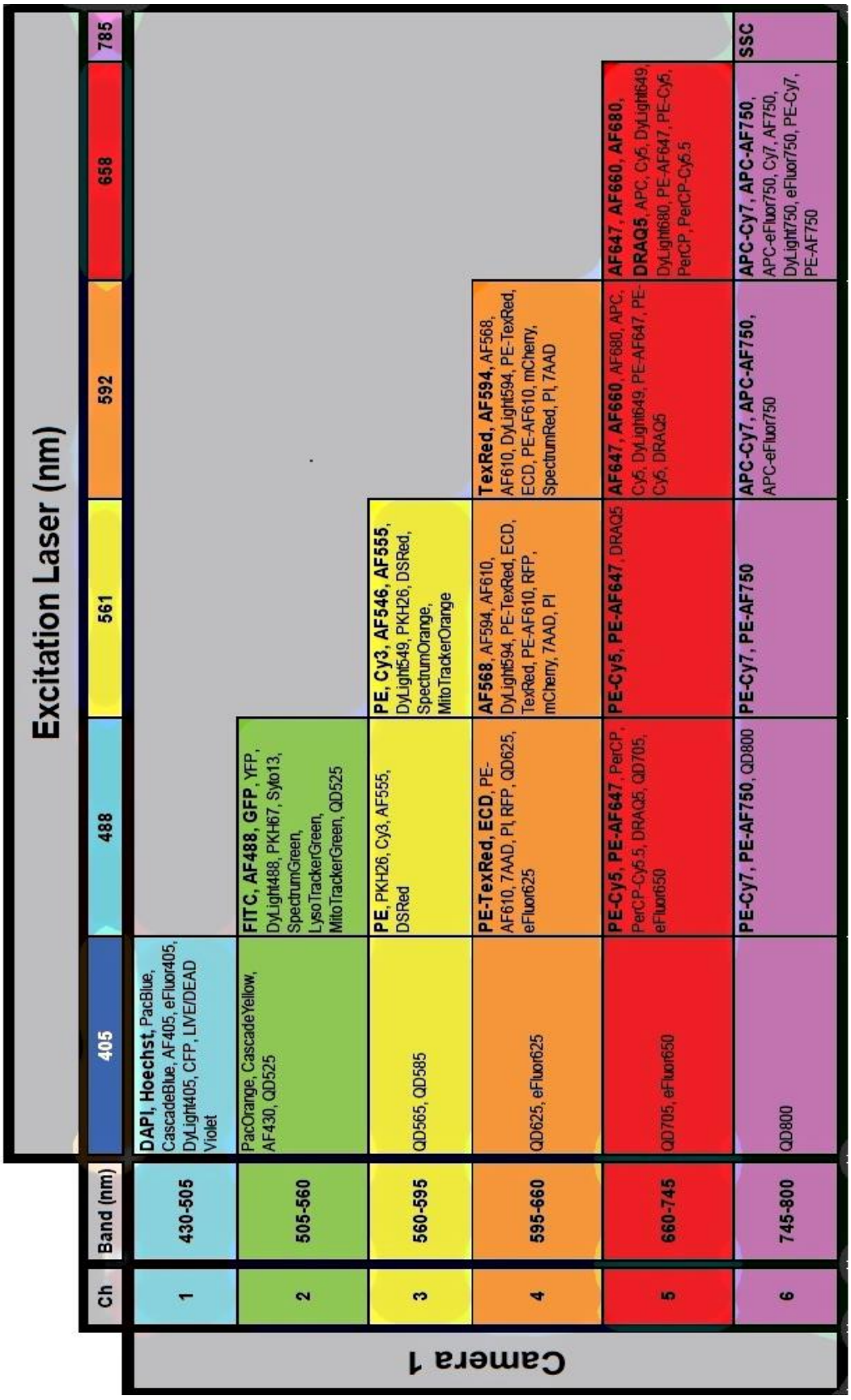

Table 2.7: Imagestream^X fluorochrome chart.

Image compensation

Compensation was performed using the samples that had been stained with Draq5 only. Images for these samples were captured without the BF illumination or scatter as it was important to detect intensity of fluorescence in these samples with only a single source of illumination. Here, the 488nm laser was set at 75mW. A compensation matrix was generated using the Ideas™ software using control files created for the Draq5 samples. This is a table of coefficients whereby detected light from each image is placed into the proper channel (Ch05 for Draq5) on a pixel by pixel basis. The coefficients are normalised to 1 and each coefficient represents the leakage of either fluorochrome into juxtaposed channels.

		Ch01	Ch02	Ch03	Ch04	Ch05	Ch06
Ch01		1	0.061	0	0	0.036	0
Ch02		0	1	0	0	0.125	0
Ch03		0	0.277	1	0	0.100	0
Ch04		0	0.518	0	1	0.143	0
Ch05		0	0.208	0.01	0	1	0
Ch06		0.02	0.087	0.03	0	0.352	1

Table 22.8: Table of a compensation matrix created in IdeasTM software. The values in this table represent coefficients of leakage into juxtaposing channels. It can be seen that as you move away from the principal channel (indicated as having a value of 1), the coefficient of leakage is decreasing. Values that have a margin of error that is less than 0.001 was used.

The sample FRDA untreated samples were used to create a template file with which all other samples in the investigation would be analysed with. This file was chosen due to it being likely to be the highest induction of γH2AX foci and therefore the brightest intensity of AF488. Templates were created for each individual cell line.

The .rif file created by the Inspire™ software was loaded into the Ideas™ software. Cell images were examined in BF, AF488 (γH2AX foci) and Draq5 (nuclear morphology) channels. The image gallery properties were adjusted to optimise the displayed fluorescent images.

The analysis process comprises a multistep process and initially uses a series of predefined "building blocks" provided within the software. These tools generate a series of scatter and histogram plots which allow for the identification of single and focussed cells, stained for both Draq5 and AF488. Identification of single cells is determined by the creation of a scatter plot of the population defined by cell area and cell aspect ratio from the BF images whereby each dot within the scatter represents a single cell. The single cell region was defined by visually validating the BF images and gated using the polygon region tool (refer to Figure 2.7 below)

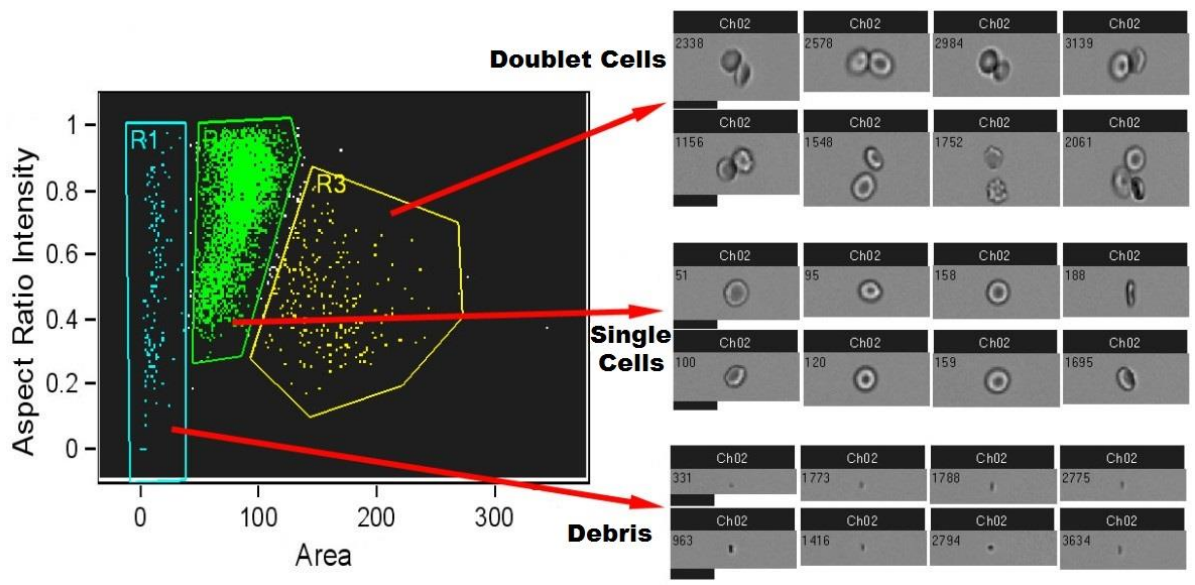

Figure 2.7: Gating for single cells. Identification of single cells within the population based upon cell area and aspect ratio. Single cells are gated using the polygon tool. The area marked in blue indicates either debris or beads that have been collected during the run and the area indicated in yellow represents doublet cells. These are all excluded from the single cell population that has been gated.

Using the “In Focus” tool, a histogram of the single cell population gated above was produced. The cells were distributed into “bins” based on the calculated focus of the BF images. Clicking on individual bins enables visualisation of all images within that particular bin in the image gallery. Single cells in focus were defined using the line region tool as shown in Figure 2.8.

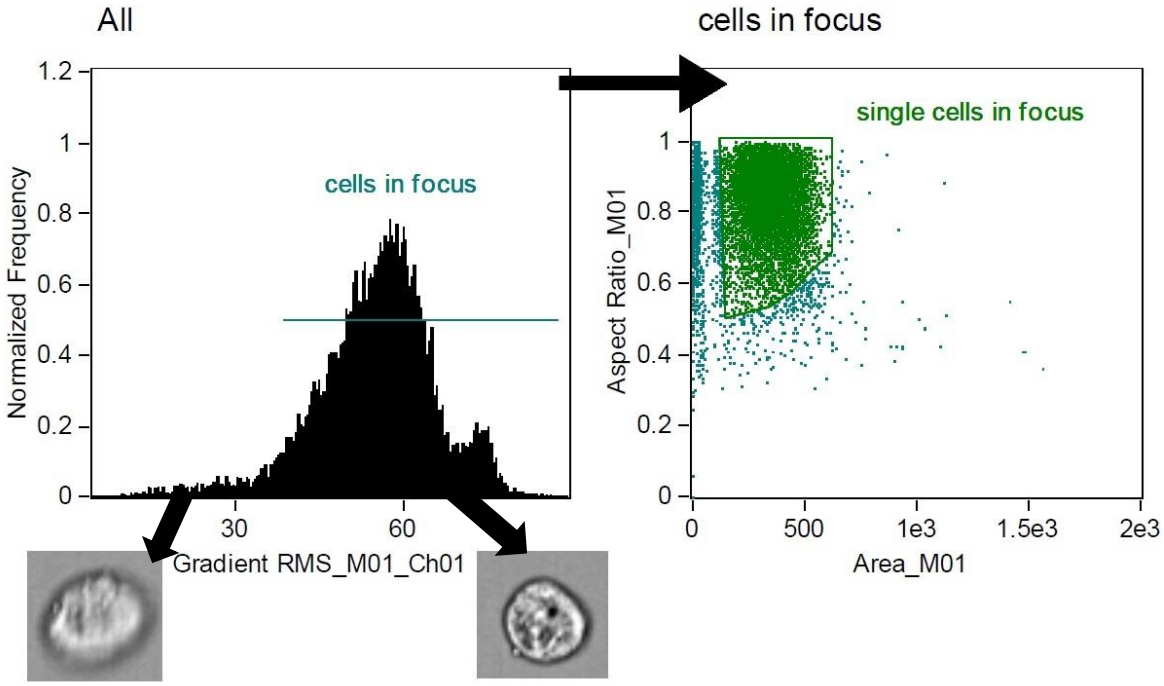

Figure 2.8: Gating for cells in focus.

Using the fluorescence positive two colour tool, a scatter plot was then generated of the single cells in focus that stained for both PE and Draq5. The polygon tool was utilised to gate the cells that satisfied these parameters.

Masking and determination of the number of γH2AX foci in each nucleus

To determine the number of γH2AX foci within the nucleus of each cell, a series of masks were created which identified the region of interest. To ensure that γH2AX foci within each cell were identified correctly, a “truth population” of cells with known numbers of γH2AX foci ranging from 0 - 30 or more was created. Using this population

of cells, a spot mask was created using the spot function of the Mask Manager. Using the spot to background ratio, foci were masked that were at least two-fold brighter than the background with a minimum diameter of 2 pixels. A nuclear morphology mask was then created using the Draq5 (Ch05, nuclear staining) image of each cell. To determine the number of γH2AX foci within the nuclear region of each cell, these two masks were combined using Boolean logic. Cells are first shown unmasked, then with the application of a morphology mask and a spot mask; finally showing localisation of γH2AX foci within the nuclear region of the cell.

2.2.40 *In situ* detection of γH2AX foci

Cell preparation and cell irradiation:

Cells were cultured and maintained, as previously described in T75 flasks (Fisher Scientific), to reach 70% to 80% confluency. All cell lines were irradiated as proliferating monolayers with 2 Gy gamma irradiation from a 60Cobalt source (Puridec Irradiation Technologies Ltd, Oxon, UK) at a distance of 25 cm from the gamma source. This provided a dose rate of 1.3 – 1.4 Gy/min. Cells were fixed and the total nuclear fluorescence was determined through immunoflurescent microscopy.

For the γH2AX assay adherent cells were grown on poly-prep slides (Sigma- Aldrich) 24 hours before treatment with DNA-damaging agents (in our case ionizing radiation). After irradiation, cells were fixed using 4% formaldehyde in PBS for 15 minutes and permeabilised using 0.2% Triton-X100 solution in dH_2O for 10 minutes at 4°C.

Non-specific sites on the cell were then blocked using blocking buffer. A total of 100µl of blocking buffer was added to each slide, slides covered with parafilm and placed in a humidified dark box. After 1 hour incubation the primary anti-body mouse

monoclonal anti-serine139 γH2AX antibody (Millipore) was added to the slides at a concentration of 1:1000. The slides were covered with parafilm and were placed in a humidified dark box for 1 hour.

The slides were then washed 3 times for 5 minutes with TBST solution (8.8 grams of NaCl + 0.2 grams of KCL + 3 grams of tris base + 500 µl tween 20 in 1 litre of dH2O. pH 7.4). The secondary antibody (Alexa Fluor®488 rabbit anti-mouse IgG antibody, (Invitrogen)) was added at a dilution rate of 1:1000. A total of 100µl of diluted antibody was added to the slides and were covered with parafilm and placed in a humidified chamber for 1 hour. The slides were then washed 3 times for 5 minutes in TBST and then 3 times for 5 minutes in PBS only. The slides were de-hydrated in an ethanol series (70%, 90% and 100%) for 5 minutes each time. Once the slides were air dried, a total of 15 µl of mounting medium containing DAPI (Vector Laboratories) was added to each slide and covered with a cover slip and sealed using clear nail varnish. γH2AX foci were counted in the nuclei of at least 100 cells for each cell line in untreated cells as well as treated cells fixed at 30 minutes, 5, 24, 48 and 72 hours post irradiation. Microscopy was carried out using an Axioscope 2 fluorescence microscope with a 100-fold magnification objective (Zeiss, Goettingen, Germany).

2.2.41 Localisation of intermediate and mature forms of frataxin to subcellular compartments

Separation of cytosolic, mitochondrial and nuclear fractions was performed using a cell fractionation kit (Abcam) following the manufacturer's recommendations. Briefly, human and mouse fibroblast cells were grown in T75 tissue culture flasks to confluency. After cell trypsinisation and centrifugation, each subcellular fraction was

used for the identification of the intermediate and mature forms of frataxin by measuring these in the protein isolates. Buffer A was used to wash cells, followed by resuspension to a concentration of 6.6×10^6 cells per ml. Cellular extractions were obtained after two sequential detergent-extraction steps. The purity of each fraction was assessed by Western blotting against GAPDH (cytoplasmic), SOD2 (mitochondrial) and Emerin (nuclear) proteins. The following antibodies were used for western blotting: an anti-frataxin monoclonal antibody (1:100, MAB1594, Millipore), mouse monoclonal anti-GAPDH antibody (1:2000, ab9484, Abcam), mouse monoclonal anti-SOD2 antibody (1:1000, ab16956 Abcam), mouse monoclonal anti-Emerin antibody (1:1000, NCL-Emerin, Leica Biosystems) and a rabbit anti-mouse IgG HRP conjugated secondary antibody (1:2000, ab97046, Abcam). Detection was performed using the chemiluminescent reagent (Bio-Rad) and bands were visualized using the Molecular Imager® Gel Doc XR+ system (Bio-Rad), and densitometry was carried out using Image Lab™ 4.1 analysis software (Bio-Rad).

2.2.42 Statistical analysis

Statistical analyses such as descriptive measurements and graphical visualization were carried out using Microsoft Excel 2007 software. All other measurements comparing sample groups were analysed using student's T-test or two-way analysis of variance (ANOVA) to assess the significance of the differences of the group data.. In all cases a statistical significance level of 5% was chosen.

CHAPTER 3 – *FXN* CLONING, VIRAL PRODUCTION AND TITRATION

3.1 Aims

- Cloning the *FXN* gene into a lentivirus (LV) delivery vector.
- Mapping and characterisation of the backbone vector and vectors required for viral production.
- Evaluation of the function of the gene delivery vector.
- Lentivirus production and titration.

3.2 Introduction

Lentiviruses (LV) have been used to effectively transduce both stem cells (Follenzi *et al.*, 2000, O'rourke *et al.*, 2005) and terminally differentiated cells, especially neurons (Naldini *et al.*, 1996a, Miyoshi *et al.*, 1997) and have been shown to be effective in the treatment of animal models of genetic diseases by both *in vivo* and *ex-vivo* approaches (Waddington *et al.*, 2004, Bigger *et al.*, 2006). Hence, these vectors are currently being used in clinical trials (Escors and Breckpot, 2010).

Dr. Themis and colleagues have previously demonstrated there is widespread reporter gene transfer and long-term gene expression in immunocompetent MF-1 outbred mice following delivery either before or after birth (Themis *et al.*, 2005, Kang *et al.*, 2005). From this work, it was found that LV delivery mainly reached the liver. However, gene expression was observed in virtually all other tissues of the mouse, including the kidney, heart, brain, spinal cord, skeletal muscle, lung, eye and pancreas. Furthermore, it was demonstrated that LV-mediated delivery of the human Factor IX (hFIX) gene could achieve permanent correction of haemophilia B in the mouse model of this disease (FIX-KO) (Bigger *et al.*, 2006). In this study, the most current vector systems available were tested including LV-derived from non-primate equine infectious anaemia

(EIAV) SMART 2 and primate HIV-1 based HR'SIN-cPPT-SEW viruses. Interestingly the mice treated with EIAV vectors developed liver tumours at high frequency, whereas HIV-1 based LV produced life-long correction of genetic disease with no side effects (n>100), demonstrating the bio-safety of HIV-1 LV for gene therapy (Nowrouzi *et al.*, 2013).

The potential to direct LV more efficiently to tissues other than the liver was explored by testing LV pseudotyped with alternative virus glycoprotein envelopes in the mouse. Although targeting was not tissue specific, each envelope offered effective gene transfer to tissues that were previously more difficult to reach. These tissues included cells in the brain, cerebellum, spinal cord, dorsal root ganglia, peripheral nerves, heart, liver and muscle (Figure 3.1).

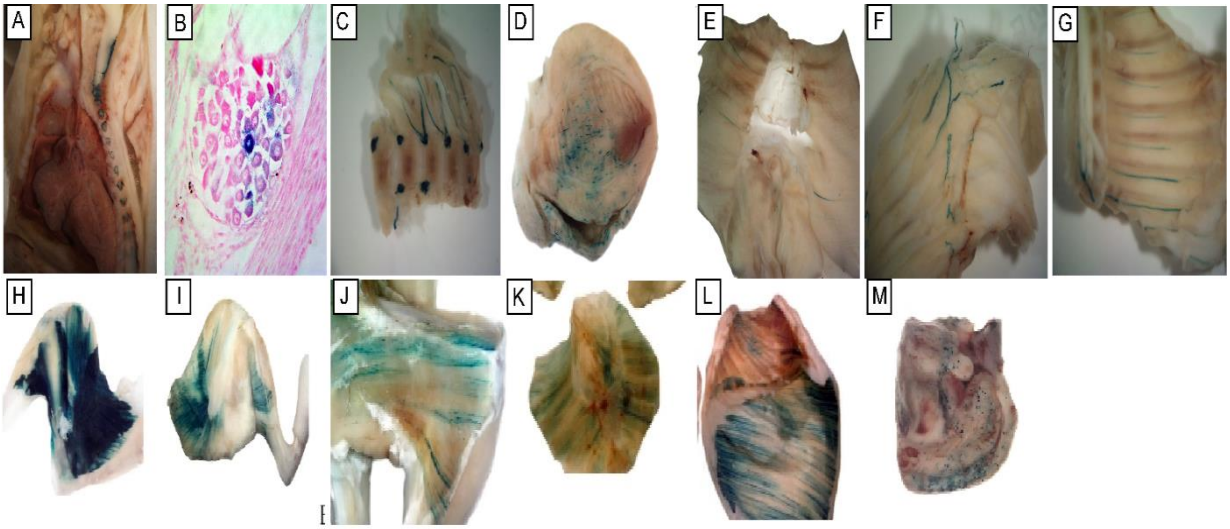

Figure 3.1: β-galactosidase expression after injection of pseudotyped LV in the mouse. **A)** intraspinal (i.s.) injection of rabies pseudotype reaches the dorsal root ganglia (DRG) x10; **B)** intravenous injection (i.v.) of VSV-G pseudotype also results in DRG expression x200 and **C)** DRG x40; **D)** i.v. with rabies pseudotype reaches the nerves of the heart and **E)** the diaphragm and **F)** outside the ribs and **G)** the spinal cord and inside the ribs; **H)** extensive muscle delivery to the gluteus medius, quadriceps and biceps femoris by intramuscular injection (i.m.) with VSV-G pseudotype and **I)** mokola envelope and **J)** ebola pseudotype; **K)** intraperitoneal injection using VSV-G pseudotype reaches the diaphragm and **L)** the abdominal muscles and **M)** the heart (Gregory *et al.*, 2004).

Previously, research by Dr. Themis has shown that LV pseudotyped with the VSV-G envelop carrying GFP, injected via different routes in late gestation and neonatal outbred MF-1 mice, reached organs and provided long-term gene expression in tissues affected by FRDA. With this knowledge and experience, full-length human *FXN* cDNA and GFP will be cloned into the pHR'SIN-cPPT-MCS-WPRE (LV MCS), (Multiple cloning site (MCS)) vector using standard restriction digestion and ligation. Both vectors pHR'SIN-cPPT-GFP-WPRE (LV GFP) and pHR'SIN-cPPT-*FXN*-WPRE (LV *FXN*) will be used to generate high titre viruses pseudotyped with the VSV-G envelope.

The aim of this chapter is to create lentiviral constructs with strong promoters that are already known to drive high level of gene expression both *in vitro* and *in vivo*. These vectors will be: (a) propagated in virus-producer cells and ultracentrifuged to reach high titres for the infection of HEK 293T cells to titrate the LV and (b) tested for the absence of replication-competent (RC) LV that would be deleterious to cells intended to be infected *in vitro* in the investigation.

3.3 Vector construction

To construct the frataxin delivery vector and produce VSV-G pseudotyped particles, the frataxin gene was cloned into lentiviral multiple cloning site vector ((pHR'SIN-cPPT-MCS-WPRE) (LV-MCS)). This vector was provided by Dr. Steve Howe from UCL, UK (Figure 3.2).

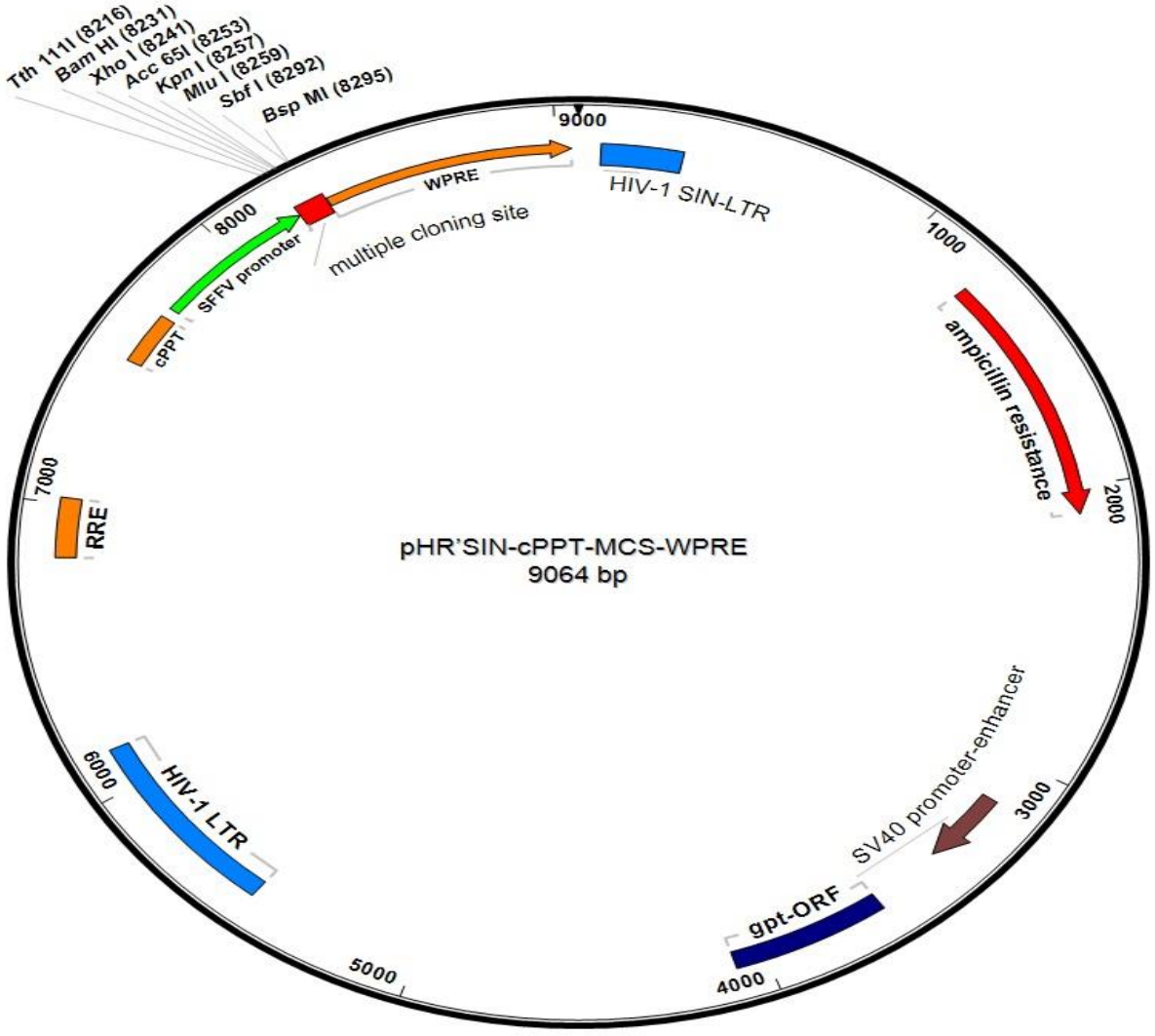

Figure 3.2: Schematic map of the pHR'SIN-cPPT-MCS-WPRE vector displaying unique cloning sites. LTR: Log terminal repeats. RRE: rev response element. cPPT central polypurine tract. SFFV promoter: spleen focus forming virus promoter. WPRE: Woodchuck hepatitis virus post-transcription regulatory element. Gpt ORF: Programmed Translational Frame shift.

3.3.1 LV-MCS vector mapping and characterisation

Restriction enzyme digestion of the LV-MCS vector was performed to verify the integrity of the vector. Unique restriction sites were identified using sequence editing software, SeqBuilder (DNASTAR Inc.) and digestion was performed on the LV-MCS. The vector was linearized with *Eco*RI, *Sac*II, *Pvu*I, *Hpa*I, *Bam*HI and *Xho*I restriction enzymes to form a 9064 bp band. In addition a double digest was carried out at the site of the cloning using *Bam*HI and *Xho*I restriction enzymes. This double digest cuts the plasmid into two, forming a 9054 bp and a 10 bp band (Figure 3.3).

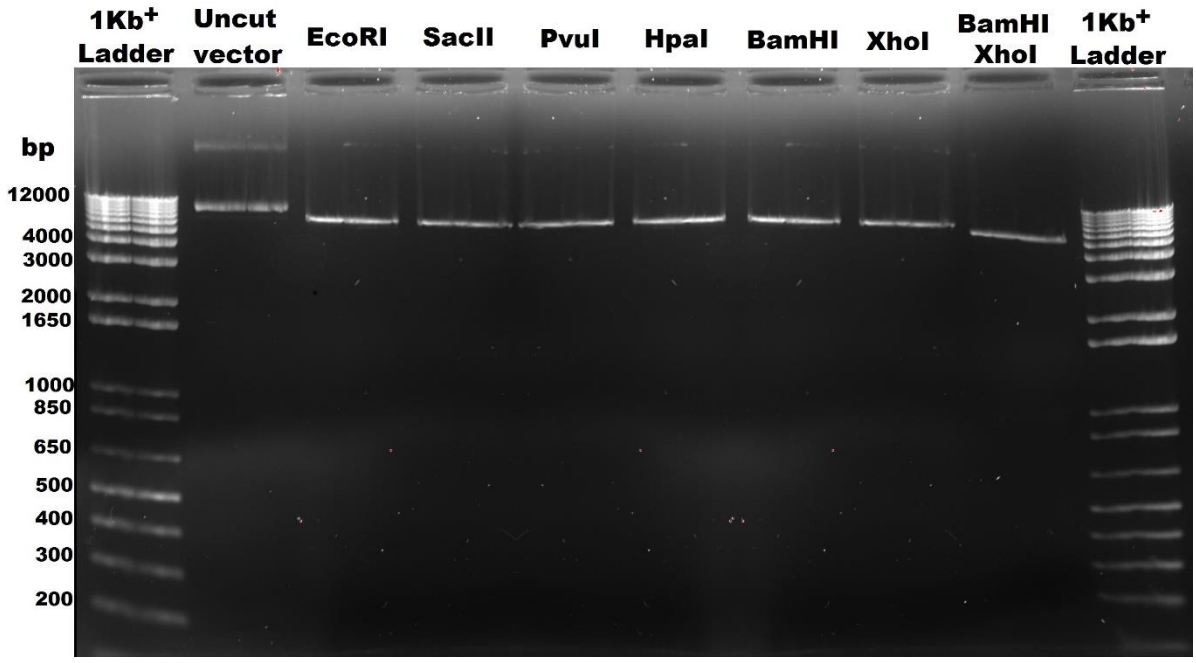

Figure 3.3: Characterization of LV-MCS with restriction enzyme digestion using 1% agarose gel. LV-MCS plasmid was linearized with *Eco*RI, *Sac*II, *Pvu*I, *Hpa*I, *Bam*HI and *Xho*I restriction enzymes to produce a 9064 bp band. *Bam*HI and *Xho*I double digest formed a 9054 bp linearized band. A 1Kb^{+} DNA ladder (Invitrogen) was used for size evaluation. DNA was loaded on 1% agarose gel and run at 70 mV.

3.3.2 Amplification of the frataxin gene

Initially, the full human frataxin sequence (Gene bank number: U43747) was purchased from ATCC Global Bioresource Centre in pTLX1 plasmid vector (ATCC number: 99619). By using primer designing software, Primer Select (DNASTAR Inc.), one set of primers (HKH-*FXN*-F and HKH-*FXN*-R) was designed to amplify the *FXN* gene. Since the chosen cloning sites into the LV-MCS were *Bam*HI and *Xho*I, the sequence of these restriction sites was added to the 5' end of the HKH-*FXN*-F and HKH-*FXN*-R primers with two random nucleotides in between the restriction sites sequence and the primer sequence (Chapter 2, section 2.1.5). The frataxin sequence was then amplified to produce a 626 bp product by polymerase chain reaction (PCR) using Qiagen PCR Master Mix Kit which includes Taq DNA Polymerase in a premixed format (Qiagen). The conditions and the PCR master mix components are shown in Table 3.1 and Table 3.2.

Component	50 µl Rxn	Final conc.
2X Taq PCR Master Mix (1.5 mM MgCl2 at 1X)	25 µl	1X
10 µM Forward Primer	2.5 µl	0.5 µM
10 µM Reverse Primer	2.5 µl	0.5 µM
Template DNA	1 µl	N/A
PCR-grade water	Up to 50 µl	N/A

Table 3.1: The PCR master mix containing the appropriate volume of all reaction components for amplification of the frataxin gene from pTLX1 plasmid.

Step	Temperature	Duration	Cycles
Initial denaturation	95ºC	3 min	1
Denaturation	95ºC	1 min	35
Annealing	58°C	1 min	35
Extension	72°C	1 min	35
Final extension	72°C	5 min	1
Hold	4°C	∞	1

Table 3.2: The PCR cycle conditions for amplification of the frataxin gene from pTLX1 plasmid.

3.3.3 TA cloning and sequencing

Since the Taq DNA polymerase used in the PCR reaction had the ability to add extra adenine nucleotide (A overhangs) to both ends of the PCR product (Figure 3.4), the segments of DNA amplified was gel extracted and purified using QIAquick Gel Extraction Kit (Qiagen). The purified DNA was then TA cloned into pCR™4-TOPO® vector (Figure 3.5) using the TOPO® TA Cloning® Kit (Invitrogen) with One Shot® TOP10 Chemically Competent *E.* coli provided in the kit. Transformed cells were grown overnight at 37ºC on agar plates containing 50 µg/ml of ampicillin (Figure 3.6), then the formed colonies were grown in LB broth and the plasmids were isolated using QIAprep Spin Miniprep Kit (Qiagen). Plasmids were analysed for the inserts by performing PCR (Figure 3.7). Plasmids containing the insert were then sent to Beckman Coulter Genomics for sequencing before cloning into LV-MCS.

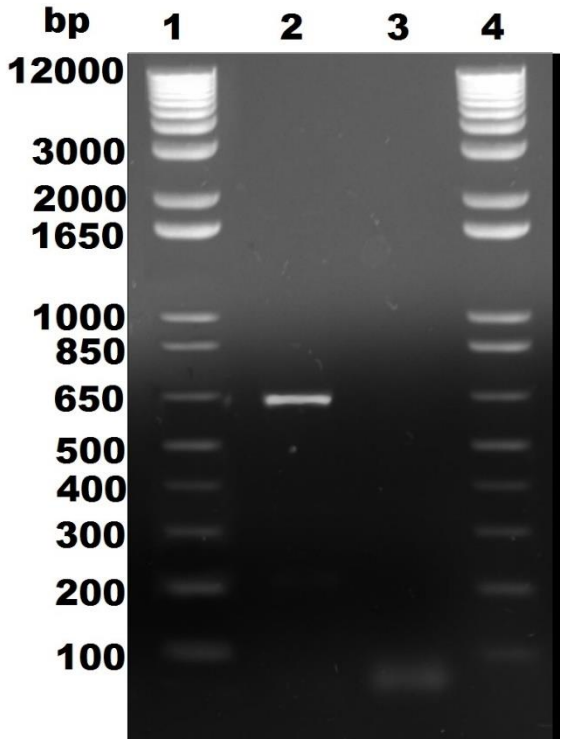

Figure 3.4: Frataxin amplification from pTLX1 plasmid vector using PCR. Lane 1) 1Kb+ DNA ladder, Lane 2) 626bp frataxin amplicon, Lane 3) PCR negative control, Lane 4) 1 Kb^{+} DNA ladder. DNA was loaded on 1% agarose gel and run at 70 mV.

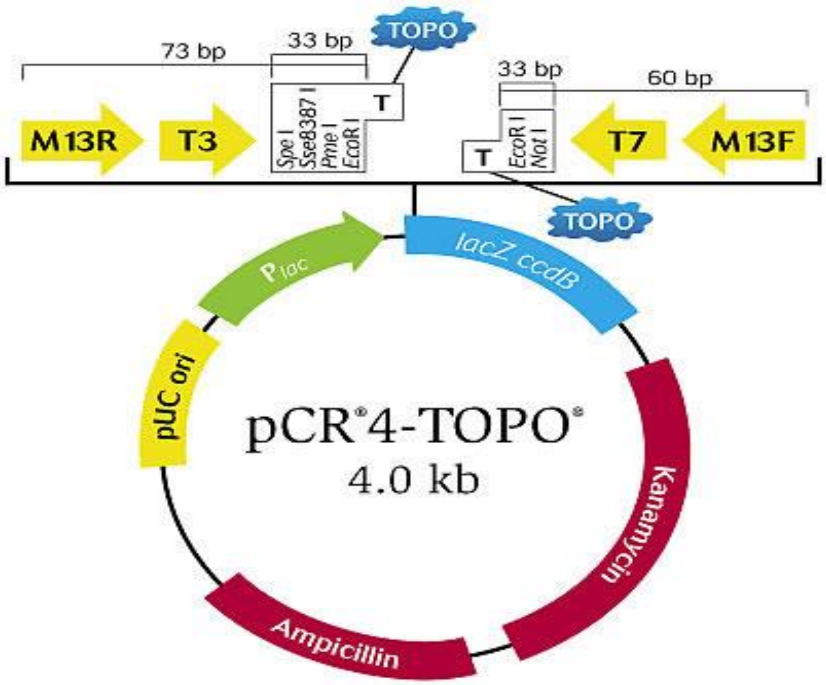

Figure 3.5: Map of pCR®4-TOPO® vector with shortened distance between sequencing primer sites and the insert site, allowing for less vector sequencing and more insert sequence.

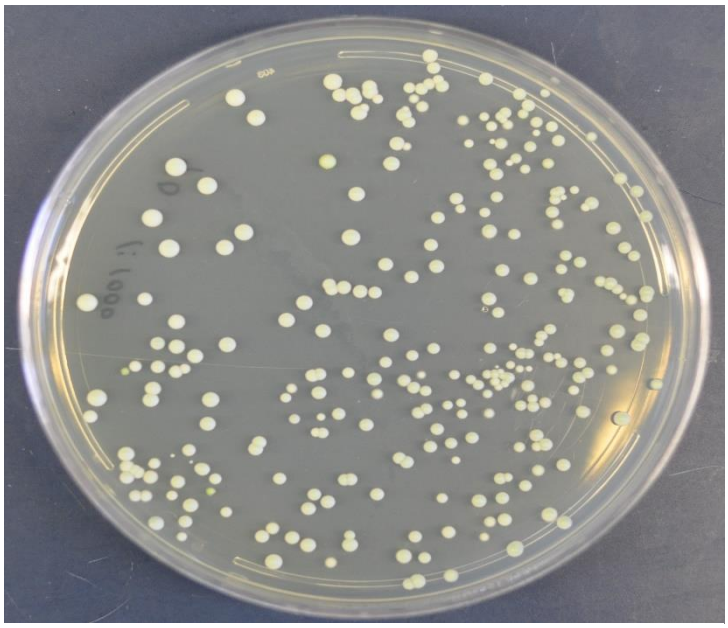

Figure 3.6: Formed colonies up on transformation of competent cells. Colonies were picked and analysed for the integrity of the insert.

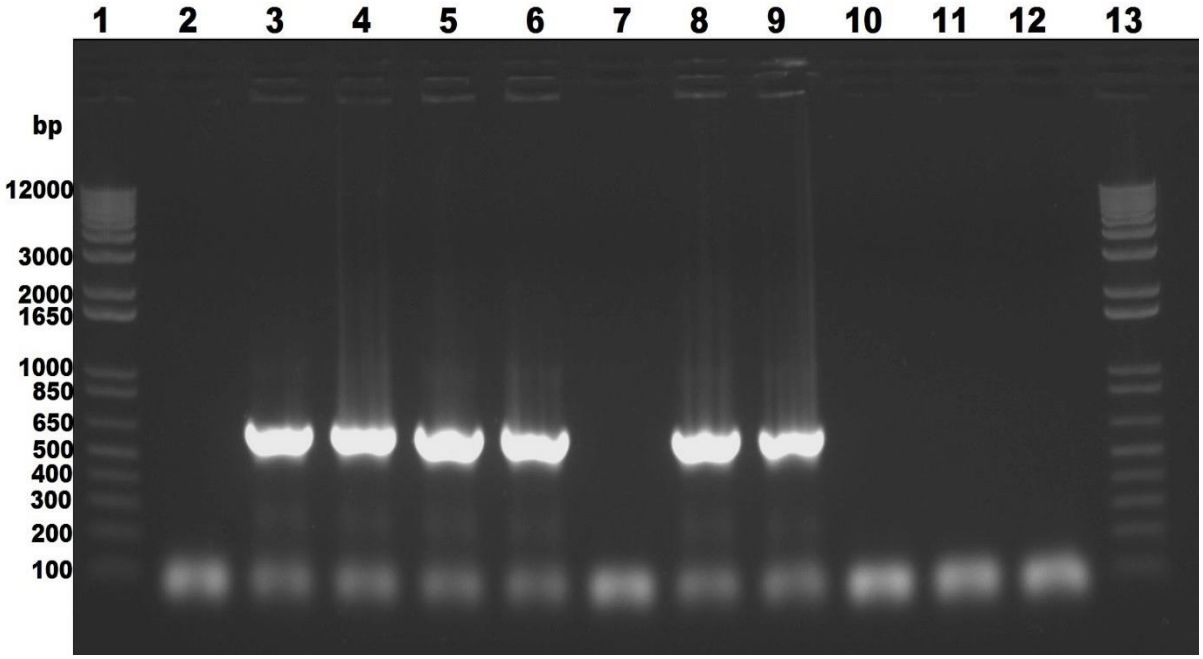

Figure 3.7: Agarose gel electrophoresis showing the PCR analysis of the transformed competent cells. Colonies with the correct insertion have produced a 626 bp fragment. Lane 1 & Lane 13: 1 Kb^{+} DNA ladder. Lane 2, Lane 7, Lane 10 and Lane 11: had no insertion and were discarded. Lane 3-6 and Lane 8-9: have produced the 626 bp fragment and these plasmids were sent for sequencing. Lane 12: PCR negative control. DNA was loaded on 1% agarose gel and run at 70 mV.

3.3.4 Subcloning the *FXN* gene into LV-MCS

Once the correct sequence and orientation of the *FXN* insert was confirmed, the insert was released from pCR®4-TOPO® vector by restriction digestion with *Bam*HI and *Xho*I restriction enzymes (Figure 3.8). Subsequently, the released fragment was gel extracted using QIAquick Gel Extraction Kit (Qiagen) and ligated into LV-MCS using T4 DNA Ligase (New England Biolabs). The molar ratio of the Vector:Insert was calculated using NEBioCalculator online software (New England Biolabs). The components and the volumes of the ligation reaction are shown in Table 3.3.

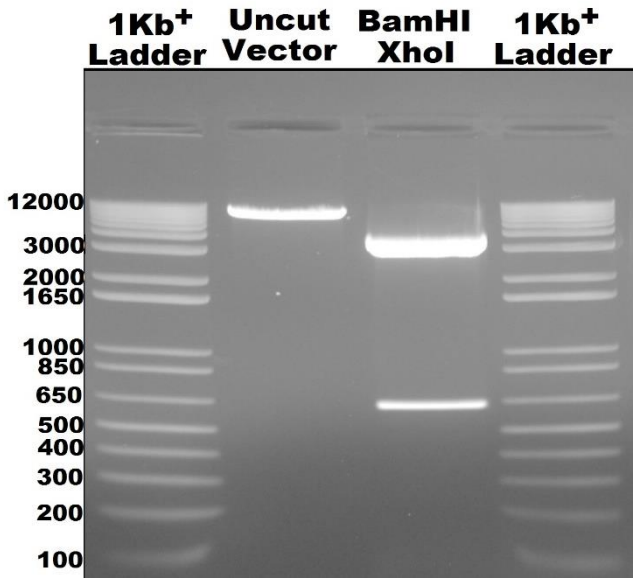

Figure 3.8: pCR®4-TOPO® vector restriction digestion with *Bam*HI and *Xho*I released the 626 bp frataxin insert. This fragment was gel extracted and sub cloned into LV-MCS. DNA was loaded on 1% agarose gel and run at 70 mV.

COMPONENT	20µl REACTION
10X T4 DNA Ligase Buffer	2 µl
Vector DNA	50 ng (0.020 pmol)
Insert DNA	37.5 ng (0.060 pmol)
Nuclease-free water	20 µl
T4 DNA Ligase	1 µl

Table 3.3: Ligation reaction components and volumes with T4 DNA Ligase.

Following the ligation of the *FXN* gene into LV-MCS, the integrity and correct orientation of the insert was further tested by enzyme restriction digestion with *Bam*HI and *Xho*I restriction Enzymes, PCR amplification of the *FXN* gene (Figure 3.9) and sequencing. The result was a new lentiviral vector containing the human *FXN* gene (LV *FXN*) (Figure 3.10).

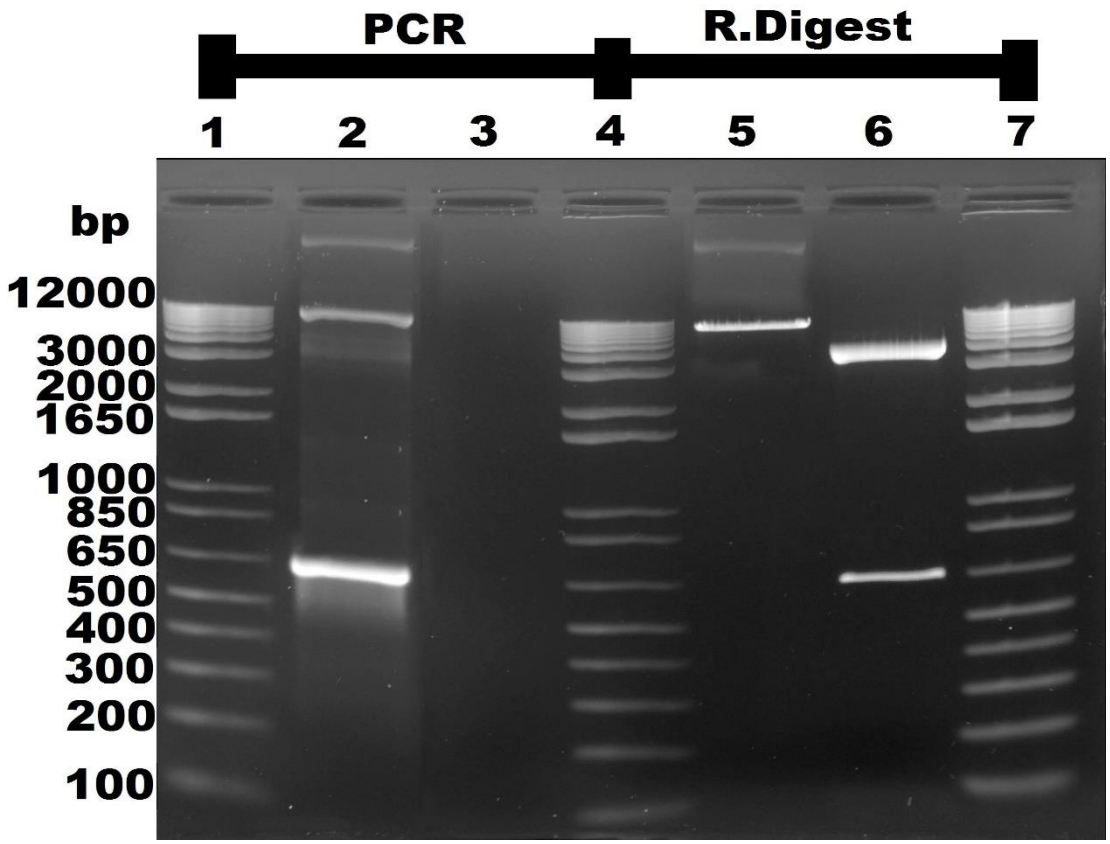

Figure 3.9: Confirmation of insertion of the *FXN* gene into the LV MCS by PCR analysis (Lane 2 & Lane 3) and restriction digest (Lane 5 & Lane 6). Lane 1, Lane 4 & Lane 7: 1 Kb^{+} DNA Ladder. Lane 2: 626 bp *FXN* insert amplified by PCR. Lane 3: PCR negative control. Lane 5: Uncut LV *FXN*. Lane 6: restriction digest of LV *FXN* with *Bam*HI and *Xho*I restriction enzymes producing a 9054 bp band and releasing the 626bp *FXN* insert. DNA was loaded on 1% agarose gel and run at 70 mV.

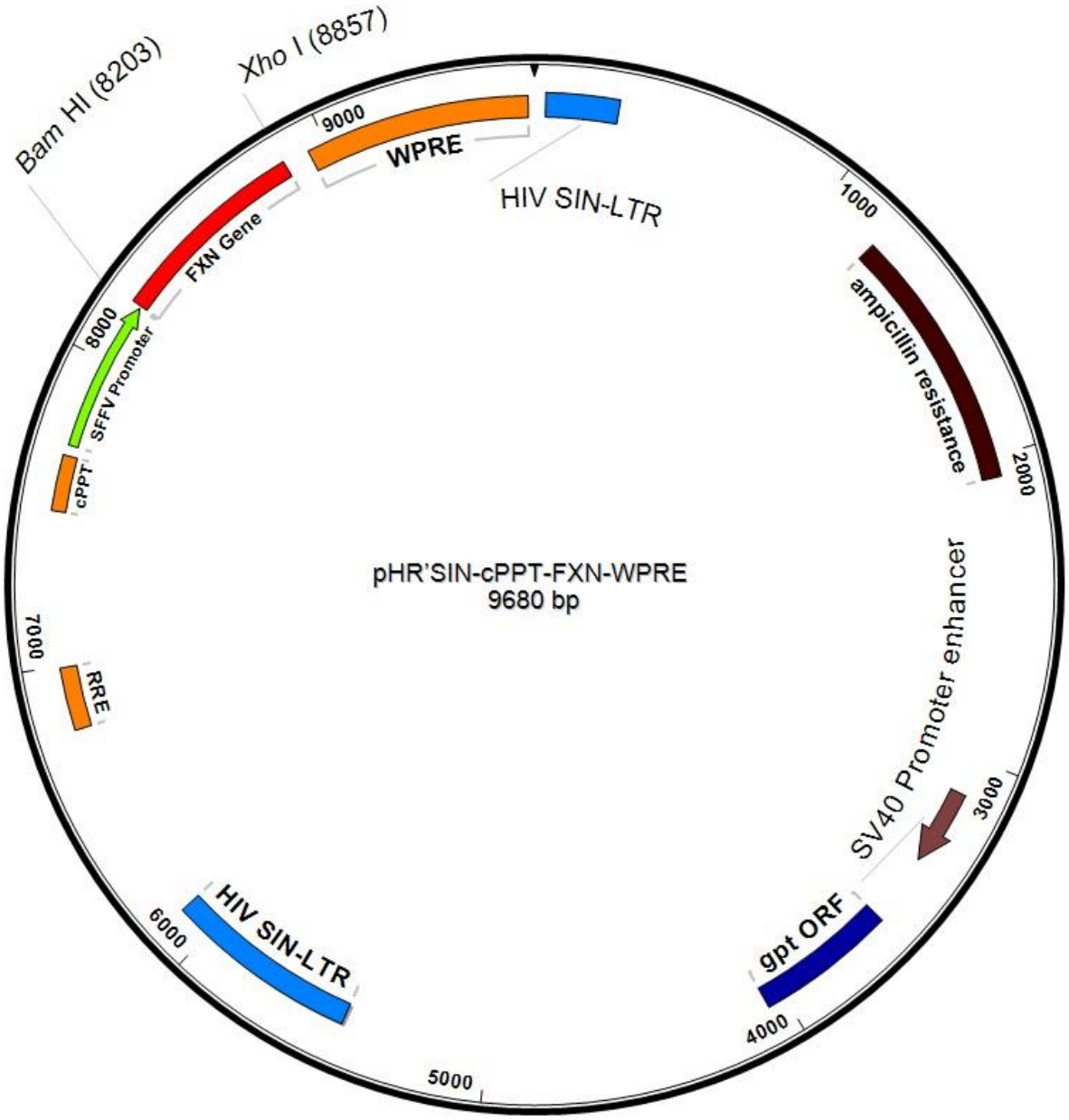

Figure 3.10: Schematic map of the pHR'SIN-cPPT-*FXN*-WPRE vector displaying unique cloning sites. LTR: Log terminal repeats. RRE: rev response element. cPPT central polypurine tract. SFFV promoter: spleen focus forming virus promoter. WPRE: Woodchuck hepatitis virus post-transcription regulatory element. Gpt ORF: Programmed Translational Frame shift.

3.3.5 Characterisation and mapping of the Env, Gag-pol and LV GFP vectors

Following LV *FXN* construction, other plasmids required for viral production including Env plasmid coding for VSV-G envelop (pMD2.G), Gag-pol plasmid coding for the capsid of the virus (pCMV-dR8.74) and the reporter vector construct (pHR'SIN-cPPT-SFFV-GFP-WPRE) LV GFP was characterized and mapped by restriction enzyme digest. The Env plasmid was linearized with *Hind*III and *Not*I restriction enzymes and a double digest of this plasmid with *Cla*I and *Sca*I restriction enzymes produced a 3953 bp and 1871 bp bands which have matched the sequence provided for this vector (Figure 3.11 and Figure 3.12).

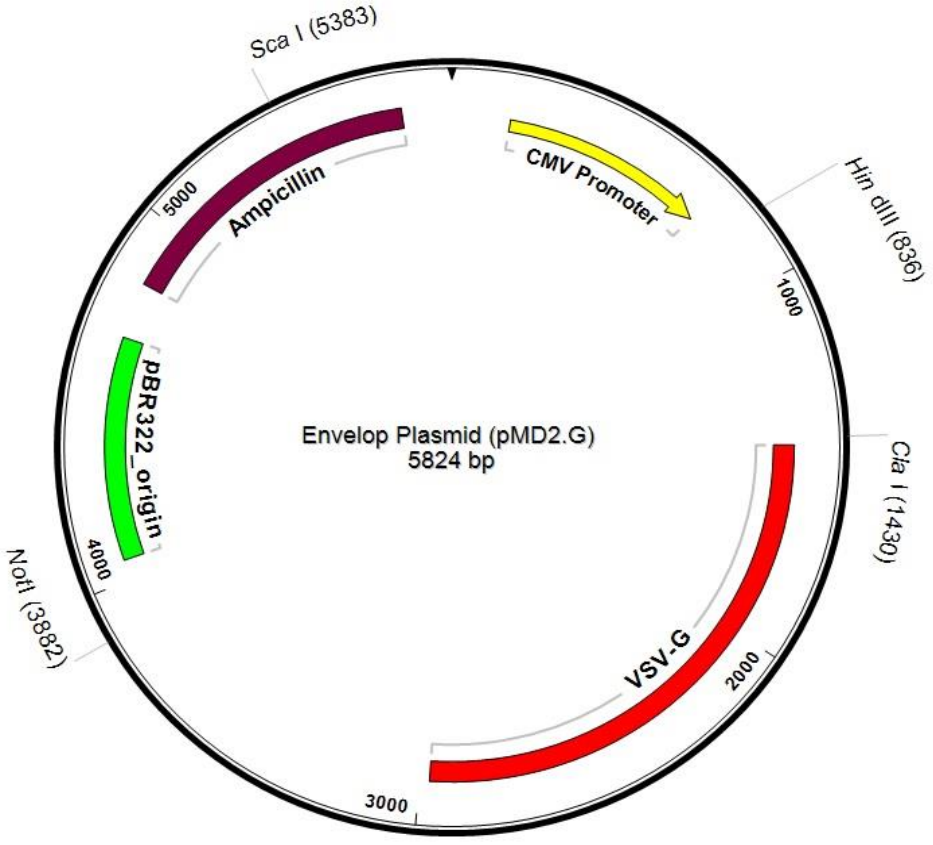

Figure 3.11: Schematic map of the 5824 bp Env plasmid coding for the VSV-G envelope. Unique sites used for the characterisation of the plasmid are shown.

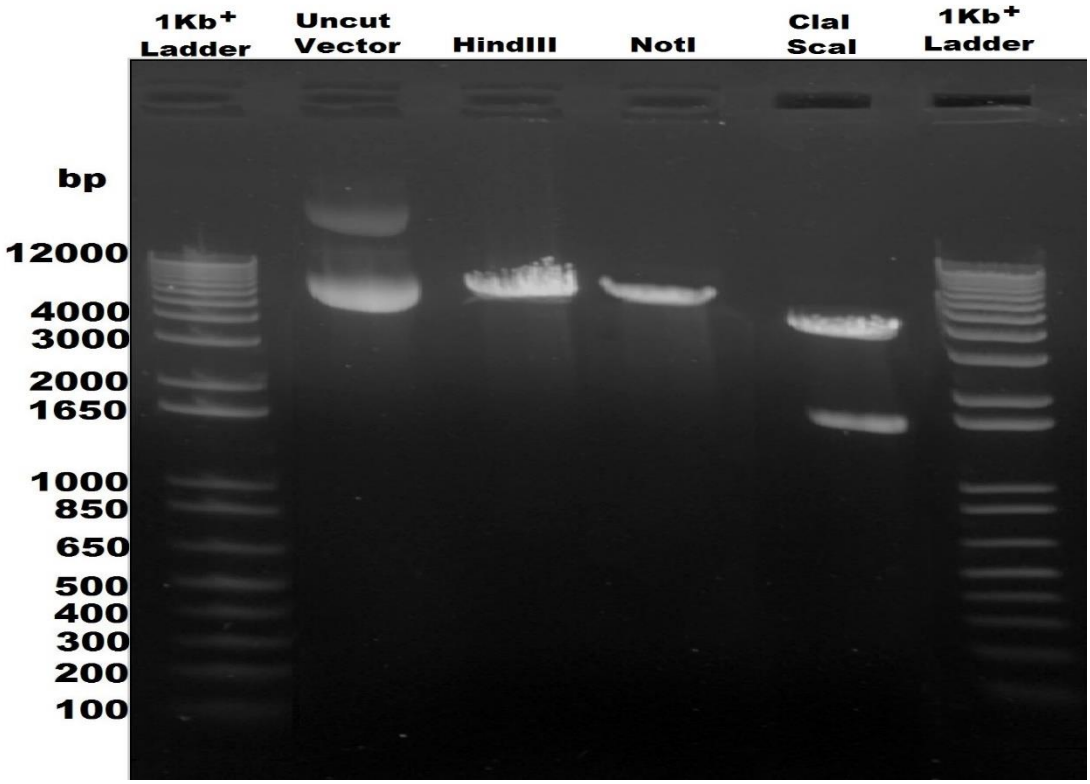

Figure 3.12: Characterisation of Env plasmid by restriction digest. Digestion with *Hind*III and *Not*I restriction enzymes has linearized the 5824 bp plasmid. A double digest with *Cla*I and *Sca*I produced 3953 bp and 1871 bp bands, which confirms the integrity of the plasmid. 1 Kb+ DNA ladder. DNA was loaded on 1% agarose gel and run at 70 mV.

The Gag-pol plasmid (pCMV-dR8.74) was mapped and characterised by restriction digestion. Digestion with *EcoR*I has linearized the vector, *Hind*III cuts the plasmid at 5 sites producing 4141 bp, 3674 bp, 2823 bp, 656 bp and 627 bp bands. The restriction digest with *Hinc*II cuts the plasmid at 4 sites producing 7522 bp, 2626 bp, 1750 bp, 23 bp bands. In addition *Pvu*II restriction enzyme cuts the plasmid at 4 sites producing 5498 bp, 3225bp, 2154 bp and 1044 bp bands. The integrity of the plasmid was verified by restriction digestion and was found to correlate with the sequence that was provided (Figure 3.13 and Figure 3.14).

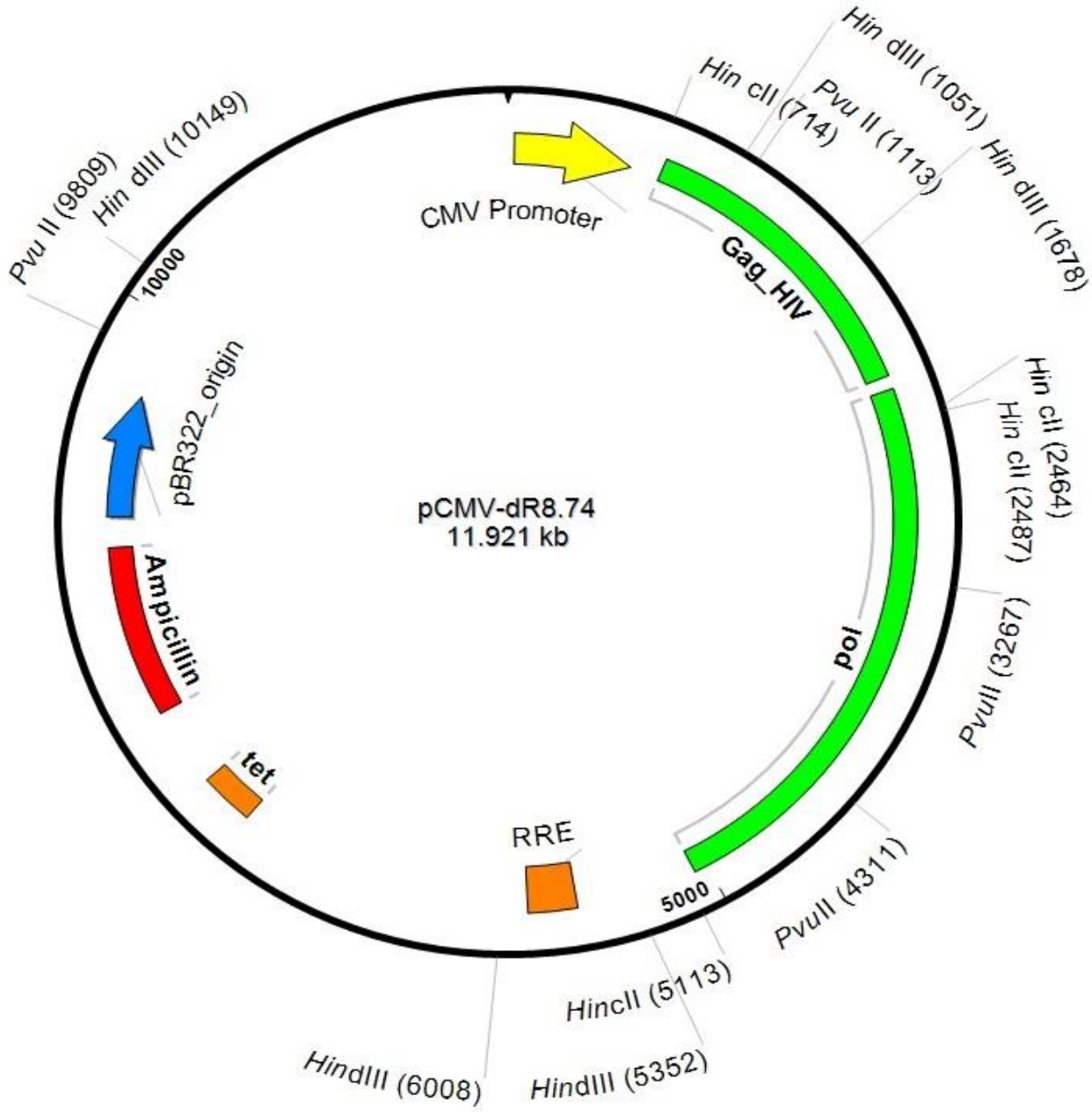

Figure 3.13: Schematic map of pCMV-dR8.74 plasmid. This 11.9 kb plasmid coding for the *gag-pol* gene was mapped and the restriction sites for characterization of the plasmid was identified. *Eco*RI with 1 site, *Hind*III with 5 sites, *Pvu*II with 4 sites and HincII with 4 sites were the restriction enzymes that were selected for the characterisation of the plasmid.

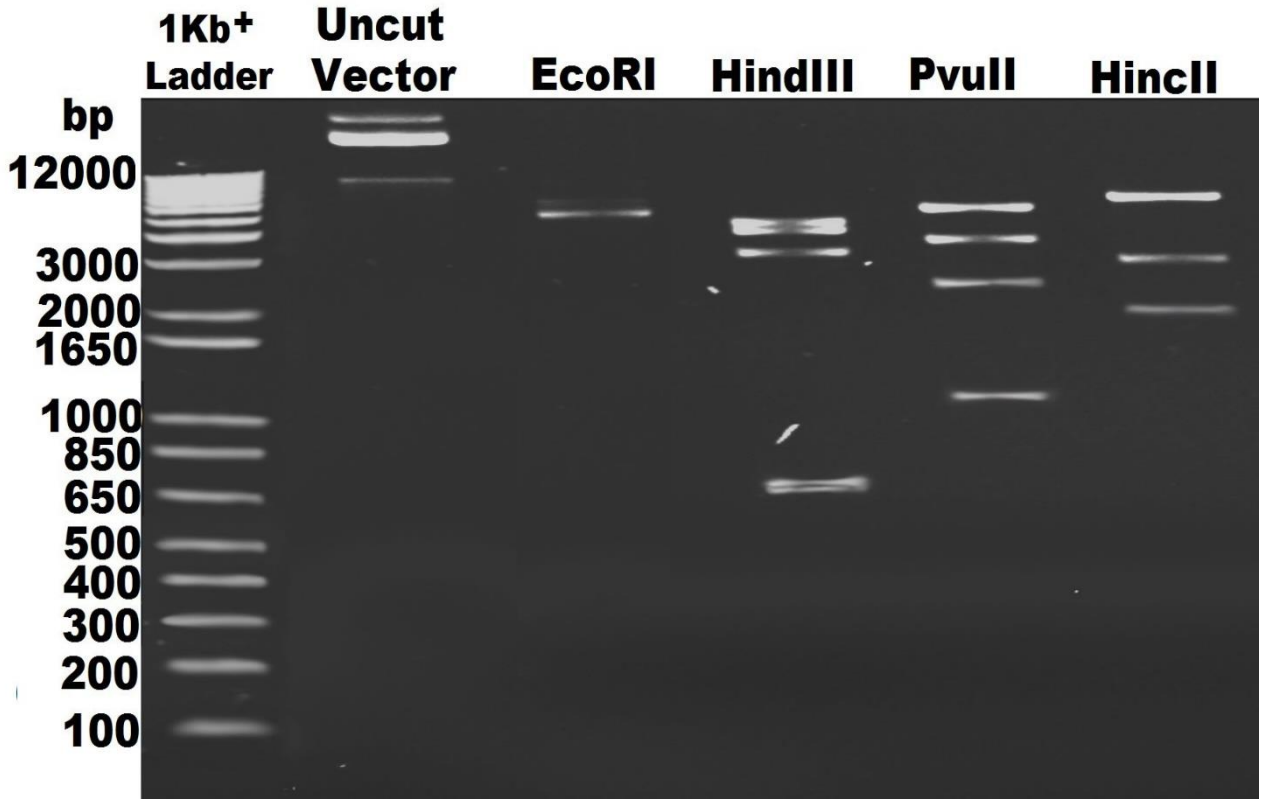

Figure 3.14: pCMV-dR8.74 vector was digested with *Eco*RI to give a linearized 11.9 kb band, *Hind*III with 5 sites produced 4141 bp, 3674 bp, 2823 bp, 656 bp and 627 bp bands, PvuII with 4 sites produced 5498bp, 3225bp, 2154bp, 1044bp bands. *Hinc*II with 4 sites produced 7522 bp, 2626 bp, 1750 bp, 23 bp bands. 1 Kb^+ DNA ladder**.** DNA was loaded on 1% agarose gel and run at 70 mV.

The 9662 bp LV GFP plasmid was also mapped and characterised with restriction digestion by digestion with *Bam*HI, *Xho*I, *Bsp*MI. Furthermore the 770 bp eGFP gene was released by double restriction digest with *Bam*HI and *Xho*I. The integrity of the plasmid was verified by restriction digestion and was found to correlate with the sequence that was provided (Figure 3.15 and Figure 3.16).

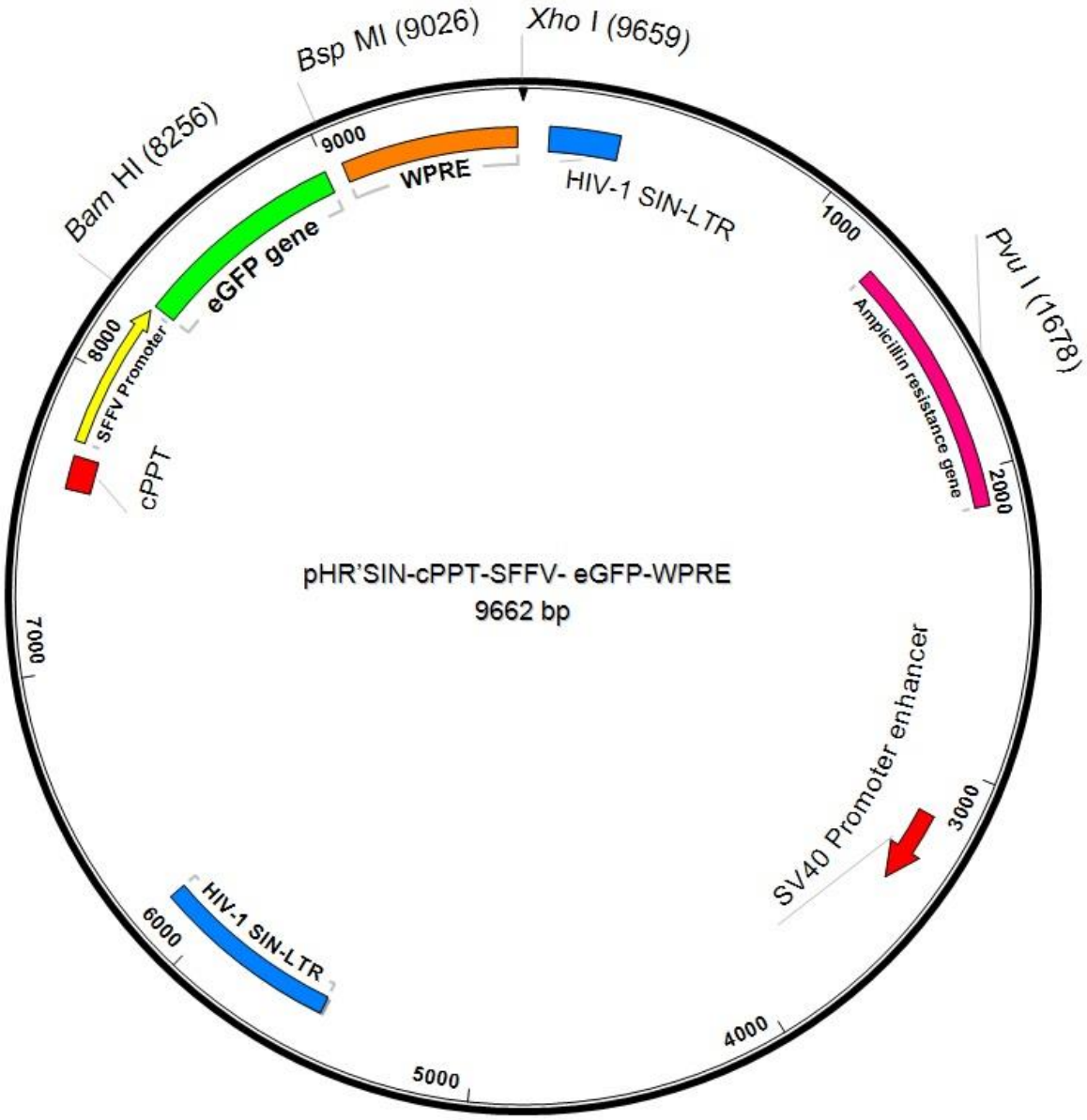

Figure 3.15: Schematic map of the LV GFP plasmid. The unique site on this 9662 bp plasmid was selected and was used to test the integrity and sequence of the plasmid. Restriction digest with *Bam*HI, *Bsp*MI, *Xho*I and *Pvu*I linearized the plasmid and produced a 9662 bp band. cPPT central polypurine tract. SFFV promoter: spleen focus forming virus promoter. WPRE: Woodchuck hepatitis virus post-transcription regulatory element.

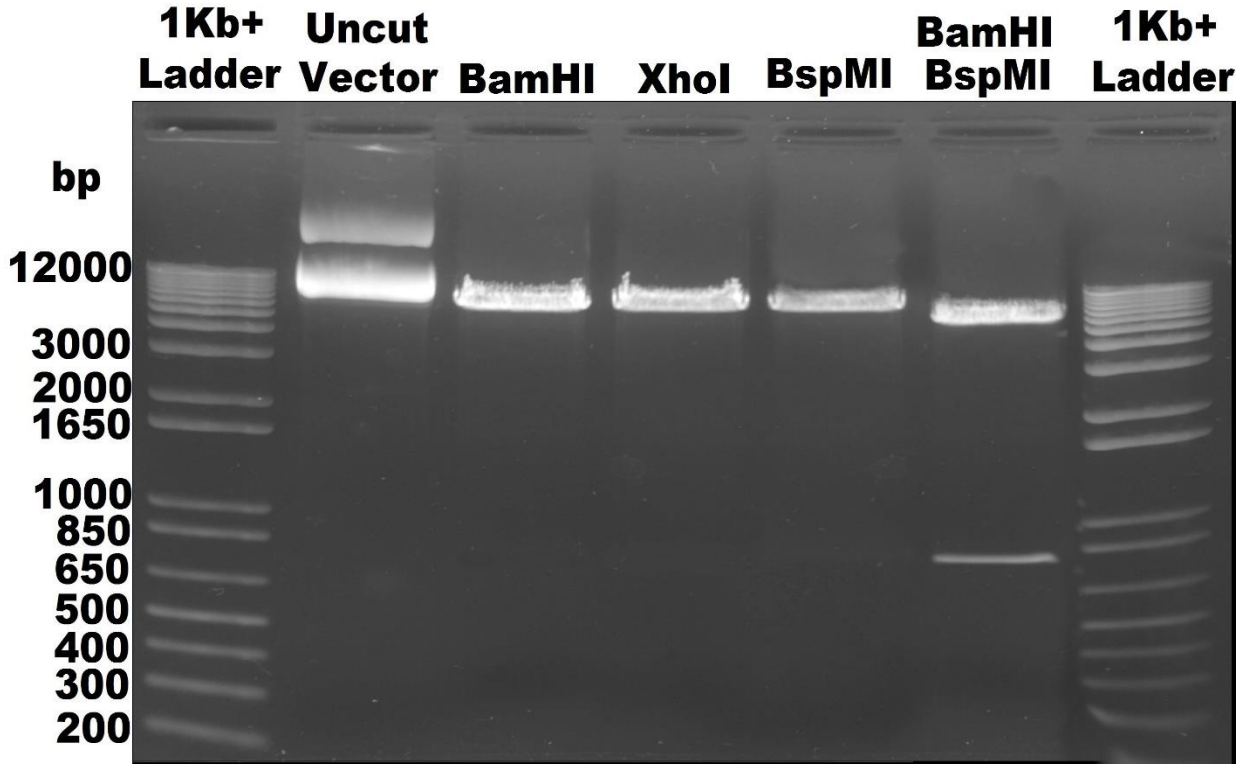

Figure 3.16: Restriction digest of the LV GFP vector. Restriction digest with *Bam*HI, *Xho*I and *Bsp*MI have linearized the 9662 bp plasmid. Additionally, a double digest with *Bam*HI and *Bsp*MI has released the 770 bp eGFP gene. This was matched with sequence of this plasmid. 1 Kb^+ DNA ladder. DNA was loaded on 1% agarose gel and run at 70 mV.

3.4 Evaluation of the function of the gene delivery vector

To begin this study, the functionality of the plasmid to be used to generate the lentivirus carrying *FXN* and GFP, required evaluation in a cell line that allows efficient transfection levels. Since HEK 293T cells allow highly efficient transfection and gene expression, these cells were transfected with the control LV GFP plasmid and the LV *FXN* plasmid. Once the protocol for the transfection was optimised, transfections using optimal conditions were performed to measure mRNA and protein levels of frataxin. For the optimisation of the PEI transfection protocol, the toxicity of the transfection agent PEI on HEK 293T cells was tested. In addition, the amount of DNA required to achieve the best level of transfection was determined.

3.4.1 Measurement of the toxicity of PEI

Firstly, the maximum amount of PEI that HEK 293T cells can tolerate was determined. Cells were exposed to between 5 µg to 25 µg of PEI for 4 hours and were examined 24 hours after exposure. As shown in Figure 3.17 cells exposed to 15 µg did not survive the treatment (D-F), cells exposed to 10 µg survived but showed negative changes in their morphology (C), cells exposed to 5 µg tolerated the treatment well (B) and are comparable to untreated cells (A). Thus, HEK 293T cells can tolerate a maximum of 10µg of PEI. However lower level of PEI (5µg) is used for the transfection of HEK 293T cells.

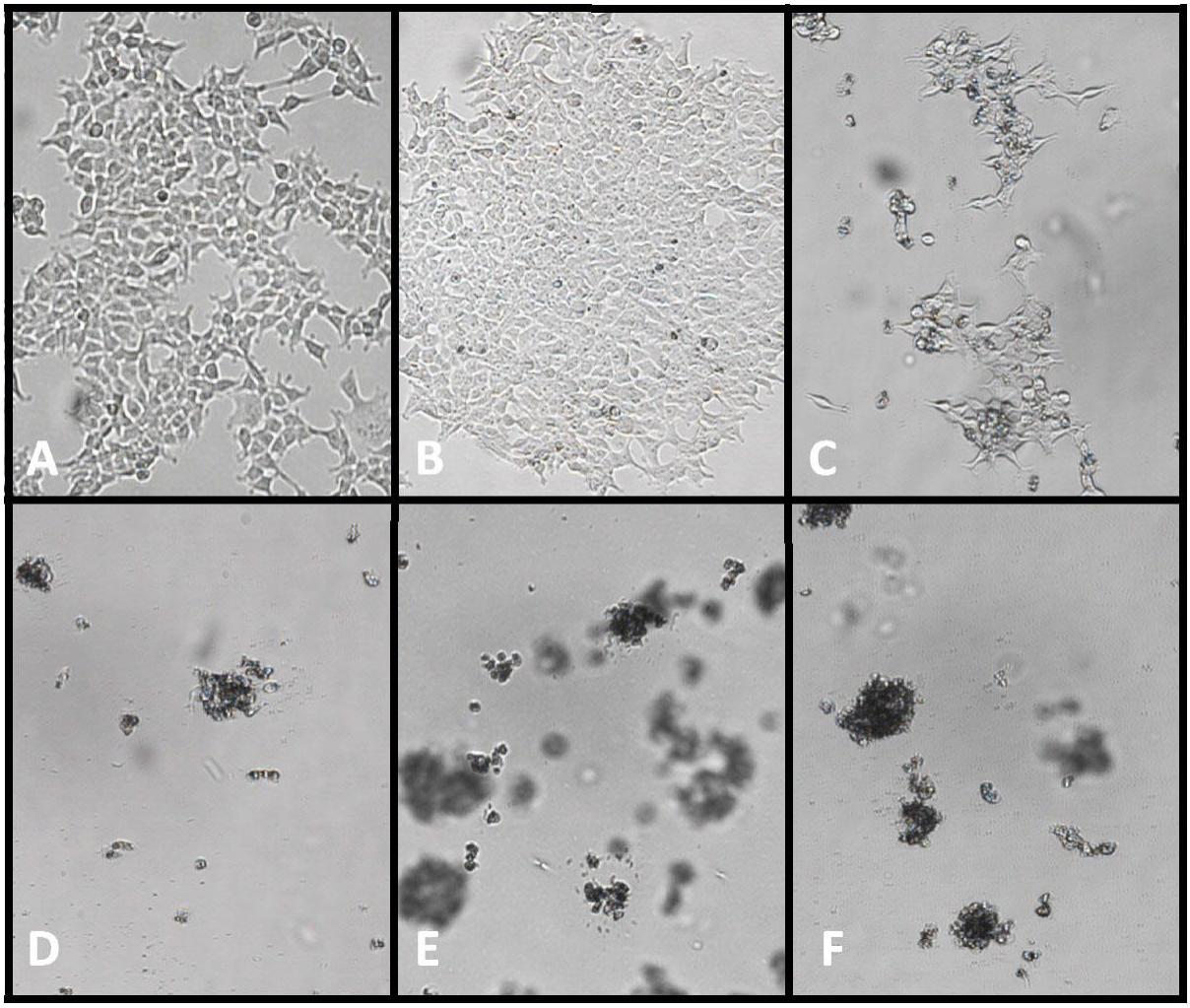

Figure 3.17: PEI toxicity test was performed on HEK 293T cells in a 6-well plate containing (A) 0 µg, (B) 5 µg, (C) 10 µg, (D) 15 µg, (E) 20 µg, (F) 25 µg. The PEI was removed after a 4 hour incubation and replaced by complete DMEM. Pictures were taken 24 hours after exposure under light microscopy with 10X magnification.

3.4.2 Determination of transfection efficiency using different amounts of DNA

HEK 293T cells were transfected using 5 µg PEI with different amounts of LV GFP vector ranging between 2 µg to 6 µg to determine the amount of DNA needed for an optimal transfection. Figure 3.18 shows pictures of untreated (A) and transfected cells (B-F).

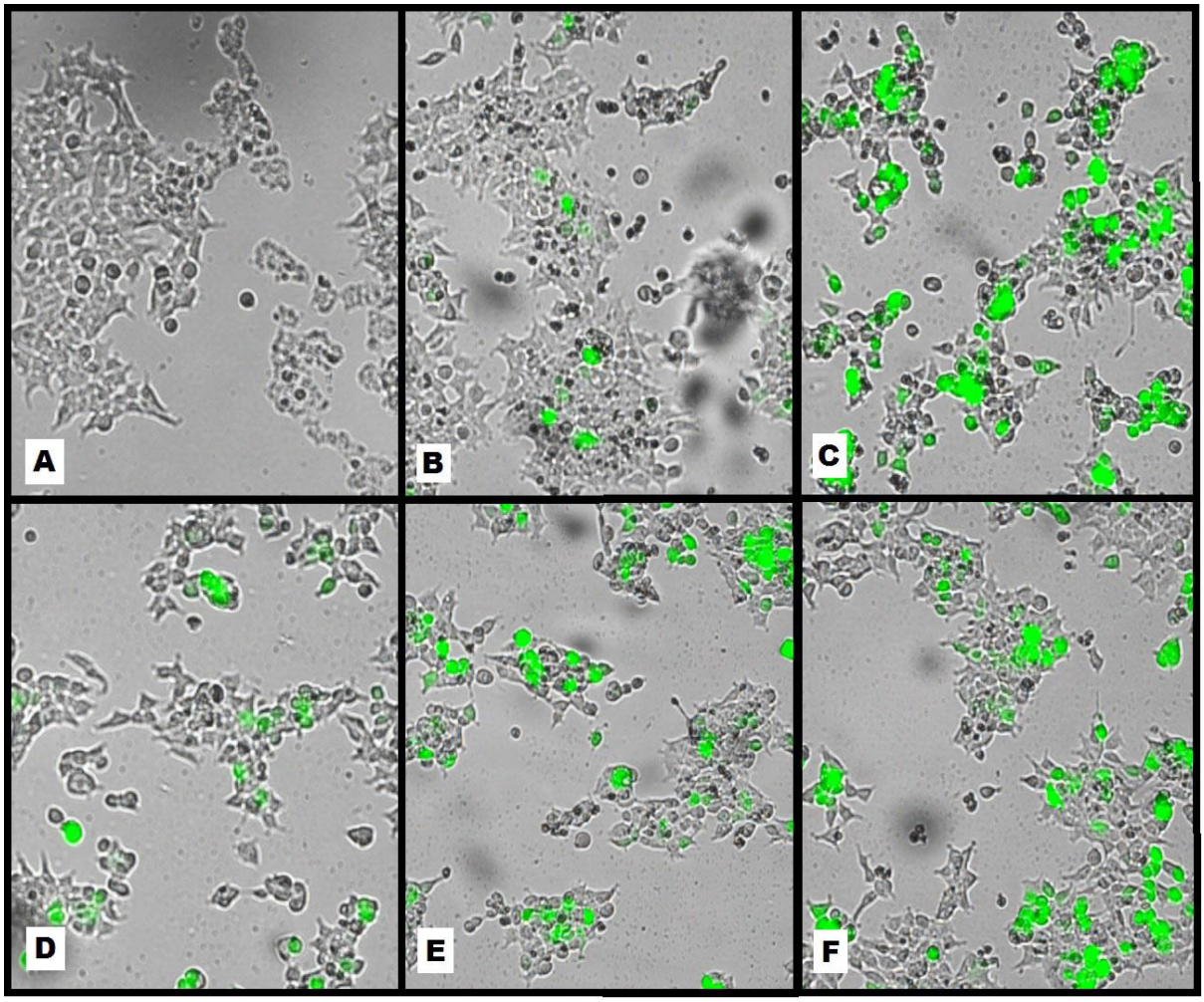

Figure 3.18: Determination of the optimal amount of DNA for PEI transfection transfected with 2 µg (B), 3 µg (C), 4 µg (D), 5 µg (E) or 6 µg (F) of LV GFP vector DNA. The transfection solution was replaced after 4 hours of incubation with complete DMEM and pictures were taken 24 hours after treatment using JuLI™ Smart Fluorescent Cell Analyser microscope with 10X magnification. Green cells represent GFP-expressing, and thus, transfected cells.

To determine the level of transfection, using image processing software, Image J (U. S. National Institutes of Health) acquired images were merged and the number of GFP-positive cells were analysed in a total of 100 cells. The mean of the three repeats was calculated, respectively, and is presented in Figure 3.19. A transfection rate of about 83% was reached using 3 µg of DNA, around 60% cells were transfected when 4-6 µg of DNA were used, and only around 24% when 2 µg DNA were used. Thus, the highest level of transfection was achieved using 3 µg of DNA. Hence, the best ratio of PEI:DNA to carry out transfection was 2:1. This ratio was used for all further transfections carried out in this project.

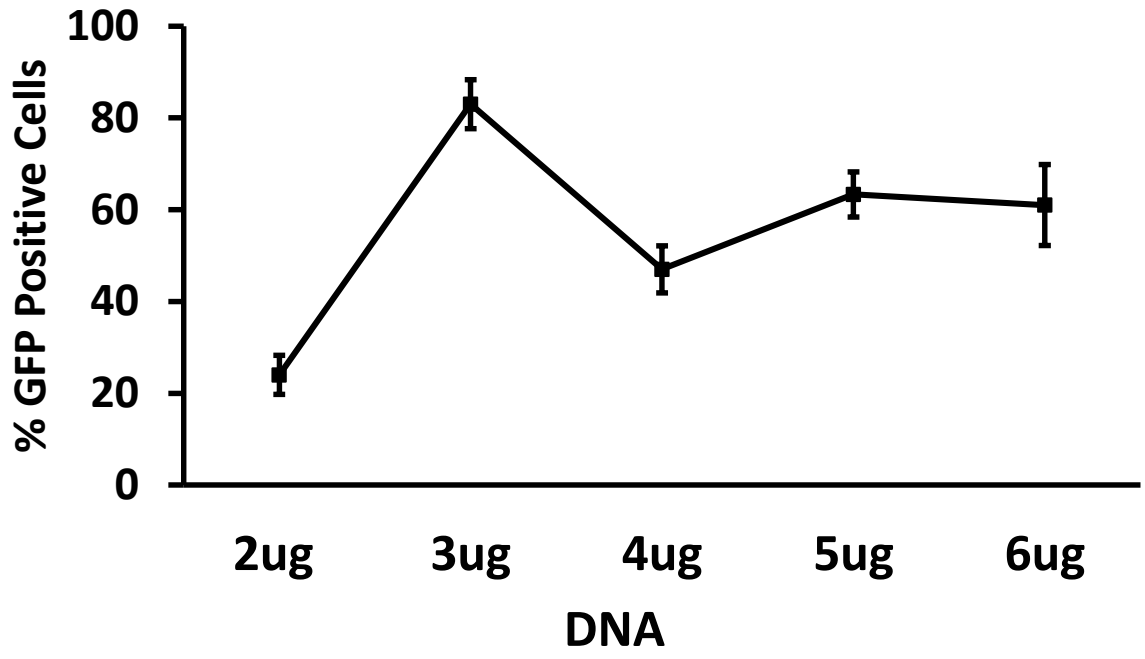

Figure 3.19: Transfection rate of PEI transfection with LV GFP vector into HEK 293T cells. The percentage of GFP positive cells is presented in accordance to the DNA amount used. Each data set represents the mean of three counting repeats of 100 cells. Error bars mean SEM. The highest percentage of GFP-positive cells was observed when 3 µg of DNA was used. This result established an optimum ratio of PEI: DNA (2:1) for all further transfection experiments.

3.4.3 Measurement of *FXN* mRNA expression following transfection of HEK 293T cells with LV *FXN*

Using Real-time PCR (RT-PCR) (Chapter 2, section 2.2.30) the levels of *FXN* mRNA expression was measured following the transfection of HEK 293T cells by LV *FXN* and LV GFP plasmid. The RNA was isolated as described in Chapter 2, section 2.2.25 (Figure 3.20A), then DNaseI treated (Chapter 2, section 2.2.26) to remove any residual plasmid DNA that may have been carried over from transient transfection (Thermo Scientific) (Figure 3.20B) and then converted to cDNA (Chapter 2, section 2.2.27). The data revealed that the levels of *FXN* mRNA expression slightly decreased to 95% compared to untreated HEK 293T cells (100%). However, the data showed no significant difference with *P* value of 0.3, when transfected with LV *FXN,* the levels of FXN mRNA expression increased by 24% compared to untreated cells, the statistical significance of the differences was evaluated by two-way ANOVA and all values were significant with $P \leq 0.05$ (Figure 3.21).

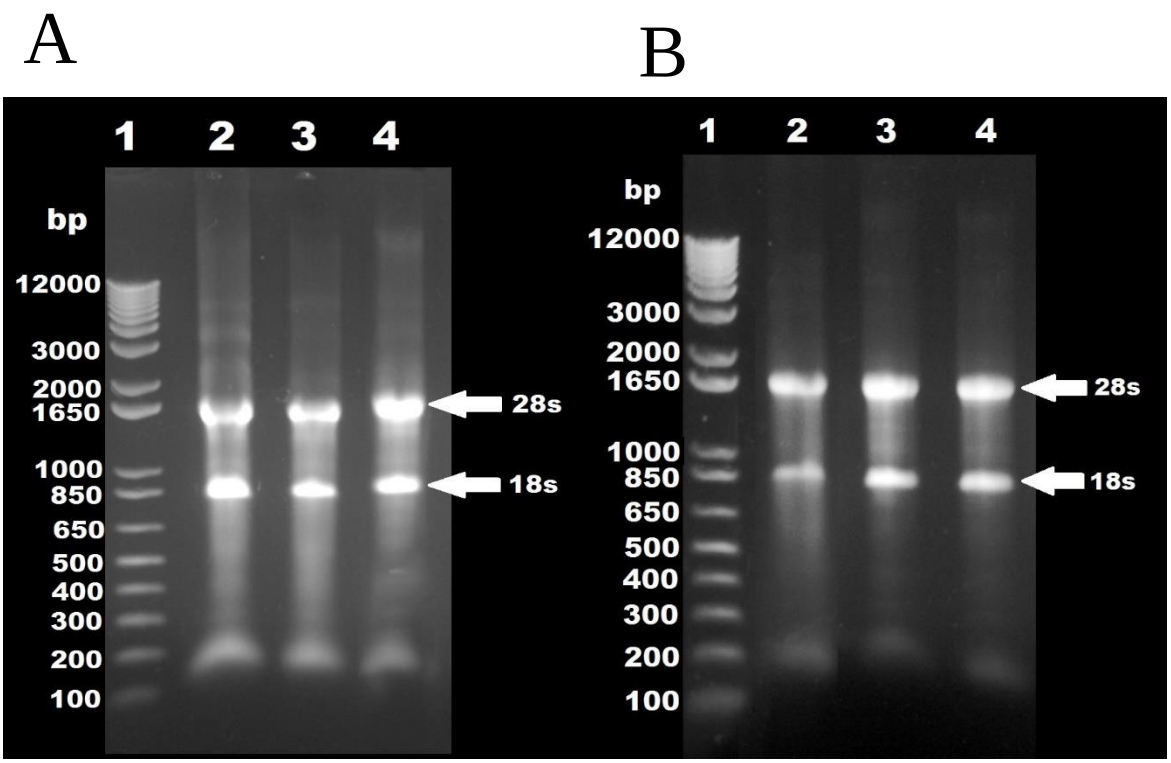

Figure 3.20: Gel electrophoresis of the RNA samples using 1% agarose gel. **A)** RNA samples were extracted 24 hours after transfection with LV GFP and LV FXN. Lane 1: 1Kb$^+$ DNA ladder, Lane 2: Untreated HEK 293T, Lane 3: HEK 293T transfected with LV GFP, Lane 4: HEK 293T transfected with LV FXN. **B)** RNA samples treated with DNaseI to remove any transit DNA. Lane 1: 1Kb$^+$ DNA ladder, Lane 2: Untreated HEK 293T, Lane 3: HEK 293T transfected with LV GFP, Lane 4: HEK 293T transfected with LV FXN. Sharp, distinct bands corresponding to 28S (upper bands) and 18S (lower bands) ribosomal RNA indicate intact RNA.

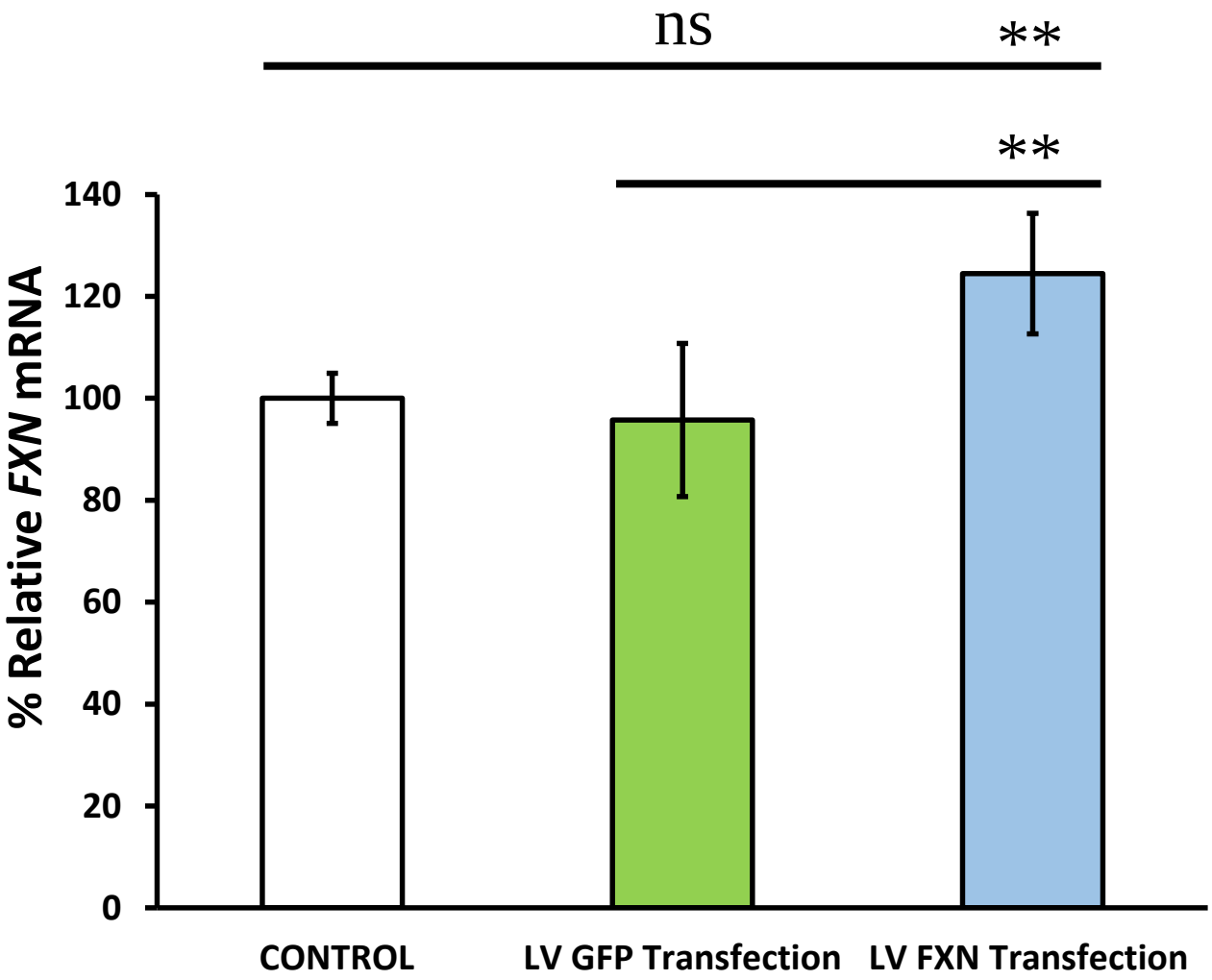

Figure 3.21: *FXN* mRNA expression by qRT-PCR in HEK 293T cells after transfection with LV *FXN* and LV GFP vectors. LV GFP transfected HEK 293T showed 95% expression compared to 100% in untreated cells. HEK 293T cells transfected with LV *FXN* showed a 24% increase compared to untreated cells. Statistical differences between the control and transfected cell lines are indicated by the top line drawn over the bars while the bottom line indicates the differences LV FXN transfection and LV GFP transfection. Error bars indicate SEM and values represent mean ± SEM. Asterisks indicate significant differences between the treated samples and control (ns= P >0.05 and ** P <0.01).

3.4.4 Measurement of *FXN* protein expression following transfection of HEK 293T cells with LV *FXN*

Frataxin protein expression was measured after the transfection of HEK 293T cells with LV FXN and LV GFP backbone vectors. Total protein was extracted as described in Chapter 2, section 2.2.31 and the concentration was measured using a Pierce™ BCA Protein Assay Kit (Thermo Scientific) (Chapter 2, section 2.2.32). Subsequently the protein samples were subjected to frataxin protein quantity dipstick assay kit (MitoSciences) (Chapter 2, section 2.2.33) and the levels of *FXN* protein expression was determined. LV GFP transfection of HEK 293T cells showed insignificant (*P* value <0.3) decrease with 97% *FXN* protein expression compared to untreated HEK 293T 100%. Interestingly, the levels of *FXN* expression had increased by 3.9 fold (392%) (*P* value <0.0001) when compared to untreated HEK 293T cells. HEK 293T cells transfected with LV GFP transfection did not show a significant difference compared to untreated HEK293T cells with a *P* value of 0.5. Statistical significance of the differences was evaluated by two-way ANOVA. (Figure 3.22 and Figure 3.23). This may suggest even with low levels of *FXN* mRNA expression, high levels of protein expression can be reached following overexpression of frataxin.

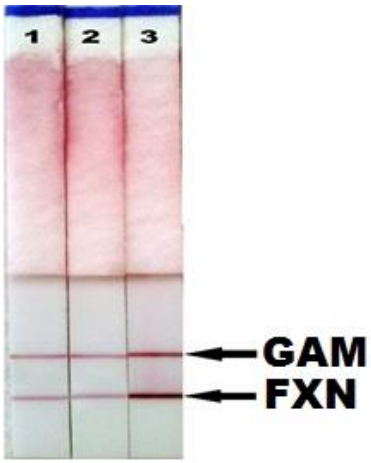

Figure 3.22: Quantification of human *FXN* using dipstick immunoassay. Upper bands correspond to internal control (goat anti-mouse antibody (GAM)); lower bands correspond to human frataxin (*FXN*). 1) Untreated control. 2) LV GFP transfection. 3) LV FXN transfection.

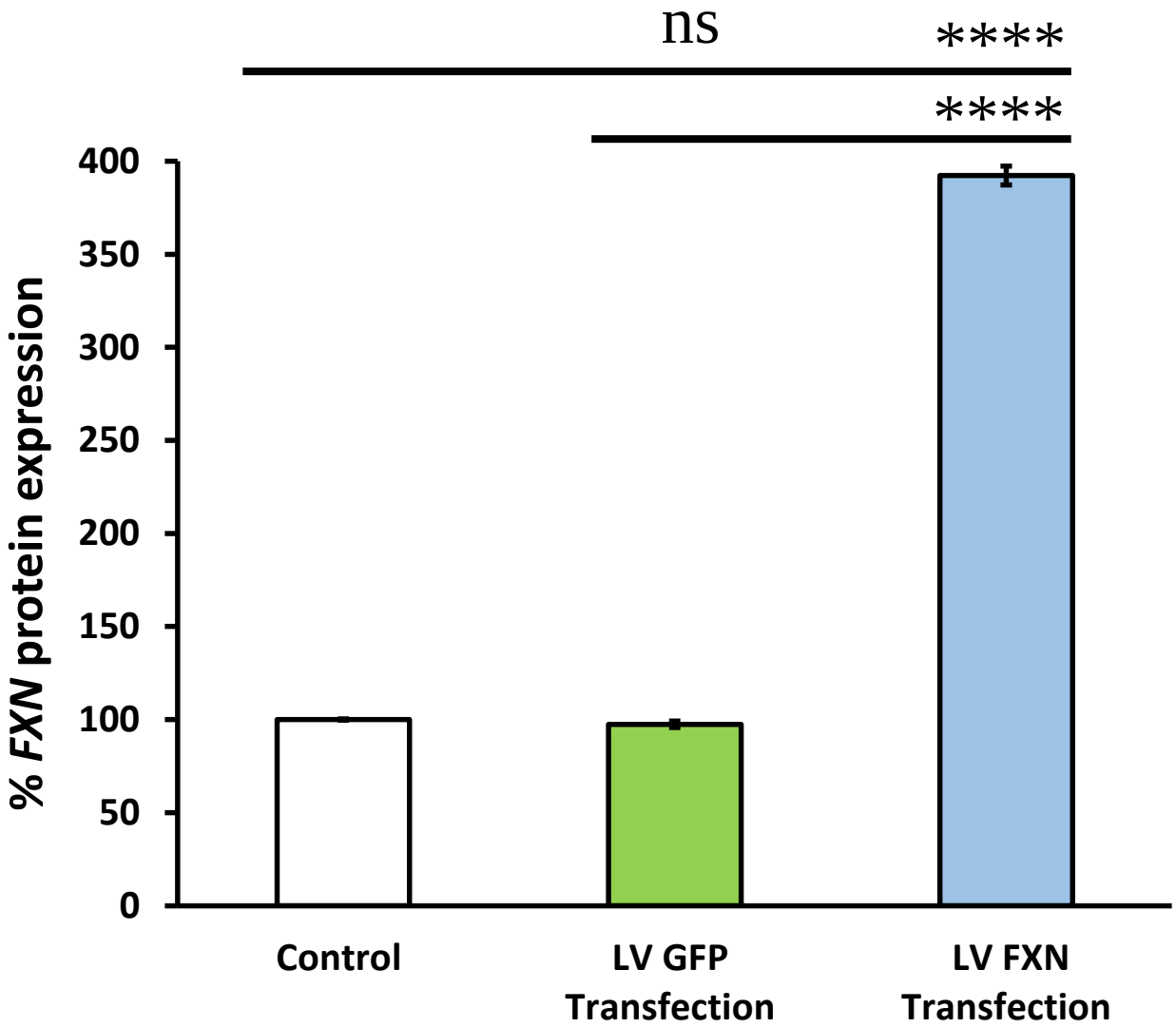

Figure 3.23: HEK 293T *FXN* protein expression following the transfection with LV GFP and LV *FXN* backbone vectors. The levels of *FXN* protein slightly decreased to 97% when transfected with LV GFP but this result was not significant. The LV *FXN* transfection showed an increase in FXN protein expression to 392% compared to control HEK 293T cells 100%. Statistical differences between the control and transfected cell lines are indicated by the top line drawn over the bars while the bottom line indicates the differences LV GFP transfection and LV FXN transfection. Statistical differences between LV FXN treatment and normal control (HEK293T) are indicated by the top line drawn over the bars while the bottom line indicates the differences between LV FXN transfection and LV GFP transfection. Error bars indicate SEM and values represent mean ± SEM. Asterisks indicate significant differences between the treated cells and HEK 293T control (ns=*P* >0.05 and ****P <0.0001).

3.5 Lentiviral production and titration of VSV-G pseudotyped particles carrying the *FXN* and GFP gene.

Once the plasmid expression as well as functionality and delivery of *FXN* sequence had been verified, the constructed vector along with gag-pol plasmid and VSV-G plasmid were transfected into the producer cell line HEK 293T, using PEI as a transfection reagent. The VSV-G pseudotyped particles were generated as described in Chapter 2, section 2.2.18. The lentivirus carrying reporter gene GFP (LV GFP) was produced in parallel to the lentivirus carrying *FXN* gene (LV *FXN*). This allowed to estimate the transfection efficiency by counting the green GFP-expressing cells and served as a control for infection of the FRDA cell lines. LV GFP was also used to measure the infectious unit (IFU) to estimate the viral titer. Viral particles harvested 48 and 72 hours post transfection were collected and further concentrated using ultracentrifugation (Beckman Coulter). The titer of the concentrated virus was estimated using Lenti-X qRT-PCR Titration Kit (Clone tech) (Chapter 2, section 2.2.20). The kit employs a quick RNA purification step and determines viral RNA genome content using qRT-PCR using SYBR® technologies. The RNA genome copy number in a sample dilution is determined by finding the copy number that corresponds to its Ct value on a standard curve generated from serial dilutions of the calibrated Lenti-X RNA Control Template provided in the kit. The viral copy number of the LV GFP and LV *FXN* was the average of three independent experiments performed in triplicate and estimated to be $7x10^9$ copies/ml (Figure 3.24). Since the titre of both viral particles were the same it confirmed the fact that LV GFP will give an indication of the infectivity of the LV *FXN*, hence both viruses were used in parallel in all experiments to confirm the delivery of *FXN* and the reliability of the method. In

addition, the use of the LV GFP helped to understand the toxicity of viral delivery without the presence of the frataxin.

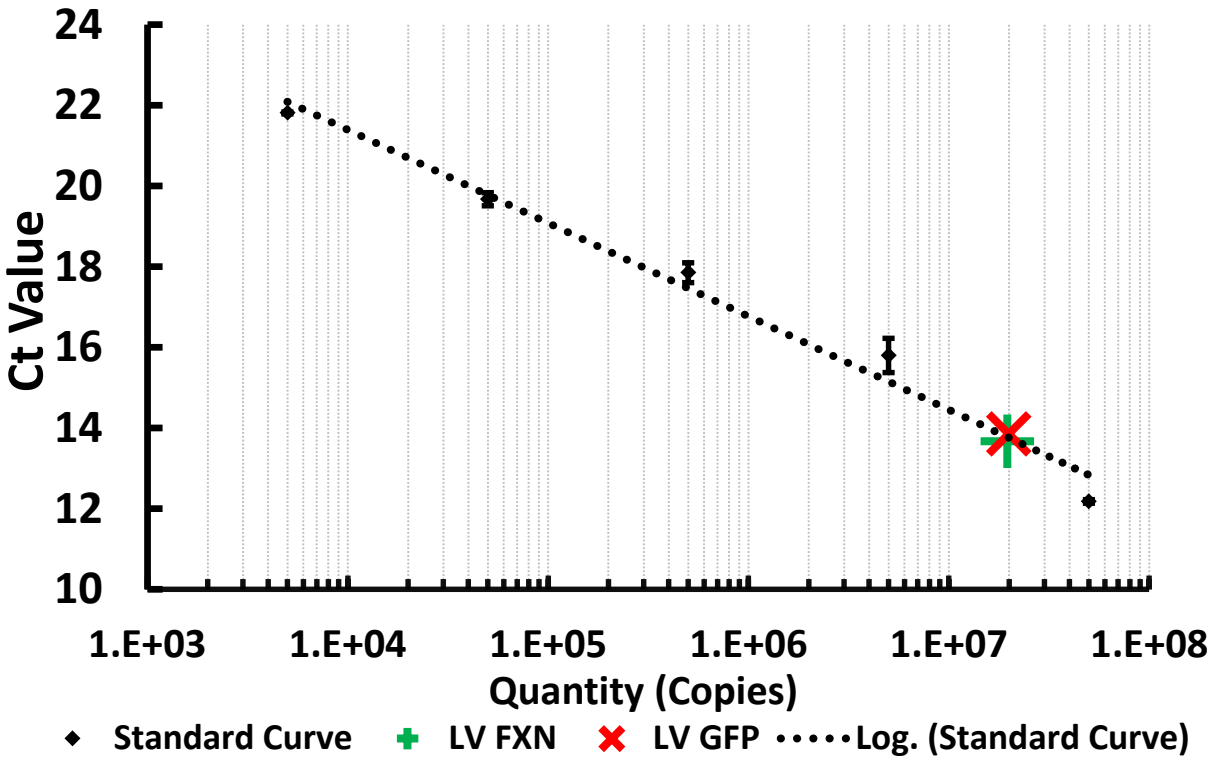

Figure 3.24: Viral RNA titration of LV GFP and LV *FXN* using the Lenti-X qRT-PCR titration Kit. A standard curve created from Ct values generated by Lenti-X RNA Control Template demonstrating a strong linear correlation between the Ct values and the RNA copy numbers (log scale). RNA copy number of LV GFP and LV *FXN* was established by using the Ct values against the standard curve ($7X10^9$). Each point on standard curve represents the average of three repeats in one experiment. Error bars indicate SEM.

3.5.1 Correlating RNA titer with infectivity

The first time the qRT-PCR titration was performed, the IFU value was also determined by an independent means (e.g. via imaging flow cytometry) in order to establish a relationship between the two values. A ratio between different titrations was

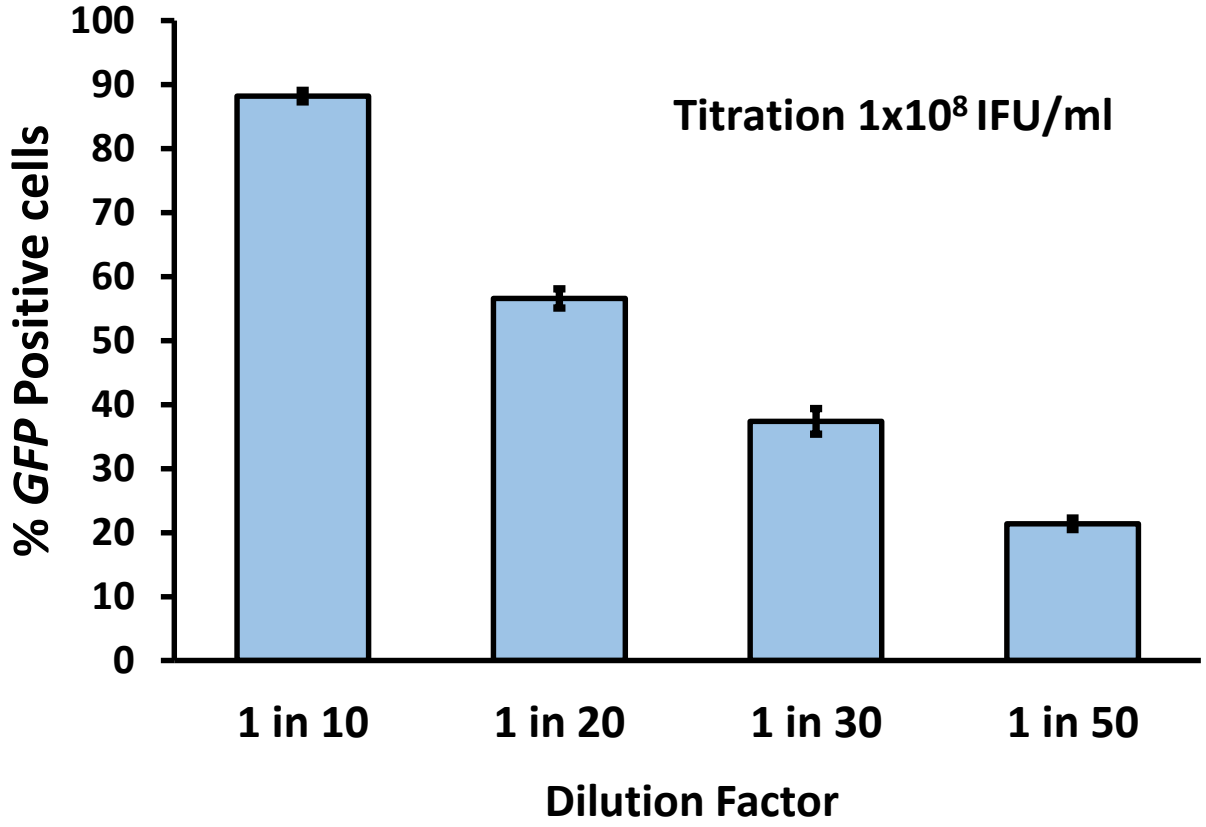

Figure 3.25: Viral titration using Imagestream^X. The percentage of GFP-positive HEK 293T cells was measured to estimate the IFU/ml. The number of the positive cells decreases as the virus gets diluted. Each column represents the average of five independent experiments where n≃20000. Error bars indicate SEM.

established and used for subsequent, similarly prepared virus supernatants. To determine infectivity titer, HEK 293T cells were infected with same stock of LV GFP that was used for qRT-PCR titration. Cells were infected with serially diluted LV GFP, then harvested 48 hours post infection and analysed using Imagestream^X. The viral titre was then calculated as described in Chapter 2, section 2.2.19. Figure 3.25 shows the percentage of transduced HEK 293T by LV GFP. The number of GFP-positive cells decline as the virus dilution increases. The calculated titration for this batch of virus was 1X10^8 IFU/ml. RT:Imagestream^X ratio (copies/IFU), or infectivity coefficient was calculated by dividing the qRT-PCR copies/ml by the IFU/ml value from

Imagestream^X titration. In this experiment the values were divided ($7X10^9/1X10^8$) and the ratio assessed to be 70. This coefficient was then used to calculate the IFU/ml for subsequent qRT-PCR titration results (Table 3.4).

qRT-PCR (copies/ml)	Imagestream^X (IFU/ml)	Titration Ratio (copies/IFU)
7.00E+09	1.00E+08	70

Table 3.4: Representative ratio between different titration values measured by qRT-PCR and Imagestream^X to establish an infectivity coefficient (70).

CHAPTER 4 - *IN VITRO* GENE DELIVERY AND PHENOTYPE CORRECTIONS

4.1 Aims

- To deliver high titre virus carrying GFP and frataxin to FRDA fibroblasts.
- To assess gene delivery and measure *FXN* gene expression pre-translationally and post-translationally.
- To evaluate toxicity and safety of the gene therapy.
- To investigate correction of disease-associated phenotype.

4.2 Introduction

Extensive studies on HIV based lentiviral vectors have evolved them into safer and more effective vectors. Lentiviral vectors offer several attractive properties as gene delivery tools including:

(i) Permanent gene delivery through stable vector integration into host genome (Mitrophanous *et al.*, 1999).

(ii) Potentially safer integration site profile (Montini *et al.*, 2009).

(iii) Ability to infect both dividing and non-dividing cells (Banasik and McCray, 2010).

(iv) Capability of self-inactivation and no expression of viral proteins after vector transduction.

(v) Broad tissue tropisms, including important gene- and cell-therapy target cell types (Themis *et al.*, 2005).

Accordingly, lentivector technologies now have widespread use in basic biology and translational studies for stable transgene overexpression. With the availability of a safer and advanced vector in our laboratory, we intend to permanently deliver *FXN*

gene into human and mouse FRDA primary fibroblasts for the correction of Friedreich ataxia.

4.2.1 Decreased aconitase activity and mitochondrial respiratory chain function in FRDA disease

Aconitase is a Krebs-cycle enzyme that converts citrate to isocitrate, and belongs to the family of iron-sulfur containing dehydratases whose activities depend on an intact cubane $[4Fe\text{-}4S]^{2+}$ cluster (Gardner, 2002, Beinert *et al.*, 1996). Loss of mitochondrial aconitase activity is an intracellular indicator of superoxide generation and oxidative damage in FRDA and also of ageing (Schapira, 1999, Yan *et al.*, 1997).

In many degenerative disorders the link between elevated levels of pro-oxidants and declines in mitochondrial aconitase activity have been established. Deficiency in the frataxin protein results in diminished activity of various mitochondrial iron-sulfur proteins including aconitase. Previous studies of FRDA patient and mouse model tissues have demonstrated impaired activity of the aconitase enzyme and mitochondrial respiratory chain (MRC) complexes I, II, and III (Bradley *et al.*, 2000). Aconitase activity is altered in patients' heart biopsies (Rotig et al. 1997), in the mouse models YG8R (Al-Mahdawi et al. 2006) and in conditional knock-out mice (Puccio et al. 2001). This evidence suggest that recovery of the aconitase activity may indicate the correction of the FRDA phenotype following *FXN* delivery.

In this chapter, each LV expressing the GFP reporter and the *FXN* genes will be used to infect human FRDA primary fibroblasts and mouse primary fibroblasts cells derived from our FRDA mouse model (YG8sR). We also assess how efficiently and safely these cells are transduced by LVs and measure the levels of *FXN* gene expression

reached following infection by each vector. In addition, we intend to examine these treated cell lines for any disease related phenotypes.

4.3 Determination of the MOI for the transduction of the FRDA fibroblasts

When transducing a lentivirus into a cell line for the first time, a range of MOIs should be tested. To accomplish this, $5x10^4$ human FRDA primary fibroblasts (GMO3665) and mouse FRDA primary fibroblasts (YG8sR) that were growing exponentially were seeded into a 6 well plate and transduced with LV GFP at MOIs of 1, 5, 10, 15 and 20. Transduced cells were counted for viability using trypan blue (Sigma) Chapter 2, section 2.2.5 and then number of the GFP-positive cells were measured using Imaging flow cytometry Imagestream^X as described in Chapter 2, section 2.2.21.

When human FRDA fibroblast cells were transduced at MOIs of 1 and 5, only 4% and 23% of the cells were expressing GFP, respectively, with no significant cell death (98% and 98%) compared to untreated control cells. Transduction at a MOI of 10 produced 87% GFP-positive cells and no significant cell death was observed (98%) compared to the untreated control cells. 84% of the cells were expressing GFP when transduced with MOI of 15. However, only 51% of the cells survived compared to the untreated control. Transduction with a MOI of 20 was too toxic to the human primary fibroblasts and no cells survived to measure for the GFP expression (Figure 4.1). In mouse FRDA primary fibroblasts 5% of the cells were GFP-positive when transduced at a MOI of 1 with a cell viability of 99% compared to untreated FRDA cells. In cells infected at a MOI of 5, 30% positive for the expression of GFP and at a MOI of 10, 90% were GFP-positive cells and there was no cell death 99% and 99% respectively, compared to the untreated control cells. When using a MOI of 15 and 20, the number of GFP-positive cells were slightly reduced to 88% and 89% and with 64% and 45% cells surviving,

respectively, compared to the untreated cells (Figure 4.2). These data suggests that a MOI of 10 achieved the highest infection rate and the lowest cell toxicity in both human and mouse FRDA fibroblasts and this MOI was used throughout the experiments to infect the cells in this project.

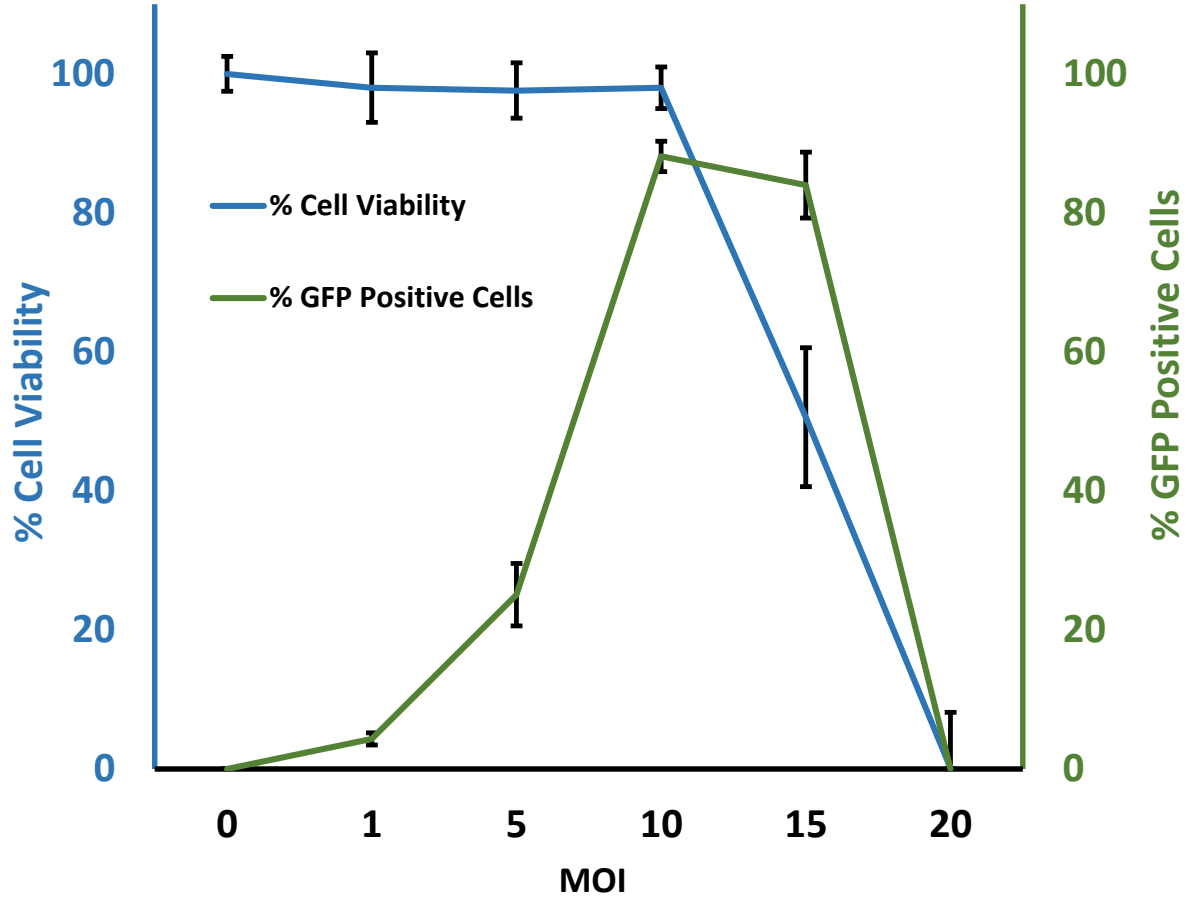

Figure 4.1: A graph showing the transduction of human FRDA fibroblasts (GMO3665) with a range of MOI. 98% of the cells survived compared to untreated cells when using MOIs of 1 and 5 but only 5% and 25% of the cells were expressing GFP respectively. The highest percentage of infection with the least amount of cell death was observed at a MOI of 10 with 87% of the cells positive for GFP and 98% cell survival compared to untreated cells. At a MOI of 15, 84% of cells were GFP-positive but only 51% of the cells survived compared to untreated cells. An MOI of 20 was very toxic to the cells and no cells survived this level of infection. For each point of measurement on the graph the values represent an average of three independent experiments where n=12000. Error bars indicate SEM. All data shown are significant with P <0.05.

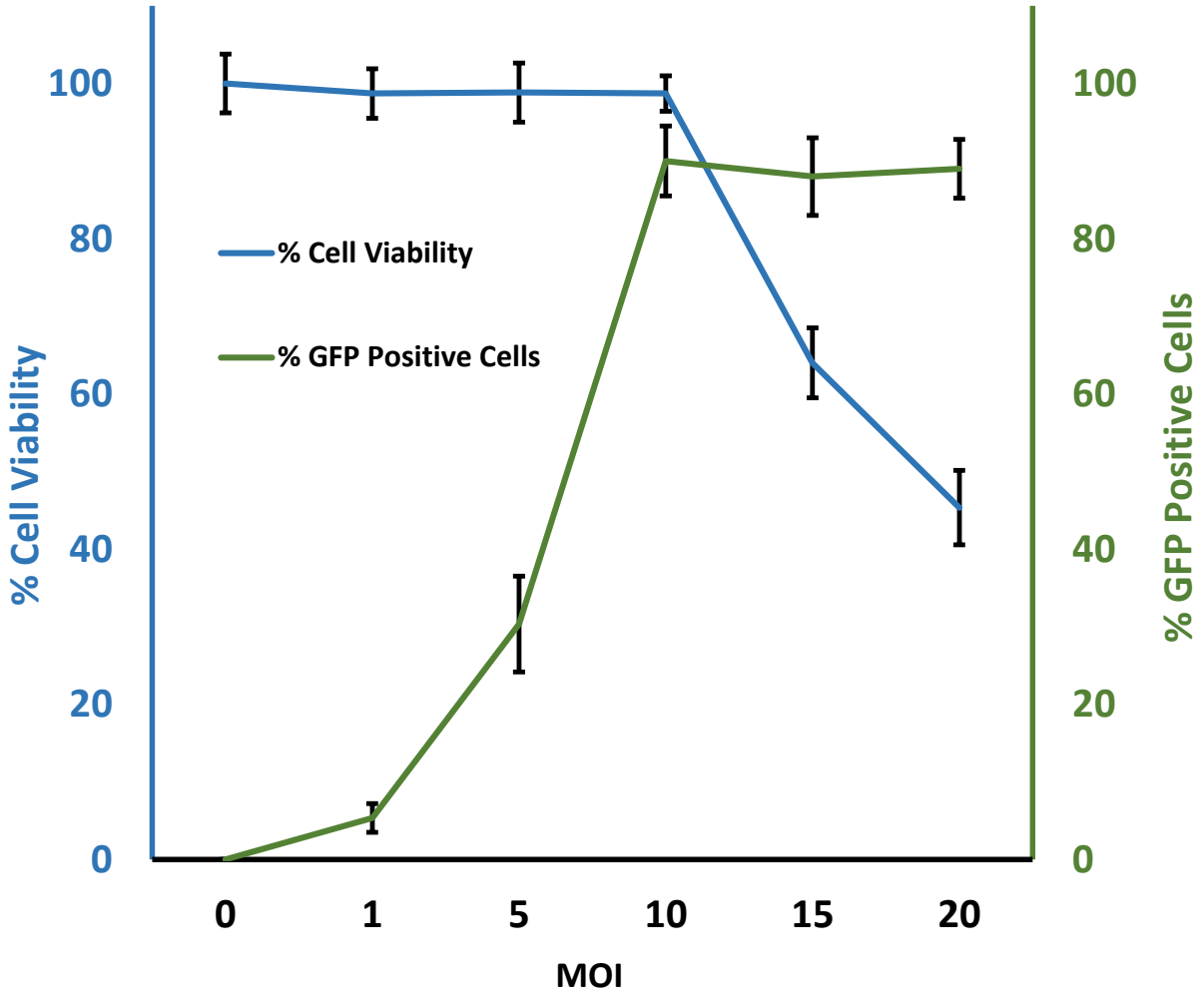

Figure 4.2: Transduction of mouse FRDA fibroblasts (YG8sR) with a range of MOI. 99% of the cells survived compared to untreated cells when using MOI of 1 and 5 but only 5% and 30% of the cells were expressing GFP respectively. The highest percentage of infected cells with the least amount of cell death was observed at a MOI of 10 with 90% of the cells positive for GFP and 99% cell survival compared to untreated cells. At a MOI of 15, 88% of the cells were positive for GFP but only 64% of the cells had survived compared to untreated cells. A MOI of 20 showed higher toxicity to the cells with cell survival of 45% compared to untreated cells and 89% of cells infected with GFP. At each point on the graph an average of three independent experiments were carried out where n=13000. Error bars indicate SEM. All data shown are significant with P <0.05.

4.4 Delivering GFP and *FXN* into human and mouse FRDA fibroblasts

To investigate the permanency and the safety of lentivirus mediated *FXN* gene delivery for the correction of Friedreich ataxia, LV GFP and LV *FXN* with titres of $1x10^8$ were used to infect human FRDA primary fibroblasts (GMO3665) and mouse FRDA primary fibroblasts (YG8sR). FRDA fibroblasts were seeded to reach a confluency of 70% to 80% and were transduced at a MOI of 10. Cells were incubated with the viral supernatant for 6 hours and then the viral supernatant was removed and cells were allowed to recover for a period of 24-48 hours. To improve transduction efficiency further, double transduction was performed by adding new viral supernatant at a MOI of 10 and then incubated for 6 hours, resulting in a final transduction time of 12 hours and a total MOI of 20.

To measure the stability and longevity of the viral expression the number of GFP-positive cells were counted 48 hours and 8 weeks post-transduction of human and mouse FRDA fibroblasts. Live cells were analysed using JuLI™ Smart Fluorescent Cell Analyser microscope (Ruskinn Technology). 10× magnification was used for viewing GFP expression under an ultraviolet light source with 488 nm excitation and an emission at 520nm. Using image processing software, ImageJ (U. S. National Institutes of Health) acquired images were merged and the number of GFP-positive cells were analysed.

Additionally, to further confirm the data obtained from live imaging microscopy, cells were fixed 48 hours and 8 weeks post-infection and the number of the GFP-positive cells were measured using Imagestream^X, as described in Chapter 2, section 2.2.21.

The data revealed that 48 hours after LV GFP infection 92% and after 8 weeks 88% of the cells were positive for GFP expression in human FRDA fibroblasts (GMO3665), which demonstrates that the expression is stable and permanent over a long period of time (Figure 4.3). Also in mouse FRDA fibroblasts (YG8sR), 48 hours after LV GFP infection 97% and after 8 weeks 93% of the cells were positive for GFP expression. The minor change in the number of GFP-positive cells over a period of time indicates long term and stable expression of the transgene (Figure 4.4).

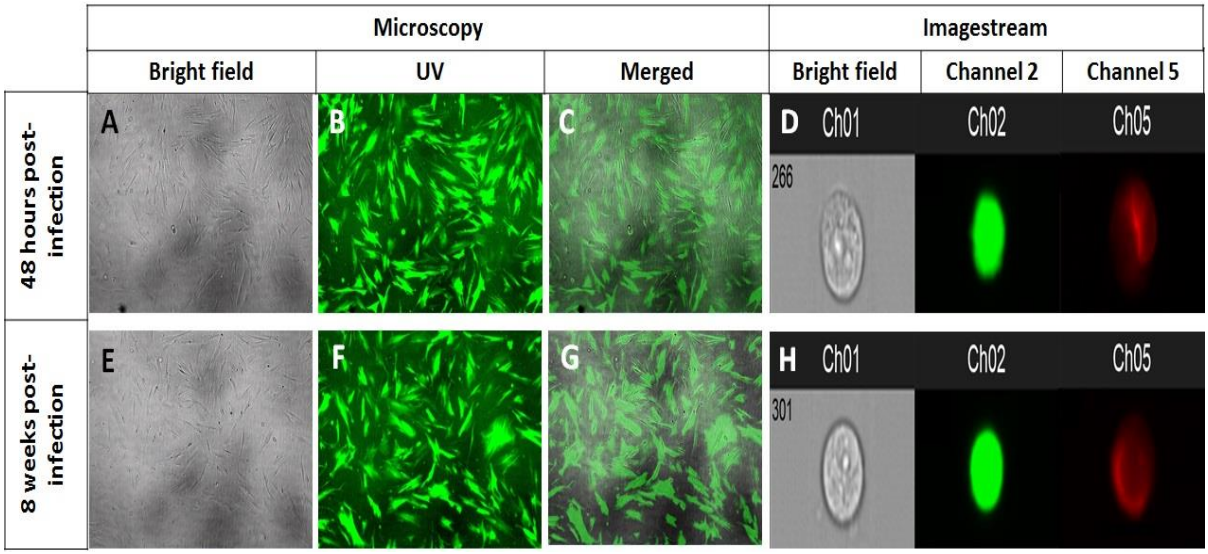

Figure 4.3: GFP gene expression in human primary FRDA fibroblasts (GMO3665) following transduction with LV GFP pseudotyped particles. The percentage of GFP-expressing cells measured by light microscopy and imaging flow cytometry 48 hours and 8 weeks post-infection. A-C) Human primary fibroblasts 48 hours post infection. A) Bright field B) GFP-positive cells which are green under ultraviolet light C) Merging of the two images (A and B). E-G) Human primary fibroblasts 8 weeks post infection. E) Bright field. F) GFP-positive cells which are green under ultraviolet light. G) merging of two images (E and F). D and H) GFP expression in human primary fibroblast measured 48 hours and 8 weeks post infection by Imaging flow cytometry CH01) Bright field, CH02) Green GFP channel and CH05) DRAQ5 far-red DNA stain. 48 hours after LV GFP infection 92% and after 8 weeks 88% of the cells were positive for GFP expression in human primary FRDA fibroblasts.

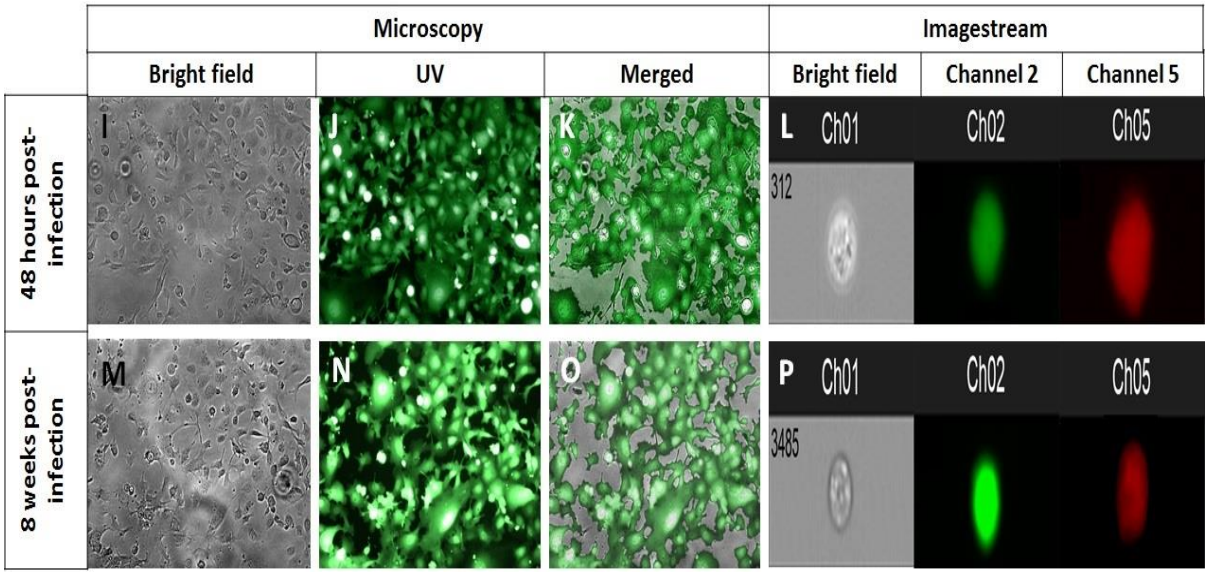

Figure 4.4: GFP gene expression in mouse primary FRDA fibroblasts (YG8sR) following transduction with LV GFP pseudotyped particles. The percentage of GFP expressing cells measured by light microscopy and imaging flow cytometry 48 hours and 8 weeks post-infection. **I-K**) Mouse primary fibroblasts 48 hours post infection. I) Bright field J) GFP-positive cells which are green under ultraviolet light K) Merging of the two images (I and J). M-O) Mouse primary fibroblasts 8 weeks post infection. M) Bright field N) GFP-positive cells which are green under ultraviolet light O) merging of the two images (M and N). L and P) GFP expression in mouse primary FRDA fibroblasts measured 48 hours and 8 weeks post infection by Imaging flow cytometry CH01) Bright field, CH02) Green GFP channel and CH05) DRAQ5 far-red DNA stain. 48 hours after LV GFP infection 97% and after 8 weeks 93% of the cells were positive for GFP expression in mouse primary FRDA fibroblasts.

4.5 Determination of viral copy number

To ensure that the LV GFP and LV *FXN* have integrated the transgene into the host genome the viral copy number was determined using Q-PCR. The construct plasmid containing the cloned *FXN* sequence was used to generate a standard curve using Q-PCR. A genomic DNA sample with a known copy number of 4 was also used to confirm the reliability of the standard curve as described in Chapter 2, section 2.2.24. The copy number of infected human and mouse FRDA fibroblasts was measured at early (48 hours) and late (8 weeks) time points to confirm the stability of viral integration. The result showed the viral copy number 48 hours post infection in human FRDA fibroblasts infected with LV GFP and LV *FXN* were 0.96 and 0.97, respectively. After 8 weeks, the viral copy number remained approximately the same at 0.92 and 0.97, respectively (Figure 4.5). In mouse FRDA fibroblasts 48 hours post infection a copy number of 1.86 when infected with LV GFP, and a copy number of 1.05 when infected with LV *FXN* was determined. The results after 8 weeks remained unchanged with a copy number of 1.79 when infected with LV GFP, and a copy number of 0.95 when infected with LV *FXN* (Figure 4.6). It was noticed that the copy number of mouse FRDA fibroblasts upon infection with LV GFP was higher compared with infection with LV *FXN*, this may indicate that these cells are better transduced with virus carrying the GFP compared to the virus carrying the *FXN* gene.

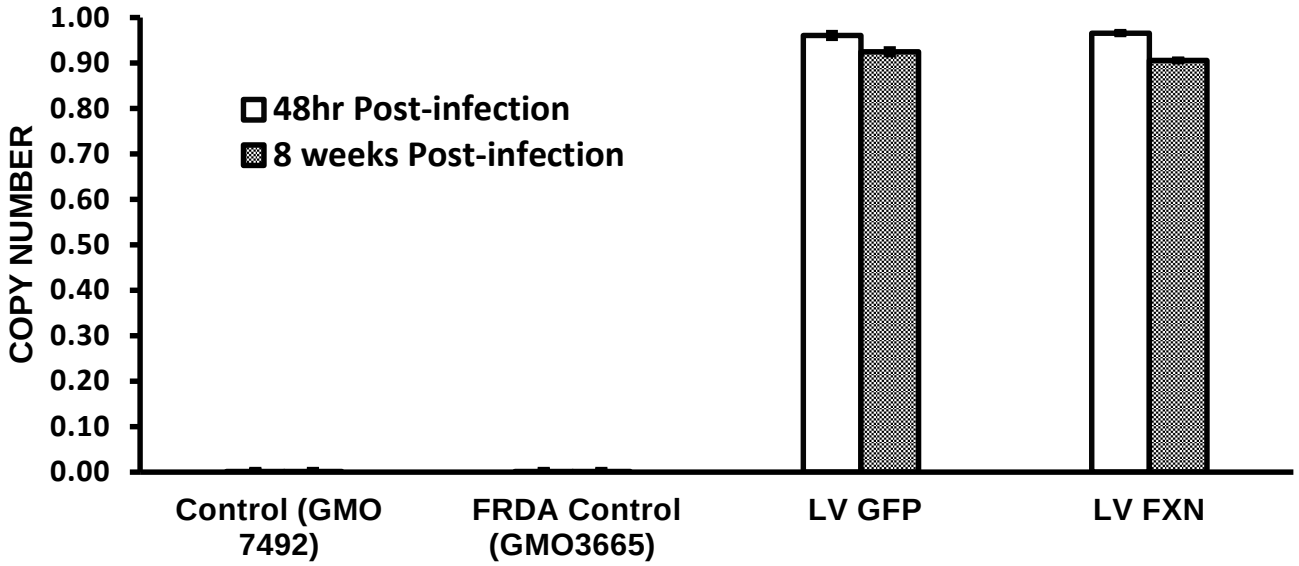

Figure 4.5: Viral genome copy number in human FRDA fibroblasts (GMO3665) infected with LV GFP and LV *FXN* measured by qRT-PCR. Human FRDA fibroblasts 48 hours post infection showed a copy number of 0.96 when infected with LV GFP and a copy number of 0.97 when infected with LV *FXN*. 8 weeks post infection with LV GFP, the human FRDA fibroblasts showed a copy number of 0.92 and 0.91 when infected with LV *FXN*. The results for each time point are the average of three independent experiments performed in duplicate. Error bars indicate SEM and values represent mean ± SEM.

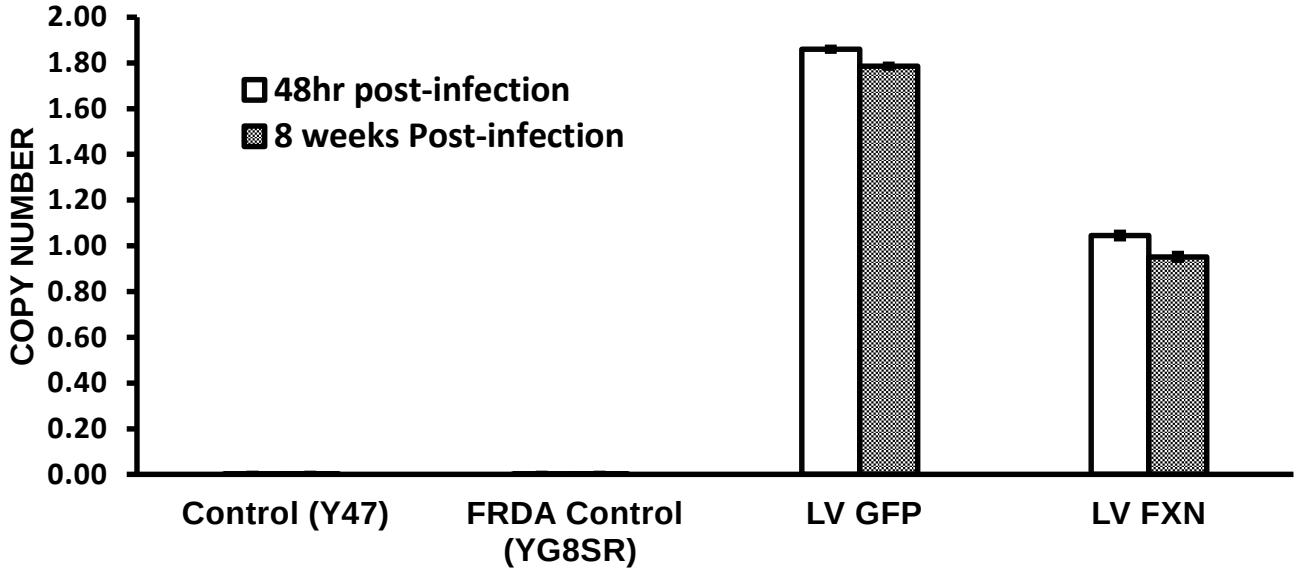

Figure 4.6: Viral genome copy number in mouse FRDA fibroblasts (YG8sR) infected with LV GFP and LV *FXN* measured by qRT-PCR. Mouse FRDA fibroblast 48 hours post infection showed a copy number of 1.86 when infected with LV GFP and a copy number of 1.05 when infected with LV *FXN*. 8 weeks post infection with LV GFP, the mouse FRDA fibroblasts showed a copy number of 1.79 and 0.95 when infected with LV *FXN*. The results for each time point are the average of three independent experiments performed in duplicate. Error bars indicate SEM and values represent mean ± SEM.

4.6 *FXN* mRNA expression following gene delivery

The *FXN* mRNA expression in human and mouse FRDA fibroblasts was measured 1-2 weeks post infection then at 6 – 8 weeks and at 12 weeks post infection to assess the levels of the *FXN* expression over a longer period of time. Total RNA was extracted from LV GFP and LV *FXN* infected human and mouse FRDA fibroblasts as described in Chapter 2, section 2.2.25, DNaseI treated (ThermoScientific) (Chapter 2, section 2.2.26) and converted to cDNA using a cDNA synthesis kit (Invitrogen), as previously described in chapter 2, section 2.2.27. The synthesized cDNA was used as a template for qRT-PCR reactions. The normal human fibroblast GMO7492 was used as a control for this experiment and all data obtained was normalised to the endogenous control genes *GAPDH* and *HPRT* then calibrated to normal fibroblasts expression and the mean of normal control is set to 100%.

The levels of *FXN* mRNA expression in untreated human FRDA fibroblasts were 0.5 fold (P <0.001), 0.47 fold (P <0.01) and 0.33 fold (P <0.001) at 1 - 2 weeks, 6 - 8 weeks and at 12 weeks, respectively, when compared to normal human fibroblasts. Within 1 to 2 weeks post infection of human FRDA fibroblasts with LV *FXN*, *FXN* mRNA expression had increased dramatically by 48 fold (P <0.001) compared to the normal human fibroblasts. The level of *FXN* mRNA expression then reduced at 6 – 8 weeks post infection but was still 28 fold (P <0.001) greater than normal fibroblasts. Further reduction in *FXN* mRNA expression was detected after 12 weeks with mRNA levels 22 fold (P <0.001) higher than normal human fibroblasts. LV GFP transduced cells showed no significant increase in *FXN* mRNA expression when compared to untreated FRDA cells (P >0.05), as expected, at all-time points. Statistical significance of the differences for this experiment was evaluated by two-way ANOVA and all the LV FXN

infected FRDA cells were significant compared to normal and untreated FRDA cell line (Figure 4.7A, B & C).

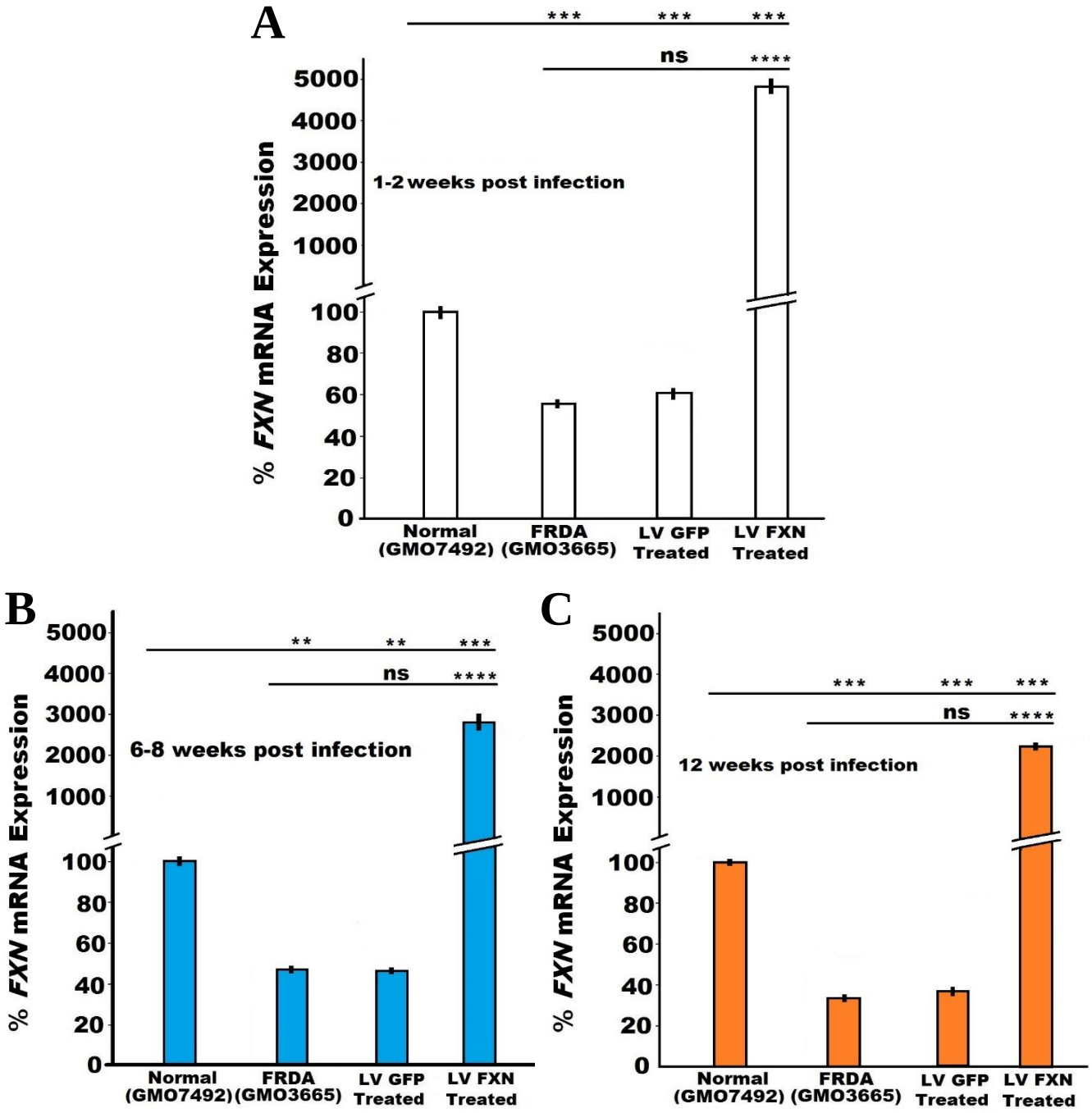

Figure 4.7: Quantification of *FXN* mRNA expression measured using qRT-PCR, in human primary fibroblast (Normal= GMO7492, FRDA & Treated =GMO3665) at **A)** 1-2, **B)** 6-8 and **C)**12 weeks post LV *FXN* and LV GFP treatment. *mRNA* expression values were first normalized to *GAPDH* and HPRT then calibrated to normal fibroblasts expression and the mean of normal control is set to 100%. Each result is the mean of two independent experiments where n=3 in each experiment. Statistical differences between LV FXN treatment and normal control (GMO7492) are indicated by the top line drawn over the bars while the bottom line indicates the differences between LV FXN treatment and untreated FRDA (GMO3665).The error bars represent the SEM. Significance levels are represented by asterisks: ***P* <0.01 and ****P* <0.001, **** *P* <0.0001 and ns= *P* >0.05.

Similarly, RNA was extracted and converted into cDNA, as previously described, from mouse primary fibroblasts. The normal mouse fibroblast Y47 was used as the control for this experiment and all data obtained was normalised to the endogenous control genes *GAPDH* and *HPRT*, calibrated to normal fibroblasts expression and the mean of normal control is set to 100%.

FXN mRNA expression was measured in mouse FRDA fibroblasts treated with LV GFP and LV *FXN*, 1 - 2 weeks post infection and at a later time points at 6 - 8 weeks and at 12 weeks post infection. 1 - 2 weeks post infection the *FXN* mRNA expression in untreated mouse FRDA cells was 0.2 fold (P <0.001) and after treatment has increased by 42 fold (P <0.001) compared to the normal primary mouse fibroblasts. 6-8 weeks after treatment the *FXN* mRNA was found to be higher than in normal fibroblasts by 29 fold (P <0.001) but had decreased compared to the earlier measurement. In untreated mouse FRDA fibroblasts the *FXN* mRNA levels remained low at 0.16 fold (P <0.001) compared normal mouse fibroblasts at this time point. 12 weeks post infection, a further reduction was observed. However the *FXN* mRNA levels remained higher than in normal fibroblast by 24 fold (P <0.001), while untreated FRDA fibroblasts expressing 0.2 fold (P <0.001) compared to normal mouse fibroblasts. LV GFP transduced cells showed no significant increase in *FXN* mRNA levels when compared to untreated FRDA cells (P >0.05) as expected at all time points (Figure 4.8A, B & C). Statistical significance of the differences for this experiment was evaluated by two-way ANOVA and all the LV FXN infected FRDA cells were significant compared to normal and untreated FRDA cell line. Although the levels of expression continued to be higher than in normal mouse fibroblasts, these levels did decrease over time. It is likely that the decrease in *FXN* mRNA expression is due to shut down

and methylation of SFFV promoter as this has been reported in other studies using this promoter (Herbst *et al.*, 2012).

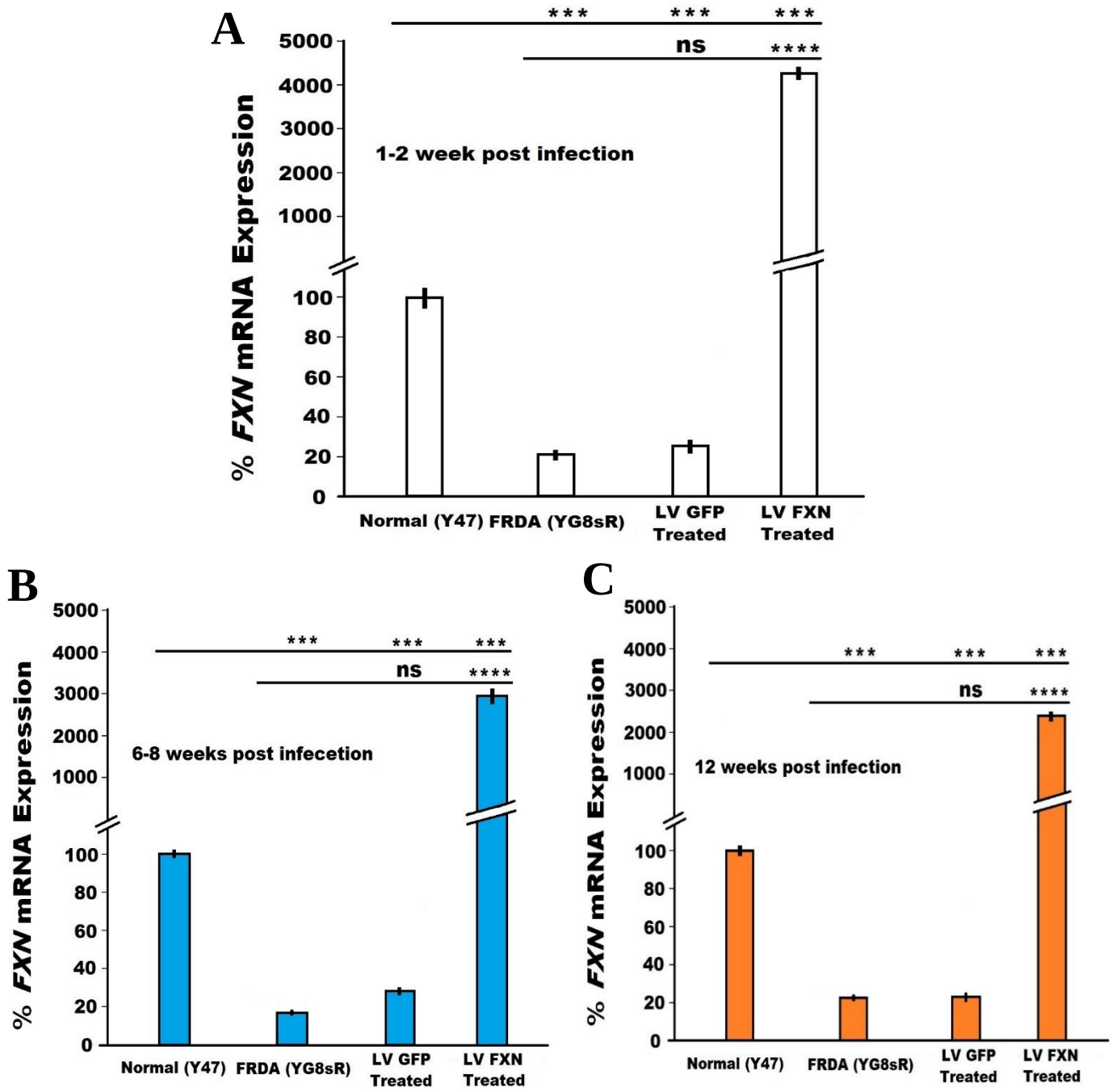

Figure 4.8: A graph showing the relative levels of *FXN* mRNA levels in mouse primary fibroblasts which were measured using qRT-PCR. (Normal = Y47, FRDA & Treated=YG8sR). Expression was measured **A)** 1 - 2 weeks, **B)** 6 - 8 weeks and at **C)** 12 weeks post LV *FXN* and LV GFP treatment. *mRNA* expression values were first normalized to *GAPDH* and HPRT then calibrated to normal fibroblasts expression and the mean of normal control is set to 100%. Each result is the mean of two independent experiments where n=3 in each experiment. Statistical differences between LV FXN treatment and normal control (Y47) are indicated by the top line drawn over the bars while the bottom line indicates the differences between LV FXN treatment and untreated FRDA (YG8sR). The error bars represent the SEM. Significance levels are represented by asterisks *** P <0.001, **** P <0.0001 and ns= P >0.05.

4.7 *FXN* protein expression following gene delivery

The frataxin protein expression was measured using lateral flow immunoassay with the Frataxin Protein Quantity Dipstick Assay Kit (MitoSciences), as described in Chapter 2, section 2.2.33. The levels of protein was assessed immediately after each mRNA measurement to evaluate the pre- and post-translational activity of frataxin. Protein expression in both human and mouse fibroblasts was measured at 1 - 2 weeks, 6 - 8 weeks and at 12 weeks after treatment with LV GFP and LV *FXN*.

Normal human fibroblasts GMO7492 were used as the control for this experiment and all data obtained was calibrated to normal fibroblasts expression and the mean of normal control is set to 100%. Frataxin protein levels remained significantly low at 0.48 fold (P <0.001), 0.42 fold (P <0.001) and 0.45 fold (P <0.01) at 1 - 2 weeks, at 6 - 8 weeks and 12 weeks, respectively, compared to untreated normal human fibroblasts. 1 - 2 weeks post infection the levels of protein expression in treated FRDA fibroblasts had increased to approximately 20 fold (P <0.001) compared to the normal human fibroblasts. 6 - 8 weeks after LV *FXN* infection the protein levels had decreased to 15 fold (P <0.001) compared to normal fibroblasts and a further reduction was observed 12 weeks after LV *FXN* transduction with 13 fold (P <0.001) higher than in normal fibroblasts. As expected, the levels of frataxin protein expression did not change significantly after LV GFP treatment at all time points compared to untreated FRDA fibroblasts (P >0.05). Statistical significance of the differences for this experiment was evaluated by two-way ANOVA and all the LV FXN infected cells were significant compared to normal and untreated FRDA cell line (Figure 4.9A, B & C).

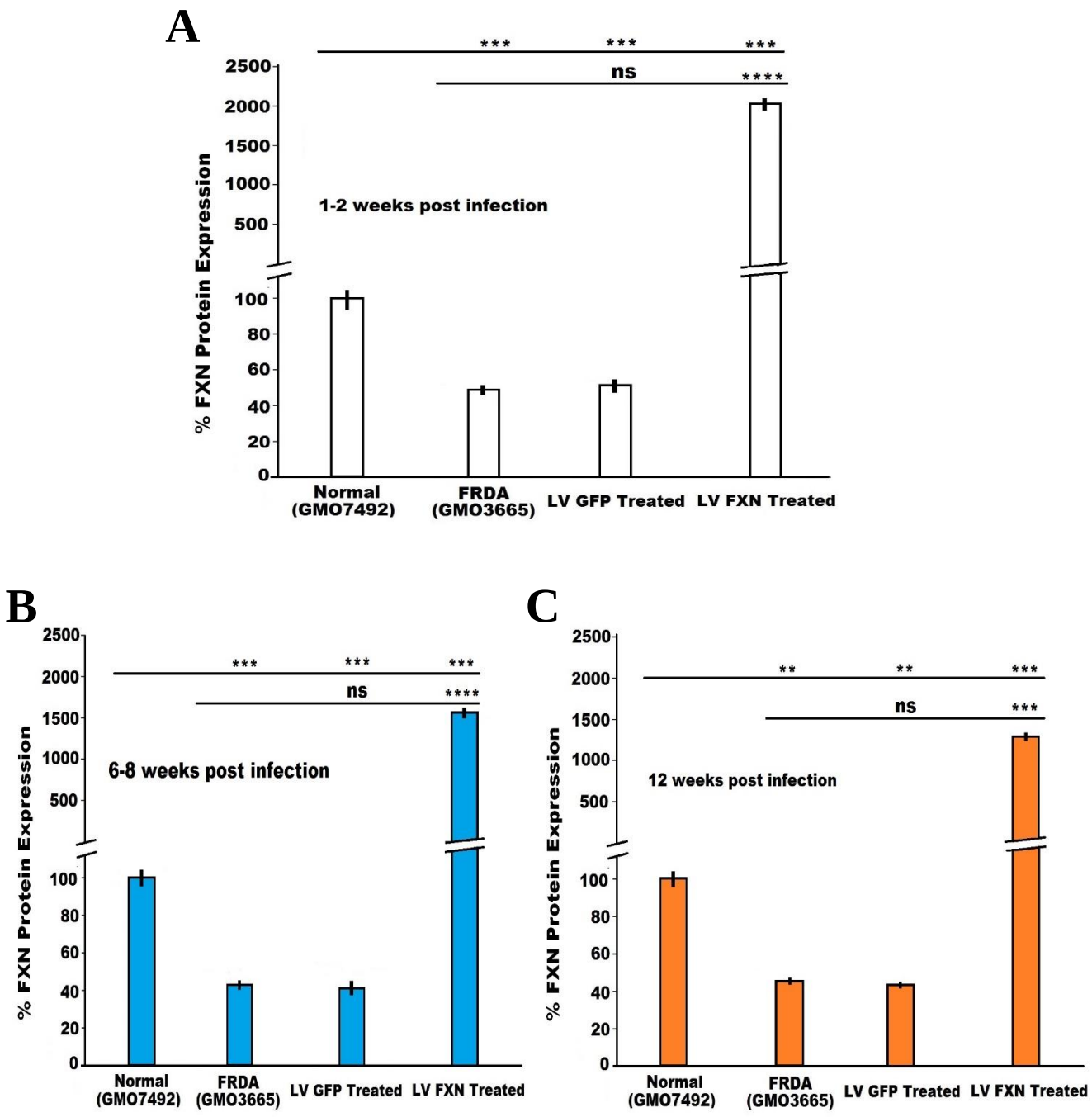

Figure 4.9: A graph showing the relative levels of *FXN* protein expression in human primary fibroblasts (Normal= GMO7492, FRDA & Treated =GMO3665) at **A)** 1 – 2 weeks, **B)** 6 - 8 weeks and at **C)** 12 weeks post LV *FXN* and LV GFP treatment. The results are the mean of two independent experiments, where n=3 for all samples. The relative levels of frataxin expression is shown and the mean of the normal control is set to 100%. Statistical differences between LV FXN treatment and normal control (GMO7492) are indicated by the top line drawn over the bars while the bottom line indicates the differences between LV FXN treatment and untreated FRDA (GMO3665). The error bars represent the SEM. Significance levels are represented by asterisks: ***P* <0.01, *** *P* <0.001, **** *P* <0.0001 and ns= *P* >0.05.

Normal mouse fibroblasts Y47, were used as the control for measuring frataxin protein levels. All data obtained was calibrated to the frataxin levels in these normal mouse fibroblasts and the level of expression in the normal control is set at 100%. At 1 - 2 weeks post treatment with LV *FXN* the levels of frataxin expression in treated mouse FRDA fibroblasts had increased to 3.5 fold (P <0.001) compared to the normal fibroblasts. Protein expression before treatment was measured to be 0.2 fold (P <0.001) in untreated FRDA fibroblasts compared to the normal Y47 fibroblasts. The levels of frataxin protein at 6 - 8 weeks post infection with LV *FXN* had decreased by 0.5 folds when compared to the first measurement at 1 – 2 weeks. However, the levels still remained high at 3 fold (P <0.001) higher than in the normal Y47 fibroblasts, while the untreated FRDA fibroblasts expressed 0.19 fold (P <0.001) frataxin protein compared to normal Y47 fibroblasts. At 12 weeks after infection, the levels of frataxin protein had decreased further but were 2.3 folds (P <0.001) higher compared to normal Y47 fibroblasts. Frataxin protein expression was 0.19 fold (P <0.001) in untreated FRDA fibroblasts compared to normal Y47 cell lines. As expected, the levels of *FXN* protein expression did not change significantly after LV GFP treatment at all time points compare to the normal control and untreated FRDA cells. Statistical significance of the differences for this experiment was evaluated by two-way ANOVA and all the LV FXN infected cells were significant compared to normal and untreated FRDA cell line (Figure 4.10A, B & C).

Overall, a similar pattern to the *FXN* mRNA expression was seen and the protein level also decreased over time like the mRNA expression, indicating that the protein and mRNA expression are proportional in FRDA fibroblasts. However, it is evident that very high levels of mRNA expression is required in order to have relatively high protein

expression. For example, at 1 - 2 weeks post infection the mRNA levels had increased by 48 fold in human FRDA fibroblasts whilst the protein levels only increased by 20 fold compared with normal human fibroblasts. Similarly, in mouse FRDA fibroblast 1 - 2 weeks post infection with LV *FXN,* the mRNA levels had increased by 42 fold whilst the protein levels have increased by 3.5 fold compared to normal Y47 fibroblasts.

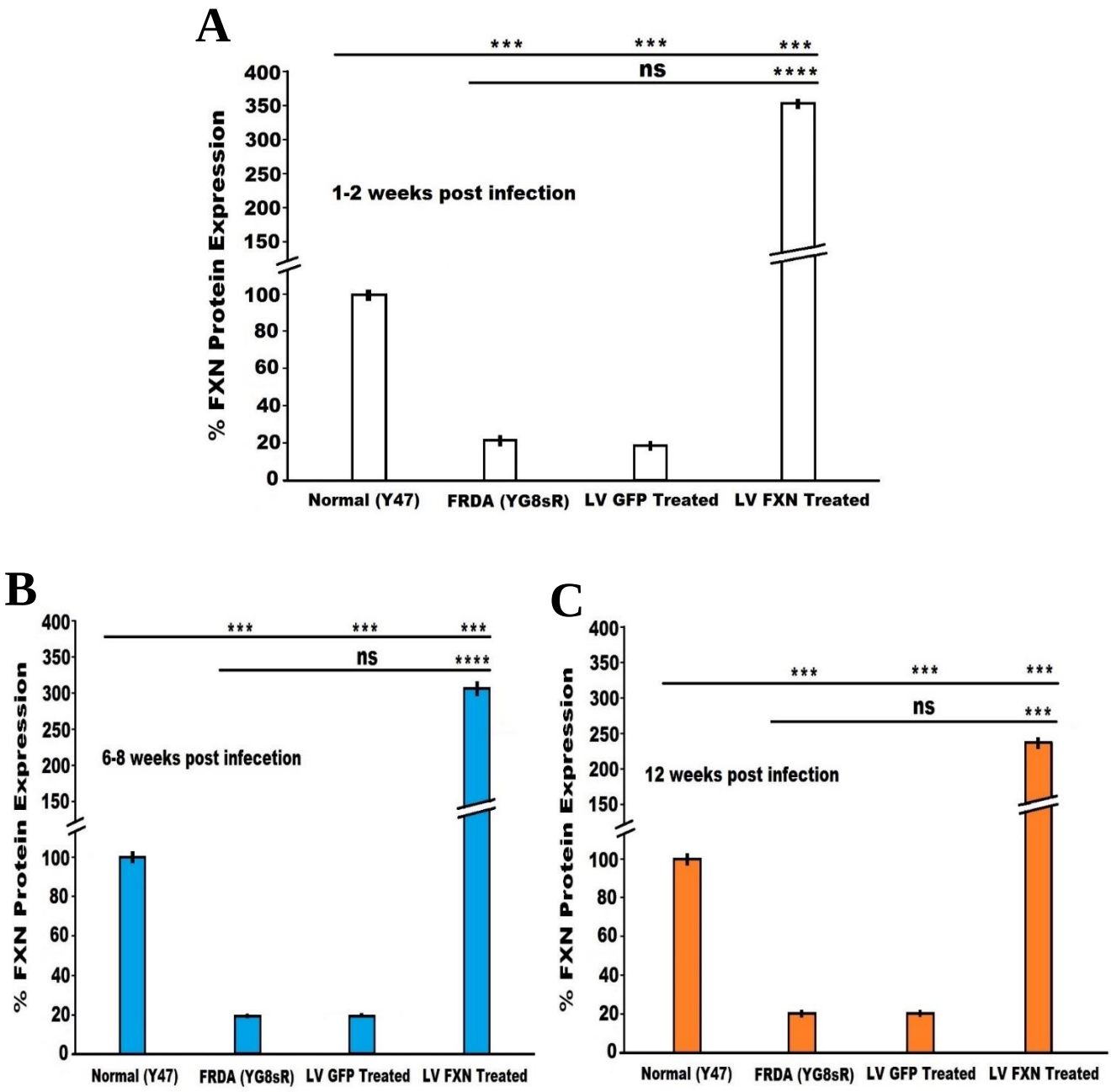

Figure 4.10: A graph showing the relative levels of *FXN* protein expression in mouse primary fibroblasts (Normal = Y47, FRDA & Treated=YG8sR) at **A)** 1 – 2 weeks, **B)** 6 - 8 weeks and at **C)** 12 weeks post LV *FXN* and LV GFP treatment. The results are the mean of two independent experiments where n=3 for all samples. The relative levels of frataxin expression is shown where 100% is the normal level of frataxin in the control primary fibroblasts. Statistical differences between LV FXN treatment and normal control (Y47) are indicated by the top line drawn over the bars while the bottom line indicates the differences between LV FXN treatment and untreated FRDA (YG8sR). The error bars represent the SEM. Significance levels are represented by asterisks: *** P <0.001, **** P <0.0001 and ns= P >0.05.

4.8 Evaluation of lentiviral treatment for toxicity by determining population doubling

To investigate the toxicity levels and cell viability after lentiviral treatment, the growth characteristics of the four cell lines were identified by measuring population doubling times of the treated and untreated human and mouse FRDA fibroblasts. These measurements were taken over a period of 45 days for the human cell lines and over 60 days for the mouse cell lines, as described in Chapter 2, section 2.2.34. Growth curves and cumulative population doubling analysis were performed and any changes in population doubling rate will represent an indication of toxicity of this treatment to the cultured cells.

LV *FXN* and LV GFP treated human FRDA cells (GMO3665) were seeded in parallel to untreated human FRDA cells (GMO3665) and control normal human fibroblasts (GMO7492). Their growth rate was measured and compared to detect any changes compare to untreated cells. Untreated FRDA fibroblasts (GMO3665) with the fastest growth rate had a cumulative population doubling of 24 over 45 days. After treatment with LV GFP no significant changes was observed with a cumulative population doubling of 25 over 45 days. Normal human primary fibroblasts (GMO7492) exhibited a slower growth rate compared to human FRDA fibroblasts with a cumulative population doubling of 17 over 45 days. After LV *FXN* treatment of FRDA fibroblasts had a cumulative population doubling of 20 over a period of 40 days. This result, although not significant showed growth rate which decreased in doubling time towards the normal control cell line (GMO7492). Overall, this indicated that the lentiviral treatment did not affect the growth characteristics of FRDA cells and when treated with

LV *FXN* the growth rate seemed to have shifted slightly towards normal levels (Figure 4.11) (Table 4.1).

Cell line	days in culture	CPD at day 30	CPD at final day
Normal GMO7492	43	13	17
FRDA GMO3665)	43	17	24
LV GFP treatment	45	20	25
LV *FXN* treatment	38	18	20

Table 4.1: Cumulative population doubling of the human fibroblasts at different days in culture. CPD: Cumulative population doubling.

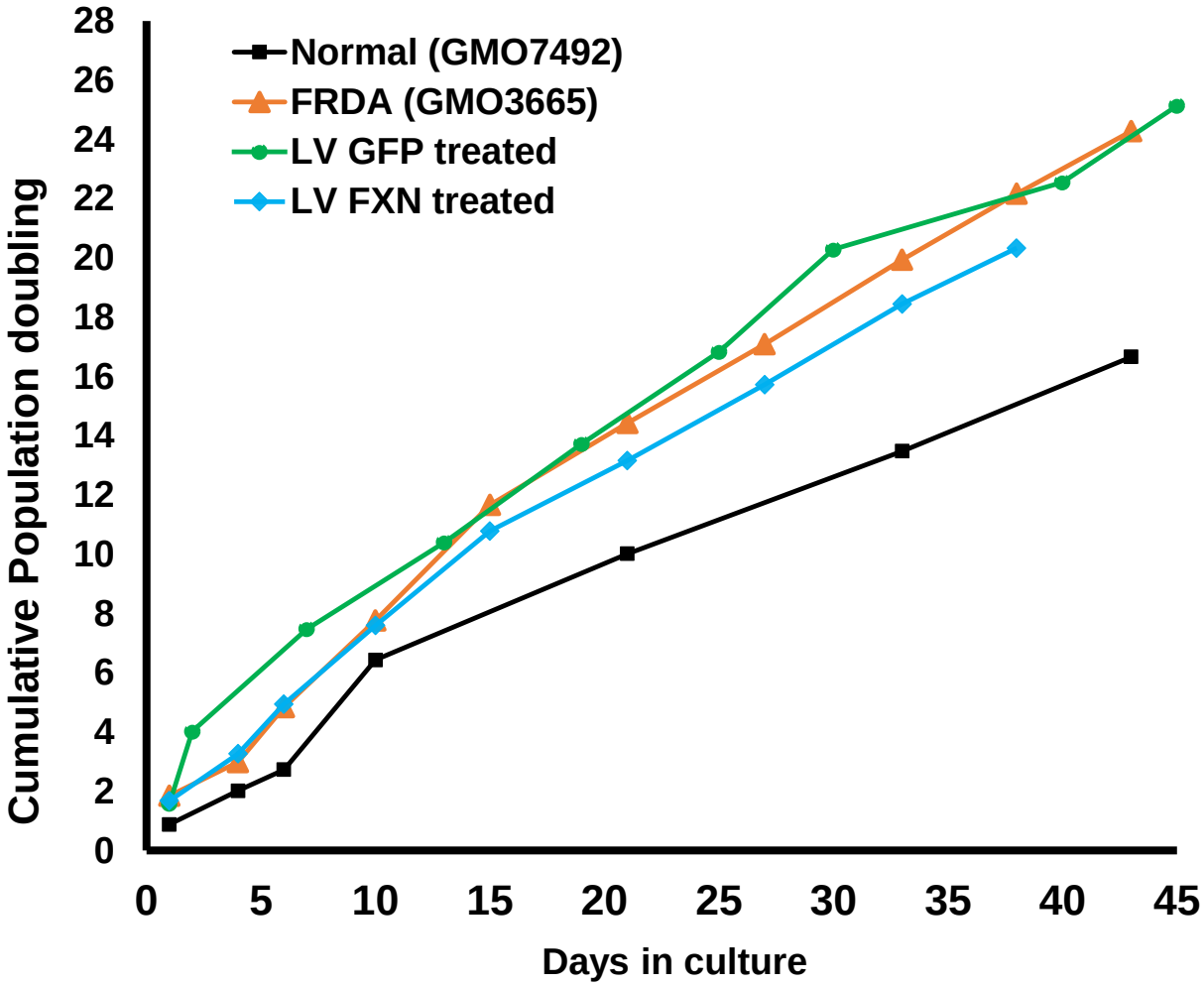

Figure 4.11: A graph of the cumulative population doubling of the human primary fibroblast cell lines after treatment (Normal (GMO7492), FRDA (GMO3665), LV GFP treated FRDA fibroblast and LV *FXN* treated FRDA fibroblasts, from passage 10 over a time frame of 45 days.

In mouse cell lines LV *FXN* and LV GFP treated FRDA fibroblasts (YG8sR) were grown in parallel to the normal mouse fibroblasts (Y47) and untreated FRDA fibroblasts (YG8sR). After treatment of FRDA fibroblast with LV GFP cells did not display any change of growth characteristics compared to the untreated FRDA fibroblasts indicating that the therapy did not have any adverse effects on their normal growth. Cumulative population doubling for both LV GFP treated fibroblasts and untreated fibroblasts was 33 over period of 50 days. FRDA fibroblasts treated with LV *FXN* did not show any change in their growth rate compared to FRDA fibroblast until day 30, where the growth started to shift to towards the normal control fibroblasts. After day 30 the change was significant and the growth appeared to be slower than untreated FRDA fibroblasts (Figure 4.12). The cumulative population doubling of LV *FXN* treated FRDA fibroblasts was 29 over period of 58 days and for normal Y47 fibroblasts was 27 over period of 59 days. Table 4.2 shows the changes in cumulative population doubling over period of 30 and 59 days in culture.

Cell line	days in culture	CPD at day 30	CPD at final day
Normal Y47	59	18	27
FRDA YG8sR	50	24	33
LV GFP treatment	59	22	40
LV *FXN* treatment	56	20	29

Table 4.2 Cumulative population doubling of the mouse fibroblasts at different days in culture. CPD: Cumulative population doubling.

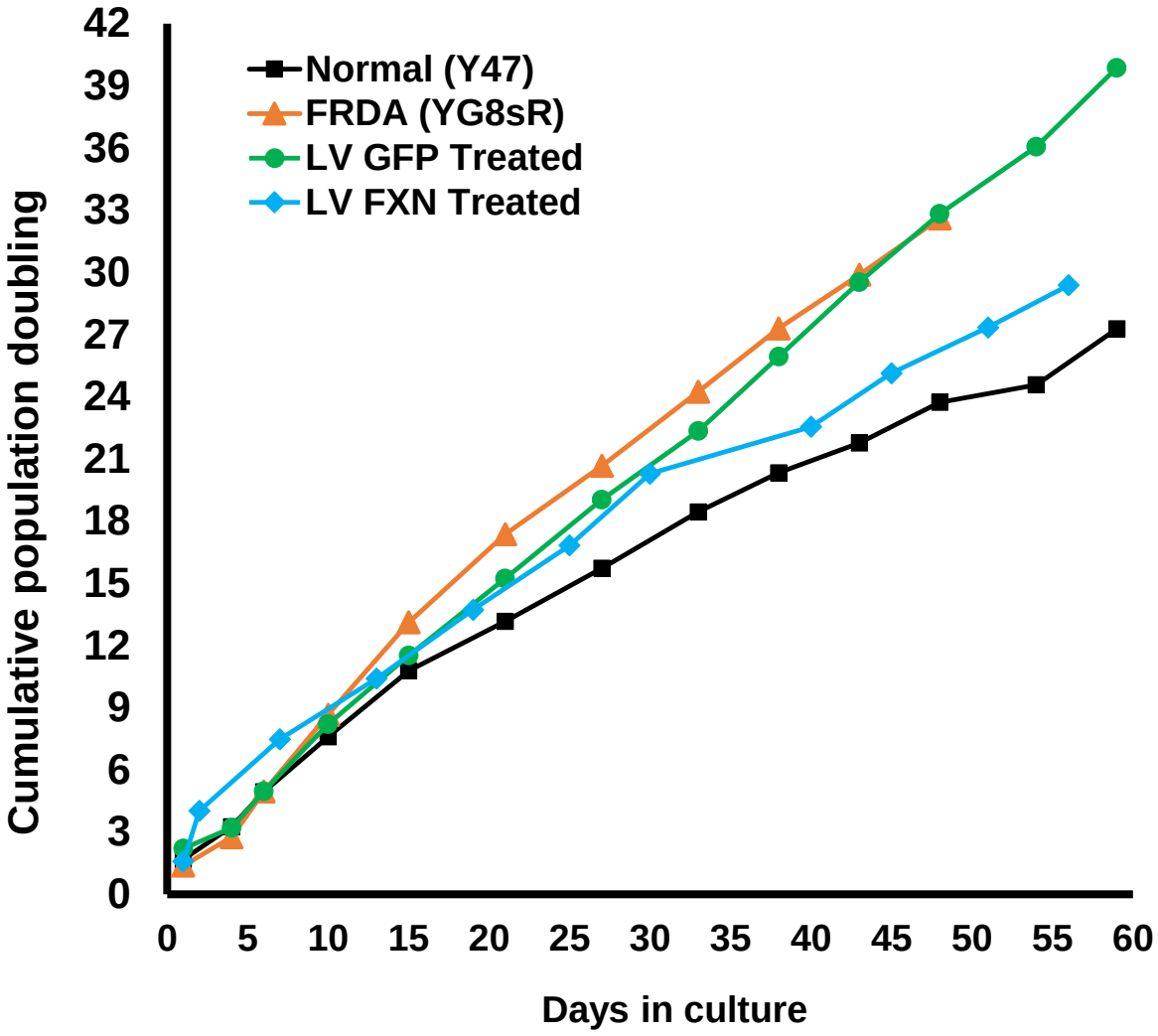

Figure 4.12: A graph showing the cumulative population doubling of the mouse primary fibroblast cell lines after treatment (Normal (Y47), FRDA (YG8sR), LV GFP treated FRDA fibroblasts and LV *FXN* treated FRDA fibroblasts, from passage 8 over a time frame of 60 days.

4.9 Clonogenic cell survival assay following lentiviral treatment

The clonogenic cell survival assay determines the ability of a cell to proliferate indefinitely, thereby retaining its reproductive ability to form a large colony or a clone. This cell is then said to be clonogenic. A cell survival curve is therefore defined as a relationship between the dose of the agent or treatment used to produce an insult and the fraction of cells retaining their ability to reproduce. Therefore to assess the proliferation of LV GFP and LV *FXN* treated FRDA fibroblasts and to determine if *FXN* delivery will improve the clonogenic survival rate of FRDA cells this assay was carried out. 2 weeks after transduction of fibroblasts, single cell suspensions were obtained by trypsinisation, and appropriate cell numbers were seeded into petri dishes (ten replicates of each in 15 mm dishes). A range of between 50 - 150 colonies was achieved for each cell line. Colonies were fixed, stained and counted as described in Chapter 2, section 2.2.6. Normal fibroblasts (Human: GMO7492, Mouse: Y47) were used as the controls and all data obtained was calibrated to normal fibroblasts levels and the mean of normal control is set at 100%. Both human and mouse FRDA fibroblasts showed a significant increase in cell proliferation after treatment with LV *FXN* (Human: 99% (P >0.05) & Mouse 97% (P <0.05)) when compared to untreated FRDA fibroblasts (Human: 93% (P <0.0001) & Mouse: 88% (P <0.0001)) and cell survival had increased to the levels reached by normal control fibroblasts (100%) (Figure 4.13A & B). However, LV GFP treatment did not have any effect on the proliferation of FRDA fibroblasts and no significant changes was noticed compared to untreated FRDA cells (Human 92% (P <0.0001) & Mouse 88% (P <0.0001)). Statistical significance of the differences for this experiment was evaluated by two-way ANOVA

and all the LV FXN infected cells were compared to normal and untreated FRDA cell line.

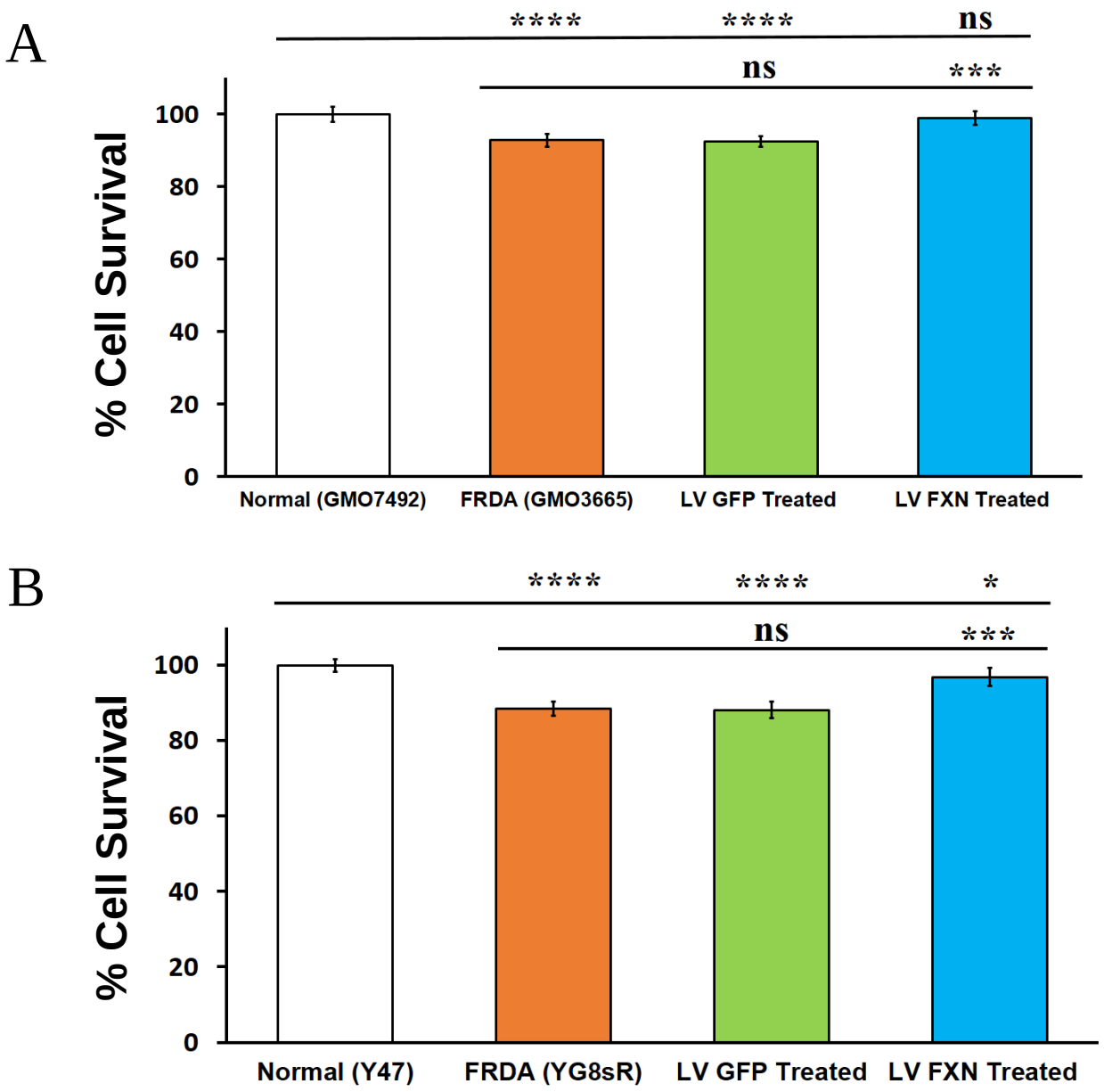

Figure 4.13: Clonogenic cell survival assays performed on **A)** human and **B)** mouse FRDA fibroblasts after treatment with LV GFP and LV *FXN* 2 weeks post infection. Data shown are relative to the value of normal cell line which was set to be 100%. Both human and mouse FRDA cell lines showed improvement in cell survival after treatment with LV *FXN*. Statistical differences between LV FXN treatment and normal control are indicated by the top line drawn over the bars while the bottom line indicates the differences between LV FXN treatment and untreated FRDA. Each result is the average of ten independent experiments. Error bars indicate SEM and values represent mean ± SEM. Significance levels are represented by asterisks: **** P <0.0001, * P <0.05 and ns= P >0.05.

4.10 Restoring aconitase activity following *FXN* gene delivery

Aconitase is an iron-sulphur protein involved in iron homeostasis and found to be deficient in FRDA cells. Aconitase activity can undergo reversible citrate-dependent modulation in response to pro-oxidants. Frataxin interacts with aconitase and reduces the level of oxidant-induced inactivation, and converts inactive enzyme to its active form. Thus, frataxin is an iron chaperone protein that protects the aconitase iron sulphur cluster from disassembly and promotes enzyme reactivation. Loss of aconitase activity in cells or other biological samples treated with pro-oxidants has been interpreted as a measure of oxidative damage. Aconitase activity in human and mouse fibroblasts was measured 2 weeks after treatment with LV GFP and LV *FXN* using the Aconitase Assay Kit (Cayman Chemical). In the assay, citrate is converted by aconitase into isocitrate, which is further processed resulting in a product that converts a nearly colourless probe into an intensely coloured form with a λmax at 450nm (Chapter 2, section 2.2.35). Normal fibroblast (Human: GMO7492, Mouse: Y47) were used as the controls and all data obtained was calibrated to normal fibroblasts levels and the mean of normal control is set to 100%. As previously expected, the aconitase activity was reduced in human and mouse FRDA fibroblasts to 66% (P <0.01) and 59% (P <0.01) compared to the normal fibroblasts (100%), respectively. After transduction of FRDA fibroblasts cells with LV *FXN* these levels were elevated to 90% (P <0.05) in human fibroblasts and almost to levels measured in normal mouse fibroblasts with 99% activity (P >0.05). Statistical significance of the differences for this experiment was evaluated by two-way ANOVA and all the LV FXN

infected cells were significant compared to untreated FRDA cell line (Figure 4.14A & B).

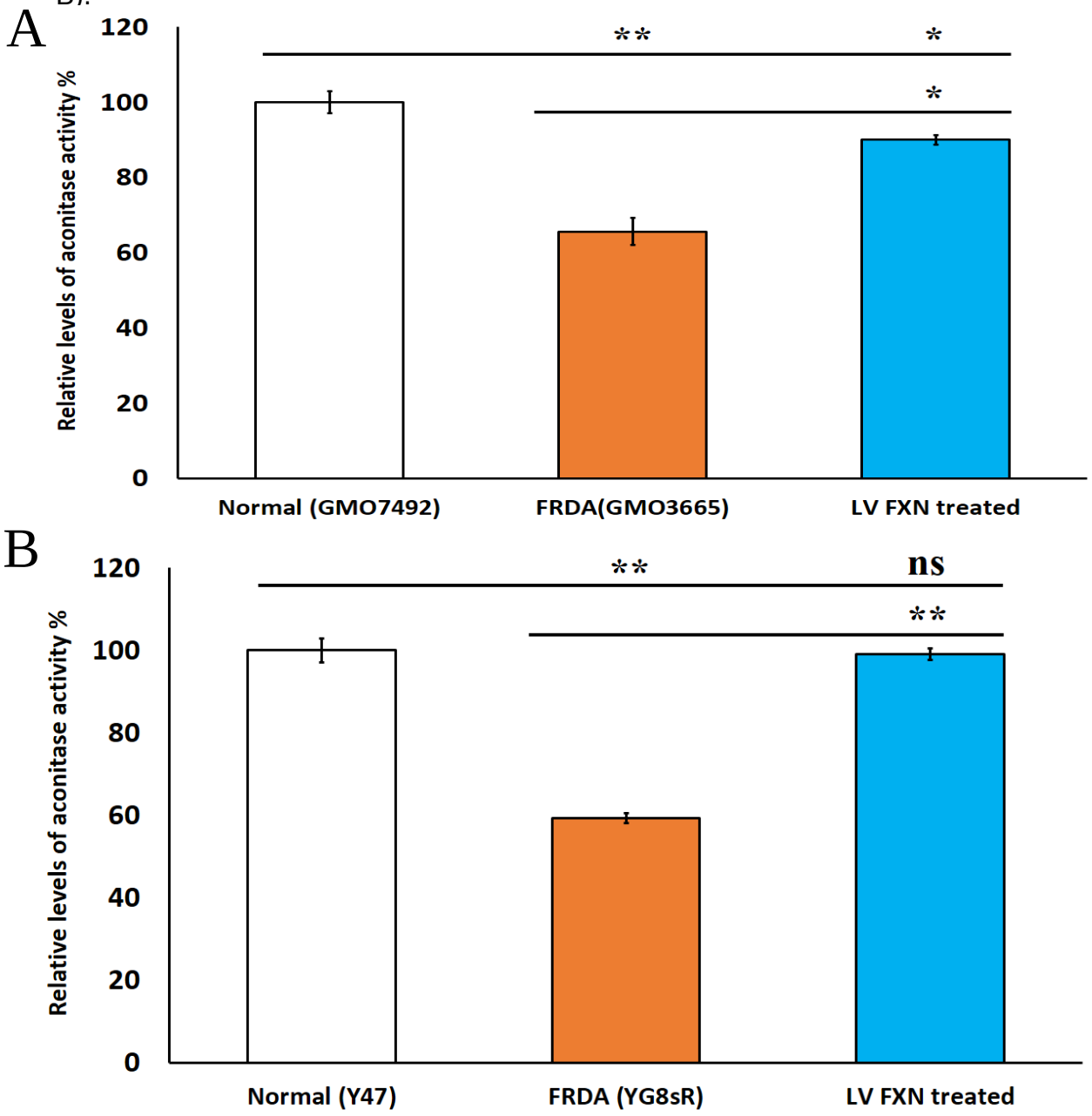

Figure 4.14: Relative levels of aconitase activity following treatment with LV *FXN* in **A)** human primary fibroblasts (Normal= GMO7492, FRDA & Treated =GMO3665) and **B)** mouse primary fibroblasts (Normal = Y47, FRDA & Treated=YG8sR). Aconitase activity was first normalized to the activity of normal fibroblasts and the mean of normal control is set to 100%. Aconitase activity in mouse FRDA fibroblast has increased from 59% to 99% after LV *FXN* treatment and aconitase activity in human FRDA fibroblast has increased from 66% to 90% after *FXN* LV treatment. (n=3, error bars represent SEM). Statistical differences between LV FXN treatment and normal control are indicated by the top line drawn over the bars while the bottom line indicates the differences between LV FXN treatment and untreated FRDA. Significance levels are represented by asterisks: **P* <0.05, ***P* <0.01 and ns= *P* >0.05.

CHAPTER 5 – REDUCED SENSITIVITY TO OXIDATIVE STRESS AND REPAIR OF DNA DAMAGE IN FRIEDREICH ATAXIA

5.1 Aims

- Measure oxidative stress levels in FRDA cell lines following lentiviral delivery of *FXN*.
- Examine the sensitivity of FRDA fibroblast cell lines by exposure to increasing concentrations H_2O_2.
- Evaluate DNA damage profile in FRDA cells before and after lentiviral *FXN* delivery.
- Investigate the role of *FXN* in response to DNA damage.

5.2 Oxidative stress in Friedreich ataxia

Oxidative stress describes the overload of cells with reactive oxygen species (ROS) either caused by increased production of ROS or decreased defence mechanisms against ROS. There is some evidence available showing that oxidative stress is increased in FRDA cells (Schulz *et al.*, 2000). However, this evidence is still limited as will be discussed below.

5.2.1 Generation of Reactive Oxygen Species

In many compartments of the cell various enzymes are potential generators of reactive oxygen species (ROS) (Balaban *et al.*, 2005). Within the plasma membrane NADPH oxidases (Lambeth, 2004, Suh *et al.*, 1999) and many enzymes in the cytosol including cyclooxygenases are capable of producing ROS. Another source of ROS are in peroxisomes which are produced in these organelles during lipid metabolism. However, the majority (around 90%) of ROS is produced by the mitochondria where they arise as a consequence of oxidative phosphorylation. This process describes the controlled oxidation of NADH or FADH to produce a proton gradient and thereby

potential energy to drive synthesis of ATP by ATP synthetase. This reaction, shown schematically in Figure 5.1, is catalysed by a chain of four complexes (I to IV) called the electron transport chain (ETC), which transports electrons in a stepwise manner to the last complex (IV), where they are used to reduce oxygen to form water (Balaban *et al.*, 2005, Lagouge and Larsson, 2013). At several sites of this chain, especially at complexes I and III (Chen *et al.*, 2003, Kushnareva *et al.*, 2002), electrons may directly react with oxygen or other electron acceptors to form ROS and other free radicals. These molecules have the potential to react with macromolecules within the cell including DNA, proteins and lipids leading to a change in their structure and function (Balaban *et al.*, 2005, Lagouge and Larsson, 2013, Pandolfo, 2012).

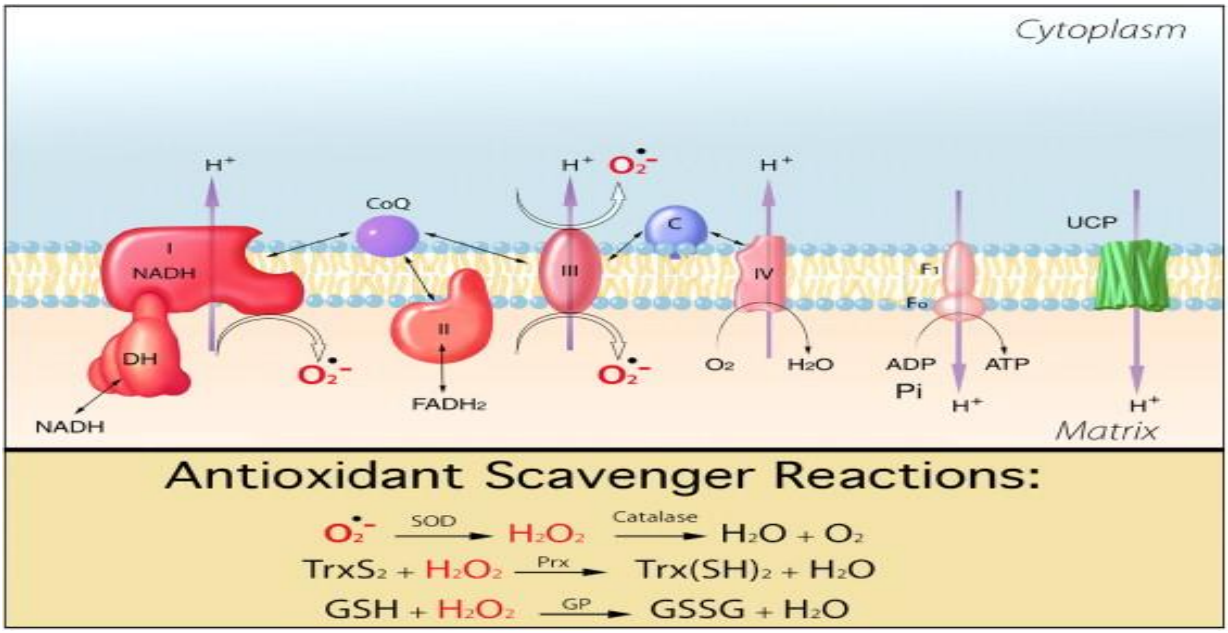

Figure 5.1: Schematic model of ROS generation in the mitochondria. The major production sites of ROS sites are complex I and III. Antioxidant enzymes include various isoforms of superoxide dismutase (SOD), peroxiredoxin (Prx) and glutathione peroxidase (GP). The scavenging reaction of the peroxiredoxin family requires other cellular dithiol proteins such as thioredoxin (TrxS2). The different complexes of oxidative phosphorylation are colour coded with regard to the magnitude for reducing oxygen, with red (dehydrogenases [DH] and site I) having the highest potential and pink (site IV) the lowest potential. The family of uncoupling protein (UCP), here denoted in green, reduces the overall mitochondrial membrane potential (Balaban *et al.*, 2005).

5.2.2 Elimination of reactive oxygen species

Cells have developed different mechanisms to eliminate ROS. This detoxification is performed first by superoxide dismutase (SOD) which converts superoxide (O_2^-) into hydrogen peroxide (H_2O_2) (Balaban *et al.*, 2005, McCord and Fridovich, 1969); this in turn can be scavenged by different enzymes. Catalase converts it to water and oxygen (Radi *et al.*, 1991). Glutathione peroxidase (GP) or peroxiredoxin (Prx) are able to convert H_2O_2 to water and an oxidised form of an antioxidant normally cellular dithiol proteins, such as glutathione (GSH) and thioredoxin (TrxS2) (Figure 5.1) (Chang *et al.*, 2004). Additionally, cells have non-enzymatic ROS scavengers including the vitamin C ascorbate, flavonoids and carotenoids, which contribute to the elimination of ROS (Balaban *et al.*, 2005, Lagouge and Larsson, 2013).

5.2.3 Oxidative stress in Friedreich ataxia

The role of oxidative stress in the pathology of FRDA is a controversial subject. This is due to limited direct evidence of increased oxidative stress in patient cells. However, there is some evidence to justify the assumption that oxidative stress occurs in FRDA (Armstrong *et al.*, 2010). Even under physiological conditions ROS are generated by the ETC, as described earlier. Due to defective Fe-S cluster biosynthesis ETC complexes I and III have decreased activity in FRDA. This dysfunction of the respiratory enzymes may lead to an increased production of ROS (Armstrong *et al.*, 2010). There is evidence available that the mitochondrial SOD enzyme normally induced by iron or oxidative stress is activated less in FRDA (Jiralerspong *et al.*, 2001). This lack of induction of the superoxide scavenger may lead to higher levels of this

free radical. However, direct evidence of increased levels of superoxide is limited to a single report (Napoli *et al.*, 2006).

Increased levels of O_2 ultimately lead to increased levels of H_2O_2. In FRDA only indirect evidence of increased levels of H_2O_2 supports this assumption (Armstrong *et al.*, 2010) as low levels of GSH correlate with increased levels of H_2O_2. There is evidence showing decreased levels of GSH in a yeast model of FRDA (Auchère *et al.*, 2008). In a Drosophila model of FRDA, the disease phenotype could be rescued by H_2O_2 scavenging enzymes (Anderson *et al.*, 2008), providing indirect evidence that increased H_2O_2 levels and thus oxidative stress play a role in the pathogenesis of FRDA.

In FRDA, iron which is not used for Fe-S cluster synthesis accumulates in mitochondria. If it is not further processed immediately it can become oxidised and precipitates in the mitochondria. In the Fenton reaction Fe^{2+} is oxidised by H_2O_2 to form Fe^{3+} and the highly toxic hydroxyl radical which is generated causes oxidative damage; in particular lipid peroxidation. The increased levels of H_2O_2 present in FRDA feed this reaction (Armstrong *et al.*, 2010, Pandolfo, 2012). Additionally there is evidence showing that frataxin is able to convert the reactive Fe^{2+} to a redox-inactive mineral (Nichol *et al.*, 2003). A deficiency of frataxin thereby leads to increased levels of Fe^{2+} also feeding the Fenton reaction (Armstrong *et al.*, 2010, Pandolfo, 2012). Although these results provide evidence for increased oxidative stress in FRDA more evidence is required to fully understand the role of oxidative stress in this disease. Frataxin deficient cells are highly sensitive to oxidative stress and have reduced capability to handle oxidative insults (Payne and Wagner, 2012). Although the exact function of frataxin is not fully understood, once transported to the mitochondrion it is

known to be essential for iron homeostasis; in particular for the de novo biosynthesis of iron sulphur cluster (ISC) proteins and heme biosynthesis (Schmucker *et al.*, 2011). It is, thereby, involved in activation of the tricarboxylic cycle enzyme aconitase, which can be used as an indicator of low levels of frataxin protein and mitochondrial damage (Payne and Wagner, 2012). Deficiency in frataxin results in impaired biosynthesis and the function of ISC proteins of the ETC leading to reduced ATP and energy production (Lodi *et al.*, 1999). Cells highly dependent on aerobic respiration and high ATP levels such as neurons in the brain and spinal cord, cardiomyocytes and pancreatic beta cells especially succumb to this imbalance in energy homeostasis and this is believed to cause the neurological and cardiac symptoms and the high prevalence of diabetes in FRDA patients. What causes the variable cell death within tissues, however, is still unclear (Richardson *et al.*, 2013).

5.3 DNA damage in Friedreich ataxia

DNA is the most 'looked after' macromolecule in our cells. Histones are specialised proteins which bind as octamers to DNA molecules to form nucleosomes: the smallest packaging state of DNA. Nucleosomes are further packaged into different stages of chromatin fibres, which build up our chromosomes (Shi and Oberdoerffer, 2012, Talbert and Henikoff, 2010). Even though DNA is rather well protected by this packaging, different endogenous and exogenous insults can lead to DNA damage. Different repair mechanisms are available to reverse this damage. However not all damage can be repaired and this results in an accumulation of mutations in our DNA over time.

5.3.1 Different types and sources of DNA damage

Two types of DNA alterations are apparent in cells. Spontaneous DNA damage is caused by endogenous damaging sources such as replication errors or ROS. Misincorporation of dNTPs during replication, interconversion between DNA bases by deamination, a loss of bases by depuration or modification of DNA bases by alkylation may lead to point mutations in DNA. ROS which are increased during oxidative stress may oxidise DNA bases and cause DNA breaks (Ciccia and Elledge, 2010). Environmental DNA damage is caused by exogenous genotoxic agents. Physical sources can be distinguished from chemical sources. The most toxic agent is ionizing radiation that is capable of oxidising bases and inducing single and double strand breaks (SSBs and DSBs respectively). Ultraviolet radiation is a source for pyrimidine dimers. Different chemical agents create various DNA lesions. Alkylating agents lead to adducts on DNA bases, crosslinking agents create inter- and intra-strand crosslinks and topoisomerase inhibitors induce SSBs and DSBs (Ciccia and Elledge, 2010).

5.3.2 DNA damage response and repair pathways

The DNA damage response (DDR) is a complex network of signalling pathways that senses DNA damage and transmits this signal to effectors which in turn repair the present damage. Different mechanisms are available in the cell that are specialised in handling different types of DNA lesions: The mismatch repair (MMR) deals with misincorporated dNTPs, base excision repair (BER) deals with modified DNA bases, nucleotide excision repair (NER) with adducts or pyrimidine dimers, and the interstrand crosslink (ICL) repair pathway deals with interstrand crosslinks and SSB repair (Ciccia and Elledge, 2010).

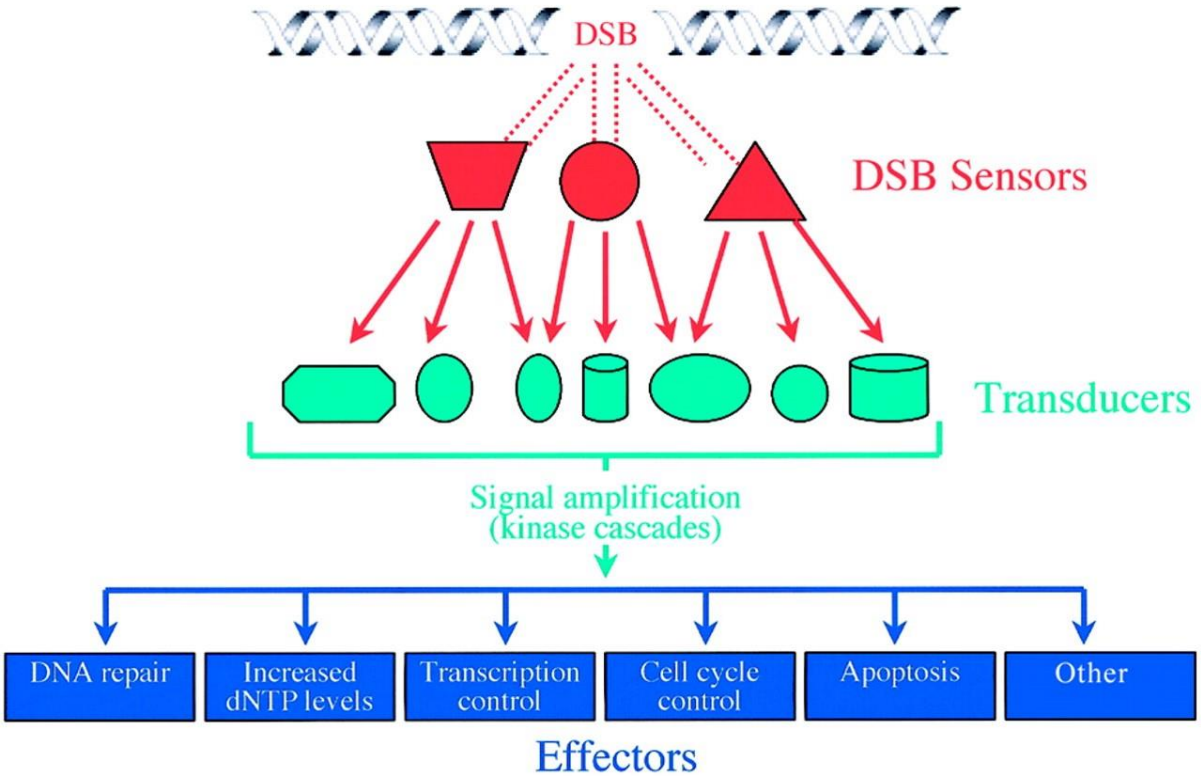

Figure 5.2: Schematic representation of the cellular response to DNA DSBs. Multiple sensor proteins detect the DSB and transmit the signal to transducers which amplify the signal and transfer it to effector proteins. A range of downstream effectors regulate various aspects of cellular function.

Two different mechanisms repair DSBs which is the most lethal DNA lesion. Homologous recombination (HR) repairs DSBs during S and G2 phase using the sister chromatid as a template and thus repairing the lesion without causing mutations. Non-homologous end-joining (NHEJ), the second and predominant mechanism to repair DSBs, re-joins the two strands by removing some of the terminal bases to create a template for the repair machinery. However, by doing so some of the information coded in the DNA sequence is lost and mutations may be generated (Bourton *et al.*, 2012, Ciccia and Elledge, 2010). In the DDR, DSBs are sensed by the specialised MRN-complex, which activates a PI-3-kinase called ataxia telangiectasia mutated (ATM), a main mediator of the DDR. ATM phosphorylates many mediators and

effectors of the DDR including H2AX, a histone variant. This signalling network finally recruits the repair machinery to the DNA lesion to repair it (Ciccia and Elledge, 2010).

5.3.3 The histones

DNA wraps around two molecules each of the histone proteins H2A, H2B, H3 and H4 to build one nucleosome. These proteins can be modified by different post-translational modifications, including methylation, acetylation or phosphorylation. These modifications are used to control the accessibility of the DNA and its packaging stage. Additionally, the incorporation of histone variants (including macro-H2A, H2AX and H2AZ) modulates the function of the nucleosomes. Overall these modifications of histones influence the transcription of DNA to RNA, DNA repair, chromosomes segregation and gene silencing (Shi and Oberdoerffer, 2012, Talbert and Henikoff, 2010).

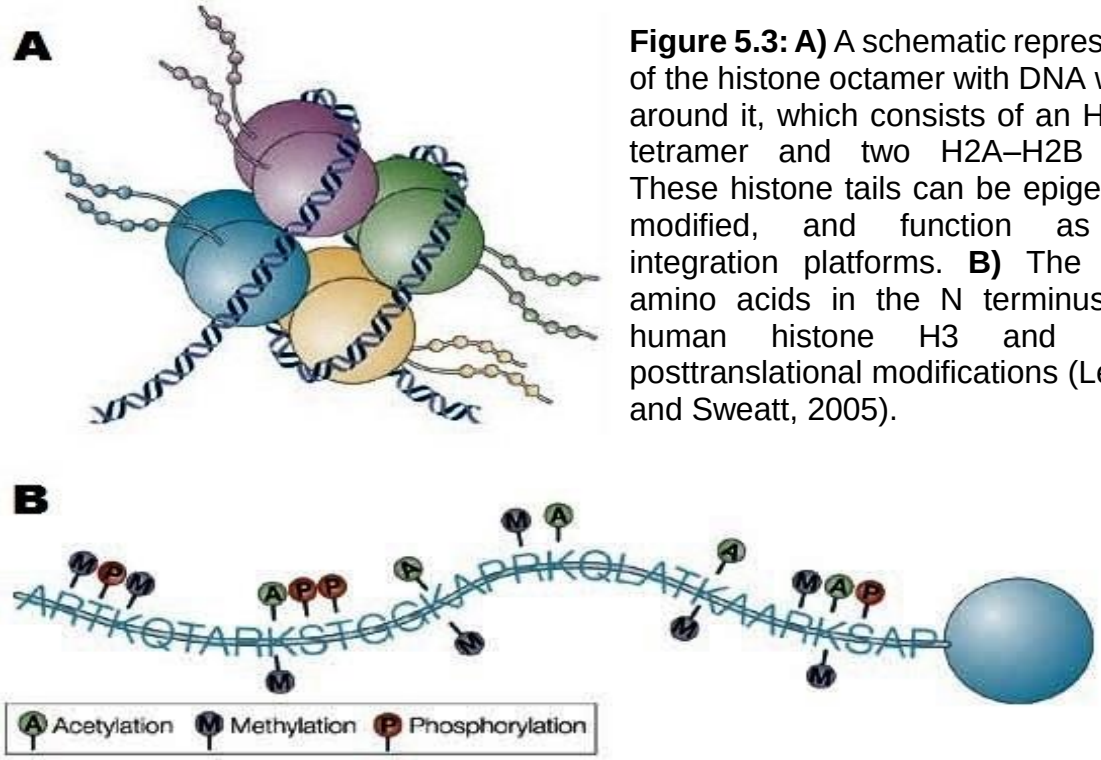

Figure 5.3: A) A schematic representation of the histone octamer with DNA wrapped around it, which consists of an H32–H42 tetramer and two H2A–H2B dimers. These histone tails can be epigenetically modified, and function as signal integration platforms. **B)** The first 30 amino acids in the N terminus of the human histone H3 and possible posttranslational modifications (Levenson and Sweatt, 2005).

H2AX, the variant of histone H2A, accounts for 2-10% of the H2A complement in mammalian tissues. The C-terminal motif SQ(D/E)(I/L/Y)-(end) distinguishes H2AX from the other H2A variants. The serine residue in this motif, which is on position 139, becomes phosphorylated upon DNA damage induction; especially after DSBs (Rogakou *et al.*, 1998). This phosphorylated form of H2AX is termed γH2AX.

5.3.4 γH2AX - a marker for DNA damage

Using fluorochrome-coupled antibodies the rapid accumulation of γH2AX foci can be observed at any nascent DNA DSB. The first foci become visible within three minutes after DSB induction (for example by γ-irradiation) increasing in size until thirty minutes after irradiation (Sedelnikova *et al.*, 2003). Phosphorylated molecules of H2AX spread over tens of kilobases of DNA flanking the break site. Once DSB repair starts and the lesions are removed, the number of γH2AX foci decreases (Celeste *et al.*, 2003, Valdiglesias *et al.*, 2013). In untreated cells background levels of γH2AX foci formation can be measured. This constitutive H2AX phosphorylation differs between cell lines and between cell cycle phases (Albino *et al.*, 2006, Tanaka *et al.*, 2006). Physiological recombination events, such as V (D)J-recombination, class-switch events, or recombination events, during meiosis are responsible for a part of these background levels. Additionally, as described earlier, DNA is continuously exposed to damage by endogenous sources, especially to oxidants. These increased levels of oxidants and oxidative stress may lead to an increased number of DSBs, more DNA that is damaged and ultimately genetic instability (Sedelnikova *et al.*, 2003, Tanaka *et al.*, 2006). Thus, oxidative stress in FRDA may also have the potential to lead to genome instability.

5.3.5 Techniques to measure γH2AX foci formation

Two main techniques are established to measure γH2AX foci formation; both are based on the detection of γH2AX proteins by fluorochrome-linked antibodies. This fluorescent immunohistochemical visualisation of γH2AX foci is a versatile approach which allows both quantification and localisation of DSBs (Valdiglesias *et al.*, 2013). Classical γH2AX immunostaining (which uses 100x magnification microscopes for analysis) allows the detection of individual nuclei and number of foci per nucleus and thus, the damage distribution within cells. However, this technique is laborious and subjected to human errors. Alternatively, analysis using flow cytometry allows the rapid measurement of thousands of cells thereby increasing the statistical significance of the data obtained. Moreover, a simultaneous assessment of other proteins is possible. Unfortunately, the number of foci per cell cannot be counted by conventional flow cytometry (Valdiglesias *et al.*, 2013). Imaging flow cytometry presents a novel approach combining these two techniques with each other. By using this method, images of thousands of cells can be captured within minutes and computer based analysis allows the assessment of the number of foci for each cell. A study comparing imaging flow cytometry with classical microscope analysis provided evidence that both methods produce similar profiles for the γH2AX formation after DSB induction by γ-irradiation (Bourton *et al.*, 2012). On average, the in situ method counted higher numbers of foci probably due to a higher magnification used (imaging flow cytometry used only 40x magnification in contrast to the in situ approach with a 100x magnification). Overall, imaging flow cytometry provides a novel approach that produces results with higher statistical significance combining the advantages of both flow cytometry and microscopy (Bourton *et al.*, 2012). New machines with higher

magnifications are becoming available, extinguishing the disadvantage of low magnification associated with imaging flow cytometry.

5.3.6 DNA damage in Friedreich ataxia

Evidence produced using a yeast model of FRDA suggests that increased levels of DNA damage occurs in FRDA. The absence of frataxin in this yeast model lead to nuclear damage, measured by the inducibility of a nuclear DNA damage reporter, increased recombination and mutation events counting for chromosomal instability and a greater sensitivity to DNA damaging agents (Karthikeyan *et al.*, 2002). The same workgroup later showed that reduced levels of frataxin in a rad52 mutant yeast strain caused cells to arrest at the G2/M checkpoint of the cell cycle (Karthikeyan *et al.*, 2003). This evidence suggests that DNA damage, especially the number of DSBs, is possibly induced by increased levels of ROS. A different study produced evidence of increased mitochondrial and nuclear DNA damage in peripheral blood mononuclear cells (PBMCs). First, changes in gene expression measured by transcriptional profiling suggest that cells of FRDA patients show genotoxic stress. Second, increased levels of mitochondrial and nuclear DNA damage in PMBCs of FRDA patients was found compared to normal controls when directly measured by qPCR (Haugen *et al.*, 2010). Oxidative stress (OS) is known to be associated with genome instability (Negrini *et al.*, 2010) and in FRDA cells that lack *FXN* expression, the reduced ability for DNA damage repair is evident (Schmucker *et al.*, 2011, Schulz *et al.*, 2006). It is unclear whether low *FXN* expression leads to high levels of ROS and whether DNA damage is the only cause of neuronal degeneration.

In this chapter the effects of *FXN* gene delivery on oxidative stress will be studied and also the sensitivity of FRDA fibroblast cell lines to oxidative stress, by exposure to

increasing concentrations of H_2O_2 will be examined. Additionally genome instability profile will be investigated before and after *FXN* gene delivery using the histone variant marker γH2AX, and then the FRDA fibroblasts will be challenged with γ-irradiation to induce DNA damage in order to investigate the DNA damage repair potential in LV *FXN* treated FRDA cells versus untreated FRDA cells.

5.4 Measurement of oxidative stress in FRDA and normal fibroblasts

The levels of OS was examined in both human and mouse FRDA fibroblasts before and after treatment with LV *FXN* and LV GFP by measuring oxidized proteins, as described in Chapter 2 section 2.2.37 using OxyBlot™ Protein Oxidation Detection Kit (Millipore). This kit provides the chemical and immunological reagents necessary to perform the immunoblot detection of carbonyl groups introduced into proteins by oxidative reactions. To assess the reliability and accuracy of the kit, normal mouse fibroblasts (Y47) were subjected to H_2O_2-induced OS with a final concentration of 150 µM for 30 minutes and 60 minutes. Following treatment of protein samples bands were visualised using the Molecular Imager® Gel Doc XR+ system (Bio-Rad), and densitometry was carried out using Image Lab™ 4.1 analysis software (Bio-Rad). The levels of protein oxidation increased in correlation with increased exposure to H_2O_2 treatment and it was evident that changes in oxidative stress can be detected using this kit. The levels of oxidative stress increased from 100% in normal Y47 mouse fibroblasts to 187% after 30 minutes and 271% after 60 minutes of exposure. (Figure 5.4A & B).

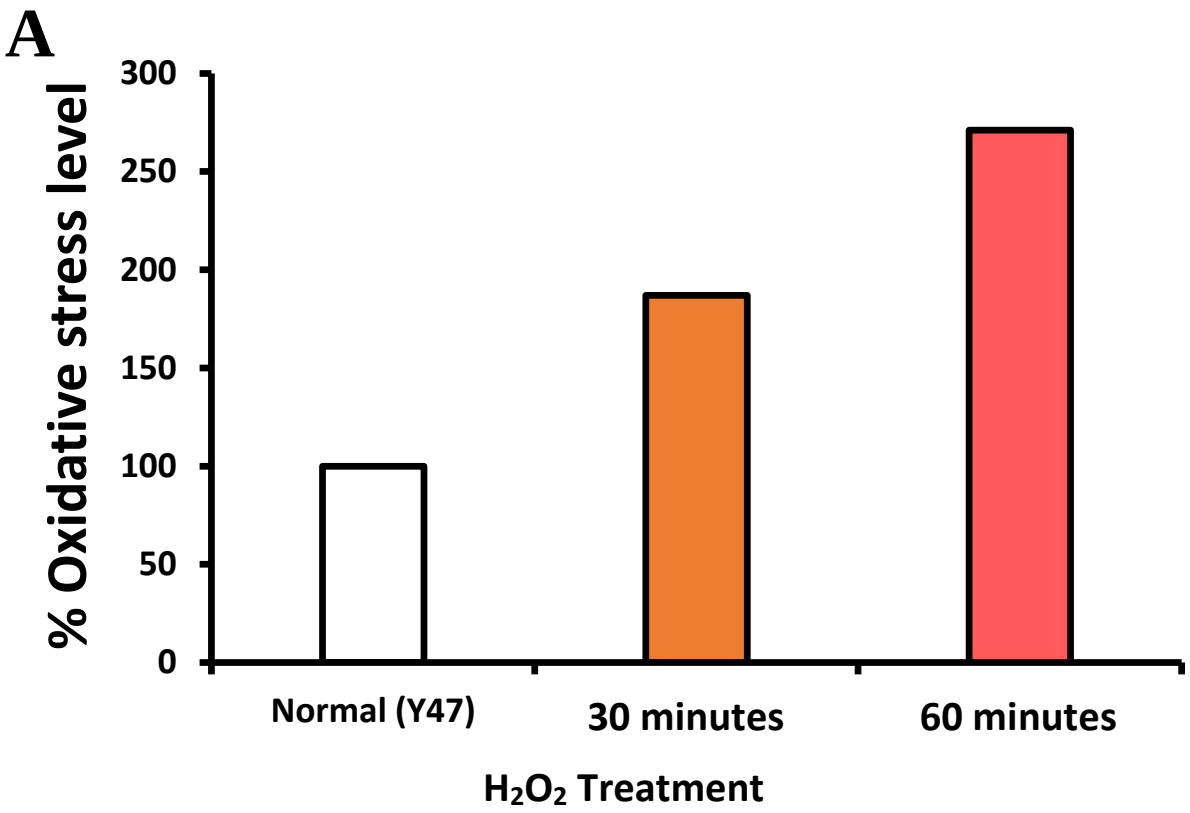

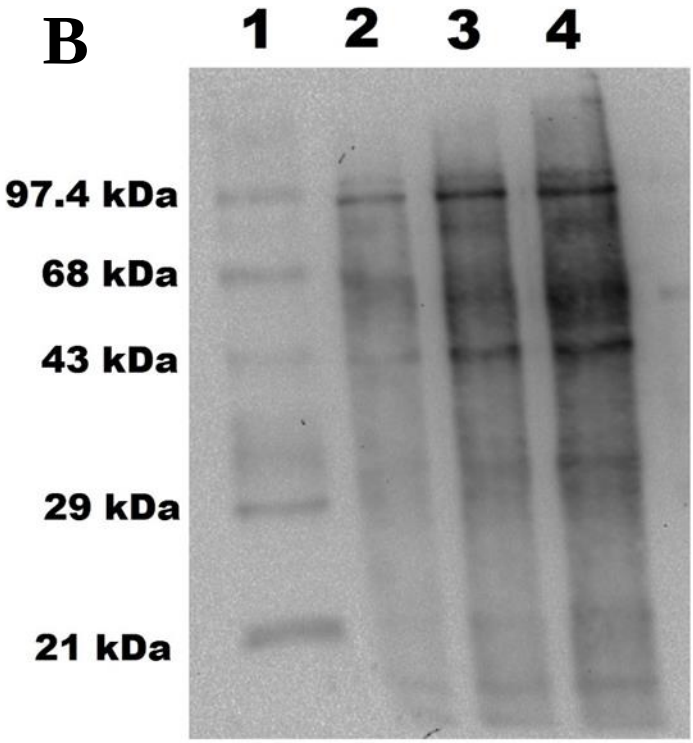

Figure 5.4: A) H_2O_2-induced oxidative stress measurement with OxyBlot™ Protein Oxidation Detection Kit. The levels of protein oxidation had increased to 187% after 30 minutes and 271% after 60 minutes following treatment compared to normal set as 100%. **B)** Protein oxidation visualised using ImageLab software. Lane 1: Protein Ladder. Lane 2: Untreated normal mouse fibroblasts Y47. Lane 3: 30 minutes exposure to H_2O_2. Lane4: 60 minutes exposure to H_2O_2.

Oxidative levels were measured two weeks post viral treatment and normal human fibroblasts GMO7492 along with normal mouse fibroblasts Y47, were used as controls for this experiment and all data obtained was calibrated to normal fibroblasts levels and the mean of normal control was set at 100%. Human FRDA fibroblasts and FRDA fibroblasts treated with LV GFP showed the highest levels of OS with 193% and 172% (P <0.001) compared with normal fibroblasts. Statistical significance of the differences for this experiment was evaluated by two-way ANOVA and the data showed was no significant difference between the untreated FRDA cells and FRDA cells treated with LV GFP. Interestingly the levels of OS decreased significantly to 26.6% (P <0.001) after treatment with LV *FXN* compared to normal fibroblasts (Figure 5.5A & B). Untreated mouse FRDA fibroblasts also showed high levels of OS with levels at 172% (P <0.001) and this level of OS remained unchanged at 172.4% when treated with LV GFP (P <0.001) compared to normal fibroblasts. There was no significant difference between the untreated FRDA cells and cells treated with LV GFP. LV *FXN* treatment of mouse FRDA fibroblasts reduced the OS significantly to 28% (P <0.001) compared to normal fibroblasts (Figure 5.6A & B).

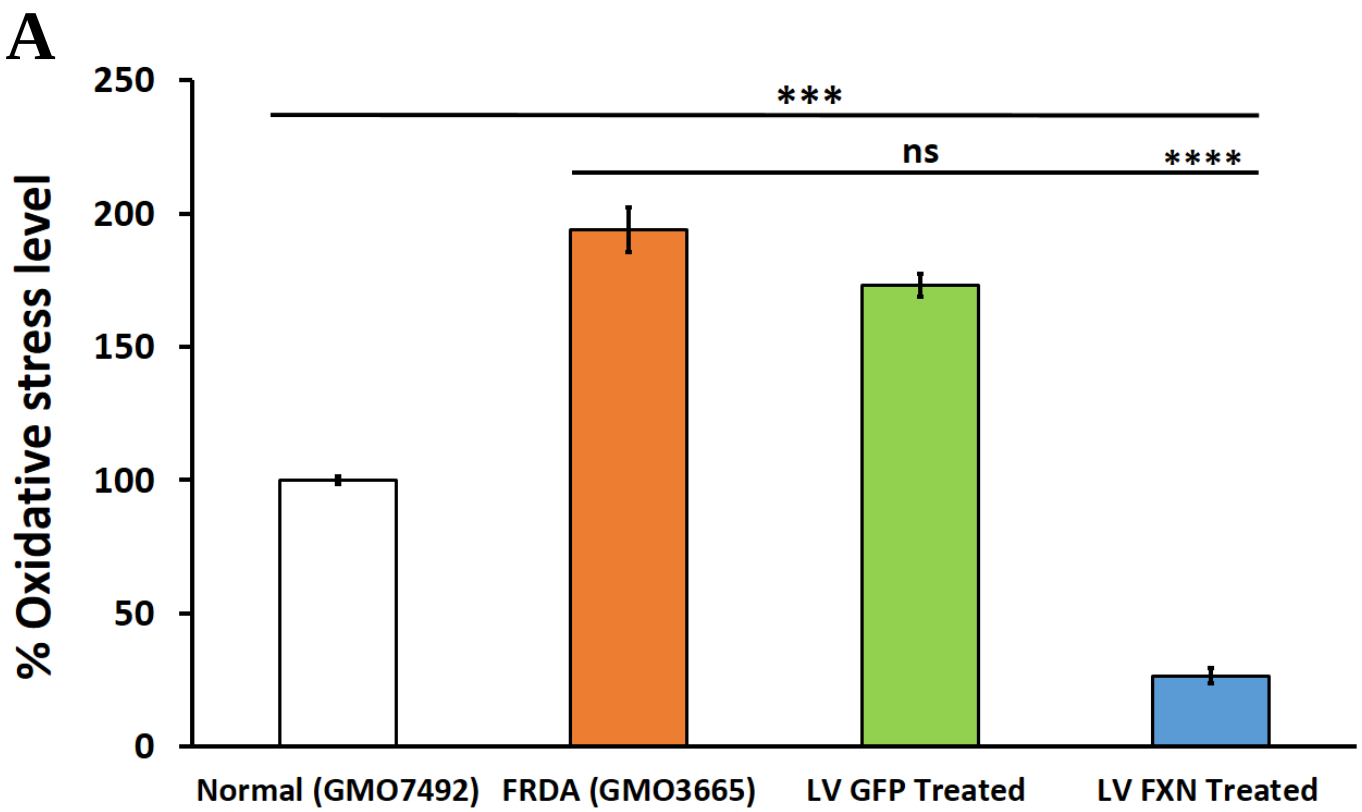

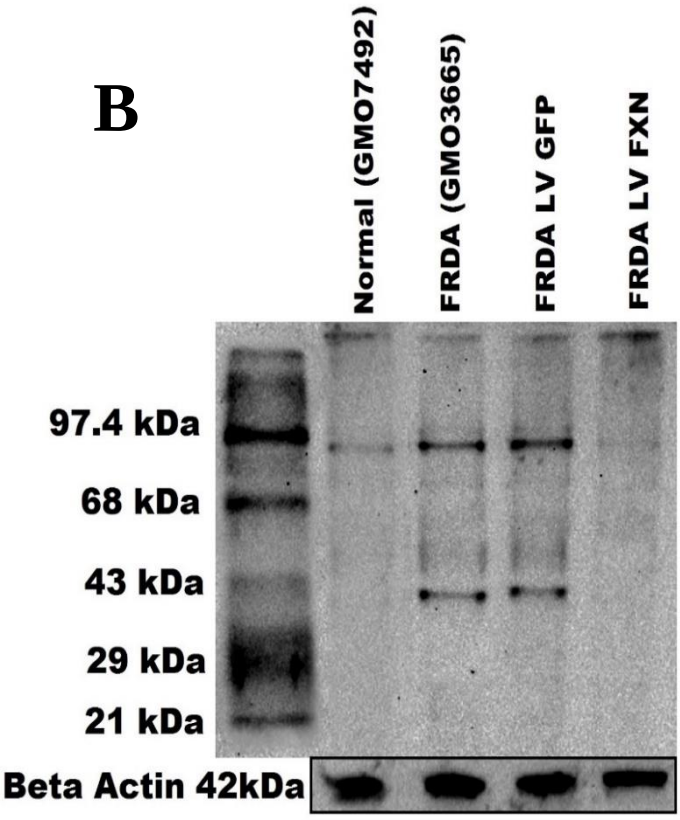

Figure 5.5 A & B: Human oxidized proteins as a measure of oxidative stress (OS) were identified and quantified using the Oxyblot™ kit. OS levels were compared between normal human fibroblasts, untreated FRDA fibroblasts and FRDA fibroblasts treated with either the LV GFP or LV *FXN*. In untreated human FRDA cells and LV GFP treated cells, oxidative stress levels was 193% and 172%, respectively compared with the levels found in normal fibroblasts (set at 100%). When the FRDA cells received LV *FXN* treatment OS levels was significantly reduced to 26%. Results are taken from the average of 5 independent experiments. Statistical differences between LV FXN treatment and normal control (GMO7492) are indicated by the top line drawn over the bars while the bottom line indicates the differences between LV FXN treatment and untreated FRDA (GMO3665). Error bars represent SEMs. Significance levels are represented by asterisks: ****P <0.0001, ***P <0.001 and ns= P >0.05**.**

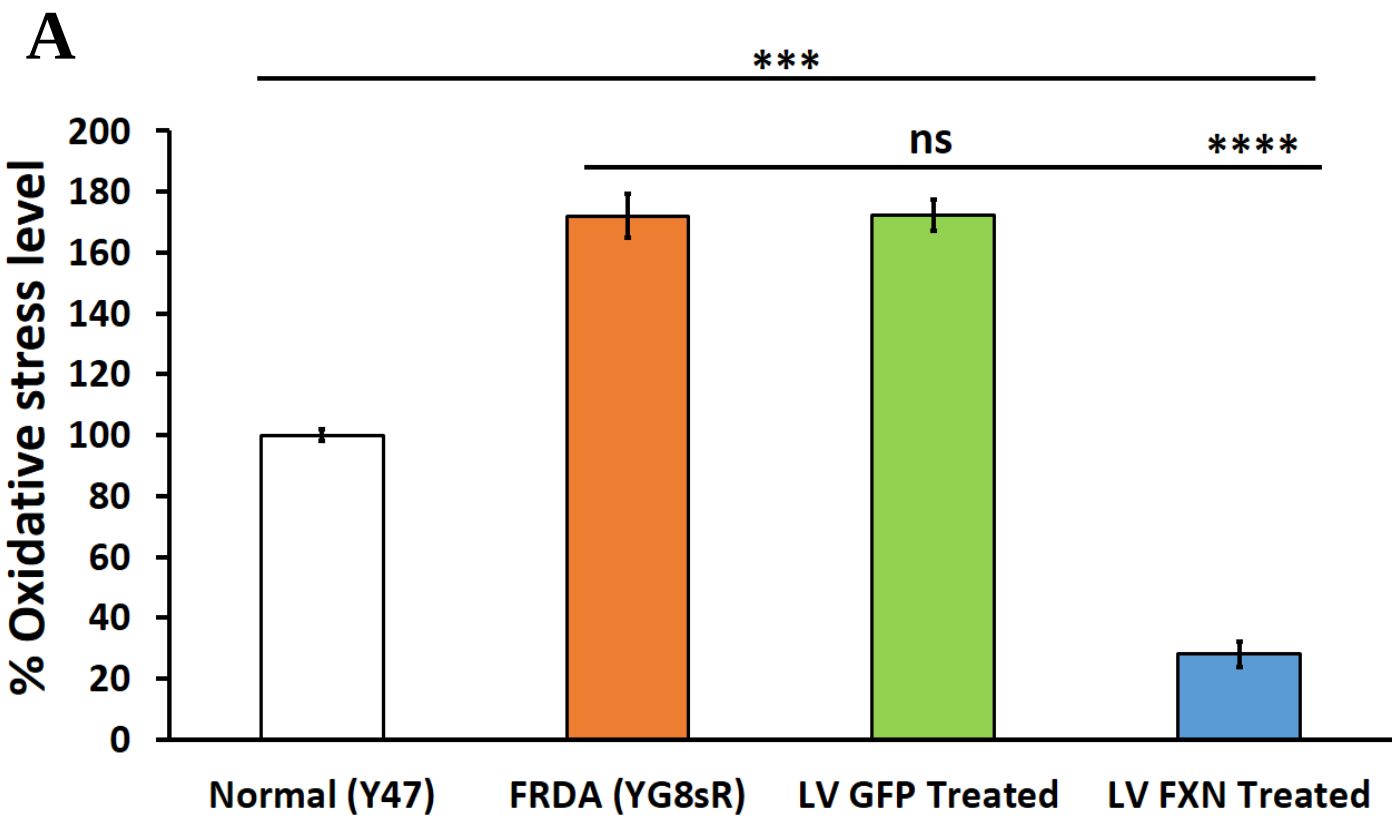

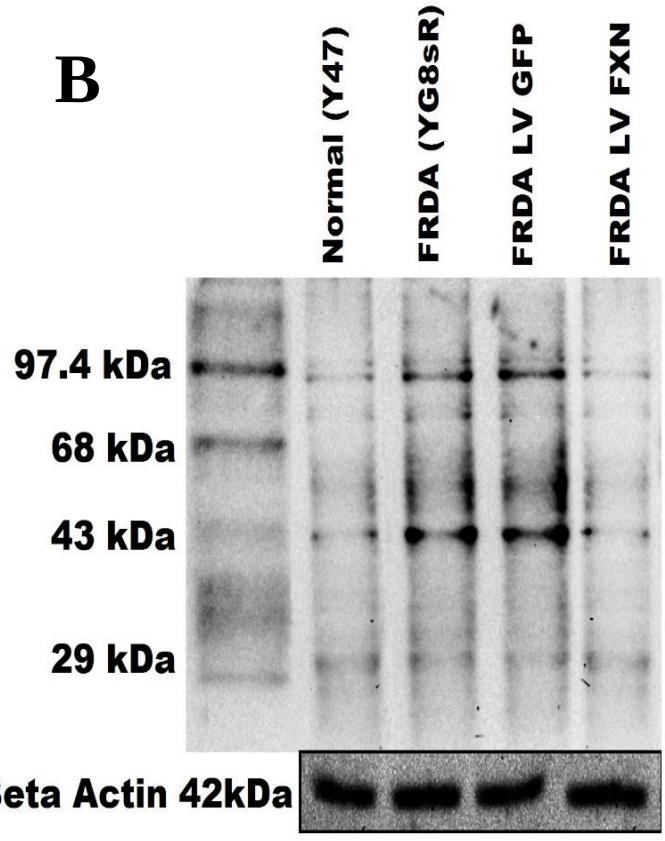

Figure 5.6 A & B: Mouse oxidized proteins as a measure of oxidative stress (OS) were identified and quantified using the Oxyblot™ kit. OS levels were compared between normal mouse fibroblasts, untreated FRDA fibroblasts and FRDA fibroblasts treated with either the LV GFP or LV *FXN*. In untreated mouse FRDA cells and LV GFP treated cells, oxidative stress levels was 172% and 172.4%, respectively, compared with the levels found in normal fibroblasts (set at 100%). When the FRDA cells received LV *FXN* treatment oxidative stress levels was significantly reduced to 28%. Results are taken from the average of 5 independent experiments. Statistical differences between LV FXN treatment and normal control (Y47) are indicated by the top line drawn over the bars while the bottom line indicates the differences between LV FXN treatment and untreated FRDA (YG8sR). Error bars represent SEMs. Significance levels are represented by asterisks: ****P <0.0001, ***P <0.001 and ns= P >0.05.

5.5 Cell viability with increasing levels of H_2O_2 induced oxidative stress

Normal and FRDA human and mouse fibroblasts were exposed to OS induced by increasing concentrations of H_2O_2 (50, 100, 150, 200 µM) for 6 hours after which time cell viability was determined by trypan blue exclusion (Chapter 2, section 2.2.5). Statistical significance of the differences for this experiment was evaluated by two-way ANOVA and both human and mouse FRDA cells exhibited significantly greater sensitivity compared to untreated controls at all doses (P <0.01) compared normal control cell line and when treated with LV GFP there was no significant change compared to the FRDA fibroblasts. Cell viability improved significantly in both human and mouse FRDA fibroblasts following *FXN* gene delivery (Figure 5.7 and Figure 5.8). This data suggests that *FXN* overexpression improved the sensitivity of FRDA cells to oxidizing reagent. Table 5.1 and Table 5.2 shows the percentage of viable cells with P values compared to untreated FRDA cells of human and mouse fibroblasts cells following treatment with increasing dose of H_2O_2.

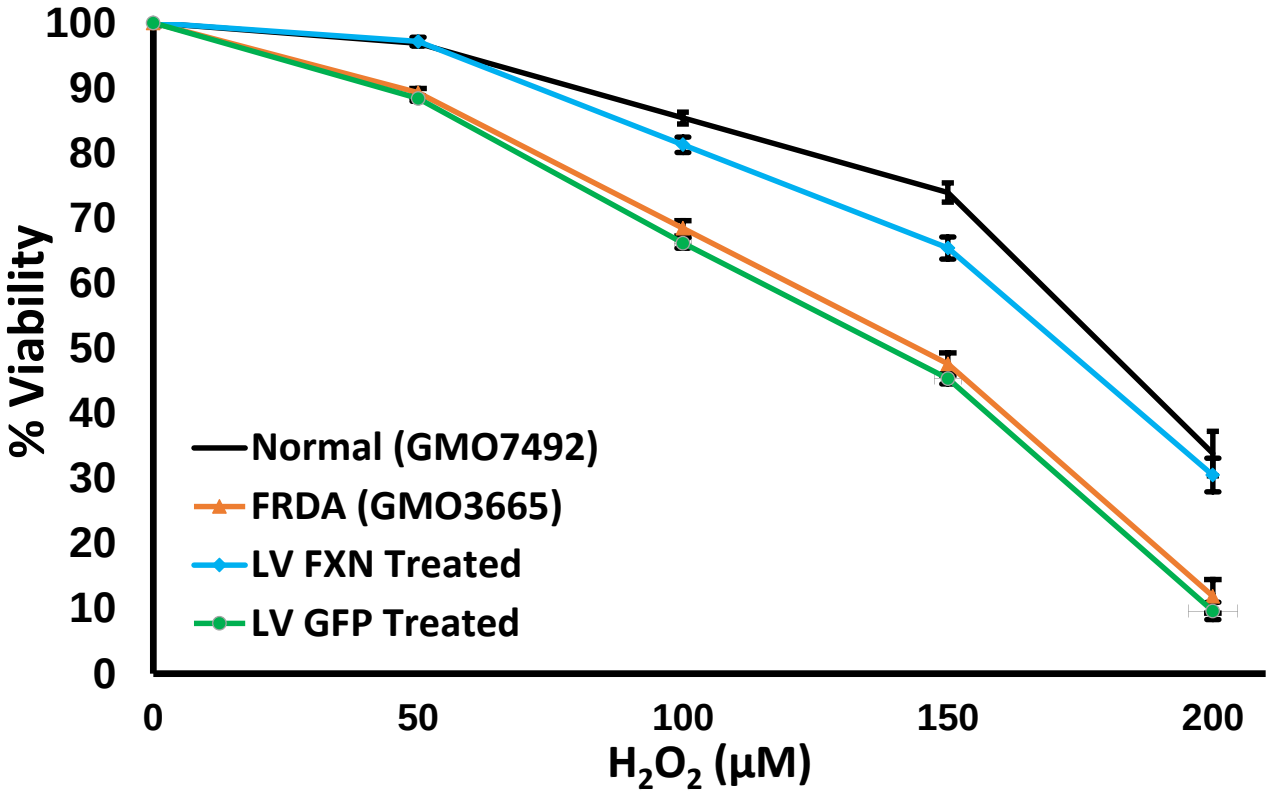

Figure 5.7: A graph showing the viability of human with increasing oxidative stress. Sensitivity of human primary fibroblasts (Normal= GMO7492, FRDA & Treated =GMO3665) after treatment with LV *FXN* and LV GFP. Cells were exposed to increasing concentrations (50, 100, 150, 200 µM) of H_2O_2 for 6 hours, after which time viability was determined by the trypan blue exclusion assay. Means of 4 independent experiments are shown and error bars represent SEM. Significance levels were $P < 0.05$ at all H_2O_2 concentrations compared to normal control and FRDA cells after LV FXN treatment.

H_2O_2 µM	FRDA (GMO3665)	LV GFP Treated		LV FXN Treated	
0	100	100	***P* value**	100	***P* value**
50	89	88	$P > 0.05$	97	$P < 0.001$
100	68	66	$P > 0.05$	81	$P < 0.01$
150	48	45	$P > 0.05$	65	$P < 0.001$
200	12	10	$P > 0.05$	31	$P < 0.001$

Table 5.1: Percentage viability of human normal and FRDA fibroblasts after induction with increasing concentrations of H_2O_2.

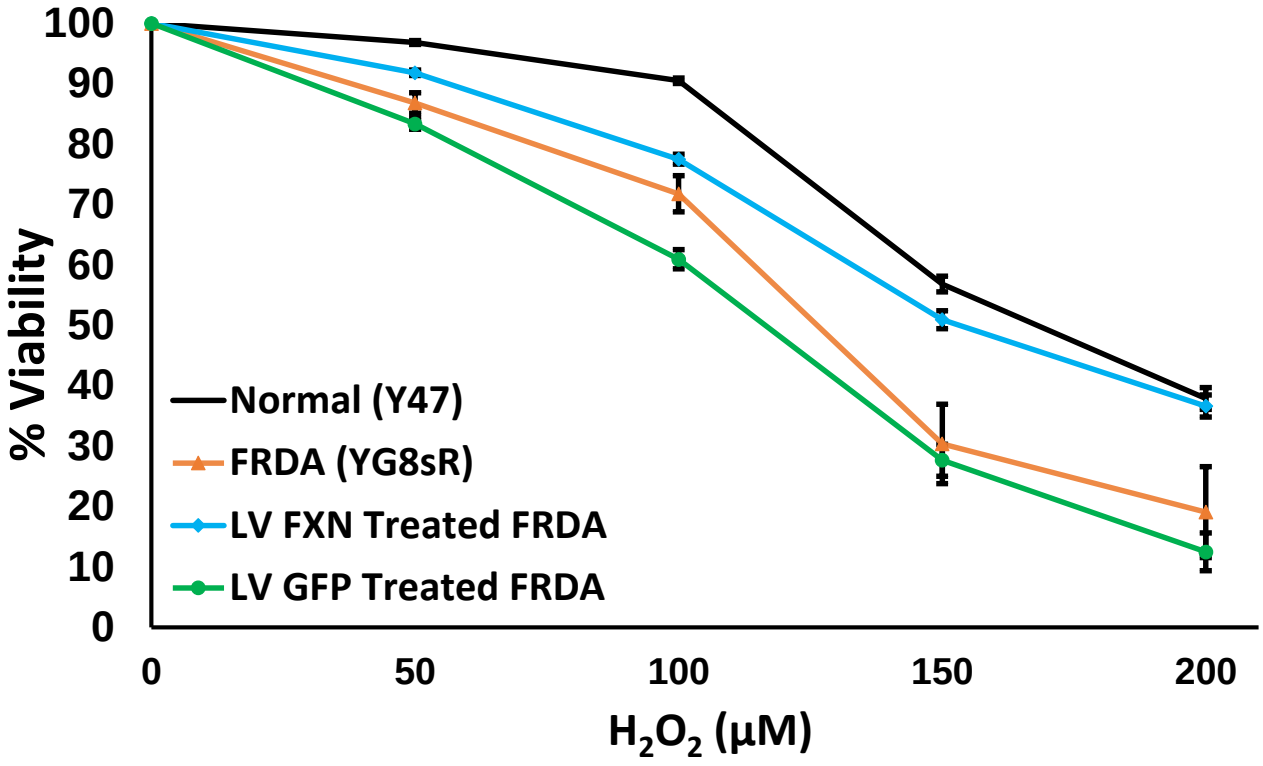

Figure 5.8: A graph showing the viability of mouse primary fibroblasts with increasing oxidative stress. Sensitivity of mouse primary fibroblasts (Normal= Y47, FRDA & Treated =YG8sR) after treatment with LV *FXN* and LV GFP. Cells were exposed to increasing concentrations (50, 100, 150, 200 µM) of H_2O_2 for 6 hours, after which time viability was determined by the trypan blue exclusion assay. Means of 4 independent experiments are shown and error bars represent SEM. Significance levels were P <0.05 at all H_2O_2 concentrations Significance levels were P < 0.05 at all H_2O_2 concentrations compared to normal control and FRDA cells after LV FXN treatment.

H_2O_2 µM	FRDA (YG8sR)	LV GFP Treated		LV *FXN* Treated	
0	100	100	***P* value**	100	***P* value**
50	87	83	*P* >0.05	92	*P* <0.05
100	72	61	*P* >0.05	78	*P* <0.05
150	30	28	*P* >0.05	51	*P* <0.01
200	19	12	*P* >0.05	37	*P >0.01*

Table 5.2: Percentage viability of mouse normal and FRDA fibroblasts after induction with increasing concentrations of H_2O_2.

5.6 Clonogenic cell survival following treatment with H_2O_2

Once the cell viability was determined the ability of the cells to survive was examined using the clonogenic assay as described in Chapter 2, section 2.2.6. In this assay normal and FRDA human and mouse fibroblasts were treated with 150 µM of H_2O_2 for six hours and after two weeks the number of surviving colonies were counted. Normal human fibroblasts GMO7492 and normal mouse fibroblasts Y47, were used as controls for this experiment and all data obtained was calibrated to normal fibroblasts levels and the mean of normal control is set at 100%. Human FRDA fibroblasts exhibited 68% cell survival (P <0.0001) and after treatment with LV *FXN* cell survival of FRDA fibroblast has increased to 91% (P >0.05) compared to normal fibroblasts. FRDA cell treated with LV GFP did not show any significant difference compared to FRDA fibroblasts (P >0.05) and displayed 67% cell survival (P <0.0001) compared to normal cells. Mouse FRDA fibroblasts had decreased levels of cell survival at 60% (P <0.0001) and this levels increased to 91% (P >0.05) after treatment with LV *FXN*. Mouse FRDA cells treated with LV GFP did not show any significant changes compared to FRDA cells (P >0.05) and showed cell survival at 59% (P <0.0001) compared to normal fibroblasts. Statistical significance of the differences for this experiment was evaluated by two-way ANOVA. Overall, both human and mouse FRDA fibroblasts treated with *FXN* gene transfer showed significant increases in survival compared to untreated FRDA cells and similar to normal fibroblasts (Figure 5.9A & B).

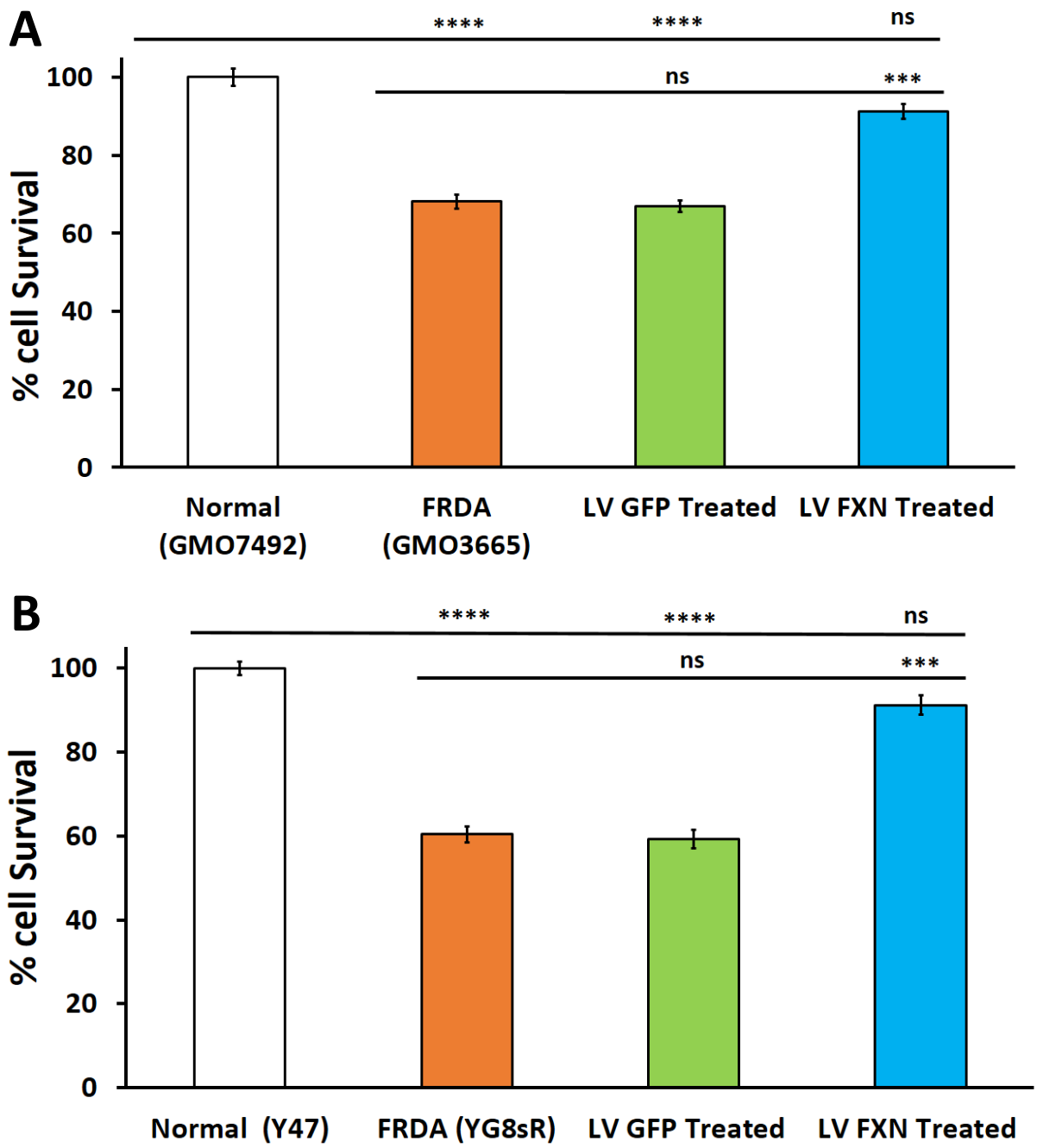

Figure 5.9: Graph showing cell survival in the presence of 150 µM H_2O_2. Clonogenic cell survival assays were performed on **A)** human and **B)** mouse FRDA fibroblast after treatment with 150 µM H_2O_2. Survival of cells treated with LV *FXN* and LV GFP was expressed as a percentage of survival of untreated control cells. The data are an average of ten independent experiments. Statistical differences between LV FXN treatment and normal control are indicated by the top line drawn over the bars while the bottom line indicates the differences between LV FXN treatment and untreated FRDA. Error bars represent SEM. Significance levels are represented by asterisks: ****P <0.0001, ***P <0.001 and ns= P >0.05.

5.7 Genome instability in FRDA cells is reversed following FXN gene delivery

Since FRDA cells have been shown to be associated with genomic instability and have an impaired ability to repair damaged nuclear DNA, the levels of DSB was measured in human and mouse FRDA fibroblasts following *FXN* gene transfer using imaging flow cytometry Imagestream^X as described in Chapter 2, section 2.2.39 and immunocytochemical detection as described in Chapter 2, section 2.2.40. In these methods, γH2AX recruitment to DNA DSB is detected and the numbers of DSB positive nuclear foci is compared with the number found in normal fibroblasts. Using imaging Imagestream^X the levels of DSB in human FRDA fibroblasts was found to be elevated to 4 foci/cell (P <0.001) compared to 2.1 foci/cell in normal human fibroblasts and this level was reduced to 1.99 foci/cell after treatment with LV FXN compared to untreated FRDA fibroblasts (P <0.001) (Figure 5.10A). A similar pattern was observed in mouse fibroblasts where mouse FRDA fibroblasts had the highest DSB with 4.5 foci/cell (P <0.001) compared with normal Y47 cells with 2.8 foci/cell. The levels of DSB breaks in FRDA cells decreased to 2.7 foci/cell (P <0.001) after treatment with LV *FXN* compared to untreated FRDA fibroblasts (Figure 5.10B). From these results, an improvement of DNA damage profile was evident following LV FXN treatment. Statistical significance of the differences for this experiment was evaluated by two-way ANOVA.

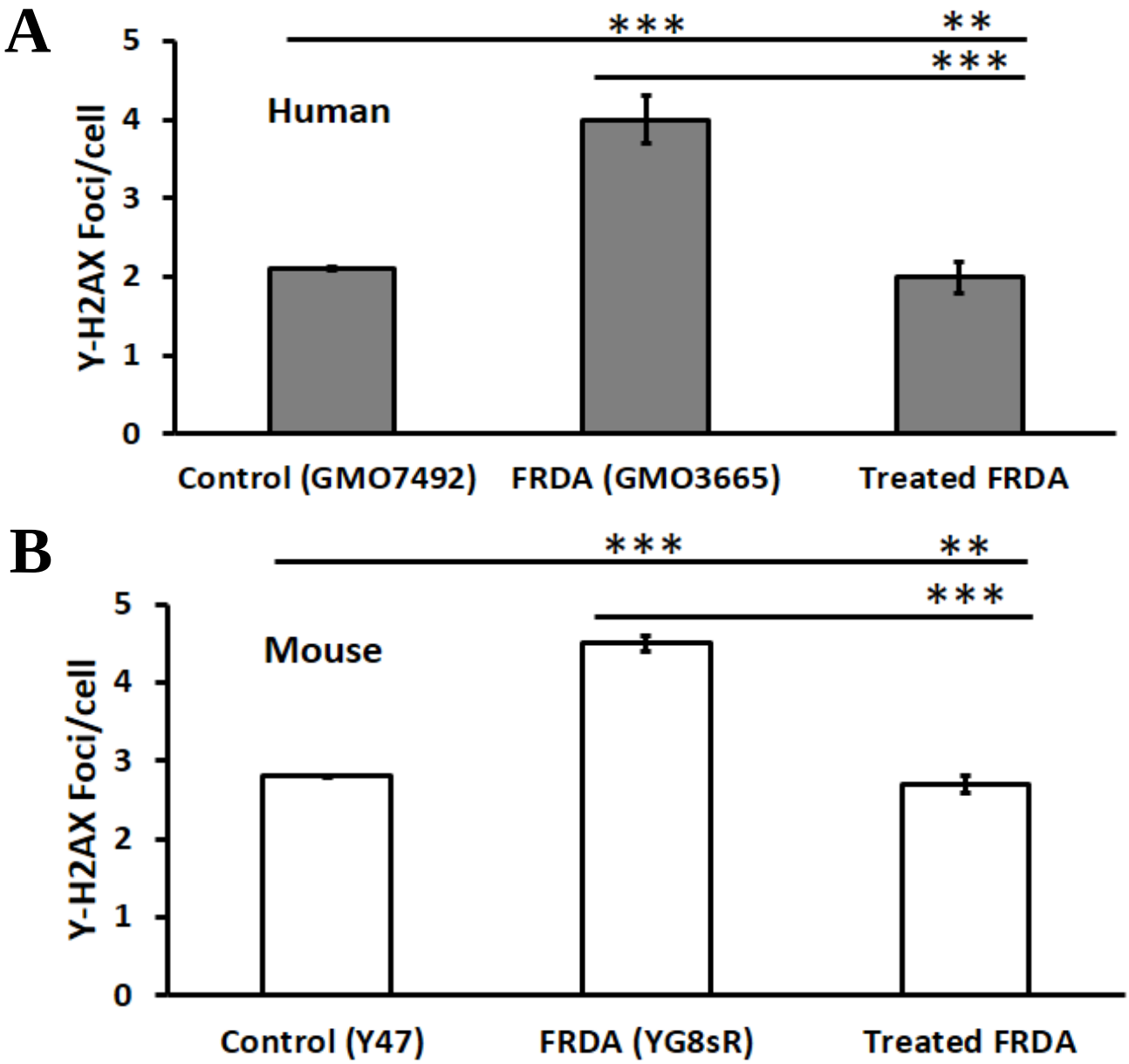

Figure 5.10: A graph showing the mean number of γH2AX foci per cell as measured by Imagestream^X. In both **A)** human and **B)** mouse primary fibroblasts, the mean was calculated over 3 experiments for normal fibroblasts and 5 experiments for FRDA fibroblasts and LV *FXN* treated fibroblasts. (n=28000 for human normal fibroblasts GMO7492:, n=40464 for human FRDA fibroblasts GMO3665, and n=39664 for LV *FXN* treated FRDA fibroblasts) (n=15000 for mouse normal fibroblasts Y47, n=19000 for mouse FRDA fibroblasts YG8sR, and n=23000 for LV *FXN* treated FRDA fibroblasts).In human cell lines, FRDA fibroblasts with the mean of 4 showed higher numbers of γH2AX foci per cell compared to normal cells with 2.1 and LV *FXN* treated cells with 1.99 foci per cell. In mouse cell lines, FRDA fibroblasts with the mean of 4.5 showed higher numbers of γH2AX foci per cell compared to normal cells with 2.8 and LV *FXN* treated cells with 2.7 foci per cell. The mean was calculated from two independent experiments performed in duplicate. Statistical differences between LV FXN treatment and normal control are indicated by the top line drawn over the bars while the bottom line indicates the differences between LV FXN treatment and untreated FRDA. Error bars show the SEM. Significance levels are represented by asterisks: ** P <0.01 and *** P <0.001.

Although the improvement of the LV *FXN* treatment was visible by this method and high numbers of cells were counted for each cell line (10,000 to 50,000), the numbers of foci/cell detected was found to be generally higher compared to the previously published data. This was due to the low magnification (X40) used in this system which led to imprecise/high number of foci/cells. Hence, this experiment was repeated using immunocytochemical detection of γH2AX foci which higher magnification (X100) to detect γH2AX foci. Using this technique human FRDA cells exhibited 0.9 foci/cell (P <0.001) compared to human normal fibroblast with 0.34 foci/cell. DSB level have reduced to 0.46 foci/cell after treatment with LV FXN compare to untreated FRDA fibroblasts (P <0.001). YG8sR mouse FRDA fibroblasts also showed a highest number of DSB with 1.9 foci/cell (P <0.001) compared to normal Y47 cells with 0.56 foci/cell. Also a reduction in DSB was observed in FRDA fibroblasts when treated with LV *FXN* with 0.8 foci/cell compared to untreated FRDA fibroblasts (P <0.001) (Figure 5.11). Statistical significance of the differences for this experiment was evaluated by two-way ANOVA. This data confirmed the previous finding that LV *FXN* treatment helps to improve genomic instability.

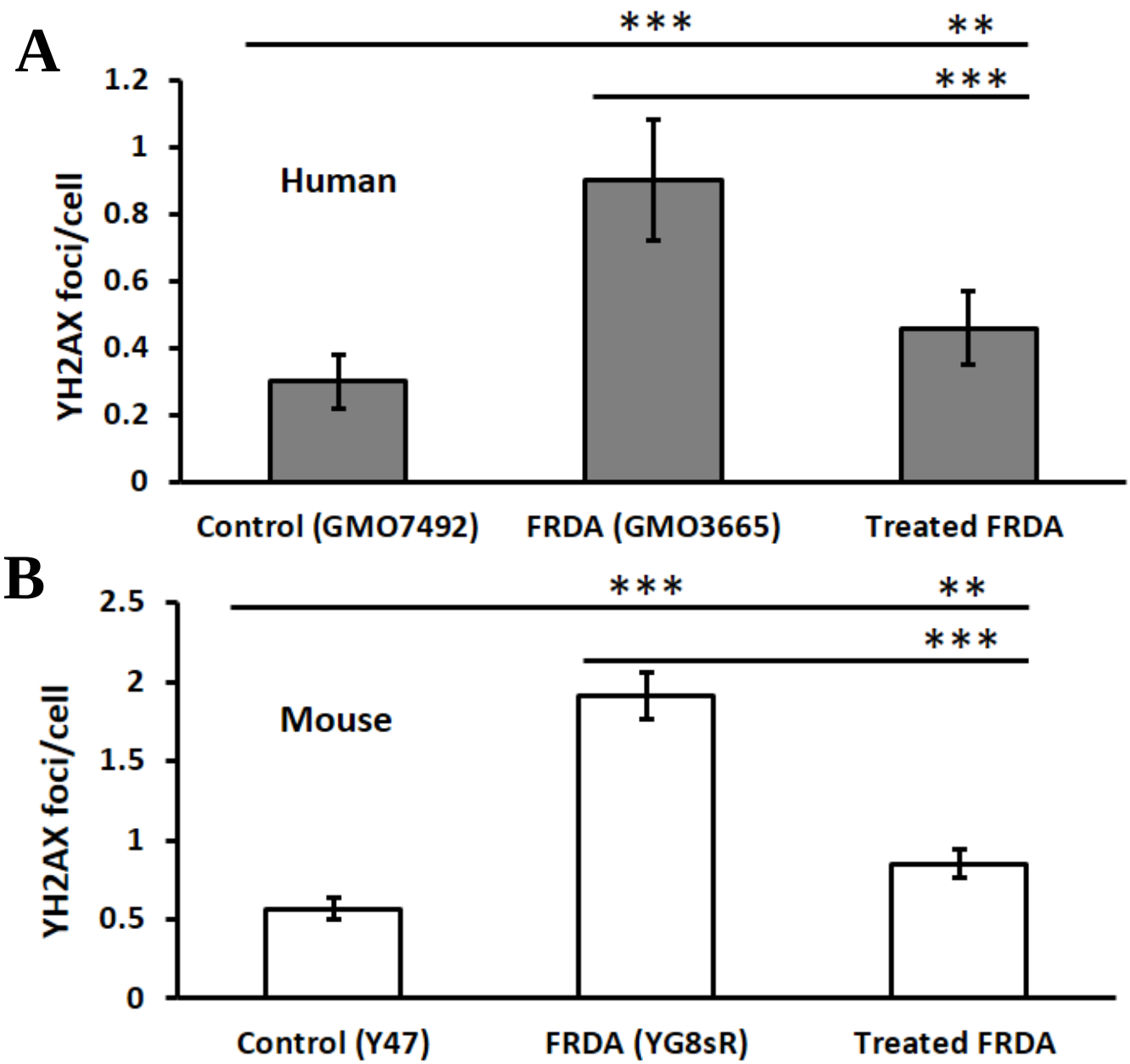

Figure 5.11: A graph showing the mean number of γH2AX foci per cell measured by immunocytochemistry. **A)** human primary fibroblasts, normal fibroblasts (GMO7492, n=400), FRDA fibroblasts (GMO3665, n=400) and LV *FXN* treated FRDA fibroblasts (GMO3665 n=400) and **B)** mouse primary fibroblasts, normal fibroblasts (Y47, n=400), FRDA fibroblasts (YG8sR, n=400) and LV *FXN* treated FRDA fibroblasts (YG8sR n=400). In human cell lines, FRDA fibroblasts with a mean of 0.9 showed higher numbers of γH2AX foci per cell compared to Normal cells with 0.3 and *FXN*-treated cells with 0.46 foci per cell. In mouse cells, FRDA fibroblasts with a mean of 1.9 showed higher numbers of γH2AX foci per cell compared to normal cells with 0.56 and LV *FXN*-treated cells with 0.8 foci per cell. The mean was calculated from two independent experiments performed in duplicate. Statistical differences between LV FXN treatment and normal control are indicated by the top line drawn over the bars while the bottom line indicates the differences between LV FXN treatment and untreated FRDA. Error bars show the SEM. Significance levels are represented by asterisks: ** P <0.01 and *** P <0.001.

5.8 *FXN* gene delivery restores DNA damage repair in FRDA fibroblasts

Once the reduced levels of DSB following LV *FXN* gene delivery was established, the DNA damage repair profile of human and mouse FRDA fibroblasts subjected to low level (2 Gy) radiation was assessed by measuring the recruitment and clearance of the phosphorylated γH2AX histone marker over a 48 hour period initially and then over a 72 hour period.

All samples as proliferating monolayers were subjected to 2 Gy gamma irradiation from a 60Cobalt source (Puridec Irradiation Technologies Ltd, Oxon, UK), as described in Chapter 2, section 2.2.39. Cells were then fixed at 0.5 hr, 24 hr, 48hr and 72 hr and stained for γH2AX marker, as described previously (Chapter 2, section 2.2.39). Initially, LV *FXN* treated human and mouse fibroblasts were analysed up to 48 hours and the peak number of foci/cell was observed at 0.5 hr and 5 hr post irradiation and the DNA repair took place after a 24 hr period. At 48 hr although the levels of γH2AX foci had decreased in human and mouse FRDA fibroblasts to 0.68 foci/cell (P <0.001) and 0.87 foci/cell (P <0.05), respectively, these levels were still higher compared to the normal cells with 0.3 foci/cell for normal human fibroblast (GMO7492) and 0.5 foci/cell for normal mouse fibroblasts (Y47). However, in both human and mouse fibroblasts the DSB levels were significantly lower when compared to FRDA fibroblasts (P <0.001) (Figure 5.12 and Figure 5.13). Statistical significance of the differences for this experiment was evaluated by two-way ANOVA. The number of γH2AX foci in human and mouse fibroblasts at each time point is summarised in Table 5.3 and Table 5.4.

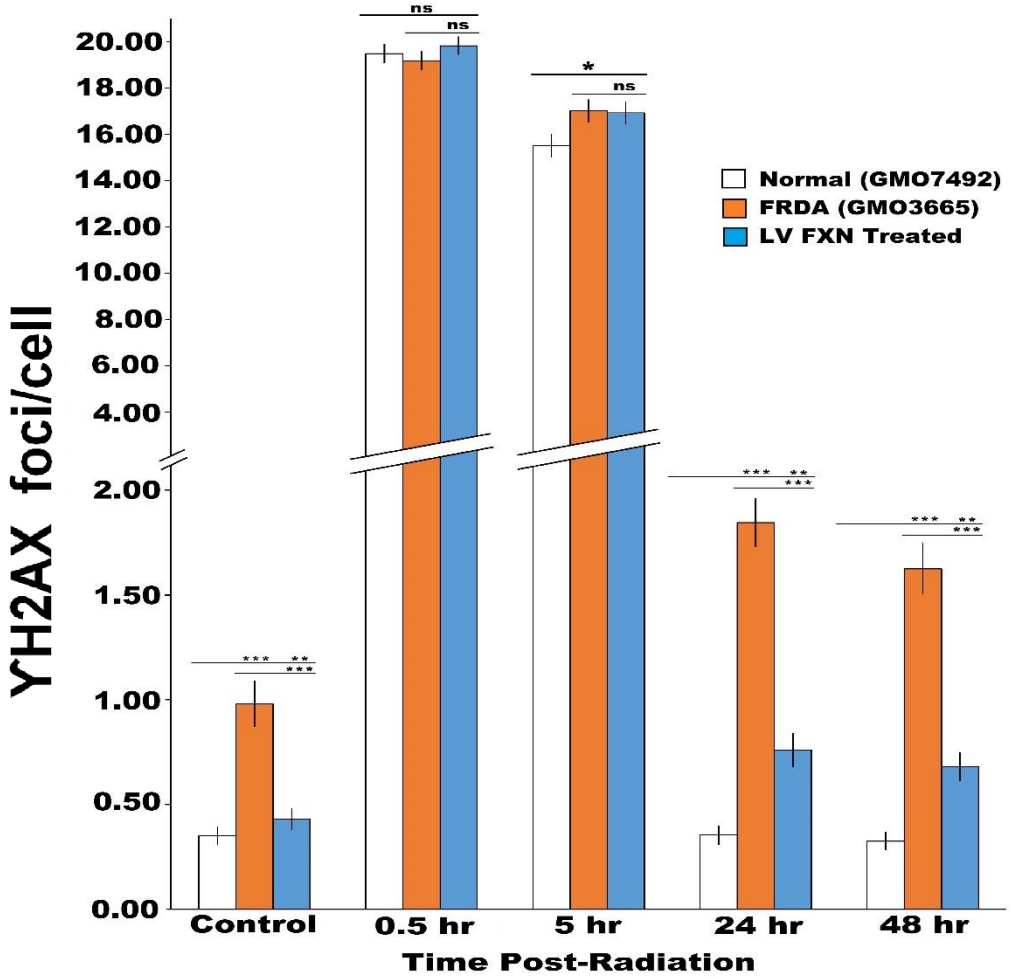

Figure 5.12: A graph showing the mean number of γH2AX foci per cell measured by immunocytochemistry after 0.5, 5, 24 and 48 hours post irradiation at 2 Gy in human primary fibroblasts (Normal: GMO7492, n=400. FRDA: GMO3665, n=400. LV *FXN* treated FRDA: GMO3665 n=400) calculated from two independent experiments performed in duplicate. Statistical differences between LV FXN treatment and normal control (GMO7492) are indicated by the top line drawn over the bars while the bottom line indicates the differences between LV FXN treatment and untreated FRDA (GMO3665). Error bars represent SEM. Significance levels are represented by asterisks: ns= *P* >0.05, **P* <0.05, ***P* <0.01 and ****P* <0.001.

Sample	Untreated	0.5 hr	5 hr	24 hr	48 hr
Normal GMO7492	0.35	19.4	15.5	0.3	0.32
FRDA GMO3665	0.98	19.1	17.0	1.8	1.6
LV *FXN* treated	0.43	19.8	16.9	0.7	0.68

Table 5.2: Summary of the γH2AX foci per cell at 0.5 hr, 5 hr, 24 hr and 48 hr post radiation in human fibroblasts.

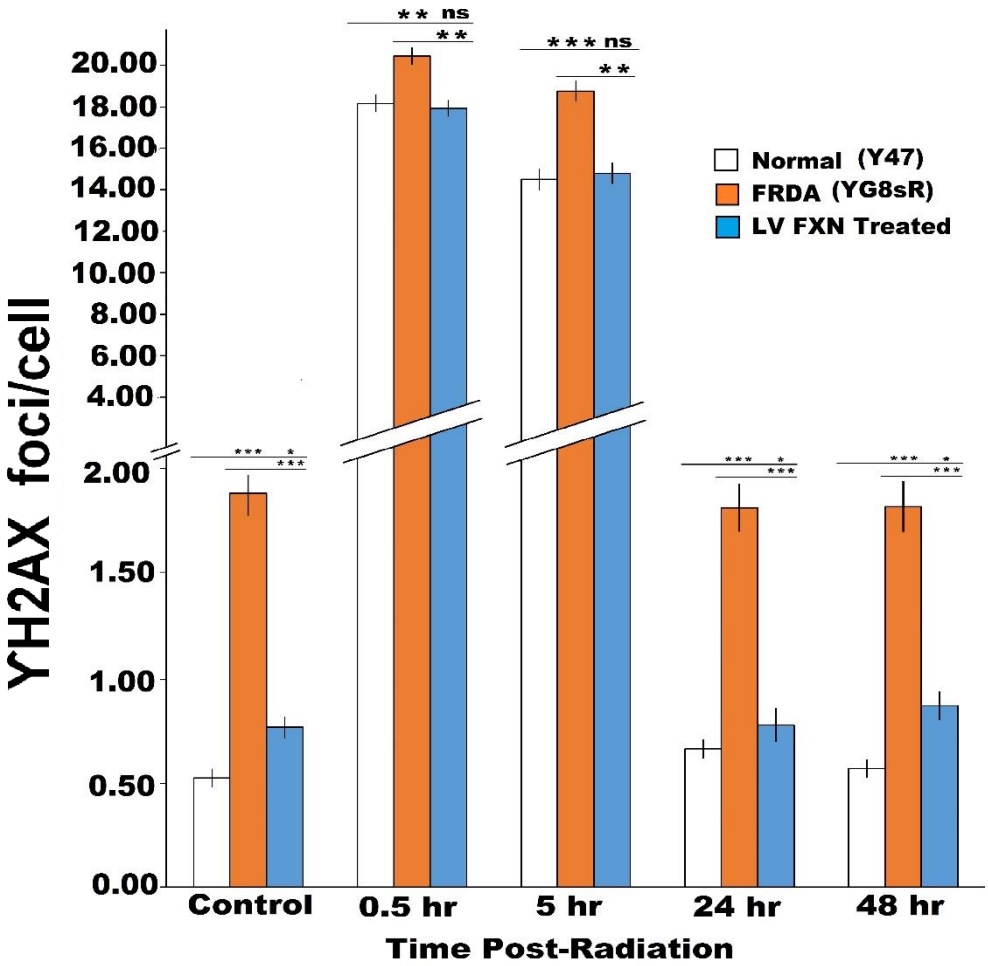

Figure 5.13: A graph showing the mean number of γH2AX foci per cell measured by immunocytochemistry after 0.5, 5, 24 and 48hours post irradiation at 2 Gy in mouse primary fibroblasts (Normal: Y47, n=400. FRDA: YG8sR, n=400. LV FXN treated FRDA: YG8sR n=400) calculated from two independent experiments performed in duplicate. Statistical differences between LV FXN treatment and normal control (Y47) are indicated by the top line drawn over the bars while the bottom line indicates the differences between LV FXN treatment and untreated FRDA (YG8sR). Error bars represent SEM. Significance levels are represented by asterisks: ns= *P* >0.05, *P <0.05, **P* <0.01 and *** *P* <0.001.

Sample	Untreated	0.5 hr	5 hr	24 hr	48 hr
Normal Y47	0.52	18.1	14.5	0.6	0.57
FRDA YG8sR	1.88	20.4	18.7	1.8	1.8
LV *FXN* treated	0.77	17.9	14.7	0.78	0.87

Table 5.3: Summary of the γH2AX foci per cell at 0.5 hr, 5 hr, 24 hr and 48 hr post radiation in mouse fibroblasts.

To further investigate if the levels of DSB will reduce to the levels observed in normal cells, this experiment was repeated with the addition of a 72 hr time point post radiation. Similar to previous data γH2AX foci peaked at 0.5 hr and 5 hr post radiation and repair took place 24 hr post radiation in both human and mouse fibroblasts. In human FRDA fibroblasts treated with LV *FXN* the repair appears to be slower and further reduction of γH2AX foci was observed with 0.49 foci/cell (P <0.001) compared to 0.67 foci/cell (P <0.001) at 48hr time point. The same pattern of DNA damage repair is observed in the LV *FXN* treated FRDA mouse however there was not a significant change in number of γH2AX foci between the 48 hr (0.83 foci/cell (P <0.05)) and the 72 hr time points (0.82 foci/cell (P <0.05)). In both FRDA fibroblasts treated with *FXN*, however, DNA damage repair potential is restored albeit with levels of DSBs slightly higher than the numbers observed in normal fibroblasts (Figure 5.14 and 5.15). Statistical significance of the differences for this experiment was evaluated by two-way ANOVA. The number of γH2AX foci in human and mouse fibroblasts at each time point is summarised in Table 5.5 and Table 5.6.

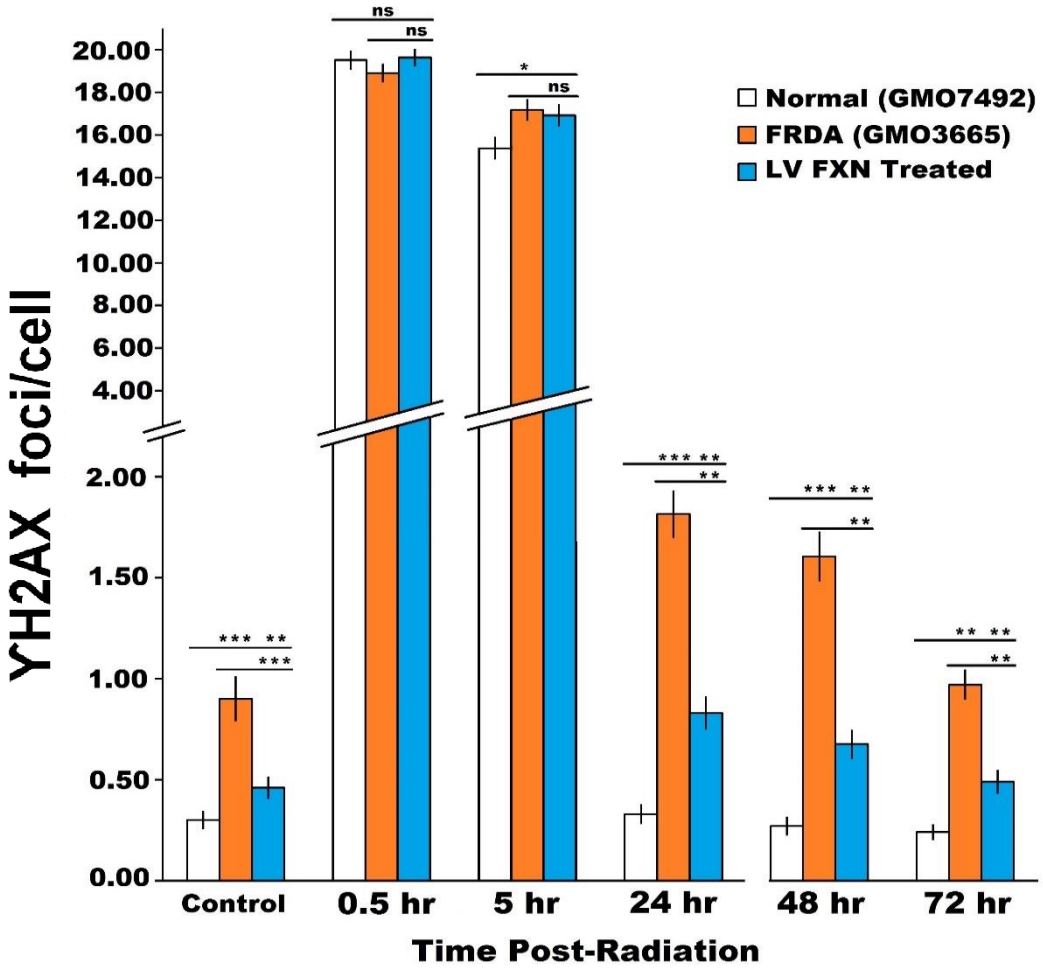

Figure 5.14: A graph showing the mean number of γH2AX foci per cell measured by immunocytochemistry after 0.5, 5, 24, 48, 72 hours post irradiation at 2 Gy in human primary fibroblasts (Normal: GMO7492, n=400. FRDA: GMO3665, n=400. LV *FXN* treated FRDA: GMO3665 n=400) calculated from two independent experiments performed in duplicate. Statistical differences between LV FXN treatment and normal control (GMO7492) are indicated by the top line drawn over the bars while the bottom line indicates the differences between LV FXN treatment and untreated FRDA (GMO3665).Error bars represent SEM. Significance levels are represented by asterisks: * *P* <0.05, ** *P* <0.01 and *** *P* <0.001.

Sample	Untreated	0.5 hr	5 hr	24 hr	48 hr	72 hr
Normal (GMO7492)	0.3	19.27	15.14	0.33	0.27	0.24
FRDA (GMO3665)	0.9	18.67	16.94	1.82	1.61	0.97
LV *FXN* Treated	0.46	19.39	16.69	0.83	0.68	0.49

Table 5.4: Summary of the γH2AX foci per cell at 0.5 hr, 5 hr, 24 hr and 48 hr post radiation in human fibroblasts.

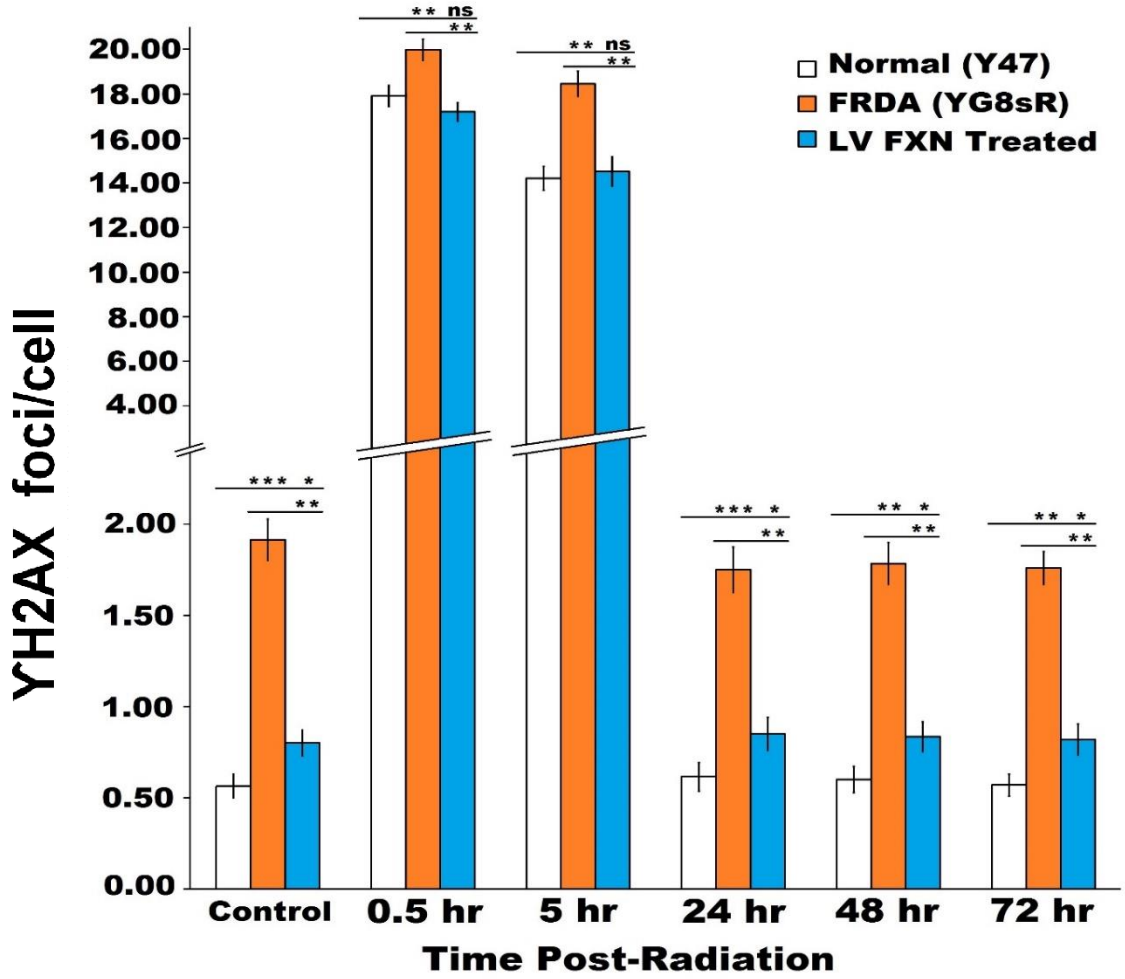

Figure 5.15: A graph showing the mean number of γH2AX foci per cell measured by immunocytochemistry after 0.5, 5, 24, 48, 72 hours post irradiation at 2 Gy in mouse primary fibroblasts (Normal: Y47, n=400. FRDA: YG8sR, n=400. LV *FXN* treated FRDA: YG8sR n=400) calculated from two independent experiments performed in duplicate. Statistical differences between LV FXN treatment and normal control (Y47) are indicated by the top line drawn over the bars while the bottom line indicates the differences between LV FXN treatment and untreated FRDA (YG8sR). Error bars represent SEM. Significance levels are represented by asterisks: * *P* <0.05, ***P* <0.01 and *** *P* <0.001.

Sample	Control	0.5 hr	5 hr	24 hr	48 hr	72 hr
Normal (Y47)	0.57	17.97	14.28	0.62	0.6	0.57
FRDA (YG8sR)	1.92	20.05	18.52	1.75	1.79	1.76
LV *FXN* Treated	0.8	17.26	14.58	0.85	0.84	0.82

Table 5.5: Summary of the γH2AX foci per cell at 0.5 hr, 5 hr, 24 hr and 48 hr post radiation in mouse fibroblasts.

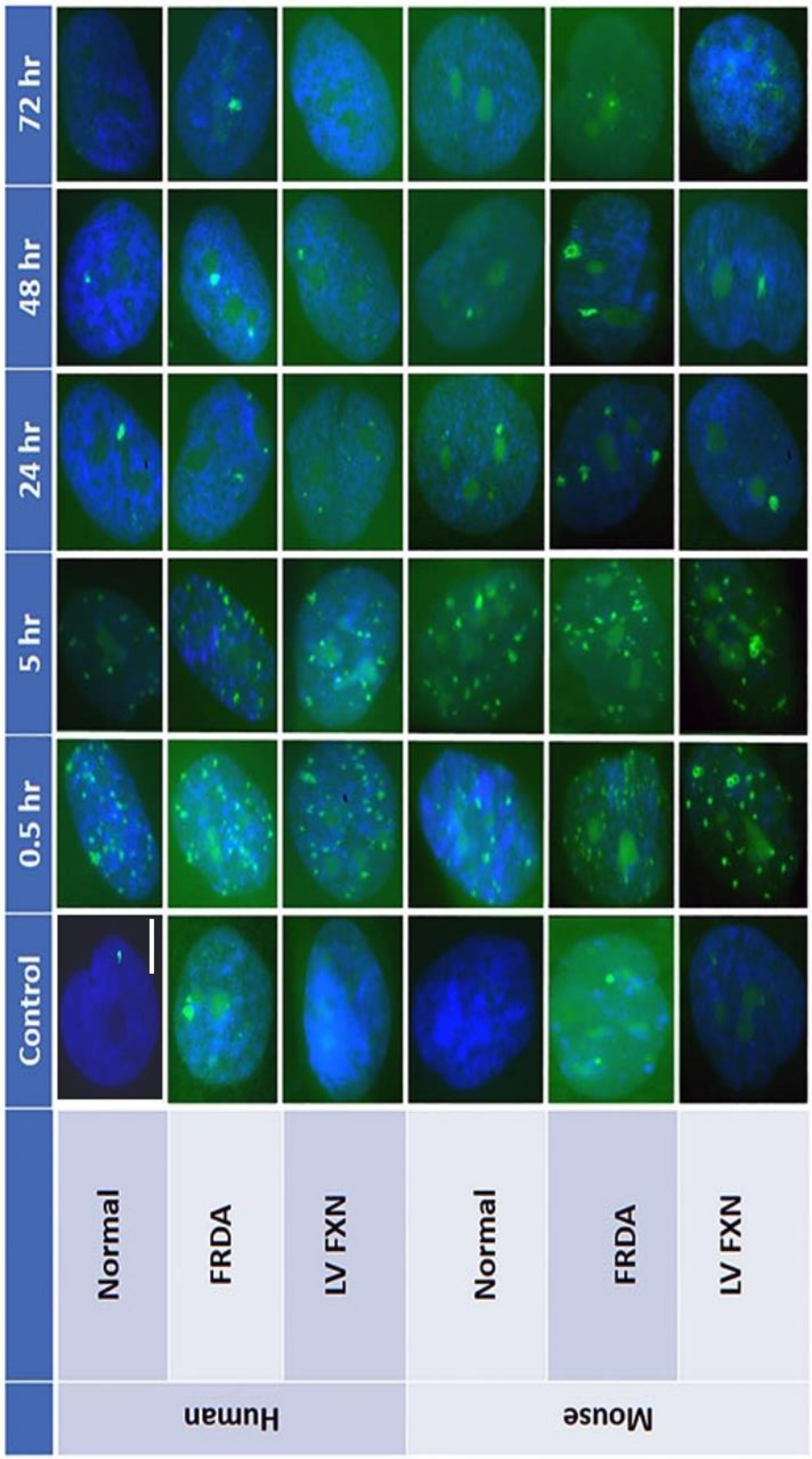

Figure 5.16: Analysis of genome instability via immunocytochemistry of fixed cells and γH2AX foci per cell. Genome instability can be measured via immunostaining of γH2AX which is recruited to DNA double strand breaks (DSB). FRDA cells have more DSB than normal fibroblasts. When FRDA fibroblasts are subjected to 2Gy radiation they are less able to repair. The ability to repair DSBs is restored following delivery with LV FXN. Scale bars, 10 μm.

5.9 Localisation of frataxin isoforms to subcellular compartments

Frataxin protein processing involves the production of a transient intermediate form and the fully mature form, of which the latter is known to localise to mitochondria. Fibroblast cells treated with LV FXN and treated with LV GFP along with untreated YG8sR mouse model and human patients and control normal fibroblasts were fractionated to isolate mitochondria, nuclei and cytoplasmic fractions. Each fraction was subjected to Western analysis for the presence of these forms using a primary antibodies and secondary-HRP conjugated antibody to identify both intermediate and mature human and mouse forms of frataxin as described in Chapter 2 section 2.2.41. As expected, high frataxin protein levels were found in the mitochondria in the 14 kDa mature form. In the cytoplasm, the 19 kDa transient intermediate form was also identified. In addition, a weak band representing the mature form was identified in the normal control mouse fibroblast nuclei and a stronger band was found in the nuclei of the mouse FRDA fibroblasts treated with pHR'SIN-cPPT-SFFV-FXN-WPRE (Figure 5.17A and B). Neither the intermediate or mature forms were observable in the nuclei of human patient and healthy fibroblasts.

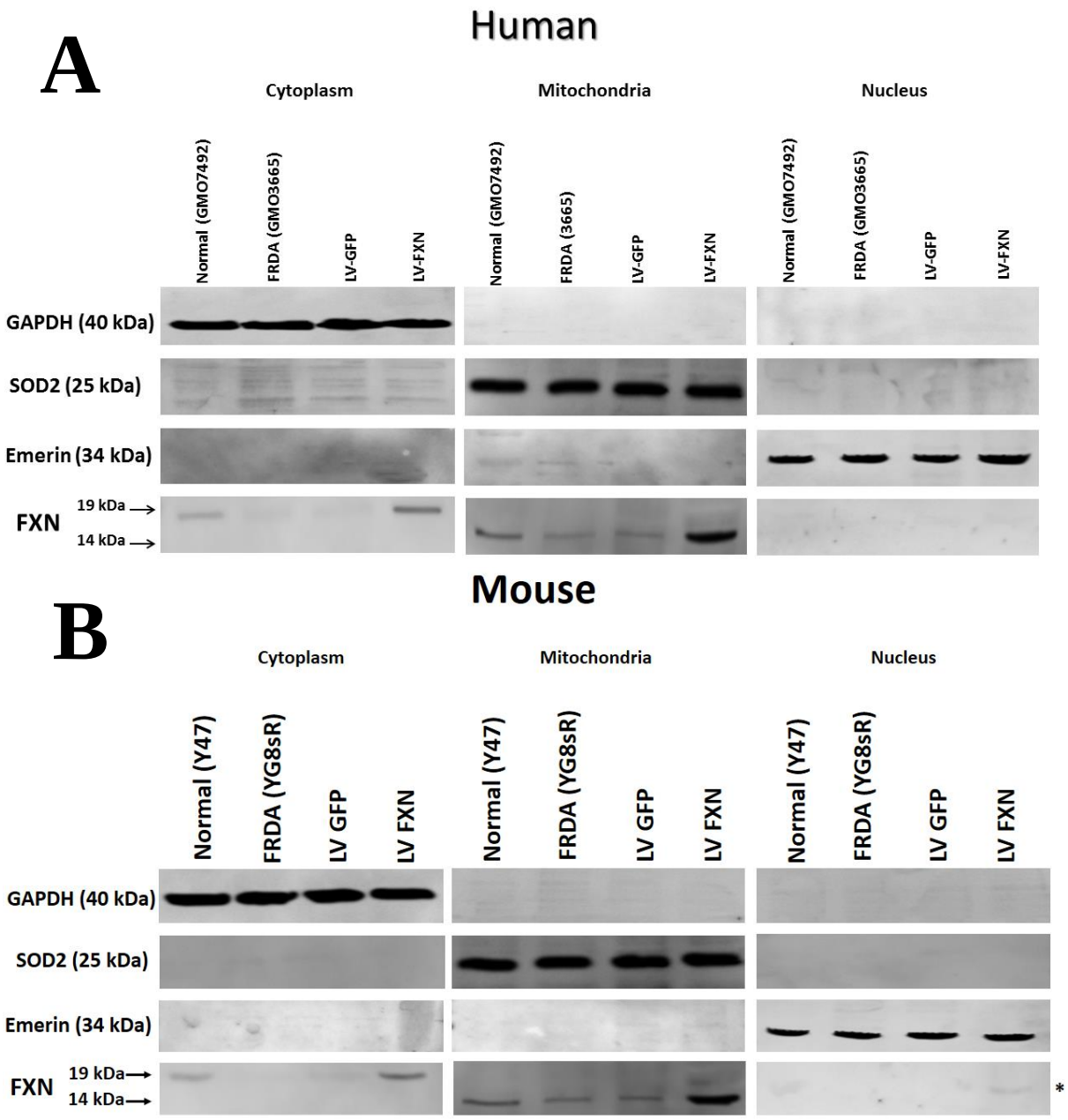

Figure 5.17: Localisation of intermediate and mature forms of frataxin to subcellular compartments. Western analysis of intermediate and mature forms of the frataxin protein following cell fractionation was performed on normal, FRDA and LV GFP and LV FXN treated human (A) and mouse fibroblasts (B). Frataxin isoforms were identified using antibodies that recognize the 19 kDa intermediate and 14 kDa mature forms of the protein (shown by arrows). Controls staining for the mitochondrial fraction used SOD2, for the cytoplasmic fraction used GAPDH and for the nuclear fraction used EMERIN. Only in the mouse could mature frataxin be identified in the nuclear fraction (shown by *).

CHAPTER 6 – GENERAL DISCUSSION

6.1 Discussion

FRDA pathology results from defective frataxin expression and in almost 95% of the patients the GAA repeat expansion within the first intron of the *FXN* gene results in epigenetic silencing and reduced expression of this encoded mitochondrial protein. Since FRDA is a monogenic disorder, permanent integration of a healthy *FXN* gene into the host genome to increase frataxin expression using a lentivirus is feasible. Lentivirus construct vector with a key safety feature of SIN design (pHR'SIN-cPPT-SFFV-*FXN*/GFP-WPRE) derived the *FXN* and GFP expression by SFFV promoter. This promoter is proven to drive high expression of the transgene and reach primary sites of the FRDA disease such as dorsal root ganglia, cerebellum and cardiac tissues (Themis *et al.*, 2005, Bigger *et al.*, 2006). Reduced expression of frataxin leads to impaired electron transport chain (ETC) function, which is accompanied by oxidative stress. Frataxin deficient cells are highly sensitive to oxidative stress and have reduced capability to handle oxidative insults (Payne and Wagner, 2012). The exact function of frataxin is not fully understood. Frataxin processing involves a transient intermediate form (FXN 42-210) and a mature form (FXN 81-210) of the protein that have been both identified in the cytoplasm and mitochondria of cells. Only the mature form is understood to be transported to the mitochondrion (Gakh *et al.*, 2010), which is known to be essential for iron homeostasis, in particular for the *de novo* biosynthesis of iron-sulphur cluster (ISC) proteins and heme biosynthesis (Schmucker *et al.*, 2011). It is thereby involved in activation of the tricarboxylic cycle enzyme aconitase, which can be used as an indicator of low levels of frataxin protein and mitochondrial damage (Payne and Wagner, 2012) Deficiency in frataxin results in impaired biosynthesis and

the function of ISC proteins of the ETC, leading to reduced ATP and energy production (Lodi *et al.*, 1999). Cells highly dependent on aerobic respiration and high ATP levels, such as neurons in the brain and spinal cord, cardiomyocytes and pancreatic beta cells, especially succumb to this imbalance in energy homeostasis and this is believed to cause the neurological and cardiac symptoms and the high prevalence of diabetes in patients. However, what causes the variable cell death within tissues is still unclear (Richardson *et al.*, 2013). Oxidative stress is known to be associated with genome instability (Negrini *et al.*, 2010), and in FRDA cells that have decreased frataxin expression, reduced capacity for DNA damage repair is evident (Schulz *et al.*, 2006, Schmucker *et al.*, 2011). Differential expression of genes associated with genotoxicity stress, including oxidative phosphorylation, has also been found in peripheral blood mononuclear cells of FRDA patients, where mitochondrial and nuclear DNA damage is increased (Haugen *et al.*, 2010). In the yeast model of FRDA, reduced levels of frataxin correlate with DNA damage and recombination, mutation events and genome instability. These cells are also highly sensitive to DNA-damaging agents (Karthikeyan *et al.*, 2002). Low frataxin expression is associated with increased sensitivity to ionising radiation (Chamberlain and Lewis, 1982), whereas high frataxin expression correlates with reduced levels of mitochondrial ROS. It is unclear whether low frataxin expression leading to high levels of ROS and DNA damage is the only cause of neuronal degeneration. Recently, however, the role of frataxin in DNA repair has been suggested to involve MUTYH and PARP 1 gene expression with low FXN expression being associated with microglial DNA damage (Shen *et al.*, 2016). Interestingly, overexpression of frataxin by nine fold has also been reported to be deleterious to life

span, impair locomotor ability and cause brain damage in a *Drosophila* model of FRDA (Llorens *et al.*, 2007), which would suggest any gene therapy approach to correct FRDA would require strict control of frataxin gene expression (Navarro *et al.*, 2011). Overexpression of human frataxin in transgenic mice by up to ten fold has been shown to have no deleterious effects (Miranda *et al.*, 2004). Furthermore, in a recent gene therapy study, correction of the FRDA heart pathology of the *Mck* conditional knockout mouse model with complete frataxin deletion in cardiac and skeletal muscle was achieved where frataxin was overexpressed 10 fold over that of endogenous frataxin, without deleterious side effects in the corrected mice (Perdomini *et al.*, 2014).

As it is difficult to obtain patient's neuronal cells, human FRDA primary fibroblasts (GMO3665) and mouse primary fibroblasts (YG8sR) from the FRDA mouse model in Dr. Pook's laboratory, with the lowest frataxin expression and highest GAA repeat (445/740 and 120, respectively) were obtained. These FRDA fibroblasts have been shown to be useful to study FRDA and to test treatments that reduce oxidative stress, prevent or reverse *FXN* methylation and improve cell viability (Wong *et al.*, 1999, Jauslin *et al.*, 2002, Richardson *et al.*, 2012).

Using DH5α competent cells the *FXN* gene was cloned into the construct vector. This vector was challenging to clone due to its toxicity to the competent cells and low yield, in future it is best to use Stbl4™ Competent Cells as they stabilize direct repeat and retroviral sequences. Then the integrity of the vector was confirmed by sequencing LTR3' to LTR5' region. Also the functionality of the vector was confirmed my measuring the *FXN* mRNA and protein expression after transfection of HEK 293T cells. Subsequently, lentivirus particles pseudotyped with VSV-G envelope and

carrying either *FXN* gene (LV *FXN*) or the GFP reporter gene (LV GFP) were produced with a titre of $1x10^8$ to infect the FRDA cell lines. An optimal MOI of 10 was established by infection of the fibroblasts with LV GFP and measuring the number GFP-positive cells. To achieve near 100% infection a double infection procedure was performed to reach final MOI of 20.

Viral copy number (VCN) was determined by qRT-PCR, which the human FRDA cells showed a VCN of 0.97 at 48 hr and 0.91 at 8 weeks post infection, and mouse FRDA cells showed a VCN of 1.05 at 48 hr and 0.95 at 8 weeks post infection with LV *FXN*. Long-term lentivirus gene transfer was confirmed by the fact that VCNs of both lentiviruses carrying *FXN* and GFP transgene remained constant post infection up to the 8 week time point. This was further supported by demonstrating a positive GFP expression up to 8 weeks post infection with LV GFP, using live microscopy and Imagestream^X. *FXN* mRNA expression levels in human and mouse FRDA cells was measured by qRT-PCR after *FXN* gene delivery 1-2 weeks, 6-8 weeks and 12 weeks post infection. In human FRDA fibroblasts mRNA expression had increased dramatically by 48 fold at week 1 - 2 compared to the normal fibroblasts. This level of *FXN* mRNA expression then reduced to 28 fold compared to the normal human fibroblasts at week 6 - 8 post infection. Further reduction in expression was detected after 12 weeks with mRNA levels only 22 fold higher than normal fibroblasts. In mouse FRDA fibroblasts a similar pattern was observed with *FXN* mRNA expression increased by 42 fold at week 1 - 2 post infection, 29 fold week 6 - 8 post infection and 24 fold at week 12 post infection. Generally mRNA levels were high in the first weeks following infection and then fell by approximately 50% by week 12 compared to

untreated FRDA fibroblasts. This was possibly due to shut-down of the SFFV promoter driving *FXN* expression, which has been described previously for this promoter (Herbst *et al.*, 2012). None-the-less *FXN* gene expression still remained significantly higher than the levels found in both untreated FRDA and normal fibroblasts. Levels of frataxin protein also appeared to follow a similar pattern as mRNA levels. Importantly, with this high frataxin expression in the treated human and mouse FRDA cells, population doubling times and cell survival profiles were similar to those found in control fibroblasts, demonstrating that high frataxin expression can be achieved without adverse side effects and supporting the potential for FRDA gene therapy using lentivirus mediated *FXN* delivery. This is further supported by a recent study that showed correction of cardiac hypertrophy in the *Mck* conditional knockout mouse model by AAV mediated *FXN* gene therapy where frataxin was overexpressed 10 fold over the level of endogenous frataxin expression without deleterious side effects in the treated mice (Perdomini *et al.*, 2014).

Frataxin is important for mitochondrial iron homeostasis; in particular for the *de novo* biosynthesis of ISCs and its deficiency results in lack of function of ISC-dependent proteins, such as complexes I, II and III of the ETC and the tricarboxylic acid cycle enzyme aconitase (Payne and Wagner, 2012). By *FXN* gene delivery, the activity of this enzyme was returned to near normal levels in both human and mouse cells from 65% and 60% in FRDA cells to 82% and 99% after treatment with LV FXN, respectively. Another important consequence of ETC impairment is increased levels of and sensitivity to oxidative stress (OS) in FRDA cells, which have been shown to be less capable of handling oxidative insults (Wong *et al.*, 1999, Payne and Wagner,

2012). Indeed, OS was evident in the FRDA fibroblasts by measurement of oxidised protein. The levels of OS in human FRDA cells were elevated to 193% and in mouse FRDA cells to 172% compared to 100% in the normal control. Interestingly, OS levels were significantly reduced to below normal levels to 26% in human and 28% in mouse FRDA fibroblasts after treatment with LV FXN.

Human and mouse FRDA cells were also able to tolerate OS induced by exogenous H_2O_2 with levels of survival matching that of controls. The hypothesis that OS as a result of low frataxin expression alone causes neuronal degeneration is still debatable. (Palomo *et al.*, 2011) suggested neuronal degeneration to be linked to frataxin expression after induction of frataxin deficiency followed by cell death in neuron-like cells through apoptosis, which is accompanied by up-regulation of p53, PUMA and Bax and activation of caspase-3. They also showed cell death could be prevented by interference with p53, caspase inhibitors or *FXN* gene transfer (Palomo *et al.*, 2011). Mitochondrial DNA damage is more prone to OS, which is thought to be due to the increased availability of iron in mitochondria and the generation of hydroxyl free radicals. Low levels of frataxin have also been shown in yeast to cause arrest in the cell cycle at G2/M that indicates nuclear DNA damage (Karthikeyan *et al.*, 2002). This increased susceptibility to OS appears to be coupled with a reduced capacity for DNA damage repair (Lewis *et al.*, 1979, Chamberlain and Lewis, 1982, Evans *et al.*, 1983). However, only a few of the enzymes or their associated partners involved in DNA damage repair have been found to require ISCs. Evidence for impairment for DNA damage repair in FRDA fibroblasts after ionising irradiation has previously been shown by its effects on clonal cell growth (Chamberlain *et al.*, 1981). Therefore, although

mitochondrial dysfunction and OS are central features of FRDA, impaired DNA damage repair may also play a role in cell death.

Low levels of frataxin have also been suggested to be associated with malignancies in a number of FRDA patients and even the cause of liver tumorigenesis in mice with hepatocyte-specific disruption of *FXN (*Thierbach *et al.,* 2010*)*. This observation has, however, been refuted by the analysis of a large FRDA patient cohort data and by revisiting the liver tumour pathology in the conditional knock-out frataxin mouse model (Martelli *et al.*, 2012). Frataxin has been proposed to be a tumour suppressor gene by Guccini and co-workers, who showed that frataxin modulates P53 expression in tumours in response to hypoxia (Guccini *et al.*, 2011). Schulz and co-workers have shown that frataxin suppresses tumour formation in a mouse xenograft model (Schulz *et al.*, 2006) and Chamberlain and co-workers have shown that frataxin deficiency in FRDA patients results in increased sensitivity to ionising radiation and also frataxin gene delivery can suppress the growth of several tumour cell lines (Chamberlain and Lewis, 1982). Further supporting evidence for the role of frataxin as a tumour suppressor is the fact that p53 has been shown to decrease the level of frataxin mRNA in human kidney HEK 293T cells and that the human frataxin gene proximal promoter contains a p53-responsive element (p53RE), which is involved in p53 mediated control of frataxin expression (Shimizu *et al.*, 2014). Evidence provided by a yeast model of FRDA also suggests that increased levels of DNA damage occurs in FRDA and the absence of frataxin leads to nuclear damage, chromosomal instability and a greater sensitivity to DNA-damaging agents (Karthikeyan *et al.*, 2002). In a study on FRDA peripheral blood mononuclear cells, increased mitochondrial and nuclear DNA

damage also results in changes in gene expression indicative of genotoxicity stress (Haugen *et al.*, 2010). The accumulation of DNA lesions may ultimately lead to apoptosis and cell death via p53 mediated pathways.

During DNA damage repair, DSBs are recognised by the non-homologous end-joining pathway (NHEJ) that activates the PI3-kinase, ataxia telangiectasia mutated (ATM), which in turn phosphorylates a H2AX histone variant to form γH2AX (Rogakou *et al.*, 1998). Upon DNA damage induction, especially after DSBs, γH2AX molecules spread over tens of kilobases of DNA flanking the break site and once DSB repair starts, the lesions are removed and the number of γH2AX foci decreases (Celeste *et al.*, 2003, Valdiglesias *et al.*, 2013). This signalling network, therefore, recruits the repair machinery to the DNA lesion to repair it (Ciccia and Elledge, 2010). Hence, γH2AX can be used to measure DNA damage and is useful as a marker of genome instability and DNA damage repair in cells proficient in NHEJ repair machinery. We used immunocytochemical detection of γH2AX proteins by fluorochrome-linked antibodies to quantify and localize DSBs as a measure of genome instability and DNA damage repair in human and mouse FRDA fibroblasts. Classical γH2AX immunostaining allowed the detection of individual nuclei and the number of foci per nucleus, and thus the damage distribution within cells, whereas imaging flow cytometry enabled rapid measurement of thousands of cells to provide statistical significance of DNA damage and repair after DSB induction by γ-irradiation. Both image flow cytometry and immunocytochemistry enabled the identification of higher numbers of DSB in FRDA fibroblasts compared to normal fibroblasts. Data gathered using Imagestream^X showed an increased DSBs in FRDA cells with 4 foci/cell in human and 4.5 foci/cell in

mouse compared normal controls with 2.1 foci/cell in human and 2.8 foci/cell in mouse cell line. After *FXN* gene delivery into FRDA cells number of DSBs was reduced to 1.99 foci/cell in human and 2.7 foci/cell in mouse cell lines. A similar pattern was observed when measuring γH2AX foci using immunocytochemistry with the number of foci generally decreased due to higher magnification available using this technique. Once again *FXN* delivery reduced the number of γH2AX foci to the level found in control fibroblasts. Furthermore, after γ-irradiation, cells were able to repair DSBs more proficiently after *FXN* gene transfer, although not down to the low background levels of DSBs in normal fibroblasts. This is possibly due to the fact that not all the FRDA fibroblasts were expressing lentivirus mediated *FXN*, as suggested by the fact that, even though infected cells still contained a vector copy number of 1, *FXN* expression reduced by 50% over the 12 week period when DSB foci were measured. Interestingly, it was found that OS levels of FRDA cells were 2 fold less that of control fibroblasts after gene transfer, pointing to the possibility that frataxin may be important for DNA damage repair or as mentioned this may be due to an improvement of the antioxidative response provided by *FXN* delivery. To determine whether this is the case, clones of LV *FXN* infected cells would need to be isolated and further characterised for *FXN* expression and DSB repair simultaneously. Cells could also be grown in the presence of antioxidants followed by measurement of the DNA response to irradiation. It would also be interesting to measure changes in the expression of genes associated with antioxidants and especially Nrf2 as previously described in the YG8sR mouse model (Shan *et al.*, 2013).

Because HIV-1-based lentiviruses are ideal for neuronal targeting (Blömer *et al.*, 1997) and do not cause genotoxicity in mice (Nowrouzi *et al.*, 2013), along with recent findings in Dr. Themis laboratory that lentiviruses can efficiently reach the mouse cerebellum and DRG using a reporter gene (unpublished data), the data presented in this study supports future efforts to use LV FXN (pHR'SIN-cPPT-SFFV-*FXN*-WPRE) to correct the FRDA-like phenotype in the YG8sR mouse model.

REFERENCES

ABEL, T. & ZUKIN, R. S. 2008. Epigenetic targets of HDAC inhibition in neurodegenerative and psychiatric disorders. *Current Opinion in Pharmacology,* 8**,** 57-64.

ADINOLFI, S., TRIFUOGGI, M., POLITOU, A., MARTIN, S. & PASTORE, A. 2002. A structural approach to understanding the iron-binding properties of phylogenetically different frataxins. *Human molecular genetics,* 11**,** 1865-1877.

AIUTI, A., BIASCO, L., SCARAMUZZA, S., FERRUA, F., CICALESE, M. P., BARICORDI, C., DIONISIO, F., CALABRIA, A., GIANNELLI, S. & CASTIELLO, M. C. 2013. Lentiviral hematopoietic stem cell gene therapy in patients with Wiskott-Aldrich syndrome. *Science,* 341**,** 1233151.

AIUTI, A., CATTANEO, F., GALIMBERTI, S., BENNINGHOFF, U., CASSANI, B., CALLEGARO, L., SCARAMUZZA, S., ANDOLFI, G., MIROLO, M. & BRIGIDA, I. 2009. Gene therapy for immunodeficiency due to adenosine deaminase deficiency. *New England Journal of Medicine,* 360**,** 447-458.

AIUTI, A., SLAVIN, S., AKER, M., FICARA, F., DEOLA, S., MORTELLARO, A., MORECKI, S., ANDOLFI, G., TABUCCHI, A. & CARLUCCI, F. 2002. Correction of ADA-SCID by stem cell gene therapy combined with nonmyeloablative conditioning. *Science,* 296**,** 2410-2413.

AKKINA, R. K., WALTON, R. M., CHEN, M. L., LI, Q.-X., PLANELLES, V. & CHEN, I. 1996. High-efficiency gene transfer into CD34+ cells with a human immunodeficiency virus type 1-based retroviral vector pseudotyped with vesicular stomatitis virus envelope glycoprotein G. *Journal of virology,* 70**,** 2581-2585.

AL-MAHDAWI, S., PINTO, R. M., ISMAIL, O., VARSHNEY, D., LYMPERI, S., SANDI, C., TRABZUNI, D. & POOK, M. 2008. The Friedreich ataxia GAA repeat expansion mutation induces comparable epigenetic changes in human and transgenic mouse brain and heart tissues. *Human Molecular Genetics,* 17**,** 735-746.

AL-MAHDAWI, S., PINTO, R. M., RUDDLE, P., CARROLL, C., WEBSTER, Z. & POOK, M. 2004. GAA repeat instability in Friedreich ataxia YAC transgenic mice. *Genomics,* 84**,** 301-310.

AL-MAHDAWI, S., PINTO, R. M., VARSHNEY, D., LAWRENCE, L., LOWRIE, M. B., HUGHES, S., WEBSTER, Z., BLAKE, J., COOPER, J. M. & KING, R. 2006. GAA repeat expansion mutation mouse models of Friedreich ataxia exhibit oxidative stress leading to progressive neuronal and cardiac pathology. *Genomics,* 88**,** 580-590.

ALBINO, A. P., HUANG, X., JORGENSEN, E. D., GIETL, D., TRAGANOS, F. & DARZYNKIEWICZ, Z. 2006. Induction of DNA double-strand breaks in A549 and normal human pulmonary epithelial cells by cigarette smoke is mediated by free radicals. *International journal of oncology,* 28**,** 1491-1505.

ALPER, G. & NARAYANAN, V. 2003. *Friedreich's ataxia,* New York, NY, ETATS-UNIS, Elsevier.

ANDERSON, P. R., KIRBY, K., ORR, W. C., HILLIKER, A. J. & PHILLIPS, J. P. 2008. Hydrogen peroxide scavenging rescues frataxin deficiency in a Drosophila model of Friedreich's ataxia. *Proceedings of the National Academy of Sciences,* 105**,** 611-616.

ANJOMANI VIRMOUNI, S., EZZATIZADEH, V., SANDI, C., SANDI, M., AL-MAHDAWI, S., CHUTAKE, Y. & POOK, M. A. 2015. A novel GAA-repeat-expansion-based mouse model of Friedreich's ataxia. *Disease Models and Mechanisms,* 8**,** 225-235.

ARMSTRONG, J. S., KHDOUR, O. & HECHT, S. M. 2010. Does oxidative stress contribute to the pathology of Friedreich's ataxia? A radical question. *The FASEB journal,* 24**,** 2152-2163.

AUCHÈRE, F., SANTOS, R., PLANAMENTE, S., LESUISSE, E. & CAMADRO, J.-M. 2008. Glutathione-dependent redox status of frataxin-deficient cells in a yeast model of Friedreich's ataxia. *Human molecular genetics,* 17**,** 2790-2802.

BALABAN, R. S., NEMOTO, S. & FINKEL, T. 2005. Mitochondria, oxidants, and aging. *Cell,* 120**,** 483-495.

BANASIK, M. & MCCRAY, P. 2010. Integrase-defective lentiviral vectors: progress and applications. *Gene therapy,* 17**,** 150-157.

BAUM, C., HUNT, N., HILDINGER, M., ECKERT, H. G., ZAEHRES, H., RICHTERS, A., JOHN, J., LÖHLER, J. & OSTERTAG, W. 1998. Cis-Active Elements of Friend Spleen Focus-Forming Virus: From Disease Induction to Disease Prevention. *Acta Haematologica,* 99**,** 156-164.

BAUM, C., ITOH, K., MEYER, J., LAKER, C., ITO, Y. & OSTERTAG, W. 1997. The potent enhancer activity of the polycythemic strain of spleen focus-forming virus in hematopoietic cells is governed by a binding site for Sp1 in the upstream control region and by a unique enhancer core motif, creating an exclusive target for PEBP/CBF. *Journal of Virology,* 71**,** 6323-31.

BAUM, C., KUSTIKOVA, O., MODLICH, U., LI, Z. & FEHSE, B. 2006a. Mutagenesis and oncogenesis by chromosomal insertion of gene transfer vectors. *Human gene therapy,* 17**,** 253-263.

BAUM, C., SCHAMBACH, A., BOHNE, J. & GALLA, M. 2006b. Retrovirus Vectors: Toward the Plentivirus? *Mol Ther,* 13**,** 1050-1063.

BEINERT, H., KENNEDY, M. C. & STOUT, C. D. 1996. Aconitase as iron-sulfur protein, enzyme, and iron-regulatory protein. *Chemical Reviews,* 96**,** 2335-2374.

BIFFI, A., BARTOLOMAE, C. C., CESANA, D., CARTIER, N., AUBOURG, P., RANZANI, M., CESANI, M., BENEDICENTI, F., PLATI, T. & RUBAGOTTI, E. 2011. Lentiviral vector common integration sites in preclinical models and a clinical trial reflect a benign integration bias and not oncogenic selection. *Blood,* 117**,** 5332-5339.

BIFFI, A., MONTINI, E., LORIOLI, L., CESANI, M., FUMAGALLI, F., PLATI, T., BALDOLI, C., MARTINO, S., CALABRIA, A. & CANALE, S. 2013. Lentiviral hematopoietic stem cell gene therapy benefits metachromatic leukodystrophy. *Science,* 341**,** 1233158.

BIGGER, B., SIAPATI, E., MISTRY, A., WADDINGTON, S., NIVSARKAR, M., JACOBS, L., PERRETT, R., HOLDER, M., RIDLER, C. & KEMBALL-COOK, G. 2006. Permanent partial phenotypic correction and tolerance in a mouse model of hemophilia B by stem cell gene delivery of human factor IX. *Gene therapy,* 13**,** 117-126.

BLÖMER, U., NALDINI, L., KAFRI, T., TRONO, D., VERMA, I. M. & GAGE, F. H. 1997. Highly efficient and sustained gene transfer in adult neurons with a lentivirus vector. *Journal of virology,* 71**,** 6641-6649.

BOSCH, M., EARL, P., FARGNOLI, K., PICCIAFUOCO, S., GIOMBINI, F., WONG-STAAL, F. & FRANCHINI, G. 1989. Identification of the fusion peptide of primate immunodeficiency viruses. *Science,* 244**,** 694-697.

BOUARD, D., ALAZARD-DANY, N. & COSSET, F. L. 2009. Viral vectors: from virology to transgene expression. *British Journal of Pharmacology,* 157**,** 153-165.

BOURTON, E. C., PLOWMAN, P. N., ZAHIR, S. A., SENGULOGLU, G. U., SERRAI, H., BOTTLEY, G. & PARRIS, C. N. 2012. Multispectral imaging flow cytometry reveals distinct frequencies of γ-H2AX foci induction in DNA double strand break repair defective human cell lines. *Cytometry Part A,* 81A**,** 130-137.

BOUSSIF, O., LEZOUALC'H, F., ZANTA, M. A., MERGNY, M. D., SCHERMAN, D., DEMENEIX, B. & BEHR, J.-P. 1995. A versatile vector for gene and oligonucleotide transfer into cells in culture and in vivo: polyethylenimine. *Proceedings of the National Academy of Sciences,* 92**,** 7297-7301.

BRADLEY, J., BLAKE, J., CHAMBERLAIN, S., THOMAS, P., COOPER, J. & SCHAPIRA, A. 2000. Clinical, biochemical and molecular genetic correlations in Friedreich's ataxia. *Human molecular genetics,* 9**,** 275-282.

BRIGGS, J. A. G., WILK, T., WELKER, R., KRAUSSLICH, H.-G. & FULLER, S. D. 2003. Structural organization of authentic, mature HIV-1 virions and cores. *EMBO J,* 22**,** 1707-1715.

BRUN, S., FAUCON-BIGUET, N. & MALLET, J. 2003. Optimization of transgene expression at the posttranscriptional level in neural cells: implications for gene therapy. *Molecular Therapy,* 7**,** 782-789.

BUCHHOLZ, C. J., MÜHLEBACH, M. D. & CICHUTEK, K. 2009. Lentiviral vectors with measles virus glycoproteins dream team for gene transfer? *Trends in biotechnology,* 27**,** 259-265.

BUKRINSKY, M. I., SHAROVA, N., MCDONALD, T. L., PUSHKARSKAYA, T., TARPLEY, W. G. & STEVENSON, M. 1993. Association of integrase, matrix, and reverse transcriptase antigens of human immunodeficiency virus type 1 with viral nucleic acids following acute infection. *Proceedings of the National Academy of Sciences,* 90**,** 6125-6129.

BURNETT, R., MELANDER, C., PUCKETT, J. W., SON, L. S., WELLS, R. D., DERVAN, P. B. & GOTTESFELD, J. M. 2006. DNA sequence-specific polyamides alleviate transcription inhibition associated with long GAA·TTC repeats in Friedreich's ataxia. *Proceedings of the National Academy of Sciences,* 103**,** 11497-11502.

BURNS, J. C., FRIEDMANN, T., DRIEVER, W., BURRASCANO, M. & YEE, J.-K. 1993. Vesicular stomatitis virus G glycoprotein pseudotyped retroviral vectors: concentration to very high titer and efficient gene transfer into mammalian and nonmammalian cells. *Proceedings of the National Academy of Sciences,* 90**,** 8033-8037.

BYRNES, A. P., RUSBY, J. E., WOOD, M. J. A. & CHARLTON, H. M. 1995. Adenovirus gene transfer causes inflammation in the brain. *Neuroscience,* 66**,** 1015-1024.

CAMPUZANO, V., MONTERMINI, L., MOLTÒ, M. D., PIANESE, L., COSSÉE, M., CAVALCANTI, F., MONROS, E., RODIUS, F., DUCLOS, F., MONTICELLI, A., ZARA, F., CAÑIZARES, J., KOUTNIKOVA, H., BIDICHANDANI, S. I., GELLERA, C., BRICE, A., TROUILLAS, P., DE MICHELE, G., FILLA, A., DE FRUTOS, R., PALAU, F., PATEL, P. I., DI DONATO, S., MANDEL, J.-L., COCOZZA, S., KOENIG, M. & PANDOLFO, M. 1996. Friedreich's Ataxia: Autosomal Recessive Disease Caused by an Intronic GAA Triplet Repeat Expansion. *Science,* 271**,** 1423-1427.

CANNON, J. R., SEW, T., MONTERO, L., BURTON, E. A. & GREENAMYRE, J. T. 2011. Pseudotype-dependent lentiviral transduction of astrocytes or neurons in the rat substantia nigra. *Experimental neurology,* 228**,** 41-52.

CARA, A. & REITZ, M. S. 1997. New insight on the role of extrachromosomal retroviral DNA. *Leukemia : official journal of the Leukemia Society of America, Leukemia Research Fund, U.K,* 11**,** 1395-9.

CAREY, N. & LA THANGUE, N. B. 2006. Histone deacetylase inhibitors: gathering pace. *Current Opinion in Pharmacology,* 6**,** 369-375.

CARTIER, N., HACEIN-BEY-ABINA, S., BARTHOLOMAE, C. C., VERES, G., SCHMIDT, M., KUTSCHERA, I., VIDAUD, M., ABEL, U., DAL-CORTIVO, L. & CACCAVELLI, L. 2009. Hematopoietic stem cell gene therapy with a lentiviral vector in X-linked adrenoleukodystrophy. *science,* 326**,** 818-823.

CAVADINI, P., GELLERA, C., PATEL, P. I. & ISAYA, G. 2000. Human frataxin maintains mitochondrial iron homeostasis in Saccharomyces cerevisiae. *Human molecular genetics,* 9**,** 2523-2530.

CAVAZZANA-CALVO, M., PAYEN, E., NEGRE, O., WANG, G., HEHIR, K., FUSIL, F., DOWN, J., DENARO, M., BRADY, T. & WESTERMAN, K. 2010. Transfusion independence and HMGA2 activation after gene therapy of human [bgr]-thalassaemia. *Nature,* 467**,** 318-322.

CELESTE, A., FERNANDEZ-CAPETILLO, O., KRUHLAK, M. J., PILCH, D. R., STAUDT, D. W., LEE, A., BONNER, R. F., BONNER, W. M. & NUSSENZWEIG, A. 2003. Histone H2AX phosphorylation is dispensable for the initial recognition of DNA breaks. *Nat Cell Biol,* 5**,** 675-9.

CHAMBERLAIN, S., CRAMP, W. & LEWIS, P. 1981. Defects in newly synthesised DNA in skin fibroblasts from patients with Friedreich's ataxia. *The Lancet,* 317**,** 1165.

CHAMBERLAIN, S. & LEWIS, P. 1982. Studies of cellular hypersensitivity to ionising radiation in Friedreich's ataxia. *Journal of Neurology, Neurosurgery & Psychiatry,* 45**,** 1136-1138.

CHAMBERLAIN, S., SHAW, J., ROWLAND, A., WALLIS, J., SOUTH, S., NAKAMURA, Y., VON GABAIN, A., FARRALL, M. & WILLIAMSON, R. 1988. Mapping of mutation causing Friedreich's ataxia to human chromosome 9. *Nature,* 334**,** 248-250.

CHANG, T.-S., CHO, C.-S., PARK, S., YU, S., KANG, S. W. & RHEE, S. G. 2004. Peroxiredoxin III, a mitochondrion-specific peroxidase, regulates apoptotic signaling by mitochondria. *Journal of Biological Chemistry,* 279**,** 41975-41984.

CHAPDELAINE, P., COULOMBE, Z., CHIKH, A., GÉRARD, C. & TREMBLAY, J. P. 2013. A potential new therapeutic approach for Friedreich ataxia: induction of frataxin expression with TALE proteins. *Molecular Therapy—Nucleic Acids,* 2**,** e119.

CHARNEAU, P., ALIZON, M. & CLAVEL, F. 1992. A second origin of DNA plus-strand synthesis is required for optimal human immunodeficiency virus replication. *Journal of virology,* 66**,** 2814-2820.

CHARNEAU, P., MIRAMBEAU, G., ROUX, P., PAULOUS, S., BUC, H. & CLAVEL, F. 1994. HIV-1 Reverse Transcription A Termination Step at the Center of the Genome. *Journal of Molecular Biology,* 241**,** 651-662.

CHEN, Q., VAZQUEZ, E. J., MOGHADDAS, S., HOPPEL, C. L. & LESNEFSKY, E. J. 2003. Production of reactive oxygen species by mitochondria central role of complex III. *Journal of Biological Chemistry,* 278**,** 36027-36031.

CHIRMULE, N., PROPERT, K., MAGOSIN, S., QIAN, Y., QIAN, R. & WILSON, J. 1999. Immune responses to adenovirus and adeno-associated virus in humans. *Gene therapy,* 6**,** 1574-83.

CHOE, H., FARZAN, M., SUN, Y., SULLIVAN, N., ROLLINS, B., PONATH, P. D., WU, L., MACKAY, C. R., LAROSA, G., NEWMAN, W., GERARD, N., GERARD, C. & SODROSKI, J. 1996. The ²-Chemokine Receptors CCR3 and CCR5 Facilitate Infection by Primary HIV-1 Isolates. *Cell,* 85**,** 1135-1148.

CHOI, V. W., MCCARTY, D. M. & SAMULSKI, R. J. 2005. AAV hybrid serotypes: improved vectors for gene delivery. *Current gene therapy,* 5**,** 299.

CICCIA, A. & ELLEDGE, S. J. 2010. The DNA damage response: making it safe to play with knives. *Molecular cell,* 40**,** 179-204.

CIDECIYAN, A. V., HAUSWIRTH, W. W., ALEMAN, T. S., KAUSHAL, S., SCHWARTZ, S. B., BOYE, S. L., WINDSOR, E. A., CONLON, T. J., SUMAROKA, A. & ROMAN, A. J. 2009. Vision 1 year after gene therapy for Leber's congenital amaurosis. *New England Journal of Medicine,* 361**,** 725-727.

CLARK, R., DE BIASE, I., MALYKHINA, A., AL-MAHDAWI, S., POOK, M. & BIDICHANDANI, S. 2007. The GAA triplet-repeat is unstable in the context of the human <i>FXN</i> locus and displays age-dependent expansions in cerebellum and DRG in a transgenic mouse model. *Human Genetics,* 120**,** 633-640.

COIL, D. A. & MILLER, A. D. 2004. Phosphatidylserine is not the cell surface receptor for vesicular stomatitis virus. *Journal of virology,* 78**,** 10920-10926.

COLLINS, K. L., CHEN, B. K., KALAMS, S. A., WALKER, B. D. & BALTIMORE, D. 1998. HIV-1 Nef protein protects infected primary cells against killing by cytotoxic T lymphocytes. *Nature,* 391**,** 397-401.

CONDÒ, I., VENTURA, N., MALISAN, F., RUFINI, A., TOMASSINI, B. & TESTI, R. 2007. In vivo maturation of human frataxin. *Human molecular genetics,* 16**,** 1534-1540.

COOPER, J. M. & SCHAPIRA, A. H. V. 2007. Friedreich's ataxia: Coenzyme Q10 and vitamin E therapy. *Mitochondrion,* 7**,** S127-S135.

COSSÉE, M., PUCCIO, H., GANSMULLER, A., KOUTNIKOVA, H., DIERICH, A., LEMEUR, M., FISCHBECK, K., DOLLÉ, P. & KŒNIG, M. 2000. Inactivation of the Friedreich ataxia mouse gene leads to

early embryonic lethality without iron accumulation. *Human Molecular Genetics,* 9**,** 1219-1226.

COSSÉE, M., SCHMITT, M., CAMPUZANO, V., REUTENAUER, L., MOUTOU, C., MANDEL, J.-L. & KOENIG, M. 1997. Evolution of the Friedreich's ataxia trinucleotide repeat expansion: founder effect and premutations. *Proceedings of the National Academy of Sciences,* 94**,** 7452-7457.

CRAIGIE, R. 2001. HIV Integrase, a Brief Overview from Chemistry to Therapeutics. *Journal of Biological Chemistry,* 276**,** 23213-23216.

DAHLBERG, J. E., SAWYER, R. C., TAYLOR, J. M., FARAS, A. J., LEVINSON, W. E., GOODMAN, H. M. & BISHOP, J. M. 1974. Transcription of DNA from the 70S RNA of Rous Sarcoma Virus I. Identification of a Specific 4S RNA Which Serves as Primer. *Journal of Virology,* 13**,** 1126-1133.

DANNO, S., ITOH, K., BAUM, C., OSTERTAG, W., OHNISHI, N., KIDO, T., TOMIWA, K., MATSUDA, T. & FUJITA, J. 1999. Efficient gene transfer by hybrid retroviral vectors to murine spermatogenic cells. *Human gene therapy,* 10**,** 1819-31.

DE BIASE, I., CHUTAKE, Y. K., RINDLER, P. M. & BIDICHANDANI, S. I. 2009. Epigenetic silencing in Friedreich ataxia is associated with depletion of CTCF (CCCTC-binding factor) and antisense transcription. *PLoS One,* 4**,** e7914.

DE BIASE, I., RASMUSSEN, A., ENDRES, D., AL-MAHDAWI, S., MONTICELLI, A., COCOZZA, S., POOK, M. & BIDICHANDANI, S. I. 2007a. Progressive gaa expansions in dorsal root ganglia of Friedreich's ataxia patients. *Annals of Neurology,* 61**,** 55-60.

DE BIASE, I., RASMUSSEN, A., MONTICELLI, A., AL-MAHDAWI, S., POOK, M., COCOZZA, S. & BIDICHANDANI, S. I. 2007b. Somatic instability of the expanded GAA triplet-repeat sequence in Friedreich ataxia progresses throughout life. *Genomics,* 90**,** 1-5.

DE MICHELE, G., FILLA, A., CAVALCANTI, F., DI MAIO, L., PIANESE, L., CASTALDO, I., CALABRESE, O., MONTICELLI, A., VARRONE, S. & CAMPANELLA, G. 1994. Late onset Friedreich's disease: clinical features and mapping of mutation to the FRDA locus. *Journal of Neurology, Neurosurgery & Psychiatry,* 57**,** 977-979.

DELATYCKI, M. B., WILLIAMSON, R. & FORREST, S. M. 2000. Friedreich ataxia: an overview. *Journal of Medical Genetics,* 37**,** 1-8.

DEMAISON, C., PARSLEY, K., BROUNS, G., SCHERR, M., BATTMER, K., KINNON, C., GREZ, M. & THRASHER, A. J. 2002. High-Level Transduction and Gene Expression in Hematopoietic Repopulating Cells Using a Human Imunodeficiency Virus Type 1-Based Lentiviral Vector Containing an Internal Spleen Focus Forming Virus Promoter. *Human Gene Therapy,* 13**,** 803-813.

DONELLO, J. E., LOEB, J. E. & HOPE, T. J. 1998. Woodchuck hepatitis virus contains a tripartite posttranscriptional regulatory element. *Journal of Virology,* 72**,** 5085-5092.

DRAGIC, T., LITWIN, V., ALLAWAY, G. P., MARTIN, S. R., HUANG, Y., NAGASHIMA, K. A., CAYANAN, C., MADDON, P. J., KOUP, R. A., MOORE, J. P. & PAXTON, W. A. 1996. HIV-1 entry into CD4+ cells is mediated by the chemokine receptor CC-CKR-5. *Nature,* 381**,** 667-673.

DUBY, G., FOURY, F., RAMAZZOTTI, A., HERRMANN, J. & LUTZ, T. 2002. A non-essential function for yeast frataxin in iron–sulfur cluster assembly. *Human molecular genetics,* 11**,** 2635-2643.

DULL, T., ZUFFEREY, R., KELLY, M., MANDEL, R. J., NGUYEN, M., TRONO, D. & NALDINI, L. 1998. A Third-Generation Lentivirus Vector with a Conditional Packaging System. *Journal of Virology,* 72**,** 8463-8471.

DURAND, S. & CIMARELLI, A. 2011. The Inside Out of Lentiviral Vectors. *Viruses,* 3**,** 132-159.

DVORIN, J. D., BELL, P., MAUL, G. G., YAMASHITA, M., EMERMAN, M. & MALIM, M. H. 2002. Reassessment of the roles of integrase and the central DNA flap in human immunodeficiency virus type 1 nuclear import. *Journal of virology,* 76**,** 12087-12096.

EISENMAN, R. N. & VOGT, V. M. 1978. The biosynthesis of oncovirus proteins. *Biochimica et biophysica acta,* 473**,** 187-239.

ENGELMAN, A., MIZUUCHI, K. & CRAIGIE, R. 1991. HIV-1 DNA integration: Mechanism of viral DNA cleavage and DNA strand transfer. *Cell,* 67**,** 1211-1221.

ESCARPE, P., ZAYEK, N., CHIN, P., BORELLINI, F., ZUFFEREY, R., VERES, G. & KIERMER, V. 2003. Development of a sensitive assay for detection of replication-competent recombinant lentivirus in large-scale HIV-based vector preparations. *Molecular therapy,* 8**,** 332-341.

ESCORS, D. & BRECKPOT, K. 2010. Lentiviral vectors in gene therapy: their current status and future potential. *Archivum immunologiae et therapiae experimentalis,* 58**,** 107-119.

EVANS-GALEA, M. V., CARRODUS, N., ROWLEY, S. M., CORBEN, L. A., TAI, G., SAFFERY, R., GALATI, J. C., WONG, N. C., CRAIG, J. M. & LYNCH, D. R. 2012. FXN methylation predicts expression and clinical outcome in Friedreich ataxia. *Annals of neurology,* 71**,** 487-497.

EVANS, H., PENTLAND, B. & NEWTON, M. 1983. Mutagen hypersensitivity in Friedreich's ataxia. *Annals of human genetics,* 47**,** 193-204.

FILLA, A., DE MICHELE, G. & CAVALCANTI, F. 1996. The relationship between trinucleotide (GAA) repeat length and clinical features in Friedreich ataxia. *Journal Name: American Journal of Human Genetics; Journal Volume: 59; Journal Issue: 3; Other Information: PBD: Sep 1996***,** Medium: X; Size: pp. 554-560.

FINSTON, W. I. & CHAMPOUX, J. J. 1984. RNA-primed initiation of Moloney murine leukemia virus plus strands by reverse transcriptase in vitro. *Journal of Virology,* 51**,** 26-33.

FISCHER, A. & CAVAZZANA-CALVO, M. 2008. Gene therapy of inherited diseases. *The Lancet,* 371**,** 2044-2047.

FLEMING, J., SPINOULAS, A., ZHENG, M., CUNNINGHAM, S. C., GINN, S. L., MCQUILTY, R. C., ROWE, P. B. & ALEXANDER, I. E. 2005. Partial correction of sensitivity to oxidant stress in Friedreich ataxia patient fibroblasts by frataxin-encoding adeno-associated virus and lentivirus vectors. *Human gene therapy,* 16**,** 947-956.

FOLLENZI, A., AILLES, L. E., BAKOVIC, S., GEUNA, M. & NALDINI, L. 2000. Gene transfer by lentiviral vectors is limited by nuclear translocation and rescued by HIV-1 pol sequences. *Nature genetics,* 25**,** 217-222.

FOUCHIER, R., SIMON, J., JAFFE, A. B. & MALIM, M. H. 1996. Human immunodeficiency virus type 1 Vif does not influence expression or virion incorporation of gag-, pol-, and env-encoded proteins. *Journal of virology,* 70**,** 8263-8269.

FRECHA, C., SZECSI, J., COSSET, F. L. & VERHOEYEN, E. 2008. Strategies for targeting lentiviral vectors. *Current Gene Therapy,* 8**,** 449-60.

FRIEDREICH, N. 1876. Ueber Ataxie mit besonderer Berücksichtigung der hereditären Formen. *Archiv für pathologische Anatomie und Physiologie und für klinische Medicin,* 68**,** 145-245.

FRIEDREICH, N. 1877. Ueber Ataxie mit besonderer Berücksichtigung der hereditären Formen. *Archiv für pathologische Anatomie und Physiologie und für klinische Medicin,* 70**,** 140-152.

FRIEDREICH, N. V. 1863. Ueber degenerative Atrophie der spinalen Hinterstränge. *Virchows Archiv,* 26**,** 391-419.

GAKH, O., BEDEKOVICS, T., DUNCAN, S. F., SMITH, D. Y., BERKHOLZ, D. S. & ISAYA, G. 2010. Normal and Friedreich Ataxia Cells Express Different Isoforms of Frataxin with Complementary Roles in Iron-Sulfur Cluster Assembly. *Journal of Biological Chemistry,* 285**,** 38486-38501.

GAO, L., CUETO, M. A., ASSELBERGS, F. & ATADJA, P. 2002. Cloning and Functional Characterization of HDAC11, a Novel Member of the Human Histone Deacetylase Family. *Journal of Biological Chemistry,* 277**,** 25748-25755.

GARDNER, P. R. 2002. Aconitase: sensitive target and measure of superoxide. *Methods in enzymology,* 349**,** 9-23.

GERBER, J., MÜHLENHOFF, U. & LILL, R. 2003. An interaction between frataxin and Isu1/Nfs1 that is crucial for Fe/S cluster synthesis on Isu1. *EMBO reports,* 4**,** 906-911.

GIBSON, T. J., KOONIN, E. V., MUSCO, G., PASTORE, A. & BORK, P. 1996. Friedreich's ataxia protein: phylogenetic evidence for mitochondrial dysfunction. *Trends in neurosciences,* 19**,** 465-468.

GILLET, J.-P., MACADANGDANG, B., FATHKE, R. L., GOTTESMAN, M. M. & KIMCHI-SARFATY, C. 2009. The Development of Gene Therapy: From Monogenic Recessive Disorders to Complex Diseases Such as Cancer

Gene Therapy of Cancer. *In:* WALTHER, W. & STEIN, U. S. (eds.). Humana Press.

GIMENEZ-CASSINA, A., WADE-MARTINS, R., GOMEZ-SEBASTIAN, S., CORONA, J., LIM, F. & DIAZ-NIDO, J. 2011. Infectious delivery and long-term persistence of transgene expression in the brain by a 135-kb iBAC-FXN genomic DNA expression vector. *Gene therapy,* 18**,** 1015-1019.

GLOVER, D. J., LIPPS, H. J. & JANS, D. A. 2005. Towards safe, non-viral therapeutic gene expression in humans. *Nat Rev Genet,* 6**,** 299-310.

GOMEZ-SEBASTIAN, S., GIMENEZ-CASSINA, A., DIAZ-NIDO, J., LIM, F. & WADE-MARTINS, R. 2007. Infectious delivery and expression of a 135 kb human FRDA genomic DNA locus complements Friedreich's ataxia deficiency in human cells. *Molecular Therapy,* 15**,** 248-254.

GONCALVES, S., PAUPE, V., DASSA, E. P. & RUSTIN, P. 2008. Deferiprone targets aconitase: implication for Friedreich's ataxia treatment. *BMC neurology,* 8**,** 20.

GORMAN, L., SUTER, D., EMERICK, V., SCHÜMPERLI, D. & KOLE, R. 1998. Stable alteration of pre-mRNA splicing patterns by modified U7 small nuclear RNAs. *Proceedings of the National Academy of Sciences,* 95**,** 4929-4934.

GRABCZYK, E. & FISHMAN, M. C. 1995. A Long Purine-Pyrimidine Homopolymer Acts as a Transcriptional Diode. *Journal of Biological Chemistry,* 270**,** 1791-1797.

GRABCZYK, E., MANCUSO, M. & SAMMARCO, M. C. 2007. A persistent RNA·DNA hybrid formed by transcription of the Friedreich ataxia triplet repeat in live bacteria, and by T7 RNAP in vitro. *Nucleic Acids Research,* 35**,** 5351-5359.

GRABCZYK, E. & USDIN, K. 2000a. Alleviating transcript insufficiency caused by Friedreich's ataxia triplet repeats. *Nucleic Acids Research,* 28**,** 4930-4937.

GRABCZYK, E. & USDIN, K. 2000b. The GAA•TTC triplet repeat expanded in Friedreich's ataxia impedes transcription elongation by T7 RNA polymerase in a length and supercoil dependent manner. *Nucleic Acids Research,* 28**,** 2815-2822.

GREENE, E., ENTEZAM, A., KUMARI, D. & USDIN, K. 2005. Ancient repeated DNA elements and the regulation of the human frataxin promoter. *Genomics,* 85**,** 221-230.

GREENE, E., MAHISHI, L., ENTEZAM, A., KUMARI, D. & USDIN, K. 2007. Repeat-induced epigenetic changes in intron 1 of the frataxin gene and its consequences in Friedreich ataxia. *Nucleic acids research,* 35**,** 3383-3390.

GREGORY, L. G., WADDINGTON, S. N., HOLDER, M. V., MITROPHANOUS, K. A., BUCKLEY, S. M., MOSLEY, K. L., BIGGER, B. W., ELLARD, F. M., WALMSLEY, L. E., LAWRENCE, L., AL-ALLAF, F., KINGSMAN, S., COUTELLE, C. & THEMIS, M. 2004. Highly efficient EIAV-mediated in utero gene transfer and expression in the major muscle groups affected by Duchenne muscular dystrophy. *Gene Ther,* 11**,** 1117-25.

GUCCINI, I., SERIO, D., CONDO, I., RUFINI, A., TOMASSINI, B., MANGIOLA, A., MAIRA, G., ANILE, C., FINA, D. & PALLONE, F. 2011. Frataxin participates to the hypoxia-induced response in tumors. *Cell death & disease,* 2**,** e123.

HACEIN-BEY-ABINA, S., VON KALLE, C., SCHMIDT, M., LE DEIST, F., WULFFRAAT, N., MCINTYRE, E., RADFORD, I., VILLEVAL, J.-L., FRASER, C. C. & CAVAZZANA-CALVO, M. 2003. A serious adverse event after successful gene therapy for X-linked severe combined immunodeficiency. *New England Journal of Medicine,* 348**,** 255-256.

HALWANI, R., CEN, S., JAVANBAKHT, H., SAADATMAND, J., KIM, S., SHIBA, K. & KLEIMAN, L. 2004. Cellular Distribution of Lysyl-tRNA Synthetase and Its Interaction with Gag during Human Immunodeficiency Virus Type 1 Assembly. *Journal of Virology,* 78**,** 7553-7564.

HANAUER, A., CHERY, M., FUJITA, R., DRIESEL, A. J., GILGENKRANTZ, S. & MANDEL, J. L. 1990. The Friedreich ataxia gene is assigned to chromosome 9q13-q21 by mapping of tightly linked markers and shows linkage disequilibrium with D9S15.

HARDING, A. E. 1981. Friedreich's ataxia: a clinical and genetic study of 90 families with an analysis of early diagnostic criteria and intrafamilial clustering of clinical features. *Brain,* 104**,** 589-620.

HARDING, A. E. 1984. *The hereditary ataxias and related disorders*, Churchill Livingstone.

HARRIS, R. S., BISHOP, K. N., SHEEHY, A. M., CRAIG, H. M., PETERSEN-MAHRT, S. K., WATT, I. N., NEUBERGER, M. S. & MALIM, M. H. 2003. DNA deamination mediates innate immunity to retroviral infection. *Cell,* 113**,** 803-809.

HART, P. E., LODI, R., RAJAGOPALAN, B., BRADLEY, J. L., CRILLEY, J. G., TURNER, C., BLAMIRE, A. M., MANNERS, D., STYLES, P., SCHAPIRA, A. H. V. & COOPER, J. M. 2005. Antioxidant Treatment of Patients With Friedreich Ataxia: Four-Year Follow-up. *Arch Neurol,* 62**,** 621-626.

HAUGEN, A. C., DI PROSPERO, N. A., PARKER, J. S., FANNIN, R. D., CHOU, J., MEYER, J. N., HALWEG, C., COLLINS, J. B., DURR, A. & FISCHBECK, K. 2010. Altered gene expression and DNA damage in peripheral blood cells from Friedreich's ataxia patients: cellular model of pathology. *PLoS genetics,* 6**,** e1000812.

HELSETH, E., KOWALSKI, M., GABUZDA, D., OLSHEVSKY, U., HASELTINE, W. & SODROSKI, J. 1990. Rapid complementation assays measuring replicative potential of human immunodeficiency virus type 1 envelope glycoprotein mutants. *Journal of virology,* 64**,** 2416-2420.

HERBST, F., BALL, C. R., TUORTO, F., NOWROUZI, A., WANG, W., ZAVIDIJ, O., DIETER, S. M., FESSLER, S., VAN DER HOEVEN, F. & KLOZ, U. 2012. Extensive methylation of promoter sequences silences lentiviral transgene expression during stem cell differentiation in vivo. *Molecular Therapy*.

HERMAN, D., JENSSEN, K., BURNETT, R., SORAGNI, E., PERLMAN, S. L. & GOTTESFELD, J. M. 2006. Histone deacetylase inhibitors reverse gene silencing in Friedreich's ataxia. *Nature chemical biology,* 2**,** 551-558.

HICK, A., WATTENHOFER-DONZÉ, M., CHINTAWAR, S., TROPEL, P., SIMARD, J. P., VAUCAMPS, N., GALL, D., LAMBOT, L., ANDRÉ, C. & REUTENAUER, L. 2013. Neurons and cardiomyocytes derived from induced pluripotent stem cells as a model for mitochondrial defects in Friedreich's ataxia. *Disease models & mechanisms,* 6**,** 608-621.

HIRANO, M., KATO, S., KOBAYASHI, K., OKADA, T., YAGINUMA, H. & KOBAYASHI, K. 2013. Highly efficient retrograde gene transfer into motor neurons by a lentiviral vector pseudotyped with fusion glycoprotein. *PloS one,* 8**,** e75896.

HIRAYAMA, K., TAKAYANAGI, T., NAKAMURA, R., YANAGISAWA, N., HATTORI, T., KITA, K., YANAGIMOTO, S., FUJITA, M., NAGAOKA, M. & SATOMURA, Y. 1994. Spinocerebellar degenerations in Japan: a nationwide epidemiological and clinical study. *Acta Neurologica Scandinavica,* 89**,** 1-22.

HOWE, S. J., MANSOUR, M. R., SCHWARZWAELDER, K., BARTHOLOMAE, C., HUBANK, M., KEMPSKI, H., BRUGMAN, M. H., PIKE-OVERZET, K., CHATTERS, S. J. & DE RIDDER, D. 2008. Insertional mutagenesis combined with acquired somatic mutations causes leukemogenesis following gene therapy of SCID-X1 patients. *The Journal of clinical investigation,* 118**,** 3143.

HUTHOFF, H., BUGALA, K., BARCISZEWSKI, J. & BERKHOUT, B. 2003. On the importance of the primer activation signal for initiation of tRNAlys3-primed reverse transcription of the HIV-1 RNA genome. *Nucleic Acids Research,* 31**,** 5186-5194.

HUYNEN, M. A., SNEL, B., BORK, P. & GIBSON, T. J. 2001. The phylogenetic distribution of frataxin indicates a role in iron-sulfur cluster protein assembly. *Human Molecular Genetics,* 10**,** 2463-2468.

IWAKUMA, T., CUI, Y. & CHANG, L.-J. 1999. Self-inactivating lentiviral vectors with U3 and U5 modifications. *Virology,* 261**,** 120-132.

JAUSLIN, M. L., WIRTH, T., MEIER, T. & SCHOUMACHER, F. 2002. A cellular model for Friedreich Ataxia reveals small-molecule glutathione peroxidase mimetics as novel treatment strategy. *Human molecular genetics,* 11**,** 3055-3063.

JIRALERSPONG, S., GE, B., HUDSON, T. J. & PANDOLFO, M. 2001. Manganese superoxide dismutase induction by iron is impaired in Friedreich ataxia cells. *FEBS letters,* 509**,** 101-105.

JIRALERSPONG, S., LIU, Y., MONTERMINI, L., STIFANI, S. & PANDOLFO, M. 1997. Frataxin shows developmentally regulated tissue-specific expression in the mouse embryo. *Neurobiology of disease,* 4**,** 103-113.

JONES, J., ESTIRADO, A., REDONDO, C. & MARTINEZ, S. 2013. Stem cells from wildtype and Friedreich's ataxia mice present similar neuroprotective properties in dorsal root ganglia cells.

KANG, Y., XIE, L., TRAN, D. T., STEIN, C. S., HICKEY, M., DAVIDSON, B. L. & MCCRAY, P. B. 2005. Persistent expression of factor VIII in vivo following nonprimate lentiviral gene transfer. *Blood,* 106**,** 1552-1558.

KARTHIKEYAN, G., LEWIS, L. K. & RESNICK, M. A. 2002. The mitochondrial protein frataxin prevents nuclear damage. *Human molecular genetics,* 11**,** 1351-1362.

KARTHIKEYAN, G., SANTOS, J. H., GRAZIEWICZ, M. A., COPELAND, W. C., ISAYA, G., VAN HOUTEN, B. & RESNICK, M. A. 2003. Reduction in frataxin causes progressive accumulation of mitochondrial damage. *Human molecular genetics,* 12**,** 3331-3342.

KATO, S., KOBAYASHI, K. & KOBAYASHI, K. 2014. Improved transduction efficiency of a lentiviral vector for neuron-specific retrograde gene transfer by optimizing the junction of fusion envelope glycoprotein. *Journal of neuroscience methods,* 227**,** 151-158.

KAY, M. A., GLORIOSO, J. C. & NALDINI, L. 2001. Viral vectors for gene therapy: the art of turning infectious agents into vehicles of therapeutics. *Nat Med,* 7**,** 33-40.

KAYTOR, M. D., BURRIGHT, E. N., DUVICK, L. A., ZOGHBI, H. Y. & ORR, H. T. 1997. Increased Trinucleotide Repeat Instability with Advanced Maternal Age. *Human Molecular Genetics,* 6**,** 2135-2139.

KEMP, K., MALLAM, E., HARES, K., WITHERICK, J., SCOLDING, N. & WILKINS, A. 2011. Mesenchymal stem cells restore frataxin expression and increase hydrogen peroxide scavenging enzymes in Friedreich ataxia fibroblasts. *PloS one,* 6**,** e26098.

KIM, V. N., MITROPHANOUS, K., KINGSMAN, S. M. & KINGSMAN, A. J. 1998. Minimal requirement for a lentivirus vector based on human immunodeficiency virus type 1. *Journal of virology,* 72**,** 811-816.

KINGSMAN, S., MITROPHANOUS, K. & OLSEN, J. 2005. Potential oncogene activity of the woodchuck hepatitis post-transcriptional regulatory element (WPRE). *Gene therapy,* 12**,** 3-4.

KLOCKGETHER, T. 2007. Ataxias. *Parkinsonism & related disorders,* 13**,** S391-S394.

KOEPPEN, A. H. 2013. Nikolaus Friedreich and degenerative atrophy of the dorsal columns of the spinal cord. *Journal of Neurochemistry,* 126**,** 4-10.

KOEPPEN, A. H., MORRAL, J. A., MCCOMB, R. D. & FEUSTEL, P. J. 2011. The neuropathology of late-onset Friedreich's ataxia. *The Cerebellum,* 10**,** 96-103.

KONDO, Y., SHEN, L. & ISSA, J.-P. J. 2003. Critical Role of Histone Methylation in Tumor Suppressor Gene Silencing in Colorectal Cancer. *Mol. Cell. Biol.,* 23**,** 206-215.

KOTIN, R. M., SINISCALCO, M., SAMULSKI, R. J., ZHU, X., HUNTER, L., LAUGHLIN, C. A., MCLAUGHLIN, S., MUZYCZKA, N., ROCCHI, M. & BERNS, K. I. 1990. Site-specific integration by adeno-associated virus. *Proceedings of the National Academy of Sciences,* 87**,** 2211-2215.

KOUTNIKOVA, H., CAMPUZANO, V., FOURY, F., DOLLÉ, P., CAZZALINI, O. & KOENIG, M. 1997. Studies of human, mouse and yeast homologues indicate a mitochondrial function for frataxin. *Nature genetics,* 16**,** 345-351.

KOVTUN, I. V. & MCMURRAY, C. T. 2008. Features of trinucleotide repeat instability in vivo. *Cell Res,* 18**,** 198-213.

KU, S., SORAGNI, E., CAMPAU, E., THOMAS, E. A., ALTUN, G., LAURENT, L. C., LORING, J. F., NAPIERALA, M. & GOTTESFELD, J. M. 2010. Friedreich's ataxia induced pluripotent stem cells model intergenerational GAA· TTC triplet repeat instability. *Cell stem cell,* 7**,** 631-637.

KUMARI, D., BIACSI, R. E. & USDIN, K. 2011. Repeat expansion affects both transcription initiation and elongation in friedreich ataxia cells. *Journal of Biological Chemistry,* 286**,** 4209-4215.

KUSHNAREVA, Y., MURPHY, A. & ANDREYEV, A. 2002. Complex I-mediated reactive oxygen species generation: modulation by cytochrome c and NAD (P)+ oxidation–reduction state. *Biochem. J,* 368**,** 545-553.

LABUDA, M., LABUDA, D., MIRANDA, C., POIRIER, J., SOONG, B.-W., BARUCHA, N. & PANDOLFO, M. 2000. Unique origin and specific ethnic distribution of the Friedreich ataxia GAA expansion. *Neurology,* 54**,** 2322-2324.

LAGOUGE, M. & LARSSON, N. G. 2013. The role of mitochondrial DNA mutations and free radicals in disease and ageing. *Journal of internal medicine,* 273**,** 529-543.

LAIMBACHER, A. S. & FRAEFEL, C. 2014. HSV-1 amplicon vectors as genetic vaccines. *Herpes simplex virus: methods and protocols***,** 99-115.

LAMBETH, J. D. 2004. NOX enzymes and the biology of reactive oxygen. *Nature Reviews Immunology,* 4**,** 181-189.

LANDAU, N., PAGE, K. & LITTMAN, D. 1991. Pseudotyping with human T-cell leukemia virus type I broadens the human immunodeficiency virus host range. *Journal of virology,* 65**,** 162-169.

LASPIA, M. F., RICE, A. P. & MATHEWS, M. B. 1989. HIV-1 Tat protein increases transcriptional initiation and stabilizes elongation. *Cell,* 59**,** 283-292.

LEE, K. K. & WORKMAN, J. L. 2007. Histone acetyltransferase complexes: one size doesn't fit all. *Nat Rev Mol Cell Biol,* 8**,** 284-295.

LEWIS, P., CORR, J., ARLETT, C. & HARCOURT, S. 1979. Increased sensitivity to gamma irradiation of skin fibroblasts in Friedreich's ataxia. *The Lancet,* 314**,** 474-475.

LI, K., BESSE, E. K., HA, D., KOVTUNOVYCH, G. & ROUAULT, T. A. 2008. Iron-dependent regulation of frataxin expression: implications for treatment of Friedreich ataxia. *Human Molecular Genetics,* 17**,** 2265-2273.

LI, L., VOULLAIRE, L., SANDI, C., POOK, M. A., IOANNOU, P. A., DELATYCKI, M. B. & SARSERO, J. P. 2013. Pharmacological screening using an FXN-EGFP cellular genomic reporter assay for the therapy of Friedreich ataxia. *PloS one,* 8**,** e55940.

LIM, F., PALOMO, G. M., MAURITZ, C., GIMÉNEZ-CASSINA, A., ILLANA, B., WANDOSELL, F. & DÍAZ-NIDO, J. 2007. Functional recovery in a Friedreich's ataxia mouse model by frataxin gene transfer using an HSV-1 amplicon vector. *Molecular Therapy,* 15**,** 1072-1078.

LIM, S. Y., SIVAKUMARAN, P., CROMBIE, D. E., DUSTING, G. J., PÉBAY, A. & DILLEY, R. J. 2013. Trichostatin A enhances differentiation of human induced pluripotent stem cells to cardiogenic cells for cardiac tissue engineering. *Stem cells translational medicine*, sctm. 2012-0161.

LIU, J., VERMA, P. J., EVANS-GALEA, M. V., DELATYCKI, M. B., MICHALSKA, A., LEUNG, J., CROMBIE, D., SARSERO, J. P., WILLIAMSON, R. & DOTTORI, M. 2011. Generation of induced pluripotent stem cell lines from Friedreich ataxia patients. *Stem Cell Reviews and Reports,* 7**,** 703-713.

LLORENS, J. V., NAVARRO, J. A., MARTÍNEZ-SEBASTIÁN, M. J., BAYLIES, M. K., SCHNEUWLY, S., BOTELLA, J. A. & MOLTÓ, M. D. 2007. Causative role of oxidative stress in a Drosophila model of Friedreich ataxia. *The FASEB Journal,* 21**,** 333-344.

LODI, R., COOPER, J. M., BRADLEY, J. L., MANNERS, D., STYLES, P., TAYLOR, D. J. & SCHAPIRA, A. H. 1999. Deficit of in vivo mitochondrial ATP production in patients with Friedreich ataxia. *Proceedings of the National Academy of Sciences,* 96**,** 11492-11495.

LODI, R., HART, P. E., RAJAGOPALAN, B., TAYLOR, D. J., CRILLEY, J. G., BRADLEY, J. L., BLAMIRE, A. M., MANNERS, D., STYLES, P., SCHAPIRA, A. H. & COOPER, J. M. 2001. Antioxidant treatment improves in vivo cardiac and skeletal muscle bioenergetics in patients with Friedreich's ataxia. *Annals of Neurology,* 49**,** 590-596.

MALIM, M. H. & EMERMAN, M. 2008. HIV-1 Accessory Proteins—Ensuring Viral Survival in a Hostile Environment. *Cell Host & Microbe,* 3**,** 388-398.

MANN, R. & BALTIMORE, D. 1985. Varying the position of a retrovirus packaging sequence results in the encapsidation of both unspliced and spliced RNAs. *Journal of Virology,* 54**,** 401-407.

MANN, R., MULLIGAN, R. C. & BALTIMORE, D. 1983. Construction of a retrovirus packaging mutant and its use to produce helper-free defective retrovirus. *Cell,* 33**,** 153-159.

MARMOLINO, D., MANTO, M., ACQUAVIVA, F., VERGARA, P., RAVELLA, A., MONTICELLI, A. & PANDOLFO, M. 2010. PGC-1alpha down-regulation affects the antioxidant response in Friedreich's ataxia. *Plos one,* 5**,** e10025.

MARTELLI, A., FRIEDMAN, L. S., REUTENAUER, L., MESSADDEQ, N., PERLMAN, S. L., LYNCH, D. R., FEDOSOV, K., SCHULZ, J. B., PANDOLFO, M. & PUCCIO, H. 2012. Clinical data and characterization of the liver conditional mouse model exclude neoplasia as a non-neurological manifestation associated with Friedreich's ataxia. *Disease models & mechanisms,* 5**,** 860-869.

MCCARTY, D. M. 2008. Self-complementary AAV vectors; advances and applications. *Molecular Therapy,* 16**,** 1648-1656.

MCCORD, J. M. & FRIDOVICH, I. 1969. Superoxide dismutase an enzymic function for erythrocuprein (hemocuprein). *Journal of Biological chemistry,* 244**,** 6049-6055.

MICHAEL, S., PETROCINE, S. V., QIAN, J., LAMARCHE, J. B., KNUTSON, M. D., GARRICK, M. D. & KOEPPEN, A. H. 2006. Iron and iron-responsive proteins in the cardiomyopathy of Friedreich's ataxia. *The Cerebellum,* 5**,** 257-267.

MILLER, D. G., PETEK, L. M. & RUSSELL, D. W. 2004. Adeno-associated virus vectors integrate at chromosome breakage sites. *Nature genetics,* 36**,** 767-773.

MILLER, M. D., FARNET, C. M. & BUSHMAN, F. D. 1997. Human immunodeficiency virus type 1 preintegration complexes: studies of organization and composition. *Journal of Virology,* 71**,** 5382-90.

MIRANDA, C. J., SANTOS, M. M., OHSHIMA, K., SMITH, J., LI, L., BUNTING, M., COSSÉE, M., KOENIG, M., SEQUEIROS, J., KAPLAN, J. & PANDOLFO, M. 2002. Frataxin knockin mouse. *FEBS letters,* 512**,** 291-297.

MIRANDA, C. J., SANTOS, M. M., OHSHIMA, K., TESSARO, M., SEQUEIROS, J. & PANDOLFO, M. 2004. Frataxin overexpressing mice. *FEBS letters,* 572**,** 281-288.

MITANI, K. & KUBO, S. 2002. Adenovirus As An Integrating Vector. *Current Gene Therapy,* 2**,** 135-144.

MITROPHANOUS, K., YOON, S., ROHLL, J., PATIL, D., WILKES, F., KIM, V., KINGSMAN, S., KINGSMAN, A. & MAZARAKIS, N. 1999. Stable gene transfer to the nervous system using a non-primate lentiviral vector. *Gene therapy,* 6**,** 1808-1818.

MIYOSHI, H., BLÖMER, U., TAKAHASHI, M., GAGE, F. H. & VERMA, I. M. 1998. Development of a self-inactivating lentivirus vector. *Journal of virology,* 72**,** 8150-8157.

MIYOSHI, H., TAKAHASHI, M., GAGE, F. H. & VERMA, I. M. 1997. Stable and efficient gene transfer into the retina using an HIV-based lentiviral vector. *Proceedings of the National Academy of Sciences,* 94**,** 10319-10323.

MONTERMINI, L., ANDERMANN, E., LABUDA, M., RICHTER, A., PANDOLFO, M., CAVALCANTI, F., PIANESE, L., IODICE, L., FARINA, G., MONTICELLI, A., TURANO, M., FILLA, A., DE MICHELE, G. & COCOZZA, S. 1997a. The Friedreich Ataxia GAA Triplet Repeat: Premutation and Normal Alleles. *Human Molecular Genetics,* 6**,** 1261-1266.

MONTERMINI, L., KISH, S. J., JIRALERSPONG, S., LAMARCHE, J. B. & PANDOLFO, M. 1997b. Somatic mosaicism for Friedreich's ataxia GAA triplet repeat expansions in the central nervous system. *Neurology,* 49**,** 606-610.

MONTINI, E., CESANA, D., SCHMIDT, M., SANVITO, F., BARTHOLOMAE, C. C., RANZANI, M., BENEDICENTI, F., SERGI, L. S., AMBROSI, A., PONZONI, M., DOGLIONI, C., DI SERIO, C., VON KALLE, C. & NALDINI, L. 2009. The genotoxic potential of retroviral vectors is strongly modulated by vector design and integration site selection in a mouse model of HSC gene therapy. *The Journal of Clinical Investigation,* 119**,** 964-975.

MORRAL, J. A., DAVIS, A. N., QIAN, J., GELMAN, B. B. & KOEPPEN, A. H. 2010. Pathology and pathogenesis of sensory neuropathy in Friedreich's ataxia. *Acta neuropathologica,* 120**,** 97-108.

MOSCHNER, C., PERLMAN, S. & BALOH, R. W. 1994. Comparison of oculomotor findings in the progressive ataxia syndromes. *Brain,* 117**,** 15-25.

MÜHLENHOFF, U., RICHHARDT, N., GERBER, J. & LILL, R. 2002. Characterization of Iron-Sulfur Protein Assembly in Isolated Mitochondria A REQUIREMENT FOR ATP, NADH, AND REDUCED IRON. *Journal of Biological Chemistry,* 277**,** 29810-29816.

NAKAI, H., MONTINI, E., FUESS, S., STORM, T. A., GROMPE, M. & KAY, M. A. 2003. AAV serotype 2 vectors preferentially integrate into active genes in mice. *Nature genetics,* 34**,** 297-302.

NALDINI, L., BLÖMER, U., GAGE, F. H., TRONO, D. & VERMA, I. M. 1996a. Efficient transfer, integration, and sustained long-term expression of the transgene in adult rat brains injected with a lentiviral vector. *Proceedings of the National Academy of Sciences,* 93**,** 11382-11388.

NALDINI, L., BLÖMER, U., GALLAY, P., ORY, D., MULLIGAN, R., GAGE, F. H., VERMA, I. M. & TRONO, D. 1996b. In vivo gene delivery and stable transduction of nondividing cells by a lentiviral vector. *Science,* 272**,** 263-267.

NAPOLI, E., TARONI, F. & CORTOPASSI, G. A. 2006. Frataxin, iron-sulfur clusters, heme, ROS, and aging. *Antioxidants & redox signaling,* 8**,** 506-516.

NARDIN, R. A. & JOHNS, D. R. 2001. Mitochondrial dysfunction and neuromuscular disease. *Muscle & Nerve,* 24**,** 170-191.

NATHWANI, A. C., TUDDENHAM, E. G., RANGARAJAN, S., ROSALES, C., MCINTOSH, J., LINCH, D. C., CHOWDARY, P., RIDDELL, A., PIE, A. J. & HARRINGTON, C. 2011. Adenovirus-associated virus vector–mediated gene transfer in hemophilia B. *New England Journal of Medicine,* 365**,** 2357-2365.

NAVARRO, J. A., LLORENS, J. V., SORIANO, S., BOTELLA, J. A., SCHNEUWLY, S., MARTÍNEZ-SEBASTIÁN, M. J. & MOLTÓ, M. D. 2011. Overexpression of human and fly frataxins in Drosophila

provokes deleterious effects at biochemical, physiological and developmental levels. *PloS one,* 6**,** e21017.
NEGRINI, S., GORGOULIS, V. G. & HALAZONETIS, T. D. 2010. Genomic instability—an evolving hallmark of cancer. *Nature reviews Molecular cell biology,* 11**,** 220-228.
NEIL, S. J., ZANG, T. & BIENIASZ, P. D. 2008. Tetherin inhibits retrovirus release and is antagonized by HIV-1 Vpu. *Nature,* 451**,** 425-430.
NICHOL, H., GAKH, O., O'NEILL, H. A., PICKERING, I. J., ISAYA, G. & GEORGE, G. N. 2003. Structure of frataxin iron cores: an X-ray absorption spectroscopic study. *Biochemistry,* 42**,** 5971-5976.
NIENHUIS, A. W., DUNBAR, C. E. & SORRENTINO, B. P. 2006. Genotoxicity of retroviral integration in hematopoietic cells. *Molecular Therapy,* 13**,** 1031-1049.
NOWROUZI, A., CHEUNG, W. T., LI, T., ZHANG, X., ARENS, A., PARUZYNSKI, A., WADDINGTON, S. N., OSEJINDU, E., REJA, S. & VON KALLE, C. 2013. The fetal mouse is a sensitive genotoxicity model that exposes lentiviral-associated mutagenesis resulting in liver oncogenesis. *Molecular Therapy,* 21**,** 324-337.
O'CONNOR, T. P. & CRYSTAL, R. G. 2006. Genetic medicines: treatment strategies for hereditary disorders. *Nat Rev Genet,* 7**,** 261-276.
O'ROURKE, J., OLSEN, J. & BUNNELL, B. 2005. Optimization of equine infectious anemia derived vectors for hematopoietic cell lineage gene transfer. *Gene therapy,* 12**,** 22-29.
OHSHIMA, K., SAKAMOTO, N., LABUDA, M., POIRIER, J., MOSELEY, M. L., MONTERMINI, L., RANUM, L. P. W., WELLS, R. D. & PANDOLFO, M. 1999. A nonpathogenic GAAGGA repeat in the Friedreich gene: Implications for pathogenesis. *Neurology,* 53**,** 1854-.
OTT, M. G., SCHMIDT, M., SCHWARZWAELDER, K., STEIN, S., SILER, U., KOEHL, U., GLIMM, H., KÜHLCKE, K., SCHILZ, A. & KUNKEL, H. 2006. Correction of X-linked chronic granulomatous disease by gene therapy, augmented by insertional activation of MDS1-EVI1, PRDM16 or SETBP1. *Nature medicine,* 12**,** 401-409.
PAGE, K. A., LANDAU, N. R. & LITTMAN, D. 1990. Construction and use of a human immunodeficiency virus vector for analysis of virus infectivity. *Journal of virology,* 64**,** 5270-5276.
PALOMO, G. M., CERRATO, T., GARGINI, R. & DIAZ-NIDO, J. 2011. Silencing of frataxin gene expression triggers p53-dependent apoptosis in human neuron-like cells. *Human molecular genetics,* 20**,** 2807-2822.
PANDOLFO, M. 2008. Friedreich ataxia. *Archives of neurology,* 65**,** 1296-1303.
PANDOLFO, M. 2009. Friedreich ataxia: The clinical picture. *Journal of Neurology,* 256**,** 3-8.
PANDOLFO, M. 2012. Friedreich Ataxia New Pathways. *Journal of child neurology,* 27**,** 1204-1211.
PARKINSON, M. H., SCHULZ, J. B. & GIUNTI, P. 2013. Co-enzyme Q10 and idebenone use in Friedreich's ataxia. *Journal of neurochemistry,* 126**,** 125-141.
PAYNE, R. M. & WAGNER, G. R. 2012. Cardiomyopathy in Friedreich Ataxia Clinical Findings and Research. *Journal of child neurology,* 27**,** 1179-1186.
PEARSON, C. E., EDAMURA, K. N. & CLEARY, J. D. 2005. Repeat instability: mechanisms of dynamic mutations. *Nat Rev Genet,* 6**,** 729-742.
PERDOMINI, M., BELBELLAA, B., MONASSIER, L., REUTENAUER, L., MESSADDEQ, N., CARTIER, N., CRYSTAL, R. G., AUBOURG, P. & PUCCIO, H. 2014. Prevention and reversal of severe mitochondrial cardiomyopathy by gene therapy in a mouse model of Friedreich's ataxia. *Nat Med,* advance online publication.
PEREZ, L. G., DAVIS, G. L. & HUNTER, E. 1987. Mutants of the Rous sarcoma virus envelope glycoprotein that lack the transmembrane anchor and cytoplasmic domains: analysis of intracellular transport and assembly into virions. *Journal of Virology,* 61**,** 2981-2988.
PERLMAN, S. L. 2012. A review of Friedreich ataxia clinical trial results. *Journal of child neurology,* 27**,** 1217-1222.

PHILIPPE, S., SARKIS, C., BARKATS, M., MAMMERI, H., LADROUE, C., PETIT, C., MALLET, J. & SERGUERA, C. 2006. Lentiviral vectors with a defective integrase allow efficient and sustained transgene expression in vitro and in vivo. *Proceedings of the National Academy of Sciences,* 103**,** 17684-17689.

PIZZI, C., DI MAIO, M., DANIELE, S., MASTRANZO, P., SPAGNOLETTI, I., LIMITE, GENNARO, PETTINATO, GUIDO, MONTICELM, ANTONELLA, COCOZZA, SERGIO, CONTEGIACOMO & ALMA 2007. *Triplet repeat instability correlates with dinucleotide instability in primary breast cancer,* Athens, GRECE, Spandidos.

PLASTERER, H. L., DEUTSCH, E. C., BELMONTE, M., EGAN, E., LYNCH, D. R. & RUSCHE, J. R. 2013. Development of Frataxin Gene Expression Measures for the Evaluation of Experimental Treatments in Friedreich's Ataxia. *PLoS ONE,* 8**,** e63958.

POLLARD, V. W. & MALIM, M. H. 1998. THE HIV-1 REV PROTEIN. *Annual Review of Microbiology,* 52**,** 491-532.

POOK, M. A., AL-MAHDAWI, S., CARROLL, C. J., COSSÉE, M., PUCCIO, H., LAWRENCE, L., CLARK, P., LOWRIE, M. B., BRADLEY, J. L. & COOPER, M. J. 2001. Rescue of the Friedreich's ataxia knockout mouse by human YAC transgenesis. *Neurogenetics,* 3**,** 185-193.

POTAMAN, V. N., OUSSATCHEVA, E. A., LYUBCHENKO, Y. L., SHLYAKHTENKO, L. S., BIDICHANDANI, S. I., ASHIZAWA, T. & SINDEN, R. R. 2004. Length-dependent structure formation in Friedreich ataxia (GAA)n·(TTC)n repeats at neutral pH. *Nucleic Acids Research,* 32**,** 1224-1231.

PUCCIO, H., SIMON, D., COSSÉE, M., CRIQUI-FILIPE, P., TIZIANO, F., MELKI, J., HINDELANG, C., MATYAS, R., RUSTIN, P. & KOENIG, M. 2001. Mouse models for Friedreich ataxia exhibit cardiomyopathy, sensory nerve defect and Fe-S enzyme deficiency followed by intramitochondrial iron deposits. *Nature genetics,* 27**,** 181-186.

RADI, R., TURRENS, J. F., CHANG, L. Y., BUSH, K. M., CRAPO, J. D. & FREEMAN, B. A. 1991. Detection of catalase in rat heart mitochondria. *Journal of Biological Chemistry,* 266**,** 22028-22034.

RAI, M., SORAGNI, E., CHOU, C. J., BARNES, G., JONES, S., RUSCHE, J. R., GOTTESFELD, J. M. & PANDOLFO, M. 2010. Two new pimelic diphenylamide HDAC inhibitors induce sustained frataxin upregulation in cells from Friedreich's ataxia patients and in a mouse model. *PLoS One,* 5**,** e8825.

RAMAZZOTTI, A., VANMANSART, V. & FOURY, F. 2004. Mitochondrial functional interactions between frataxin and Isu1p, the iron–sulfur cluster scaffold protein, in Saccharomyces cerevisiae. *FEBS letters,* 557**,** 215-220.

REABAN, M. E. & GRIFFIN, J. A. 1990. Induction of RNA-stabilized DMA conformers by transcription of an immunoglobulin switch region. *Nature,* 348**,** 342-344.

RÉMY, S., TESSON, L., MÉNORET, S., USAL, C., SCHARENBERG, A. & ANEGON, I. 2010. Zinc-finger nucleases: a powerful tool for genetic engineering of animals. *Transgenic Research,* 19**,** 363-371.

RICHARDSON, D. 2003. Friedreich's ataxia: iron chelators that target the mitochondrion as a therapeutic strategy? *Expert Opinion on Investigational Drugs,* 12**,** 235-245.

RICHARDSON, J. H., CHILD, L. A. & LEVER, A. 1993. Packaging of human immunodeficiency virus type 1 RNA requires cis-acting sequences outside the 5'leader region. *Journal of virology,* 67**,** 3997-4005.

RICHARDSON, T. E., KELLY, H. N., AMANDA, E. Y. & SIMPKINS, J. W. 2013. Therapeutic strategies in Friedreich's ataxia. *Brain research,* 1514**,** 91-97.

RICHARDSON, T. E., YU, A. E., WEN, Y., YANG, S.-H. & SIMPKINS, J. W. 2012. Estrogen prevents oxidative damage to the mitochondria in Friedreich's ataxia skin fibroblasts. *PLoS One,* 7**,** e34600.

ROGAKOU, E. P., PILCH, D. R., ORR, A. H., IVANOVA, V. S. & BONNER, W. M. 1998. DNA double-stranded breaks induce histone H2AX phosphorylation on serine 139. *Journal of biological chemistry,* 273**,** 5858-5868.

ROMANO, G., KASTEN, M., DE FALCO, G., MICHELI, P., KHALILI, K. & GIORDANO, A. 1999. Regulatory functions of Cdk9 and of cyclin T1 in HIV Tat transactivation pathway gene expression. *Journal of Cellular Biochemistry,* 75**,** 357-368.

ROTIG, A., LONLAY, P. D., CHRETIEN, D., FOURY, F., KOENIG, M., SIDI, D., MUNNICH, A. & RUSTIN, P. 1997. Aconitase and mitochondrial iron-sulphur protein deficiency in Friedreich ataxia. *Nature genetics,* 17**,** 215-217.

RUSCETTI, S. K. 1995. 10 Erythroleukaemia induction by the Friend spleen focus-forming virus. *Baillière's Clinical Haematology,* 8**,** 225-247.

RUSTIN, P., VON KLEIST-RETZOW, J.-C., CHANTREL-GROUSSARD, K., SIDI, D., MUNNICH, A. & RÖTIG, A. 1999. Effect of idebenone on cardiomyopathy in Friedreich's ataxia: a preliminary study. *The Lancet,* 354**,** 477-479.

SAKAMOTO, N., CHASTAIN, P. D., PARNIEWSKI, P., OHSHIMA, K., PANDOLFO, M., GRIFFITH, J. D. & WELLS, R. D. 1999. Sticky DNA: Self-Association Properties of Long GAA·TTC Repeats in R·R·Y Triplex Structures from Friedreich s Ataxia. *Molecular cell,* 3**,** 465-475.

SAKUMA, T., BARRY, MICHAEL A. & IKEDA, Y. 2012. Lentiviral vectors: basic to translational. *Biochemical Journal,* 443**,** 603-618.

SAKUMA, T., NODA, T., URATA, S., KAWAOKA, Y. & YASUDA, J. 2009. Inhibition of Lassa and Marburg virus production by tetherin. *Journal of virology,* 83**,** 2382-2385.

SANDI, C., PINTO, R. M., AL-MAHDAWI, S., EZZATIZADEH, V., BARNES, G., JONES, S., RUSCHE, J. R., GOTTESFELD, J. M. & POOK, M. A. 2011. Prolonged treatment with pimelic o-aminobenzamide HDAC inhibitors ameliorates the disease phenotype of a Friedreich ataxia mouse model. *Neurobiology of Disease,* 42**,** 496-505.

SARSERO, J. P., LI, L., HOLLOWAY, T. P., VOULLAIRE, L., GAZEAS, S., FOWLER, K. J., KIRBY, D. M., THORBURN, D. R., GALLE, A. & CHEEMA, S. 2004. Human BAC-mediated rescue of the Friedreich ataxia knockout mutation in transgenic mice. *Mammalian genome,* 15**,** 370-382.

SCHAMBACH, A., ZYCHLINSKI, D., EHRNSTROEM, B. & BAUM, C. 2013. Biosafety features of lentiviral vectors. *Human gene therapy,* 24**,** 132-142.

SCHAPIRA, A. 1999. Mitochondrial involvement in Parkinson's disease, Huntington's disease, hereditary spastic paraplegia and Friedreich's ataxia. *Biochimica et Biophysica Acta (BBA)-Bioenergetics,* 1410**,** 159-170.

SCHMUCKER, S., MARTELLI, A., COLIN, F., PAGE, A., WATTENHOFER-DONZÉ, M., REUTENAUER, L. & PUCCIO, H. 2011. Mammalian frataxin: an essential function for cellular viability through an interaction with a preformed ISCU/NFS1/ISD11 iron-sulfur assembly complex. *PloS one,* 6**,** e16199-e16199.

SCHNEIDER, R., CAMPBELL, M., NASIOULAS, G., FELBER, B. K. & PAVLAKIS, G. N. 1997. Inactivation of the human immunodeficiency virus type 1 inhibitory elements allows Rev-independent expression of Gag and Gag/protease and particle formation. *Journal of Virology,* 71**,** 4892-903.

SCHOENLE, E., BOLTSHAUSER, E., BAEKKESKOV, S., OLSSON, M. L., TORRESANI, T. & VON FELTEN, A. 1989. Preclinical and manifest diabetes mellitus in young patients with Friedreich's ataxia: no evidence of immune process behind the islet cell destruction. *Diabetologia,* 32**,** 378-381.

SCHULZ, J., DEHMER, T., SCHÖLS, L., MENDE, H., HARDT, C., VORGERD, M., BÜRK, K., MATSON, W., DICHGANS, J. & BEAL, M. 2000. Oxidative stress in patients with Friedreich ataxia. *Neurology,* 55**,** 1719-1721.

SCHULZ, T. J., THIERBACH, R., VOIGT, A., DREWES, G., MIETZNER, B., STEINBERG, P., PFEIFFER, A. F. & RISTOW, M. 2006. Induction of oxidative metabolism by mitochondrial frataxin inhibits cancer growth Otto Warburg Revisited. *Journal of Biological Chemistry,* 281**,** 977-981.

SEDELNIKOVA, O. A., PILCH, D. R., REDON, C. & BONNER, W. M. 2003. Histone H2AX in DNA damage and repair. *Cancer Biol Ther,* 2**,** 233-5.

SEGURA, M. M., MANGION, M., GAILLET, B. & GARNIER, A. 2013. New developments in lentiviral vector design, production and purification. *Expert opinion on biological therapy,* 13**,** 987-1011.

SELKIRK, S. M. 2004. Gene therapy in clinical medicine. *Postgraduate Medical Journal,* 80**,** 560-570.

SHAN, Y., SCHOENFELD, R. A., HAYASHI, G., NAPOLI, E., AKIYAMA, T., IODI CARSTENS, M., CARSTENS, E. E., POOK, M. A. & CORTOPASSI, G. A. 2013. Frataxin deficiency leads to defects in expression of antioxidants and Nrf2 expression in dorsal root ganglia of the Friedreich's ataxia YG8R mouse model. *Antioxidants & redox signaling,* 19**,** 1481-1493.

SHEN, Y., MCMACKIN, M. Z., SHAN, Y., RAETZ, A., DAVID, S. & CORTOPASSI, G. 2016. Frataxin Deficiency Promotes Excess Microglial DNA Damage and Inflammation that Is Rescued by PJ34. *PloS one,* 11**,** e0151026.

SHI, L. & OBERDOERFFER, P. 2012. Chromatin dynamics in DNA double-strand break repair. *Biochimica et Biophysica Acta (BBA)-Gene Regulatory Mechanisms,* 1819**,** 811-819.

SHIMIZU, R., LAN, N. N., TAI, T. T., ADACHI, Y., KAWAZOE, A., MU, A. & TAKETANI, S. 2014. p53 directly regulates the transcription of the human frataxin gene and its lack of regulation in tumor cells decreases the utilization of mitochondrial iron. *Gene,* 551**,** 79-85.

SMITH, J. K., CYWINSKI, A. & TAYLOR, J. M. 1984. Specificity of initiation of plus-strand DNA by Rous sarcoma virus. *Journal of Virology,* 52**,** 314-319.

SON, L. S., BACOLLA, A. & WELLS, R. D. 2006. Sticky DNA: in Vivo Formation in E. coli and in Vitro Association of Long GAA-TTC Tracts to Generate Two Independent Supercoiled Domains. *Journal of Molecular Biology,* 360**,** 267-284.

STURM, B., BISTRICH, U., SCHRANZHOFER, M., SARSERO, J. P., RAUEN, U., SCHEIBER-MOJDEHKAR, B., DE GROOT, H., IOANNOU, P. & PETRAT, F. 2005. Friedreich's Ataxia, No Changes in Mitochondrial Labile Iron in Human Lymphoblasts and Fibroblasts. *Journal of Biological Chemistry,* 280**,** 6701-6708.

SUH, Y.-A., ARNOLD, R. S., LASSEGUE, B., SHI, J., XU, X., SORESCU, D., CHUNG, A. B., GRIENDLING, K. K. & LAMBETH, J. D. 1999. Cell transformation by the superoxide-generating oxidase Mox1. *Nature,* 401**,** 79-82.

TALBERT, P. B. & HENIKOFF, S. 2010. Histone variants—ancient wrap artists of the epigenome. *Nature reviews Molecular cell biology,* 11**,** 264-275.

TANAKA, T., HALICKA, H. D., HUANG, X., TRAGANOS, F. & DARZYNKIEWICZ, Z. 2006. Constitutive histone H2AX phosphorylation and ATM activation, the reporters of DNA damage by endogenous oxidants. *Cell cycle,* 5**,** 1940-1945.

TERWILLIGER, E., BURGHOFF, R., SIA, R., SODROSKI, J., HASELTINE, W. & ROSEN, C. 1988. The art gene product of human immunodeficiency virus is required for replication. *Journal of virology,* 62**,** 655-658.

THEMIS, M., WADDINGTON, S. N., SCHMIDT, M., VON KALLE, C., WANG, Y., AL-ALLAF, F., GREGORY, L. G., NIVSARKAR, M., THEMIS, M., HOLDER, M. V., BUCKLEY, S. M. K., DIGHE, N., RUTHE, A. T., MISTRY, A., BIGGER, B., RAHIM, A., NGUYEN, T. H., TRONO, D., THRASHER, A. J. & COUTELLE, C. 2005. Oncogenesis Following Delivery of a Nonprimate Lentiviral Gene Therapy Vector to Fetal and Neonatal Mice. *Mol Ther,* 12**,** 763-771.

THIERBACH, R., DREWES, G., FUSSER, M., VOIGT, A., KUHLOW, D., BLUME, U., SCHULZ, T., REICHE, C., GLATT, H. & EPE, B. 2010. The Friedreich's ataxia protein frataxin modulates DNA base excision repair in prokaryotes and mammals. *Biochem. J,* 432**,** 165-172.

THOMPSON, A. J. V. & PATEL, K. 2009. Antisense Inhibitors, Ribozymes, and siRNAs. *Clinics in liver disease,* 13**,** 375-390.

TIPPER, C. H., CINGÖZ, O. & COFFIN, J. M. 2012. Mus spicilegus Endogenous Retrovirus HEMV Uses Murine Sodium-Dependent Myo-Inositol Transporter 1 as a Receptor. *Journal of Virology,* 86**,** 6341-6344.

TOURTELLOTTE, W. G. & MILBRANDT, J. 1998. Sensory ataxia and muscle spindle agenesis in mice lacking the transcription factor Egr3. *Nature genetics,* 20**,** 87-91.

TSUJI, #160, T., ITOH, K., BAUM, C., OHNISHI, N., TOMIWA, HIRANO, D., NISHIMURA-MORITA, Y., OSTERTAG, W., FUJITA & J. 2000. *Retroviral vector-mediated gene expression in human CD34[+]CD38[-] cells expanded in vitro : Cis elements of FMEV are superior to those of Mo-MuLV,* Larchmont, NY, ETATS-UNIS, Liebert.

VALDIGLESIAS, V., GIUNTA, S., FENECH, M., NERI, M. & BONASSI, S. 2013. γH2AX as a marker of DNA double strand breaks and genomic instability in human population studies. *Mutation Research/Reviews in Mutation Research,* 753**,** 24-40.

VAN MAELE, B., DE RIJCK, J., DE CLERCQ, E. & DEBYSER, Z. 2003. Impact of the central polypurine tract on the kinetics of human immunodeficiency virus type 1 vector transduction. *Journal of virology,* 77**,** 4685-4694.

VANKAN, P. 2013. Prevalence gradients of Friedreich's Ataxia and R1b haplotype in Europe co-localize, suggesting a common Palaeolithic origin in the Franco-Cantabrian ice age refuge. *Journal of Neurochemistry,* 126**,** 11-20.

VERMA, I. M., MEUTH, N. L., BROMFELD, E., MANLY, K. F. & BALTIMORE, D. 1971. Covalently linked RNA-DNA molecule as initial product of RNA tumour virus DNA polymerase. *Nature: New biology,* 233**,** 131-4.

VETCHER, A. A., NAPIERALA, M., IYER, R. R., CHASTAIN, P. D., GRIFFITH, J. D. & WELLS, R. D. 2002. Sticky DNA, a Long GAA·GAA·TTC Triplex That Is Formed Intramolecularly, in the Sequence of Intron 1 of the Frataxin Gene. *Journal of Biological Chemistry,* 277**,** 39217-39227.

VIGNA, E. & NALDINI, L. 2000. Lentiviral vectors: excellent tools for experimental gene transfer and promising candidates for gene therapy. *The Journal of Gene Medicine,* 2**,** 308-316.

VYAS, P. M., TOMAMICHEL, W. J., PRIDE, P. M., BABBEY, C. M., WANG, Q., MERCIER, J., MARTIN, E. M. & PAYNE, R. M. 2012. A TAT–Frataxin fusion protein increases lifespan and cardiac function in a conditional Friedreich's ataxia mouse model. *Human molecular genetics,* 21**,** 1230-1247.

WADDINGTON, S. N., NIVSARKAR, M. S., MISTRY, A. R., BUCKLEY, S. M., KEMBALL-COOK, G., MOSLEY, K. L., MITROPHANOUS, K., RADCLIFFE, P., HOLDER, M. V. & BRITTAN, M. 2004. Permanent phenotypic correction of hemophilia B in immunocompetent mice by prenatal gene therapy. *Blood,* 104**,** 2714-2721.

WANG, J., FAUST, S. M. & RABINOWITZ, J. E. 2011. The next step in gene delivery: molecular engineering of adeno-associated virus serotypes. *Journal of molecular and cellular cardiology,* 50**,** 793-802.

WANISCH, K. & YANEZ-MUNOZ, R. J. 2009. Integration-deficient Lentiviral Vectors: A Slow Coming of Age. *Mol Ther,* 17**,** 1316-1332.

WATASE, K. & ZOGHBI, H. Y. 2003. Modelling brain diseases in mice: the challenges of design and analysis. *Nat Rev Genet,* 4**,** 296-307.

WATTS, J. M., DANG, K. K., GORELICK, R. J., LEONARD, C. W., BESS JR, J. W., SWANSTROM, R., BURCH, C. L. & WEEKS, K. M. 2009. Architecture and secondary structure of an entire HIV-1 RNA genome. *Nature,* 460**,** 711-716.

WEISS, R. 2006. The discovery of endogenous retroviruses. *Retrovirology,* 3**,** 1-11.

WELLS, R., COLLIER, D., HANVEY, J., SHIMIZU, M. & WOHLRAB, F. 1988. The chemistry and biology of unusual DNA structures adopted by oligopurine.oligopyrimidine sequences. *FASEB J.,* 2**,** 2939-2949.

WELLS, R. D. 2008. DNA triplexes and Friedreich ataxia. *FASEB J.,* 22**,** 1625-1634.

WILSON, A. J., BYUN, D.-S., ARANGO, D., MURRAY, L., AUGENLICHT, L. & MARIADASON, J. 2006. Histone deacetylase 4 is downregulated in intestinal epithelial cell maturation and represses p21. *AACR Meeting Abstracts,* 2006**,** 636-a-.

WINTER, R., HARDING, A., BARAITSER, M. & BRAVERY, M. 1981. Intrafamilial correlation in Friedreich's ataxia. *Clinical genetics,* 20**,** 419-427.

WONG, A., YANG, J., CAVADINI, P., GELLERA, C., LONNERDAL, B., TARONI, F. & CORTOPASSI, G. 1999. The Friedreich's ataxia mutation confers cellular sensitivity to oxidant stress which is rescued by chelators of iron and calcium and inhibitors of apoptosis. *Human Molecular Genetics,* 8**,** 425-430.

WU, Y. & MARSH, J. W. 2003. Early Transcription from Nonintegrated DNA in Human Immunodeficiency Virus Infection. *Journal of Virology,* 77**,** 10376-10382.

YAMAGUCHI, K., ITOH, K., OHNISHI, N., ITOH, Y., BAUM, C., TSUJI, T., NAGAO, T., HIGASHITSUJI, H., OKANOUE, T. & FUJITA, J. 2003. Engineered Long Terminal Repeats of Retroviral Vectors Enhance Transgene Expression in Hepatocytes in Vitro and in Vivo. *Mol Ther,* 8**,** 796-803.

YAN, L.-J., LEVINE, R. L. & SOHAL, R. S. 1997. Oxidative damage during aging targets mitochondrial aconitase. *Proceedings of the National Academy of Sciences,* 94**,** 11168-11172.

YANEZ-MUNOZ, R. J., BALAGGAN, K. S., MACNEIL, A., HOWE, S. J., SCHMIDT, M., SMITH, A. J., BUCH, P., MACLAREN, R. E., ANDERSON, P. N., BARKER, S. E., DURAN, Y., BARTHOLOMAE, C., VON KALLE, C., HECKENLIVELY, J. R., KINNON, C., ALI, R. R. & THRASHER, A. J. 2006. Effective gene therapy with nonintegrating lentiviral vectors. *Nat Med,* 12**,** 348-353.

YOON, T. & COWAN, J. 2003. Iron-sulfur cluster biosynthesis. Characterization of frataxin as an iron donor for assembly of [2Fe-2S] clusters in ISU-type proteins. *Journal of the American Chemical Society,* 125**,** 6078-6084.

YU, S. F., VON RÜDEN, T., KANTOFF, P. W., GARBER, C., SEIBERG, M., RÜTHER, U., ANDERSON, W. F., WAGNER, E. F. & GILBOA, E. 1986. Self-inactivating retroviral vectors designed for transfer of whole genes into mammalian cells. *Proceedings of the National Academy of Sciences,* 83**,** 3194-3198.

ZANTA-BOUSSIF, M., CHARRIER, S., BRICE-OUZET, A., MARTIN, S., OPOLON, P., THRASHER, A., HOPE, T. & GALY, A. 2009. Validation of a mutated PRE sequence allowing high and sustained transgene expression while abrogating WHV-X protein synthesis: application to the gene therapy of WAS. *Gene therapy,* 16**,** 605-619.

ZENNOU, V., PETIT, C., GUETARD, D., NERHBASS, U., MONTAGNIER, L. & CHARNEAU, P. 2000. HIV-1 genome nuclear import is mediated by a central DNA flap. *Cell,* 101**,** 173-185.

ZENNOU, V., SERGUERA, C., SARKIS, C., COLIN, P., PERRET, E., MALLET, J. & CHARNEAU, P. 2001. The HIV-1 DNA flap stimulates HIV vector-mediated cell transduction in the brain. *Nature biotechnology,* 19**,** 446-450.

ZUFFEREY, R., DONELLO, J. E., TRONO, D. & HOPE, T. J. 1999. Woodchuck hepatitis virus posttranscriptional regulatory element enhances expression of transgenes delivered by retroviral vectors. *Journal of virology,* 73**,** 2886-2892.

ZUFFEREY, R., DULL, T., MANDEL, R. J., BUKOVSKY, A., QUIROZ, D., NALDINI, L. & TRONO, D. 1998. Self-Inactivating Lentivirus Vector for Safe and Efficient In Vivo Gene Delivery. *Journal of Virology,* 72**,** 9873-9880.

ZUFFEREY, R., NAGY, D., MANDEL, R. J., NALDINI, L. & TRONO, D. 1997. Multiply attenuated lentiviral vector achieves efficient gene delivery in vivo. *Nat Biotech,* 15**,** 871-875.

APPENDIX

Appendix A: Journal Submitted for Publication

Lentivirus-meditated frataxin gene delivery reverses genome instability in Friedreich ataxia patient and mouse model fibroblasts

Hassan Khonsari1,2, Marion Schneider1,2, Sahar Al-Mahdawi1,2, Yaghoub Gozaly Chianea1,2, Matthew Themis1, Christopher Parris1, Mark A. Pook1,2, Michael Themis1,2,3

1 Division of Biosciences, Department of Life Sciences, College of Health & Life Sciences, and

2 Synthetic Biology Theme, Institute of Environment, Health & Societies, Brunel University London, Uxbridge, Middlesex, UB83PH

3 Division of Ecology and Evolution, Department of Life Sciences, Imperial College London, SW72AZ

E-mail: Michael.themis@brunel.ac.uk, m.themis@imperial.ac.uk

Keywords:

Friedreich Ataxia, FRDA, Gene therapy, Lentivirus, Frataxin, DNA damage, γ-H2AX

Abstract

Friedreich ataxia (FRDA) is a progressive neurodegenerative disease caused by deficiency of frataxin protein, with the primary sites of pathology being the large sensory neurons of the dorsal root ganglia (DRG) and the cerebellum. FRDA is also often accompanied by severe cardiomyopathy and diabetes mellitus. Frataxin is important in mitochondrial iron-sulphur cluster (ISC) biogenesis and low frataxin expression is due to a GAA repeat expansion in intron 1 of the FXN gene. FRDA cells are genomically unstable, with increased levels of reactive oxygen species (ROS) and sensitivity to oxidative stress. Here we report the identification of elevated levels of DNA double strand breaks (DSBs) in FRDA patient and YG8sR FRDA mouse model fibroblasts compared to normal fibroblasts. Using lentivirus FXN gene delivery to FRDA patient and YG8sR cells, we obtained long-term overexpression of FXN mRNA and frataxin protein levels with reduced DSB levels towards normal. Furthermore, gamma irradiation of FRDA patient and YG8sR cells revealed impaired DSB repair, which recovered upon FXN gene transfer. This suggests that frataxin may be involved in DSB repair, either directly by an unknown mechanism, or indirectly via ISC biogenesis for DNA repair enzymes, which may essential for the prevention of neurodegeneration.

Introduction

Friedreich ataxia (FRDA) is an autosomal recessive inherited neurodegenerative disorder for which there is no known effective treatment or cure. Neurodegeneration is accompanied by cardiac hypertrophy and heart failure, which is the main cause of mortality usually at around 40 years of age.1 It is the most common hereditary ataxia with a prevalence of 1 in 29,000 in the Caucasian population and a carrier frequency of 1 in 85.2 Neurological symptoms include gait ataxia, dysarthria, fixation instability, loss of joint and vibratory senses, loss of tendon reflexes, abnormal Babinski sign and muscle weakness. Patients lose the ability to stand and walk within 10 to 15 years of onset and soon become wheelchair bound.3

Neurodegenerative pathology occurs primarily in the large sensory neurons of the dorsal root ganglia (DRG) and cerebellum.4 In 96% of patients with FRDA, a homozygous GAA triplet repeat expansion is found in the first intron of the frataxin (FXN) gene. The triplet repeat size correlates directly with the severity of the disease phenotype and inversely with the age of onset.2 The expansion leads to epigenetic changes and heterochromatic-silencing of the FXN gene.5 Reduced expression of frataxin leads to impaired electron transport chain (ETC) function, which is accompanied by oxidative stress. Frataxin deficient cells are highly sensitive to oxidative stress and have reduced capability to handle oxidative insults.6 The exact function of frataxin is not fully understood. Frataxin processing involves a transient intermediate form (FXN 42-210) and a mature form (FXN 81-210) of the protein that have been both identified in the cytoplasm and mitochondria of cells. Only the mature form is understood to be

transported to the mitochondrion7, which is known to be essential for iron homeostasis, in particular for the de novo biosynthesis of iron sulphur cluster (ISC) proteins and heme biosynthesis.8 It is thereby involved in activation of the tricarboxylic cycle enzyme aconitase, which can be used as an indicator of low levels of frataxin protein and mitochondrial damage.6 Deficiency in frataxin results in impaired biosynthesis and the function of ISC proteins of the ETC, leading to reduced ATP and energy production.9 Cells highly dependent on aerobic respiration and high ATP levels, such as neurons in the brain and spinal cord, cardiomyocytes and pancreatic beta cells, especially succumb to this imbalance in energy homeostasis and this is believed to cause the neurological and cardiac symptoms and the high prevalence of diabetes in patients. However, what causes the variable cell death within tissues is still unclear.10

Oxidative stress is known to be associated with genome instability11, and in FRDA cells that have decreased frataxin expression, reduced capacity for DNA damage repair is evident.8, 12 Differential expression of genes associated with genotoxicity stress, including oxidative phosphorylation, has also been found in peripheral blood mononuclear cells of FRDA patients, where mitochondrial and nuclear DNA damage is increased.13 In the yeast model of FRDA, reduced levels of frataxin correlate with DNA damage and recombination, mutation events and genome instability. These cells are also highly sensitive to DNA-damaging agents.14 Low frataxin expression is associated with increased sensitivity to ionising radiation15, whereas high frataxin expression correlates with reduced levels of mitochondrial ROS. It is unclear whether low frataxin expression leading to high levels of ROS and DNA damage is the only cause of

neuronal degeneration. Recently, however, the role of frataxin in DNA repair has been suggested to involve MUTYH and PARP 1 gene expression with low FXN expression being associated with microglial DNA damage.16 Interestingly, overexpression of frataxin by nine fold has also been reported to be deleterious to life span, impair locomotor ability and cause brain damage in a Drosophila model of FRDA17, which would suggest any gene therapy approach to correct FRDA would require strict control of frataxin gene expression.18 Overexpression of human frataxin in transgenic mice by up to ten fold has been shown to have no deleterious effects.19 Furthermore, in a recent gene therapy study, correction of the FRDA heart pathology of the Mck conditional knockout mouse model with complete frataxin deletion in cardiac and skeletal muscle was achieved where frataxin was overexpressed 10 fold over that of endogenous frataxin, without deleterious side effects in the corrected mice.20

Because sensory neurones are difficult to obtain and may not survive long-term in culture, in this study, we have used FRDA patient fibroblasts (GM03665, 445 and 740 GAA repeats) and fibroblasts of the YG8sR mouse model that carries 120 GAA repeats in intron 1 of a human FXN transgene to investigate correction of FRDA by lentivirus vectors (LVs). FRDA fibroblasts have been shown useful to model this disease as they display FRDA characteristics and are readily available. They have increased mitochondrial sensitivity to oxidative stress and respond to treatments that reduce oxidative stress and improve cell viability.21-23 They have also been shown amenable to partial correction using FXN carrying adeno-associated virus and LV gene therapy vectors.24 LVs were chosen because these vectors can transduce most cell types, especially

neuronal cells to provide permanent gene expression. To examine for the potential of deleterious effects on cells caused by high frataxin gene expression we used the strong spleen focus forming virus (SFFV) promoter internally to self-inactivating (SIN) long terminal repeats to drive frataxin expression. Following robust FXN gene transfer, we measured the effects of high FXN gene expression on oxidative stress and genome instability using the γ-H2AX histone variant marker, which is recruited to DNA DSBs. We next challenged FRDA fibroblasts with gamma radiation-induced DNA damage and profiled the DNA damage repair potential in lentivirus FXN-treated versus untreated cells. We found that high-level FXN gene expression restores cell viability, reduces genome instability and improves the DNA damage repair potential of these cells close to the levels found in normal fibroblasts. These data suggest that LV gene therapy may offer a permanent correction to FRDA.

Results

LV infection of FRDA fibroblasts is efficient and permanent

Human and YG8sR mouse model FRDA fibroblasts were exposed to two rounds of pHR'SIN-cPPT-SFFV-eGFP-WPRE LV infection each at an MOI of 10 to achieve 92% and 97% positive eGFP expressing cells, respectively as determined by light microscopy and ImageStreamX flow cytometry (Supplementary figure 1). After 8 weeks, human (GMO3665) and mouse (YG8sR) fibroblasts were once again examined for positive eGFP expression that remained in 88% and 93% of cells, respectively, demonstrating stable LV integration. Next, pHR'SIN-cPPT-SFFV-FXN-WPRE and pHR'SIN-cPPT-SFFV-eGFP-WPRE vector copy numbers were established at 48 hours and then again at 8 weeks after infection. pHR'SIN-

cPPT-SFFV-eGFP-WPRE showed a higher copy number in the mouse fibroblasts at 2 copies/cell vs 1 copy/cell in the human fibroblasts, whereas the vector copy numbers of pHR'SIN-cPPT-SFFV-FXN-WPRE for both species appeared at 1 copy/cell and remained so after 8 weeks in culture (Supplementary figure 2).

FXN gene and frataxin protein expression persist over time

We next measured FXN gene expression in pHR'SIN-cPPT-SFFV-FXN-WPRE infected cells using qRT-PCR at 2, 8 and 12 weeks post infection compared with uninfected cells and control normal human and mouse fibroblasts to determine levels and longevity of gene expression. After normalising to endogenous GAPDH gene expression, FXN expression in the human and mouse FRDA cells reached 96 and 210 fold, respectively, after infection, compared with uninfected FRDA cells 0.5 and 0.2 fold, respectively, compared to normal fibroblasts. Over time, this expression appeared to fall by approximately 50%, but FXN expression remained significantly greater than in untreated FRDA fibroblasts over the 12 weeks period after gene delivery (Figure 2). We measured frataxin protein levels in the human and mouse fibroblasts using lateral flow immunoassay. Frataxin levels of pHR'SIN-cPPT-SFFV-FXN-WPRE infected cells increased to 42 and 17 fold, respectively, compared to untreated FRDA cells and 0.48 and 0.2 fold, respectively, to that of normal fibroblasts. Frataxin protein levels also decreased in both the human and mouse fibroblasts over time. However, protein levels remained significantly higher than untreated FRDA fibroblasts (Figure 3).

Localisation of frataxin isoforms to subcellular compartments

Frataxin protein processing involves the production of a transient intermediate form and the fully mature form, of which the latter is known to localise to

mitochondria. Fibroblast cells treated with pHR'SIN-cPPT-SFFV-FXN-WPRE and treated with pHR'SIN-cPPT-SFFV-eGFP-WPRE along with untreated YG8sR mouse model and human patients and control normal fibroblasts were fractionated to isolate mitochondria, nuclei and cytoplasmic fractions. Each fraction was subjected to Western analysis for the presence of these forms using a primary antibody and secondary-HRP conjugated antibody to identify both intermediate and mature human and mouse forms of frataxin. As expected, high frataxin protein levels were found in the mitochondria in the 14 kDa mature form. In the cytoplasm, the 19 kDa transient intermediate form was also identified. In addition, a weak band representing the mature form was identified in the normal control mouse fibroblast nuclei and a stronger band was found in the nuclei of the mouse FRDA fibroblasts treated with pHR'SIN-cPPT-SFFV-FXN-WPRE (Figure 4). Neither the intermediate or mature forms were observable in the nuclei of human patient and healthy fibroblasts.

FXN gene transfer increases aconitase activity

Because aconitase enzyme activity can be used as an indicator of low levels of frataxin protein, we examined the activity of this enzyme in both sets of treated fibroblasts (Figure 5). We found that the aconitase activity for the treated human and mouse fibroblasts reached 103% and 116% of the levels found in normal fibroblasts, respectively, compared with original levels of 68% and 49%, respectively, in untreated FRDA cells. This suggests that FXN gene transfer can restore normal activity of this vital tricarboxylic acid enzyme.

High FXN expression is not deleterious to FRDA fibroblast growth and cell survival

A high level of FXN gene expression has been previously reported to be cytotoxic18 which would make gene therapy of FRDA problematic. As we achieved high level FXN expression in both human and mouse fibroblasts without observable adverse effects, we chose to evaluate cell survival and population doubling times of untreated versus pHR'SIN-cPPT-SFFV-eGFP-WPRE vector-treated cells next to control fibroblasts. Following 45 days culture growth, population doublings for FXN-treated human and mouse FRDA cells appeared unaffected in both treated populations. Cell survival also improved, as identified by clonogenic cell survival assay ($p<0.001$) in contrast to pHR'SIN-cPPT-SFFV-eGFP-WPRE-treated and untreated FRDA cells (Supplementary figure 3). This demonstrated that no adverse effects were caused by LV-mediated high FXN gene expression.

Oxidative stress is reduced by FXN gene delivery

We next investigated levels of protein oxidation as a measure of oxidative stress in FRDA cells using the Oxyblot kit immuno-detection and quantification assay. We found levels of oxidative stress in human and mouse FRDA fibroblasts to be significantly greater than in normal fibroblasts (nearly 2 fold increased). Following pHR'SIN-cPPT-SFFV-FXN-WPRE gene transfer, the level of protein oxidation in both fibroblasts was substantially reduced to 5 fold below the level in normal cells (Figure 6), whereas treatment with the control pHR'SIN-cPPT-SFFV-eGFP-WPRE vector was not able to achieve this.

FXN gene transfer improves fibroblast recovery after H2O2-induced oxidative stress

Reduced frataxin expression is accompanied by oxidative stress and FRDA cells are also known to be highly sensitive to DNA-damaging agents such as H2O2.14 Therefore, we exposed FRDA and normal human and mouse fibroblasts, together with FRDA human and mouse cells treated with FXN and eGFP gene transfer, to increasing concentrations of H2O2 (50, 100, 150, 200 μM) for 6 hours then subjected the cells to clonogenic assays after 2 weeks of cell growth. Fibroblasts treated with FXN gene transfer showed a significant increase in survival similar to normal fibroblasts over their non-treated FRDA counterparts ($p<0.05$) (Supplementary figure 4).

Genome instability in FRDA cells is reversed following FXN gene delivery

FRDA cells have been shown to be associated with genome instability11 and have an impaired ability to repair damaged nuclear DNA.15 We sought to determine whether the human and mouse FRDA fibroblasts display genome instability by using imaging flow cytometry detection and immunocytochemical detection of γ-H2AX recruitment to DNA DSBs and comparing the numbers of DSB positive nuclear foci with the number found in non-FRDA control fibroblasts. Following staining for γ-H2AX foci and nuclear DRAQ5™ staining and plotting positive foci from images of 10,000 to 50,000 cells obtained by imaging flow cytometry, we found human and mouse FRDA fibroblasts to have approximately 2 fold more DSBs than normal control fibroblasts. Treatment of FRDA fibroblasts with FXN gene transfer reduced the levels of DSBs to that found in control cells (Figure 7A). These findings were also confirmed using

immunocytochemical detection of γ-H2AX recruitment to DNA DSBs (Figure 7B). Hence, inherent genome stability in FRDA could be reversed after FXN gene delivery.

FXN gene delivery restores DNA damage repair in FRDA fibroblasts

Reduced FXN expression is known to impair DNA damage repair.14 We profiled the DNA damage repair response to low level (2Gy) γ-irradiation of the human and mouse FRDA fibroblasts and controls by measuring the recruitment and clearance of the phosphorylated γ-H2AX histone marker of DSB repair over a 72hr period when repair is believed to be complete in DNA repair proficient cells. The profile of DSB repair of control human and mouse fibroblasts showed an increased γ-H2AX signal to peak at 0.5 hours, which then reduced to background levels from 24 hours onwards. The same pattern of repair emerged in human FRDA cells, but repair was slower, taking up to 72 hours to return back to the original high number of DSB found in FRDA cells (4 times that of normal fibroblasts). A similar pattern of DNA damage repair was also observed in the FRDA mouse cells. However, in both FRDA fibroblasts treated with FXN gene transfer, DNA damage repair potential was restored, albeit with levels of DSBs slightly higher than the numbers observed in normal fibroblasts (Figure 8).

Discussion

FRDA pathology is thought to result from defective frataxin expression, which is primarily caused by GAA repeat expansion within the first intron of the FXN gene leading to its epigenetic silencing. Being a monogenic disorder, FRDA is amenable to LV gene therapy, a strategy that offers permanent FXN gene delivery and integration into the host genome. We used LVs containing the SFFV

promoter not only to determine whether LVs could correct FRDA at the molecular level, but to also investigate the effect of high level FXN expression on cells, which has been previously reported to be cytotoxic in a Drosophila model of FRDA.18 In this Drosophila model, high FXN expression was shown to reduce life span, impair locomotor ability, cause brain damage and even reduced aconitase activity.

Because it is difficult to obtain patient neurons, FRDA fibroblasts have been shown to be useful to study FRDA and to test treatments that reduce oxidative stress, prevent or reverse FXN methylation and improve cell viability.21-23 In this study, we used FRDA patient and YG8sR mouse model fibroblasts for gene transfer of pHR'SIN-cPPT-SFFV-FXN-WPRE frataxin and the pHR'SIN-cPPT-SFFV-eGFP-WPRE eGFP reporter carrying LVs, which achieved a virus copy number of around 1 and virtually 100% infection of human and mouse FRDA fibroblasts. Long-term LV FXN gene transfer was demonstrated by the fact that vector copy numbers of both LVs remained constant post infection up to the 8-week time point investigated. FXN mRNA expression levels, measured by qRT-PCR were high in the first week following infection and then fell by approximately 50% by week 12 compared to untreated cells. This was possibly due to shut-down of the SFFV promoter driving FXN expression, which has been described previously for this promoter.25 None-the-less FXN gene expression still remained significantly higher than the levels found in both untreated FRDA and normal fibroblasts. Levels of frataxin protein also appeared to follow a similar pattern. Importantly, with this high frataxin expression in the treated human and mouse FRDA cells, population doubling times and cell survival

profiles were similar to those found in control fibroblasts, demonstrating that high frataxin expression can be achieved without adverse side effects and supporting the potential for FRDA gene therapy using LV-mediated FXN delivery. This is further supported by a recent study that showed correction of cardiac hypertrophy in the Mck conditional knockout mouse model by AAV mediated FXN gene therapy where frataxin was overexpressed 10 fold over the level of endogenous frataxin expression without deleterious side effects in the treated mice.20

Frataxin is important for mitochondrial iron homeostasis; in particular for the de novo biosynthesis of ISCs and its deficiency results in lack of function of ISC-dependent proteins, such as complexes I, II and III of the ETC and the tricarboxylic acid cycle enzyme aconitase.6 By FXN gene delivery, the activity of this enzyme was returned to near normal levels in both human and mouse cells (from 68% and 49% to 103% and 116%, respectively). Another important consequence of ETC impairment is increased levels of and sensitivity to oxidative stress by FRDA cells, which have been shown to be less capable of handling oxidative insults.6, 21 Indeed, oxidative stress was evident in the FRDA fibroblasts by measurement of oxidised proteins, which was 2 fold higher, compared to control fibroblasts. LV-mediated FXN gene transfer also reduced the level of oxidized proteins down to around 2 fold below the oxidative stress levels in normal fibroblasts and these cells were also able to tolerate oxidative stress induced by exogenous H2O2 with levels of survival matching that of controls. This indicates that LV FXN gene transfer may improve the antioxidative response and may be the reason for improved genome stability.

The hypothesis that oxidative stress as a result of low frataxin expression alone causes neuronal degeneration is still in debate. Palomo et al (2011) suggested neuronal degeneration to be linked to frataxin expression after induction of frataxin deficiency followed by cell death in neuron-like cells through apoptosis, which is accompanied by up-regulation of p53, PUMA and Bax and activation of caspase-3. They also showed cell death could be prevented by interference with p53, caspase inhibitors or FXN gene transfer.26 Mitochondrial DNA damage is more prone to oxidative stress, thought to be due to increased available iron in mitochondria and the generation of hydroxyl free radicals. Low levels of frataxin have also been shown in yeast to cause arrest in cell cycle at G2/M that indicates nuclear DNA damage.14 This increased susceptibility to oxidative stress appears coupled with reduced capacity for DNA damage repair.15, 27, 28 However, only a few of the enzymes or their associated partners involved in DNA damage repair have been found to require ISCs. Evidence for impairment for DNA damage repair in FRDA fibroblasts after ionising irradiation has previously been shown by its effects on clonal cell growth.29 Hence, although mitochondrial dysfunction and oxidative stress are central features of FRDA, impaired DNA damage repair may also play a role in cell death.

Low levels of frataxin have also been suggested to be associated with malignancies in a number of FRDA patients and even the cause of liver tumorigenesis in mice with hepatocyte-specific disruption of FXN.30 This observation has, however, been refuted by the analysis of large FRDA patient cohort data and by revisiting the liver tumour pathology in the conditional knock-out frataxin mouse model.31 Frataxin has been proposed to be a tumour

suppressor gene by Guccini and co-workers, who showed that frataxin modulates P53 expression in tumours in response to hypoxia.32 Schulz and co-workers have shown that frataxin suppresses tumour formation in a mouse xenograft model12 and Chamberlain and co-workers have shown that frataxin deficiency in FRDA patients results in increased sensitivity to ionising radiation and also frataxin gene delivery can suppress the growth of several tumour cell lines.15 Further supporting frataxin in the role of tumour suppressor is the fact that p53 has been shown to decrease the level of frataxin mRNA in human kidney HEK 293T cells and that the human frataxin gene proximal promoter contains a p53-responsive element (p53RE), which is involved in p53 mediated control of frataxin expression.33 Evidence provided by a yeast model of FRDA also suggests that increased levels of DNA damage occurs in FRDA and the absence of frataxin leads to nuclear damage, chromosomal instability and a greater sensitivity to DNA-damaging agents.34 In a study on FRDA peripheral blood mononuclear cells, increased mitochondrial and nuclear DNA damage also results in changes in gene expression indicative of genotoxicity stress.13 The accumulation of DNA lesions may ultimately lead to apoptosis and cell death via p53 mediated pathways.

During DNA damage repair, DSBs are recognised by the non-homologous end-joining pathway (NHEJ) that activates the PI3 kinase ataxia telangiectasia mutated (ATM), which in turn phosphorylates an H2AX histone variant to form γ-H2AX.35 Upon DNA damage induction, especially after DSBs, γ-H2AX molecules spread over tens of kilobases of DNA flanking the break site and once DSB repair starts, the lesions are removed and the number of γ-H2AX foci

decreases.36,37 This signalling network, therefore recruits the repair machinery to the DNA lesion to repair it.38 Hence, γ-H2AX can be used to measure DNA damage and is useful as a marker of genome instability and DNA damage repair in cells proficient in NHEJ repair machinery. We used immunocytochemical detection of γ-H2AX proteins by fluorochrome-linked antibodies to quantify and localize DSBs as a measure of genome instability and DNA damage repair in the FRDA fibroblasts. Classical γ-H2AX immunostaining allowed the detection of individual nuclei and number of foci per nucleus and thus the damage distribution within cells, whereas imaging flow cytometry enabled rapid measurement of thousands of cells to provide statistical significance of DNA damage and repair after DSB induction by γ-irradiation. Both image flow cytometry and immunocytochemistry enabled the identification of higher numbers of DSB in FRDA fibroblasts compared to normal fibroblasts, albeit at different levels, possibly due to differences in the sensitivities of the two methods. Once again FXN delivery reduced the number of γ-H2AX foci to the level found in control fibroblasts. Furthermore, after γ irradiation, cells were able to repair DSBs more proficiently after FXN gene transfer, although not down to the low background levels of DSBs in normal fibroblasts. This is possibly due to the fact that not all the FRDA fibroblasts were expressing LV-mediated FXN, as suggested by the fact that, even though infected cells still contained a vector copy number of 1, FXN expression reduced by 50% over the 12 week period when DSB foci were measured.

Interestingly, we found oxidative stress levels of FRDA cells were 2 fold less that of control fibroblasts after gene transfer, pointing to the possibility that

frataxin may be important for DNA damage repair or as mentioned this may be due to an improvement of the antioxidative response provided by FXN delivery. To determine whether this is the case, clones of LV infected cells would need to be isolated and further characterised for FXN expression and DSB repair simultaneously. Cells could also be grown in the presence of antioxidants followed by measurement of the DNA response to irradiation. It would also be interesting to measure changes in the expression of genes associated with antioxidants and especially Nrf2 as previously described in the YG8sR mouse model.39

We conclude that because HIV-1-based LVs are ideal for neuronal targeting40 and do not cause genotoxicity in mice41, along with our recent findings that LVs can efficiently reach the mouse cerebellum and DRG using a reporter gene (unpublished data), the data presented in this study supports future efforts to use pHR'SIN-cPPT-SFFV-FXN-WPRE LV to correct the FRDA-like phenotype in the YG8sR mouse model. It would also be useful to perform this work in a human sensory neuronal model reprogrammed from induced pluripotent stem cells that would enable further investigations of the role of oxidative stress and genome instability in neuronal degeneration.

Materials and Methods

Construction and propagation of a lentivirus vector carrying the frataxin gene

The plasmid, pTLX1 containing the 1505bp frataxin open reading frame (GenBank: U43747.1)42 was subjected to PCR to amplify the FXN gene using the forward primer 5' TCG GGATCC GCT CCGGAGCATGTGGACTC 3' designed with a BamHI site 5' to the start codon, and the reverse primer 5' AGT CTC GAG GTA

GCA TCA AGC ATC TTT TCC GG 3' that incorporated a XhoI site 3' to the gene stop codon. The PCR amplicons were TA cloned into the pCR®2.1-TOPO® (K4500-02, Invitrogen life technologies) vector and sequenced (Beckman Coulter Genomics). The FXN gene was then excised as a BamHI–XhoI fragment and ligated into the pHR'SIN-cPPT-SFFV-MCS-WPRE lentivirus vector to generate pHR'SIN-cPPT-SFFV-FXN-WPRE, which was sequenced. The pHR'SIN-cPPT-SFFV-FXN-WPRE LV drives FXN using a strong internal SFFV promoter. The vector has SIN LTR configuration to avoid upregulation of genes located near to the insertion site (Figure 1). To generate pHR'SIN-cPPT-SFFV-FXN-WPRE particles, HEK293T cells were transfected with 3 plasmids: pHR'SIN-cPPT-SFFV-FXN-WPRE, pMD.G2 carrying the coding sequence for the VSV-G envelope glycoprotein43 and the packaging plasmid pCMVΔR8.74 carrying the gag, pol and rev genes as previously described.44, 45 In parallel the vector pHR'SIN-cPPT-SFFV-eGFP-WPRE that expressed eGFP in infected cells was also produced in HEK292T cells. Both LV vectors are SIN configuration, and carry the woodchuck hepatitis virus posttranscriptional regulatory element (WPRE).46 Briefly, 1.5x107 HEK293T cells per T-150 flask were transfected with 40 µg of the LV constructs, 17.5 µg of pMD.G2 and 32.5 µg of the pCMVΔR8.74 packaging plasmid. Complexes were produced with 0.25 mM polyethyleneimine (Sigma-Aldrich) in Opti-MEM® (Invitrogen) and incubated at room temperature for 20-30 minutes before transfection for 6 hours at 37°C in a 5% CO2 incubator, followed by replacing the medium with DMEM supplemented with 10% FBS. LVs were collected 48 hours and 72 hours post transfection. Virus supernatants were initially cleared of cell debris by low-speed centrifugation (1500 rpm, 5

minutes), filtered through a 0.45-um filter (Millipore) and concentrated 100-fold by ultracentrifugation at 90,000g for 90 minutes at 4°C (Beckman Coulter). Virus pellets were re-suspended in serum-free medium, aliquoted and stored at -80°C. LV was titrated using Lenti-X qRT-PCR (Clontech) and Quant-X™ One-Step qRT-PCR SYBR® (Clontech) kits against the internal serially diluted viral RNA stock supplied with the kit, as per manufacturer's instructions. The titre of vector particles obtained was corrected after calculating LV infectivity coefficients using eGFP positive infection of HEK293T cells. Serially diluted pHR'SIN-cPPT-SFFV-GFP-WPRE LV was used to infect HEK293T cells and infectious titre was determined using ImagestreamX flow cytometry for eGFP. LV RT titre:ImagestreamX titre ratios were calculated by dividing the qRT-PCR vector genome copies/ml by the infectious particles/ml values. This coefficient was used for pHR'SIN-cPPT-SFFV-FXN-WPRE titration which was generated in parallel to pHR'SIN-cPPT-SFFV-eGFP-WPRE. Virus titres of 1 X108 infectious particles/mL for both LV FXN and LV GFP were obtained in this way.

Cell culture

Human primary fibroblasts from FRDA patients and controls (GM03665 and GM07492, respectively) were obtained from Coriell Cell Repository, and primary fibroblasts from YG8sR FRDA mice and Y47R control mice and were isolated as previously described.5, 47 YG8sR cells carry a 120 GAA repeat in intron 1 of the human FXN transgene resulting in reduced FXN levels to 25% of normal. All experiments were performed on cells before passage 8. Cells were cultured with Dulbecco's modified essential medium (DMEM) supplemented with GlutaMAX™ (Invitrogen life technologies, UK) plus 10% fetal bovine serum (FBS) (Invitrogen)

and penicillin (100U/ml-1) and Streptomycin (100U/ml-1) (Invitrogen) in a humidified chamber at 37°C and 5% CO2.

LV infectivity and copy number analysis in FRDA human and mouse model fibroblasts

Infectivity of FRDA human and YG8sR mouse fibroblasts was established following two rounds of infection by pHR'SIN-cPPT-SFFV-eGFP-WPRE LVs at an MOI of 10. Positive eGFP expressing cells were identified by light microscopy under UV light and by imaging flow cytometry (see below). Measurements of eGFP expression were taken at 48 hours and 8 weeks post infection. High level of eGFP positive cells was obtained from both human and YG8sR mouse FRDA fibroblasts reaching close to 100%. Cells were next exposed to pHR'SIN-cPPT-SFFV-FXN-WPRE at the same MOI. Genomic DNA was extracted from cells infected with pHR'SIN-cPPT-SFFV-eGFP-WPRE and pHR'SIN-cPPT-SFFV-FXN-WPRE and purified using the phenol chloroform method.48 Quantitative PCR was performed by an ABI 7700 Sequence Detection System (ABI, Applied Biosystems) using 5'- TGTGTGCCCGTCTGTTGTGT-3' and 5'-GAGTCCTGCGTCGAGAGAGC-3' oligonucleotide primers and TaqMan probe (FAM) 5-CGCCCGAACAGGGACTTGAA-3' (TAMRA) specific for the viral woodchuck hepatitis regulatory element (WPRE) sequence contained in each LV46. The pHR'SIN-cPPT-SFFV-FXN-WPRE plasmid was used to generate a standard curve of known copy number by serial (1:10) dilution in siliconised tubes over the appropriate concentration range to achieve a reliable standard curve for each measured copy number. Five replicates per spiked sample was PCR-amplified over the complete standard-curve range. In addition, LV copy

numbers in infected cells were also measured using q-PCR on genomic DNA from the sample and comparing Ct values of this sample against the known copy number sample of a clonal sample used to make a diluted standard curve.49

Measurement of population doubling

Cell population doubling (PD) calculations were performed to determine their growth rates as described previously.50 Briefly, 5x105 cells were seeded per 10cm cell culture dish and counted at each passage. The following equation:

PD= log(final cell number) - log(initial cell number) was used to determine PD.

Log2 Log2

Clonogenic cell survival assay

Cultured cells were split, counted by haemocytometer and 100-1000 cells were plated per 10cm dish and incubated for 2 weeks at 37°C 5% CO2. Cells were stained with 1% methylene blue and the number of colonies counted. This procedure also followed LV and H2O2 treatments. For oxidative stress assay, cells were treated with H2O2 (150 µM) for 6 hours after plating. Surviving cells are expressed as a percentage of the survival of untreated cells.

Quantitative real-time PCR of frataxin expression

Total RNA was extracted from homogenized cells in Trizol reagent (Invitrogen) and quantified using a NanoDrop 1000 spectrophotometerTM (Thermo Fisher Scientific) at 260nm and mRNA was reverse-transcribed to cDNA using SuperScript III (Invitrogen). Frataxin gene expression of LV-infected and uninfected control cells was quantified by SYBR® Green (Applied Biosystems)

qRT-PCR in an ABI7900 machine using FRT-I 5'-TTGAAGACCTTGCAGACAAG-3' and RRT-II 5'-AGCCAGATTTGCTTGTTTGG-3' primers recognising both human and mouse FXN. The GAPDH or GAPDH housekeeping genes were used for normalization with human-specific primers GAPDH-hF: 5'-GAAGGTGAAGGTCGGAGT-3' and GAPDH-hR: 5'-GAAGATGGTGATGGGATTTC-3' or mouse-specific primers GAPDHmF: 5'-ACCCAGAAGACTGTGGATGG-3' and GAPDHmR: 5'-GGATGCAGGGATGATGTTCT-3'.

Frataxin protein extraction and quantification

Frataxin protein was extracted as previously described42 and the concentration was determined using the BCA Protein Assay Reagent Kit (Pierce). The lateral flow immunoassay (Abcam/MitoSciences) was performed as per manufacturer's instructions.51 Briefly, 25 µg of extracted cell protein and buffers were added to wells of a 96-well plate pre-prepared with gold-conjugated anti-frataxin monoclonal antibody (mAB). After mixing samples, a 'dipstick' assay was used to immunocapture frataxin onto designated capture zones on the dipstick. Zones representing on frataxin levels were used to quantify protein with a Hamamatsu immunochromato reader (MS1000 Dipstick reader). Absorbance values were normalized with control goat α-mouse IgG band (internal positive control) to correct for protein concentration. Data is expressed as percentage averages of the controls run on the same assay.52

Localisation of intermediate and mature forms of frataxin to subcellular compartments

Separation of cytosolic, mitochondrial and nuclear fractions was performed using a cell fractionation kit (Abcam) following the manufacturer's recommendations. Briefly, human and mouse fibroblast cells were grown in T75 tissue culture flasks to confluency. After cell trypsinisation and centrifugation, each subcellular fraction was used for the identification of the intermediate and mature forms of frataxin by measuring these in the protein isolates. Buffer A was used to wash cells, followed by resuspension to a concentration of 6.6 × 106 cells per ml. Cellular extractions were obtained after two sequential detergent-extraction steps. The purity of each fraction was assessed by Western blotting against GAPDH (cytoplasmic), SOD2 (mitochondrial) and Emerin (nuclear) proteins. The following antibodies were used for western blotting: an anti-frataxin monoclonal antibody (1:100, MAB1594, Millipore), mouse monoclonal anti-GAPDH antibody (1:2000, ab9484, Abcam), mouse monoclonal anti-SOD2 antibody (1:1000, ab16956 Abcam), mouse monoclonal anti-Emerin antibody (1:1000, NCL-Emerin, Leica Biosystems) and a rabbit anti-mouse IgG HRP conjugated secondary antibody (1:2000, ab97046, Abcam). Detection was performed using the chemiluminescent reagent (Bio-Rad) and bands were visualized using the Molecular Imager® Gel Doc XR+ system (Bio-Rad), and densitometry was carried out using Image Lab™ 4.1 analysis software (Bio-Rad).

Aconitase assay

Whole-cell extracts were obtained by homogenization of cultured cells in 50 mM Tris-HCl, pH 8.0, 10% (v/v) glycerol, 5 mM EDTA, 150 mM KCl, 1 mM phenylmethylsulfonyl Fluoride. Insoluble material was removed by

centrifugation at 10 000 g at 4°C for 10 min.42 Aconitase activity was measured using an Aconitase Assay Kit (Cayman Chemical). 50 µl whole-cell lysates were added to 200 µl of substrate mix, (50 mM Tris/HCl pH 7.4, 0.4 mM NADP, 5 mM Na citrate, 0.6 mM MgCl2, 0.1% (v/v) Triton X-100 and 1U isocitrate dehydrogenase) then the reaction was initiated by adding 50 µl of diluted substrate solution followed by incubation at 37 °C for 15 min. Absorbance was monitored by spectrophotometry every minute for 15 min at 340 nm 37 °C to determine the reaction slope. Aconitase activities of cells were then normalized to citrate synthase activities, which were determined using a citrate synthase assay kit (SIGMA, CS0720), as previously described.53

Measurement of oxidative stress in FRDA and control fibroblasts

Protein lysates were prepared as previously described54 and concentration was determined using the BCA assay kit (Pierce). Proteins were then modified by the use of the OxyBlot Protein Oxidation Detection Kit (Chemicon International), which measures carbonyl groups introduced into proteins by oxygen-derived free radicals. Oxidation levels were measured according to the manufacturer's protocol. Briefly, protein samples were diluted with lysate buffer so that 30µg of protein was present in a final 15µl volume. The protein sample was denatured by adding 15µl of 12% SDS and then split into two 10µl aliquots, each containing 10µg of protein. One aliquot was derivatised with 10µl of DNPH while the other was used as a negative control sample and 10µl of derivatisation-control solution was added instead. The derivatisation reaction was performed at room temperature for 15min, and stopped by adding 7.5µl of neutralization solution to both aliquots. The derivatised proteins were separated using 12% SDS-PAGE

and transferred to nitrocellulose. The primary antibody against 2,4-dinitrophenol (rabbit anti-DNP, 1:150 dilution) was added to the membrane and incubated for 1 hour at room temperature. The primary antibody was removed and the membrane was incubated in secondary antibody (goat anti-rabbit IgG, 1:300 dilution) for 1 hour at room temperature. Detection was performed using the chemiluminescent reagent (Bio-Rad) and bands were visualised using the Molecular Imager® Gel Doc XR+ system (Bio-Rad), and densitometry was carried out on the entire column using Image Lab™ 4.1 analysis software (Bio-Rad).

Measurement of eGFP gene expression in FRDA fibroblasts

To determine eGFP expression, live cells were analysed after pHR'SIN-cPPT-SFFV-eGFP-WPRE LV gene transfer by microscopy using a JuLI™ Smart Fluorescent Cell Analyser microscope (Ruskinn Technology). Magnification (10x) was used for viewing eGFP expression under UV light (488nm excitation and an emission at 520nm). Using Image J software, acquired images were merged and the numbers of eGFP positive cells were analysed. Cells expressing eGFP were also analysed using imaging flow cytometry. Cells were trypsinised, washed with ice cold PBS and fixed with 4% paraformaldehyde. Fixed cells were then applied to imaging flow cytometry using the ImagestreamX system (Amnis Inc.). This permits image capture of each cell in flow using a maximum of six optical channels. Using the Inspire™ data acquisition software (Amnis Inc.), images of approximately 10,000 cells were captured on channel 1 for brightfield (BF) to observe cell morphology, on channel 2 for eGFP emission and on channel 5 for blue DRAQ5™ (D5) nuclear staining. Following excitation with a

488 nm laser at a power setting of 70 mW, all images were captured using a 40× objective.

Analysis of cell images and DNA double strand break foci

Nuclear foci positive for γ-H2AX staining were quantified using approximately 10,000-50,000 images of cells captured in the Inspire™ imaging flow cytometry software. Foci were quantified as previously described.55 In brief, a series of simple building blocks were used to first identify and gate single cells, then a region was drawn to identify those single cells that are in the correct focal plane during imaging flow. Next, two 'truth' populations were identified containing images of cells that had either few foci (<5) or a large number of foci (>8-10). These populations were then used by the Ideas™ software to enumerate all of the foci in the 10,000-50,000 cells for each cell batch under analysis.56

Immunocytochemical detection of DNA damage and repair

a. Immunocytochemical detection of γ-H2AX: 1x103 cells were grown on glass slides then washed with ice-cold PBS, followed by fixation in 4% paraformaldehyde for 15 minutes. 0.2% Triton™ X-100 was used to permeabilise cells for 10 minutes at 4°C followed by the addition of blocking buffer (0.1g BSA in 50µl Triton™ X-100 and 50ml PBS) to block for 1 hour. After humidifying the parafilm covered slides in a dark box and removal of the blocking buffer, cells were incubated with primary antibody solution consisted of an anti-phospho-histone H2AX (serine 139), mouse monoclonal IgG1 antibody (clone JBW301, Millipore) (1:1,000) in blocking buffer. Excess primary antibody was removed by washing 3 times for 5 minutes in TBST solution (8.8.grams of NaCl + 0.2 grams of KCL + 3 grams of tris base + 500µl tween 20 in 1 litre of dH2O. pH 7.4), followed

by incubation for 1hr at RT in a secondary antibody solution consisting of an Alexa Fluor®488 rabbit anti-mouse IgG antibody (Invitrogen) (1:1000) in blocking buffer. Slides were each washed 3 times for 5 minutes in TBST and then 3 times for 5 minutes in PBS before being de-hydrated in ethanol (70%, 90% and 100%) for 3 minutes each time. After air drying 15µl of mounting medium containing DAPI (Invitrogen) was added to each slide and covered with a cover slip (Fisher scientific) and sealed using clear nail varnish.57, 58 Images acquisition was performed at RT using a Zeiss Axioplan 2 microscope equipped with a ×100 ZEISS Plan-NEOFLUAR 1.3 Oil objective lens and a Zeiss Axiocam colour camera under the control of AXIOVISION 4.2 software. Images used for comparison between different treatments and/or cell lines were acquired with the same instrument settings and exposure times.59b. Multispectral imaging flow cytometry detection of γ-H2AX: Imaging flow cytometry was performed using the ImagestreamX system (Amnis Inc.). Using the Inspire™ data acquisition software, images of 10,000 to 50,000 cells were captured on channel 1 for brightfield (BF), on channel 2 for Alexa Fluor®488 (AF), representing the green staining of γ-H2AX foci, and on channel 5 for DRAQ5™ nuclear staining. Following excitation with a 488 nm laser at a power setting of 75 mW, all images were captured using a 40x objective. Cell classifiers were applied to the BF channel to capture objects that ranged between 50 and 300 units on an arbitrary scale, which was established from previous studies.56 Image compensation was accomplished on untreated cells and those irradiated with 2 Gy γ-irradiation. Cells that were stained with antibody only or DRAQ5™ only were used for producing the compensation matrix. Images were collected without BF

to capture fluorescence intensity with the 488 nm laser as the single source of illumination. The Ideas™ software compensation wizard generates a table of coefficients whereby detected light that is displayed by each image is placed into the proper channel (channel 2 for antibody staining and channel 5 for DRAQ5™) on a pixel-by-pixel basis. All coefficients were normalized to 1 and each coefficient represents the leakage of fluorescent signal into adjacent channels. Calculated compensation values were applied to all subsequent analyses as appropriate.56

Irradiation of cells to generate double strand breaks

To induce DNA double strand breaks (DSB) and subsequent γ-H2AX foci induction, cells were grown overnight as proliferating monolayers on poly-prep glass slides coated with poly-L-lysine (Sigma) in eight-well glass chamber slides (Labtek). Slides from each sample were created as un-irradiated controls and the remaining slides were irradiated with 2Gy γ-radiation from a Cobalt-60 source (Puridec Technologies) sited at a distance of 25 cm with a dose rate of 0.9 Gy per minute. The cells were returned to the incubator and incubated as detailed previously. γ-H2AX foci were counted in untreated cells and those irradiated with 2Gy gamma radiation at 30 minutes, 5, 24, 48 and 72 hours post-irradiation.

Statistical analysis

All other data were analysed by the Student's t test, with a significance value set at $p < 0.05$.

Acknowledgements

We would like to acknowledge funding by Ataxia UK, FARA Australasia and FARA US for this work.

Conflict of Interest

The authors declare no conflict of interest

References

1. Pandolfo M. Friedreich ataxia: The clinical picture. J Neurol 2009; 256(1): 3-8.

2. Delatycki MB, Corben LA. Clinical features of Friedreich ataxia. Journal of child neurology 2012; 27(9): 1133-1137.

3. Pandolfo M. Friedreich Ataxia New Pathways. Journal of child neurology 2012; 27(9): 1204-1211.

4. Koeppen AH. Friedreich's ataxia: Pathology, pathogenesis, and molecular genetics. Journal of the Neurological Sciences 2011; 303(1–2): 1-12.

5. Sandi C, Al-Mahdawi S, Pook MA. Epigenetics in Friedreich's Ataxia: Challenges and Opportunities for Therapy. Genet Res Int 2013; 2013: 852080.

6. Payne RM, Wagner GR. Cardiomyopathy in Friedreich ataxia: clinical findings and research. J Child Neurol 2012; 27(9): 1179-86.

7. Gakh O, Bedekovics T, Duncan SF, Smith DY, Berkholz DS, Isaya G. Normal and Friedreich Ataxia Cells Express Different Isoforms of Frataxin with Complementary Roles in Iron-Sulfur Cluster Assembly. Journal of Biological Chemistry 2010; 285(49): 38486-38501.

8. Schmucker S, Martelli A, Colin F, Page A, Wattenhofer-Donze M, Reutenauer L et al. Mammalian frataxin: an essential function for cellular viability through an interaction with a preformed ISCU/NFS1/ISD11 iron-sulfur assembly complex. PLoS One 2011; 6(1): e16199.

9. Lodi R, Cooper JM, Bradley JL, Manners D, Styles P, Taylor DJ et al. Deficit of in vivo mitochondrial ATP production in patients with Friedreich ataxia. Proceedings of the National Academy of Sciences 1999; 96(20): 11492-11495.

10. Richardson TE, Kelly HN, Amanda EY, Simpkins JW. Therapeutic strategies in Friedreich's ataxia. Brain research 2013; 1514: 91-97.

11. Negrini S, Gorgoulis VG, Halazonetis TD. Genomic instability—an evolving hallmark of cancer. Nature reviews Molecular cell biology 2010; 11(3): 220-228.

12. Schulz TJ, Thierbach R, Voigt A, Drewes G, Mietzner B, Steinberg P et al. Induction of oxidative metabolism by mitochondrial frataxin inhibits cancer growth: Otto Warburg revisited. J Biol Chem 2006; 281(2): 977-81.

13. Haugen AC, Di Prospero NA, Parker JS, Fannin RD, Chou J, Meyer JN et al. Altered gene expression and DNA damage in peripheral blood cells from Friedreich's ataxia patients: cellular model of pathology. PLoS genetics 2010; 6(1): e1000812.

14. Karthikeyan G, Lewis LK, Resnick MA. The mitochondrial protein frataxin prevents nuclear damage. Human molecular genetics 2002; 11(11): 1351-1362.

15. Chamberlain S, Lewis PD. Studies of cellular hypersensitivity to ionising radiation in Friedreich's ataxia. J Neurol Neurosurg Psychiatry 1982; 45(12): 1136-8.

16. Shen Y, McMackin MZ, Shan Y, Raetz A, David S, Cortopassi G. Frataxin Deficiency Promotes Excess Microglial DNA Damage and Inflammation that Is Rescued by PJ34. PloS one 2016; 11(3): e0151026.

17. Llorens JV, Navarro JA, Martínez-Sebastián MJ, Baylies MK, Schneuwly S, Botella JA et al. Causative role of oxidative stress in a Drosophila model of Friedreich ataxia. The FASEB Journal 2007; 21(2): 333-344.

18. Navarro JA, Llorens JV, Soriano S, Botella JA, Schneuwly S, Martínez-Sebastián MJ et al. Overexpression of human and fly frataxins in Drosophila provokes deleterious effects at biochemical, physiological and developmental levels. PloS one 2011; 6(7): e21017.

19. Miranda CJ, Santos MM, Ohshima K, Tessaro M, Sequeiros J, Pandolfo M. Frataxin overexpressing mice. FEBS letters 2004; 572(1): 281-288.

20. Perdomini M, Belbellaa B, Monassier L, Reutenauer L, Messaddeq N, Cartier N et al. Prevention and reversal of severe mitochondrial cardiomyopathy by gene therapy in a mouse model of Friedreich's ataxia. Nat Med 2014; advance online publication.

21. Wong A, Yang J, Cavadini P, Gellera C, Lonnerdal B, Taroni F et al. The Friedreich's ataxia mutation confers cellular sensitivity to oxidant stress which is rescued by chelators of iron and calcium and inhibitors of apoptosis. Hum Mol Genet 1999; 8(3): 425-30.

22. Jauslin ML, Wirth T, Meier T, Schoumacher F. A cellular model for Friedreich Ataxia reveals small-molecule glutathione peroxidase mimetics as novel treatment strategy. Hum Mol Genet 2002; 11(24): 3055-63.

23. Richardson TE, Yu AE, Wen Y, Yang SH, Simpkins JW. Estrogen prevents oxidative damage to the mitochondria in Friedreich's ataxia skin fibroblasts. PLoS One 2012; 7(4): e34600.

24. Fleming J, Spinoulas A, Zheng M, Cunningham SC, Ginn SL, McQuilty RC et al. Partial correction of sensitivity to oxidant stress in Friedreich ataxia patient fibroblasts by frataxin-encoding adeno-associated virus and lentivirus vectors. Human gene therapy 2005; 16(8): 947-956.

25. Herbst F, Ball CR, Tuorto F, Nowrouzi A, Wang W, Zavidij O et al. Extensive methylation of promoter sequences silences lentiviral transgene expression during stem cell differentiation in vivo. Mol Ther 2012; 20(5): 1014-21.

26. Palomo GM, Cerrato T, Gargini R, Diaz-Nido J. Silencing of frataxin gene expression triggers p53-dependent apoptosis in human neuron-like cells. Hum Mol Genet 2011; 20(14): 2807-22.

27. Lewis PD, Corr JB, Arlett CF, Harcourt SA. Increased sensitivity to gamma irradiation of skin fibroblasts in Friedreich's ataxia. Lancet (London, England) 1979; 2(8140): 474-5.

28. Evans HJ, Vijayalaxmi, Pentland B, Newton MS. Mutagen hypersensitivity in Friedreich's ataxia. Ann Hum Genet 1983; 47(Pt 3): 193-204.

29. Chamberlain S, Cramp WA, Lewis PD. Defects in newly synthesised DNA in skin fibroblasts from patients with Friedreich's ataxia. Lancet (London, England) 1981; 1(8230): 1165.

30. Thierbach R, Drewes G, Fusser M, Voigt A, Kuhlow D, Blume U et al. The Friedreich's ataxia protein frataxin modulates DNA base excision repair in prokaryotes and mammals. Biochem J 2010; 432(1): 165-72.

31. Martelli A, Friedman LS, Reutenauer L, Messaddeq N, Perlman SL, Lynch DR et al. Clinical data and characterization of the liver conditional mouse model exclude neoplasia as a non-neurological manifestation associated with Friedreich's ataxia. Dis Model Mech 2012; 5(6): 860-9.

32. Guccini I, Serio D, Condo I, Rufini A, Tomassini B, Mangiola A et al. Frataxin participates to the hypoxia-induced response in tumors. Cell Death Dis 2011; 2: e123.

33. Shimizu R, Lan NN, Tai TT, Adachi Y, Kawazoe A, Mu A et al. p53 directly regulates the transcription of the human frataxin gene and its lack of regulation in tumor cells decreases the utilization of mitochondrial iron. Gene 2014; 551(1): 79-85.

34. Karthikeyan G, Lewis LK, Resnick MA. The mitochondrial protein frataxin prevents nuclear damage. Hum Mol Genet 2002; 11(11): 1351-62.

35. Rogakou EP, Pilch DR, Orr AH, Ivanova VS, Bonner WM. DNA double-stranded breaks induce histone H2AX phosphorylation on serine 139. J. Biol. Chem. 1998; 273(10): 5858-5868.

36. Celeste A, Fernandez-Capetillo O, Kruhlak MJ, Pilch DR, Staudt DW, Lee A et al. Histone H2AX phosphorylation is dispensable for the initial recognition of DNA breaks. Nature cell biology 2003; 5(7): 675-9.

37. Valdiglesias V, Giunta S, Fenech M, Neri M, Bonassi S. γH2AX as a marker of DNA double strand breaks and genomic instability in human population studies. Mutation Research/Reviews in Mutation Research 2013; 753(1): 24-40.

38. Ciccia A, Elledge SJ. The DNA damage response: making it safe to play with knives. Molecular cell 2010; 40(2): 179-204.

39. Shan Y, Schoenfeld RA, Hayashi G, Napoli E, Akiyama T, Iodi Carstens M et al. Frataxin deficiency leads to defects in expression of antioxidants and Nrf2 expression in dorsal root ganglia of the Friedreich's ataxia YG8R mouse model. Antioxidants & redox signaling 2013; 19(13): 1481-1493.

40. Blomer U, Naldini L, Kafri T, Trono D, Verma IM, Gage FH. Highly efficient and sustained gene transfer in adult neurons with a lentivirus vector. J Virol 1997; 71(9): 6641-9.

41. Nowrouzi A, Cheung WT, Li T, Zhang X, Arens A, Paruzynski A et al. The Fetal Mouse Is a Sensitive Genotoxicity Model That Exposes Lentiviral-associated Mutagenesis Resulting in Liver Oncogenesis. Mol Ther 2013; 21(2): 324-37.

42. Campuzano V, Montermini L, Lutz Y, Cova L, Hindelang C, Jiralerspong S et al. Frataxin is Reduced in Friedreich Ataxia Patients and is Associated with Mitochondrial Membranes. Human Molecular Genetics 1997; 6(11): 1771-1780.

43. Demaison C, Parsley K, Brouns G, Scherr M, Battmer K, Kinnon C et al. High-level transduction and gene expression in hematopoietic repopulating cells using a human immunodeficiency [correction of imunodeficiency] virus type 1-based lentiviral vector containing an internal spleen focus forming virus promoter. Hum Gene Ther 2002; 13(7): 803-13.

44. Zufferey R, Nagy D, Mandel RJ, Naldini L, Trono D. Multiply attenuated lentiviral vector achieves efficient gene delivery in vivo. Nat Biotech 1997; 15(9): 871-875.

45. Dull T, Zufferey R, Kelly M, Mandel RJ, Nguyen M, Trono D et al. A Third-Generation Lentivirus Vector with a Conditional Packaging System. Journal of Virology 1998; 72(11): 8463-8471.

46. Ward NJ, Buckley SMK, Waddington SN, VandenDriessche T, Chuah MKL, Nathwani AC et al. Codon optimization of human factor VIII cDNAs leads to high-level expression, vol. 117. 2011.

47. Anjomani Virmouni S, Ezzatizadeh V, Sandi C, Sandi M, Al-Mahdawi S, Chutake Y et al. A novel GAA-repeat-expansion-based mouse model of Friedreich's ataxia. 2015.

48. Charrier S, Stockholm D, Seye K, Opolon P, Taveau M, Gross DA et al. A lentiviral vector encoding the human Wiskott-Aldrich syndrome protein corrects immune and cytoskeletal defects in WASP knockout mice. Gene Ther 2004; 12(7): 597-606.

49. Themis M, Waddington SN, Schmidt M, von Kalle C, Wang Y, Al-Allaf F et al. Oncogenesis following delivery of a nonprimate lentiviral gene therapy vector to fetal and neonatal mice. Mol Ther 2005; 12(4): 763-71.

50. Greenwood SK, Hill RB, Sun JT, Armstrong MJ, Johnson TE, Gara JP et al. Population doubling: A simple and more accurate estimation of cell growth suppression in the in vitro assay for chromosomal aberrations that reduces irrelevant positive results. Enviro Mol Mutagen 2004; 43(1): 36-44.

51. Selak MA, Lyver E, Micklow E, Deutsch EC, Önder Ö, Selamoglu N et al. Blood cells from Friedreich ataxia patients harbor frataxin deficiency without a loss of mitochondrial function. Mitochondrion 2011; 11(2): 342-350.

52. Deutsch EC, Santani AB, Perlman SL, Farmer JM, Stolle CA, Marusich MF et al. A rapid, noninvasive immunoassay for frataxin: Utility in assessment of Friedreich ataxia. Molecular genetics and metabolism 2010; 101(2-3): 238-245.

53. Sandi C, Pinto RM, Al-Mahdawi S, Ezzatizadeh V, Barnes G, Jones S et al. Prolonged treatment with pimelic o-aminobenzamide HDAC inhibitors ameliorates the disease phenotype of a Friedreich ataxia mouse model. Neurobiology of Disease 2011; 42(3): 496-505.

54. Campuzano V, Montermini L, Moltò MD, Pianese L, Cossée M, Cavalcanti F et al. Friedreich's Ataxia: Autosomal Recessive Disease Caused by an Intronic GAA Triplet Repeat Expansion. Science 1996; 271(5254): 1423-1427.

55. Bourton EC, Plowman PN, Zahir SA, Senguloglu GU, Serrai H, Bottley G et al. Multispectral imaging flow cytometry reveals distinct frequencies of γ-H2AX foci induction in DNA double strand break repair defective human cell lines. Cytometry Part A 2012; 81A(2): 130-137.

56. Bourton EC, Plowman PN, Harvey AJ, Zahir SA, Parris CN. The PARP-1 inhibitor Olaparib causes retention of γ-H2AX foci in BRCA1 heterozygote cells following exposure to gamma radiation. Journal of Cancer Therapy 2013; 4(11): 44.

57. Riballo E, Kuhne M, Rief N, Doherty A, Smith GC, Recio MJ et al. A pathway of double-strand break rejoining dependent upon ATM, Artemis, and proteins locating to gamma-H2AX foci. Molecular cell 2004; 16(5): 715-24.

58. Pitiyage GN, Slijepcevic P, Gabrani A, Chianea YG, Lim KP, Prime SS et al. Senescent mesenchymal cells accumulate in human fibrosis by a telomere-independent mechanism and ameliorate fibrosis through matrix metalloproteinases. The Journal of Pathology 2011; 223(5): 604-617.

59. Marti TM, Hefner E, Feeney L, Natale V, Cleaver JE. H2AX phosphorylation within the G1 phase after UV irradiation depends on nucleotide excision repair and not DNA double-strand breaks. Proceedings of the National Academy of Sciences 2006; 103(26): 9891-9896.

Appendix B: Posters Presented

An investigation to determine the efficacy and safety of lentivirus mediated *FXN* gene delivery for the correction of Friedreich ataxia

Hassan Khonsari , Chiranjeevi Sandi, Sahar Al-Mahdawi, Steven Howe, Simon Waddington, Mark Pook and Michael Themis.
Gene Therapy Group, Division of Biosciences, Brunel University, Kingstone Lane, Uxbridge , London UK, UB8 3PH

Friedreich Ataxia

Friedreich ataxia (FRDA) is a lethal inherited neurological disorder caused by both parents passing on an expanded GAA trinucleotide repeat mutation in intron 1 of the *FXN* gene (1). This leads to reduced levels of an essential protein, called frataxin, within cells of the body. Neurons in regions of the brain, spinal cord, heart muscle cells and pancreatic cells appear to be particularly susceptible to damage because of this reduction in frataxin.

In FRDA GAA-repeat expansion in the first intron of *FRDA results in decreased levels of frataxin* owing to inhibition of transcriptional elongation. Most patients have expansions in both alleles. The longer the repeats, the lower the level of frataxin and the more severe the disease.

The YG8sR FRDA mouse model is based on expression of a GAA repeat expansion mutation containing human *FXN* transgene within a mouse frataxin null background. This model exhibits features of FRDA-like disease such as decreased motor co-ordination ability and decreased aconitase activity in heart tissue. Using this mouse model we aim to study both the long-term effects and safety of therapeutic *FXN* expression.

In vitro Studies

To drive *FXN* gene expression, LV-*FXN* have been constructed using an SFFV promoter that is found to drive high levels of reporter gene expression both *in vitro* and *in vivo* (3). These LVs carrying the eGFP reporter gene and *FXN* gene have been pseudotyped with VSV-G envelope glycoproteins, which are known to reach primary sites that are affected in the FRDA mouse model.

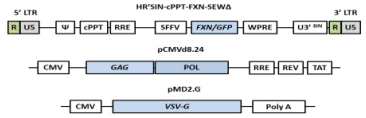

To examine the vector construct and virus infection efficiency number of positive eGFP cells in human and mouse FRDA fibroblast was measured using flowcytometry. These FRDA fibroblasts were infected with MOI of 10 and 98% of cell were positive for eGFP expression.

FRDA fibroblast treated with LV-SSFV-GFP

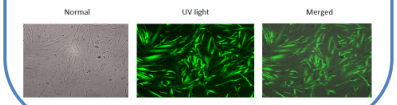

Following viral production human FRDA and mouse FRDA primary fibroblast were infected with LV-FXN and LV-eGFP pseudotyped with VSV-G envelop. To further increase the *FXN* expression these cell lines were infected once more. Copy number of 0.94 and 0.43 was achieved following second infection in mouse FRDA and human FRDA cell lines respectively. Furthermore *FXN* mRNA levels was measure using RT-qPCR and *FXN* protein was measured using sandwich ELISA quantification (Dipstick assay).

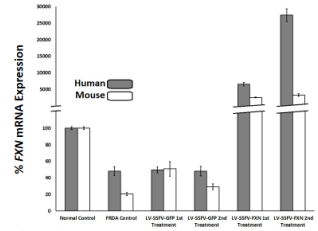

Quantification of *FXN* mRNA in expression measured using real-time RT_PCR, in mouse primary fibroblast (Normal = Y47R, FRDA & Treated=YG8sR) and human primary fibroblast (Normal= GMO7492, FRDA & Treated =GMO3665). *FXN* expression values were first normalized to GAPDH and then calibrated to normal fibroblasts expression and the mean of normal control is set to 100%. Each result is the mean of three independent experiments. The error bars represent the SEM. The Difference is statistically significant with p-values smaller than 0.05 for all samples in comparison to the untreated normal.

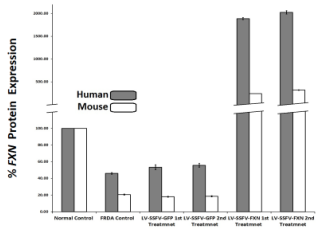

Sandwich ELISA quantification of *FXN* protein expression in mouse primary fibroblast (Normal = Y47R, FRDA & Treated=YG8sR) and human primary fibroblast (Normal= GMO7492, FRDA & Treated =GMO3665) following treatment with LV-SFFV-FXN and LV-SFFV-GFP pseudotyped with VSV-G envelop. Each result is the mean of three independent experiments. N=3 for all samples. The relative expression of frataxin is shown and the mean of normal control is set to 100%. The error bars represent the SEM. The Difference is statistically significant with p-values smaller than 0.05 for all samples in comparison to the untreated normal.

The DNA damage of Normal, untreated FRDA and FRDA LV-SFFV-FXN treated human fibroblast was investigated by measuring the number of γH2AX-foci, which directly correlates with the number of DNA double strand breaks. LV-SFFV-FXN treated FRDA fibroblasts showed decreased levels of DNA damage compared to the untreated FRDA fibroblast, suggesting that addition of copies of FXN may lead to improvement of the disease phenotype.

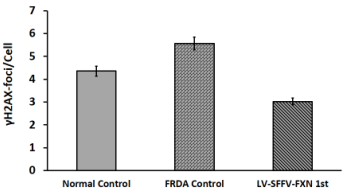

Mean number of γH2AX foci per cell measured by Image Stream. Mean calculated over the mean of 3 for Normal or 5 for FRDA and FXN experiments. Error bars show the SEM. P-values were calculated using the single values of each cell of each experiment (n=8006 for Normal, n=40464 for FRDA, and n=39664 for FXN). With a mean of 5.4 FRDA fibroblast showed higher numbers of γH2AX foci per cell compared to Normal cells with 4.3 and FXN treated cells with 3.2 foci per cell.

In vivo Studies

Routes of injection of mice **Dorsal Root Ganglia**

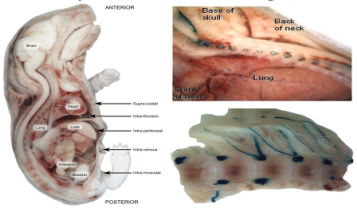

Heart **Dorsal Root Ganglia**

Neonatal and fetal mice were injected with 1x10⁹ iU/ml of LV-VSV-G pseudotyped particles (10 µl per animal).

Our group has previously demonstrated that LV-SFFV-VSV-G can provide widespread reporter gene transfer and long-term gene expression in immunocompetent outbred mice following delivery either before or after birth. We aim to repeat this study using LV-*FXN*-VSVG pseudotyped particles to evaluate gene transfer and measure the levels of correction in our mouse model (3).

Future Work

- Oxidative stress levels will determined in human and mouse FRDA fibroblast following LV-SFFV-FXN treatment.
- Measure aconitase levels to further investigation of correction of disease.
- Deliver to neuronal cells derived from our FRDA mouse model and to determine LV transduction efficiency.
- Administer LV expressing the eGFP reporter gene to and *FXN* our FRDA mouse model neonatally.
- Administer LV-*FXN* to the FRDA mouse model.

References

1. Gatchel JR, Zoghbi HY. Diseases of unstable repeat expansion: mechanisms and common principles. Nat Rev Genet. 2005 Oct;6(10):743-55.
2. Waddington SN, Buckley SM, Nivsarkar M, Jezzard S, Schneider H, Dahse T, Kemball-Cook G, Miah M, Tucker N, Dallman MJ *et al*: In utero gene transfer of human Factor IX to fetal mice can induce postnatal tolerance of the exogenous clotting Factor. *Blood* 2003, 101(4):1359-1366.
3. Themis M, Waddington SN, Schmidt M, von Kalle C, Wang Y, Al-Allaf F, Gregory LG, Nivsarkar M, Themis M, Holder MV *et al*: Oncogenesis Following Delivery of a Nonprimate Lentiviral Gene Therapy Vector to Fetal and Neonatal Mice. *Mol Ther* 2005, 12(4):763-771.

Ataxia UK Caring today, researching for tomorrow
FARA Friedreich's Ataxia Research Alliance
FRIEDREICH ATAXIA Research Association
Brunel UNIVERSITY LONDON

Poster presented at 10th Annual BSGCT conference (2013).

Lentivirus mediated *FXN* gene delivery restores genome stability and DNA damage repair potential in human and mouse FRDA fibroblasts

Hassan Khonsari , Yaghoub Gozaly , Sahar Al-Mahdawi, Steven Howe, Simon Waddington, Mark Pook and Michael Themis.

Gene Therapy Group, Division of Biosciences, Brunel University, Kingstone Lane, Uxbridge , London UK, UB8 3PH

Abstract:

Friedreich ataxia (FRDA) is a progressive neurodegenerative disease with primary sites of pathology in the large sensory neurons of the dorsal root ganglia (DRG) and dentate nucleus of the cerebellum. FRDA is also often accompanied by severe cardiomyopathy and diabetes mellitus. FRDA is caused by loss of frataxin (FXN) expression, which is due to GAA repeat expansion in intron 1 of the *FXN* gene (Fig 1). Frataxin is a mitochondrial protein important to iron-sulphur (Fe-S) cluster biogenesis and the electron transport chain (ETC). As a consequence of impaired mitochondrial energy metabolism, FRDA cells show increased levels of and sensitivity to oxidative stress, which is known to be associated with genome instability. In this study, we investigated DNA damage/repair in relation to *FXN* expression via immunostaining of YH2AX a nuclear protein that is recruited to DNA double strand breaks (DSBs). We found FRDA patient and YG8sR FRDA mouse model fibroblasts to have inherently elevated DSBs (1.8 and 0.9 foci/nucleus) compared to normal fibroblasts (0.6 and 0.2 foci/nucleus, in each case p<0.001). By delivering the *FXN* gene to these cells using a lentivirus vector (LV) at a copy number of ~1/cell, *FXN* mRNA and protein levels reached 270- and 202-fold, respectively to that of normal fibroblasts, without observable cytotoxicity. This resulted in a reduction in DSB foci to 0.7 and 0.43 (in each case p<0.001) in human and YG8sR fibroblasts, respectively and an increase in cell survival to that found for normal fibroblasts. We next irradiated the FRDA fibroblasts (2Gy) and measured their DSB repair profiles. Both human and mouse FRDA fibroblasts were unable to repair damaged DNA. However, repair returned to normal levels following LV *FXN* gene transfer. Our data suggest frataxin may be important for genome stability and cell survival. We are currently investigating whether lack of DNA damage repair in FRDA to be a factor that influences neurodegeneration.

Aim of the Study: To create a lentivirus vector carrying the *FXN* gene and to correct FRDA in human and mouse fibroblasts.

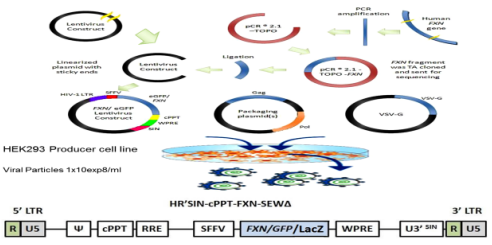

A lentivirus vector carrying the FXN gene was created via insertion of the FXN isoform 1 infront of the SFFV promoter. Vector titre reached 1x10exp8 following transfection of human 293T embryonic kidney cells

Fig 1. The GAA-repeat expansion in intron 1 of the frataxin gene decreases protein levels leading to FRDA pathology.

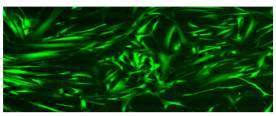

An LV GFP vector was used to show 100% gene transfer was possible to FRDA fibroblast (MOI = 10, copy number of vector genomes =1

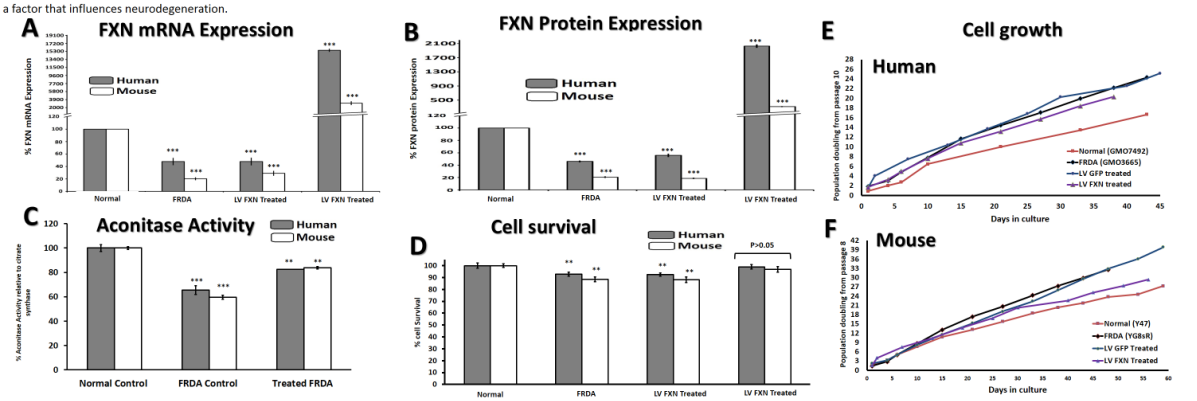

A-C) Frataxin mRNA and protein expression increases significantly in human and mouse FRDA fibroblasts treated with LV FXN along with aconitase activity. D-F) Cell survival and growth is not adversely affected following LV FXN gene transfer.

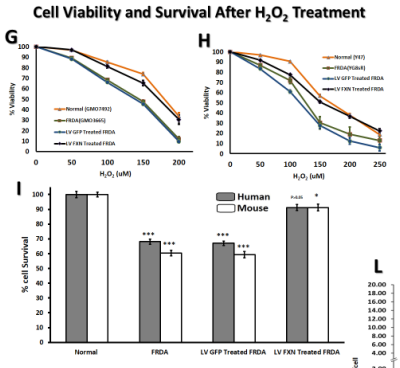

G-I)FRDA cells are more sensitive to oxidative stress when treated with H_2O_2 at increasing concentrations.

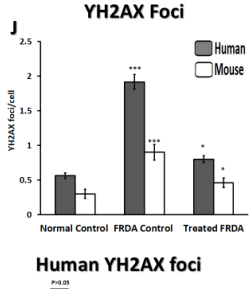

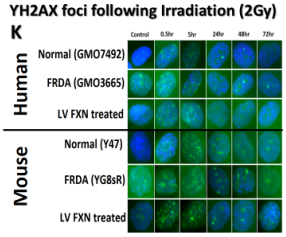

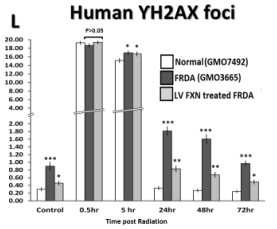

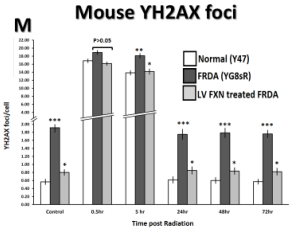

J-M) Genome instability can be measured via immunostaining of γH2AX which is recruited to DNA double strand breaks (DSB). FRDA cells have more DSB than normal fibroblasts. When FRDA fibroblasts are subjected to 2Gy radiation they are less able to repair. The ability to repair DSBs is restored following delivery with LV FXN.

Ongoing work

LV Lac Z gene transfer to mice via the intraspinal route efficiently reaches the DRG.

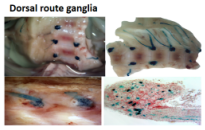

Conclusions

- **FRDA fibroblast cells are genomically unstable.**
- **FXN delivery reduces instability and improves DNA Damage repair.**
- **High FXN expression does not appear deleterious to cell survival.**
- **LV can restore FXN gene expression permanently.**
- **LV can reach DRG effectively.**

References

1. Gatchel JR, Zoghbi HY. Diseases of unstable repeat expansion: mechanisms and common principles. Nat Rev Genet. 2005 Oct;6(10):743-55.
2. Waddington SN, Buckley SM, Nivsarkar M, Jazbardi S, Schneider H, Dahse T, Kemball-Cook G, Miah M, Tucker N, Dallman MJ et al: In utero gene transfer of human Factor IX to fetal mice can induce postnatal tolerance of the exogenous clotting Factor. Blood 2003, 101(4):1359-1366.
3. Themis M, Waddington SN, Schmidt M, von Kalle C, Wang Y, Al-Allaf F, Gregory LG, Nivsarkar M, Themis M, Holder MV et al: Oncogenesis Following Delivery of a Nonprimate Lentiviral Gene Therapy Vector to Fetal and Neonatal Mice. Mol Ther 2005, 12(4):763-771.

Poster presented at International Ataxia Research Conference (2015).